

Marcus Aakre

# Impact of depositional environment and diagenesis on reservoir quality in Triassic reservoir units on the Trøndelag Platform and Ellingråsa Graben

Master's thesis in Geology

Supervisor: Arve Næss, Mai Britt E. Mørk

May 2019



Marcus Aakre

# Impact of depositional environment and diagenesis on reservoir quality in Triassic reservoir units on the Trøndelag Platform and Ellingråsa Graben

Master's thesis in Geology  
Supervisor: Arve Næss, Mai Britt E. Mørk  
May 2019

Norwegian University of Science and Technology  
Faculty of Engineering  
Department of Geoscience and Petroleum



# Abstract

The main objective for this thesis has been to determine the impact of depositional environment and diagenesis on reservoir quality in Triassic units on the Trøndelag Platform and Ellingråsa Graben. The impact of evaporites of the Triassic Lower and Upper Salt on reservoir quality has also been investigated.

This work has included a literature study on geological history, regional geology, diagenesis and reservoir quality. A set of Norwegian Sea wellbores penetrating the Triassic succession has been selected for detailed analysis. Moreover, petrophysical logs have been made from raw data obtained from the NPD Diskos Database, and sedimentological logs have been created from core photos and cores, prior to sampling from the A-cut. Furthermore, selected samples from wellbores 6610/7-2, 6507/6-1, 6507/12-1 and 6507/12-2 have been analyzed in detail by optical microscopy, SEM and XRD.

In terms of depositional environment, petrophysical and sedimentary logs confirmed existing models which demonstrate that the topography of the Trøndelag Platform was dominated by a low relief during Anisian to Rhaetian times, while the Nordland Ridge in the west stood out as a topographic high. In addition, the core and sample findings indicated an arid to semi-humid climate and that the relative sea level has been fluctuating in relation to the concealment of the Trøndelag basin.

In all four wellbores various diagenetic evolutions have been observed, but clear trends have also been identified for the wells combined. First of all, it has been observed that detrital feldspar suffered kaolinization and illitization at an early stage of diagenesis. The mineral assemblage indicated that kaolinite has been replaced by illite and chlorite in relation to the geothermal gradient. In general, massive quartz cementation seems to have been restricted by clay coating minerals. Moreover, at temperatures higher than 100°C, authigenic chlorite and growth of calcite cement has been identified. In absence of illite, chlorite have replaced smectite, while illite has been replaced by chlorite in the deepest part of the wells. Finally, in relation to the evaporitic minerals, mass transfer from the Triassic Upper Salt may have caused supra-salt precipitation of intergranular anhydrite.

By investigating the diagenetic evolution for the respective wells, including their porosity models, it became clear that the number of sub-salt zones with preserved reservoir quality was limited. It should be noted that the observed main reducing reservoir quality factors were; mineralogical immaturity, compaction, authigenic clay minerals, calcite and dolomite cements and mass transferred anhydrite. Nevertheless, in layers of preserved reservoir quality, the cementation rates were low and intragranular salt minerals have restricted extensive growth of authigenic clay minerals. Supra-salt, the porosity was found to be greater than 15% for several units at depths shallower than 2300, 2160, 3100 and 3100 m for the respective wells.

The results of this study have indicated that the Triassic evaporite layers of Carnian age have affected the surrounding reservoirs, both reducing the porosity in some areas, as well as preserving the porosity in other areas. Even if the approach of determining impact of depositional environment and diagenetic altering of reservoir quality has been covered by an extensive set of methods, a wider research work is required to get the complete picture. Therefore, utilizing the current work together with a broader data set of wellbores and samples, in addition to applying other methods such as seismic interpretation, X-ray fluorescence and radiometric dating is recommended as further work. Additionally, by expanding the investigation to other areas of the world with a similar geological setting, the understanding of the Norwegian Sea basins can be further enhanced. Finally, it could also be of value to construct the structural geological development from the observed depositional environments and diagenetic histories.

# Sammendrag

Formålet med denne masteroppgaven har vært å avgjøre hvordan avsetningsmiljø og diagenese påvirker reservoarkvaliteten i reservoarer fra trias på Trøndelagsplattformen og i Ellingråsagraben. Hvordan evaporitter fra trias påvirket reservoarkvaliteten har også vært av interesse.

Dette arbeidet har innebært et litteraturstudium i geologisk historie, regionalgeologi, diagenese og reservoarkvalitet. Videre har brønner fra Norskehavet som penetrerer triaslagrekken blitt utvalgt for grundige undersøkelser. Petrofysikk-logger ble konstruert av rådata fra databasen NPD Diskos og deretter analysert. I tillegg ble sedimentologiske logger dannet fra kjernebilder og kjerner i forkant av prøvetaking fra A-kuttet. Utvalgte prøver fra brønnene 6610/7-2, 6507/6-1, 6507/12-1 og 6507/12-2 har blitt analysert i detalj med optisk mikroskop, SEM og XRD.

Når det gjelder avsetningsmiljø bekreftet petrofysiske og sedimentære logger eksisterende modeller som viser at topografien på Trøndelagsplattformen gjennomgående bestod av et lavt relieff fra anis til ræt alder, mens Nordlandsryggen i vest stod opp som en topografisk høyde. I tillegg indikerte prøvefunnene at klimaet var tørt til semi-fuktig og at det relative havnivået fluktuerte i forhold til avlukkingen av Trøndelagsbassenget.

Det har i de fire brønnene blitt observert ulike diagenetiske utviklinger, men klare trender har også blitt identifisert for brønnene samlet. For det første har det blitt observert at detrital feltspat ble kaolinisert og illitisert i et tidlig stadie av diagenesen. Fra mineralsammensetningen ble det vist at kaolinit ble erstattet av illitt og kloritt med den geotermale gradienten. Generelt har leirbeleggende mineraler motvirket massiv sementering av kvarts. Vekst av autigen kloritt og kalsittsmentering startet ved temperaturer rundt 100°C. I fravær av illitt, har kloritt erstattet smektitt, mens kloritt erstattet illitt i de dypeste sekvensene av brønnene. Til sist, med tanke på evaporitt-mineralene, kan det se ut til at masseoppløst anhydritt har blitt overført fra saltlagene i trias og avsatt intergranulært supra-salt.

Ved å undersøke den diagenetiske utviklingen for de respektive brønnene i kombinasjon med porositetsmodellene deres, ble det åpenbart at et begrenset antall sub-salt soner hadde bevart reservoarkvalitet. Det bør merkes at de observerte

hovedfaktorene som reduserer reservoarkvaliteten var; mineralogisk umodenhet, kompaksjon, autigene leirmineraler, kalsitt- og dolomittsentering og overføring av masseoppløst anhydritt. I lagene med bevart reservoarkvalitet, var sementeringsgraden lav og intragranulære saltmineraler har motvirket omfattende vekst av autigene leirmineraler. Supra-salt var porøsiteten høyere enn 15% for flere enheter ved dybder grunnere enn 2300, 2160, 3100 og 3100 m for de respektive brønnene.

Resultatene fra dette studiet har vist at evaporitter fra trias av karn alder har påvirket de omkringliggende reservoarene, ved å gi redusert porøsitet i noen områder, men også bevart porøsitet i andre områder. Selv om fremgangsmåten for å avgjøre hvordan avsetningsmiljø og diagenese påvirker reservoarkvaliteten inneholdt bruk av petrofysiske og sedimentologiske logger, optisk mikroskopering, samt SEM- og XRD-analyser, kreves det utvidede undersøkelser for å danne et mer helhetlig bilde. Derfor er anbefalt videre arbeid å kombinere det gjennomførte arbeidet med et større datasett av brønner og prøver, samt legge til andre vitenskapelige metoder slik som seismisk tolkning, røntgenfluorescens og radiometrisk datering. Ved å utvide undersøkelsen til andre steder i verden med lik geologisk setting, kan forståelsen av Norskehavets bassenger forbedres. Avslutningsvis kan det også være verdifullt å konstruere den strukturgeologiske utviklingen fra de observerte avsetningsmiljøene og diagenetiske historiene.



# Preface

This master's thesis concludes the Master's programme within Bedrock and Resource Geology at the Norwegian University of Science and Technology (NTNU), resulting in a M.Sc. degree in Geology.

I wish to express my sincerest gratitude to my supervisor, Arve Næss, holding a Professor II position in the Department of Geoscience and Petroleum (IGP) at NTNU. His broad experience both from academic work, as well as from the Equinor Research Centre has been of great importance throughout this past year.

I would like to thank my co-supervisor, Professor Mai Britt E. Mørk from IGP. She has always been available for questions and fruitful discussions, and her expertise have been a key factor for understanding the concepts of this work.

I would also like to express my appreciation to Senior Engineers Laurentius Tjihuis and Torill Sørlokke for guidance during XRD analysis. Thanks to Staff Engineer Kjetil Eriksen for excellent preparation work on my thin sections and assistance during SEM analysis. My special thanks are extended to Professor Atle Mørk for providing his expertise opinion on the discovered fossil fragments.

The successful cooperation between NTNU and the NPD Diskos database is highly appreciated. Without having been granted the access to the database, this work would not have been possible to carry out.

Furthermore, I would like to thank my friends for the wonderful times we have shared. Also, I am grateful to my family for believing in me and supporting me throughout my life. And last but not least, Marlene Louise Lund, I am beyond grateful for the companionship, encouragement and massive support you have offered me. You lift me higher, and I would never have been where I am today if it wasn't for you.

## **Declaration of Compliance**

I hereby declare that this is an independent work according to the exam regulations of the Norwegian University of Science and Technology.

Trondheim, May 2019  
Marcus Aakre



# Contents

<b>Abstract</b>	<b>i</b>
<b>Sammendrag</b>	<b>iii</b>
<b>Preface</b>	<b>v</b>
<b>List of figures</b>	<b>xii</b>
<b>List of tables</b>	<b>xvii</b>
<b>List of abbreviations</b>	<b>xx</b>
<b>List of symbols</b>	<b>xxiii</b>
<b>1 Introduction</b>	<b>1</b>
1.1 Motivation . . . . .	2
1.2 Scope of work . . . . .	2
1.3 Outline . . . . .	3
<b>2 Geological History (Phanerozoic)</b>	<b>5</b>
2.1 Pre Triassic (541-252 Ma) . . . . .	5
2.1.1 Cambrian, Ordovician, Silurian (541-419 Ma) . . . . .	5
2.1.2 Devonian, Carboniferous, Permian (419-252 Ma) . . . . .	5
2.2 The Triassic evolution (252-201 Ma) . . . . .	6
2.3 Post Triassic (201-0 Ma) . . . . .	8
2.3.1 Jurassic (201-145 Ma) . . . . .	8
2.3.2 Cretaceous (145-66 Ma) . . . . .	8
2.3.3 Cenozoic (66-0 Ma) . . . . .	9
<b>3 Regional geology</b>	<b>11</b>
3.1 Norwegian Sea field area . . . . .	11

3.2	Tectonic history and structural elements of the Norwegian Sea	13
3.3	The Trøndelag Platform and Halten Terrace . . . . .	14
3.4	The Ellingråsa Graben . . . . .	17
3.5	Stratigraphic subdivision of the Permo-Triassic . . . . .	20
3.5.1	Lithostratigraphy of the Triassic, Mid-Norway . . . . .	22
<b>4</b>	<b>Diagenesis</b>	<b>25</b>
4.1	Conceptual regimes . . . . .	25
4.1.1	Eogenesis . . . . .	26
4.1.2	Mesogenesis . . . . .	28
4.1.3	Telogenesis . . . . .	30
4.2	Geothermal gradient . . . . .	31
4.2.1	Heat flow . . . . .	31
<b>5</b>	<b>Lithology and reservoir quality</b>	<b>33</b>
5.1	Lithology . . . . .	33
5.1.1	Evaporites . . . . .	33
5.1.2	Sandstone, claystone and shale . . . . .	35
5.2	Porosity . . . . .	39
5.2.1	Petrophysical porosity curve . . . . .	40
5.2.2	Intergranular volume . . . . .	40
5.2.3	Volumetric rock model . . . . .	40
5.3	Reservoir quality . . . . .	41
<b>6</b>	<b>Mineralogy and petrography</b>	<b>43</b>
6.1	Optical microscopy . . . . .	43
6.2	Scanning electron microscope . . . . .	43
6.3	X-ray diffraction . . . . .	44
<b>7</b>	<b>Methodology</b>	<b>47</b>
7.1	Data set . . . . .	47
7.1.1	Wellbores . . . . .	47
7.1.2	Petrophysical logging . . . . .	49
7.1.3	Sedimentological logging . . . . .	52
7.1.4	Sampling . . . . .	54
7.1.5	Facies description and facies association . . . . .	55
7.2	Geothermal gradient . . . . .	55
7.3	Mineralogical and petrographical analyses . . . . .	56
7.3.1	Thin section analysis . . . . .	56
7.3.2	Scanning electron microscope (SEM) . . . . .	60

7.3.3	X-ray diffraction (XRD) . . . . .	60
7.3.4	Applied methods . . . . .	63
7.4	Sources of error . . . . .	64
7.4.1	Data set . . . . .	64
7.4.2	Mineralogical and petrographical analysis . . . . .	65
<b>8</b>	<b>Results</b>	<b>67</b>
8.1	Petrophysical results . . . . .	67
8.1.1	Density porosity curves . . . . .	74
8.2	Sedimentological logging . . . . .	79
8.3	Facies and facies association . . . . .	85
8.3.1	Facies description . . . . .	86
8.3.2	Facies association . . . . .	94
8.4	Geothermal gradient . . . . .	96
8.5	Mineralogical and petrographical description . . . . .	100
8.5.1	Thin section and point counting results . . . . .	100
8.5.2	SEM results . . . . .	122
8.5.3	XRD results . . . . .	132
<b>9</b>	<b>Discussion</b>	<b>141</b>
9.1	Depositional environment . . . . .	141
9.1.1	Theory to be addressed . . . . .	141
9.1.2	Petrophysical logs . . . . .	142
9.1.3	Sedimentological logs . . . . .	143
9.1.4	Facies association . . . . .	146
9.1.5	Mineralogy and petrography . . . . .	146
9.1.6	Provenance . . . . .	147
9.2	Diagenetic history . . . . .	148
9.2.1	Feldspar . . . . .	148
9.2.2	Clay minerals . . . . .	149
9.2.3	Authigenic cements and evaporite minerals . . . . .	152
9.2.4	Visualization of the diagenetic history . . . . .	155
9.3	Reservoir quality . . . . .	156
9.3.1	Porosity . . . . .	156
9.3.2	Compaction, mineralogical maturity and evaporites . . . . .	158
<b>10</b>	<b>Conclusions and recommendations for further work</b>	<b>161</b>
10.1	Conclusions . . . . .	161
10.2	Further work . . . . .	164

<b>Bibliography</b>	<b>165</b>
<b>A Core logs</b>	<b>I</b>
<b>B Geothermal gradient parameters</b>	<b>XXIX</b>
<b>C Thin section results</b>	<b>XXXI</b>
<b>D Point counting results</b>	<b>XXXV</b>
<b>E SEM results</b>	<b>XXXVII</b>
E.1 EDS spectra . . . . .	XXXVII
<b>F XRD results</b>	<b>XLVII</b>

# List of figures

2.1	Reconstruction of the continents placement on the supercontinent Pangea at Middle and Late Triassic times, about 240-220 Mya. Dark blue is oceanic crust while light blue is continental crust. The white dot is the suggested location of Norway [1]. . . . .	7
3.1	Structural elements of the NCS showing the transect between the seismic lines EE' and FF' crossing the Ellingråsa Graben marked in orange. Edited from Blystad et al. [2]. . . . .	12
3.2	An overview of 20 handpicked wellbores from the Norwegian Sea in relation to their structural elements. The Ellingråsa Graben is marked in yellow and the map was made using ArcGIS on NPD FactMaps.	14
3.3	Relation of wellbores to discoveries in the Norwegian Sea area. .	15
3.4	Hydrocarbon fields close to the Ellingråsa Graben. . . . .	16
3.5	The Ellingråsa Graben, highlighted in yellow, is an area of intra-basinal elevations. . . . .	18
3.6	A reference section for the Ellingråsa Graben is given by the seismic lines SG-8710-410 in Profile EE', as well as 731-460 and 726-460 in Profile FF'. Edited from NPD - Bulletin No 8 [2]. . . . .	19
3.7	Stratigraphic overview of Late Permian and Triassic. Edited from Müller et al., 2005 [3]. . . . .	21
5.1	Successive phases of complete evaporation of seawater with the characteristic bull's eye pattern. Based on work from C.A Baar, 1977 [4].	34
5.2	QFL sandstone classification diagram. From Folk, 1970 [5]. . . .	36
5.3	Illustration of clay building blocks. Based on Ellis & Singer's work on <i>Well Logging for Earth Scientists</i> , 2008 [6]. . . . .	37
5.4	Illustration of shale and clay distribution in a sandstone. The dispersed clay show pore filling, lining and bridging clay. Based on work from Ellis & Singer, 2007 [6]. . . . .	38



5.5	A model showing the development of porosity and density with depth for shale (green) and sandstone (red). . . . .	39
5.6	Indicates the components for the bulk volume of the rock. The figure is based on work by Ellis and Singer, 2008, and the Petrophysics Advanced course by Erik Skogen, 2018 [6]. . . . .	41
6.1	Simplified sketch of the conditions required for the transmitting X-rays to diffract from a two-dimensional crystal lattice to the receiver. . . . .	45
7.1	The upper part of the log for well 6507/6-1 at a scale of 1:200. The log is generated using Techlog on raw data from the Diskos NDR. . . . .	51
7.2	An illustration of how the core is cut. The different cuts A through D are used for different purposes. . . . .	53
7.3	Shows the naming method of the collected samples from Weatherford's core storage. . . . .	54
7.4	The resulting thin sections numbered from sample 1 to 14. Dark colored glass (e.g. sample 1) have been carbon coated for SEM analysis. . . . .	57
7.5	Grain shape terminology sorted from very angular to well rounded. From Powers (1953) [7]. . . . .	58
7.6	Sorting terminology sorted from very well sorted to very poorly sorted. From Compton, 1962 [8]. . . . .	58
7.7	Feldspar preservation grades from I to V. Pictures are taken of thin sections from wellbore 6610/7-2. . . . .	59
7.8	Example of a bulk and fine fraction XRD diffractogram. The upper plot is the bulk XRD diffractogram, while the lower shows the fine fraction diffractogram. . . . .	62
8.1	Wellbore correlation of Triassic Unit Tr1 to Unit Tr5. . . . .	68
8.2	Structural elements of the NCS with the position of the wells investigated in Figure 8.1. This is an edited version of a figure from [2]. . . . .	69
8.3	Petrophysical log of wellbore 6507/12-2 showing Lower Salt and core from the respective well, constructed using Techlog. . . . .	70
8.4	Petrophysical log of wellbore 6610/7-2 showing the cored section in relation to the salt observed in the well. The figure was constructed using Techlog. . . . .	72
8.5	Petrophysical log of wellbore 6507/12-1 showing the cored section. The figure was constructed using Techlog. . . . .	73
8.6	Petrophysical log of wellbore 6507/6-1 showing the cored section. The figure was constructed using Techlog. . . . .	74

8.7	Density porosity curves for wellbore 6507/12-2. The log depth is MD. . . . .	75
8.8	Density porosity curves for wellbore 6507/12-1. . . . .	76
8.9	Density porosity curves for wellbore 6507/6-1. . . . .	77
8.10	Density porosity curves for wellbore 6610/7-2. . . . .	78
8.11	Lithological and structural legend for the sedimentary logs. . . .	80
8.12	Sedimentary log of core 4 from well 6507/12-1 at a scale of 1:100, including core description. . . . .	81
8.13	Sedimentary log of core 2 from well 6507/12-2 at a scale of 1:100, including core description. . . . .	82
8.14	Sedimentary log of core 2 from well 6610/7-2 at a scale of 1:100, including core description. . . . .	83
8.15	Sedimentary log of core 3 from well 6507/6-1 at a scale of 1:100, including core description. . . . .	84
8.16	Sedimentary log overview that compare the four chosen wells at a scale of 1:100. . . . .	85
8.17	The thin section sample cuts give an indication of which facies number (F1-F12) that belongs to the given sample number (1-14). The lower pictures shows the thin section sample cuts from the back side. Numbering of samples at the lower picture follows the method used in the upper picture. Sample 9 is a swelling clay type, and did not make it to the wall of fame. . . . .	87
8.18	Facies number 1 (sample 10, see Table 8.1 and 8.3) is the light gray matrix facies, F2 (A and B - sample 13 and 5) is the red to brown matrix facies, F3 is the pinkish-gray matrix facies, F4 (sample 11) is the green matrix facies. . . . .	89
8.19	Facies number 5 (sample 14) is the stylolite facies, F6 is the breccia facies, F7 is the wavy laminated facies, F8 (sample 5) is the calcite nodule facies and F9 (sample 9) is the swelling facies. . . . .	91
8.20	10A is a proposed interpretation of 10B (sample 11) and illustrate both the planar laminated and the cross-bedded facies. 11A and 11B show the cross-bedded facies. 11A is an interpretation of 11B (sample 6). . . . .	93
8.21	A plot showing geothermal gradients and penetration depth for the individual wells. . . . .	97
8.22	Geothermal gradient for well 6507/12-2. The depth from RKB to the sea floor is 286 m, and has to be added to the depth to get the MD. . . . .	98
8.23	Geothermal gradient for well 6507/12-1. The depth from RKB to the sea floor is 250 m, and has to be added to the depth to get the MD. . . . .	99
8.24	Geothermal gradient for well 6610/7-2 and well 6507/6-1. . . . .	100

8.25	Sample plot in the QFL sandstone classification diagram. . . . .	101
8.26	Sample 1, 6507/6-1, 3044.45 m. Objective magnification marked in yellow. Multiplying by the eyepiece magnification of 10 gives the correct zoom. . . . .	103
8.27	Thin section images of sample 3, 6507/12-1, 3711.5 m . . . . .	105
8.28	Thin section images of sample 4, 6507/12-1, 3717.0 m . . . . .	107
8.29	Molluscs from sample 4, 6507/12-1, 3717.0 m . . . . .	108
8.30	Sample 5, 6507/12-2, 4982.3 m . . . . .	110
8.31	Thin section images of sample 13, 6507/12-2, 4983.9 m . . . . .	111
8.32	Thin section images of sample 10, 6610/7-2, 4180.4 m . . . . .	113
8.33	Thin section images of sample 11, 6610/7-2, 4184.65 m . . . . .	115
8.34	Thin section images of sample 14, 6610/7-2, 4187.15 m . . . . .	117
8.35	Thin section images of sample 14, 6610/7-2, 4187.15 m . . . . .	118
8.36	Thin section images of sample 12, 6610/7-2, 4194.05 m . . . . .	120
8.37	A bar plot visualizing the point counting results. The samples are sorted with respect to depth, with the shallowest sample in the top. . . . .	121
8.38	Results from SEM analysis performed on sample 1 at a magnification of 600x. . . . .	122
8.39	Results from SEM analysis performed on sample 1 at a magnification of 1300x. . . . .	123
8.40	Results from SEM morphology of sample 1 at a magnification of 4000x in A, and 3000x in B. . . . .	124
8.41	Results from SEM analysis of sample 3 at a magnification of 500x. . . . .	125
8.42	Results from SEM analysis of sample 5 at a magnification of 700x. . . . .	126
8.43	Results from SEM analysis of sample 5 at a magnification of 1100x. . . . .	126
8.44	Results from SEM analysis performed on sample 11 at a magnification of 800x. . . . .	127
8.45	Results from SEM analysis performed on sample 11 at a magnification of 2200x. . . . .	128
8.46	Results from SEM morphology of sample 11 at a magnification of 2500x. . . . .	129
8.47	Results from SEM analysis of sample 12 at a magnification of 130x. . . . .	130
8.48	Results from SEM analysis of sample 12 at a magnification of 250x. . . . .	130
8.49	Results from SEM analysis performed on sample 13 at a magnification of 1800x. . . . .	131
8.50	Bulk- and fine fraction XRD diffractograms of the subarkosic sample 1 from Unit Tr3. . . . .	133
8.51	Bulk XRD diffractograms of sample 3 (siltstone) from Unit Tr5. . . . .	135
8.52	Bulk XRD diffractograms of sample 5 (siltstone) from Unit Tr3. . . . .	135

8.53	Bulk- and fine fraction XRD diffractograms for sample 11 (arkose) from Unit Tr3. . . . .	137
8.54	Bulk- and fine fraction XRD diffractograms for sample 12 (arkose) from Unit Tr3. . . . .	138
8.55	Bulk XRD diffractograms for sample 13 (claystone) situated in Unit Tr3. . . . .	139
8.56	A bar plot showing the bulk XRD mineral composition from the six examined samples. . . . .	140
9.1	Proposed depositional environment of described wells during the Triassic Period. . . . .	145
9.2	Interpretation showing diagenetic stable intervals, diagenetic unstable intervals and intervals of absence for the respective minerals listed to the left, in terms of temperature in the respective wellbores. . . .	155
A.1	Sedimentary log of well 6610/7-2 . . . . .	IV
A.2	Sedimentary log of well 6507/12-1 . . . . .	VII
A.3	Sedimentary log of well 6507/6-1 . . . . .	XV
A.4	Sedimentary log of well 6608/8-1 . . . . .	XIX
A.5	Sedimentary log of well 6608/11-1 . . . . .	XXV
A.6	Sedimentary log of well 6507/12-2 . . . . .	XXVIII
E.1	The resulting EDS spectra for quartz - SiO <sub>2</sub> . . . . .	XXXVII
E.2	EDS spectra for K-feldspar (orthoclase or microcline) - KAlSi <sub>3</sub> O <sub>8</sub> .XXXVIII	
E.3	EDS spectra for alkali feldspar (sanidine) - Na <sub>0,3</sub> K <sub>0,7</sub> AlSi <sub>3</sub> O <sub>8</sub> . . . XXXVIII	
E.4	The resulting EDS spectra of albite - NaAlSi <sub>3</sub> O <sub>8</sub> . . . . .	XXXIX
E.5	The resulting EDS spectra for plagioclase (andesine): 33% albite - NaAlSi <sub>3</sub> O <sub>8</sub> , 67% anorthite - CaAl <sub>2</sub> Si <sub>2</sub> O <sub>8</sub> . . . . .	XXXIX
E.6	The resulting EDS spectra for muscovite - KAl <sub>2</sub> (AlSi <sub>3</sub> O <sub>10</sub> )(F,OH) <sub>2</sub> . . . . .	XL
E.7	The resulting EDS spectra for biotite - K(Mg,Fe) <sub>3</sub> AlSi <sub>3</sub> O <sub>10</sub> (F,OH) <sub>2</sub> . . . . .	XL
E.8	The resulting EDS spectra for kaolinite - Al <sub>4</sub> [Si <sub>4</sub> O <sub>10</sub> ](OH) <sub>8</sub> . . . . .	XLI
E.9	EDS spectra for illite - K <sub>1,5</sub> (Si <sub>8</sub> Al <sub>1,5</sub> (Al <sub>4</sub> Fe <sub>4</sub> Mg <sub>4</sub> )O <sub>20</sub> (OH) <sub>4</sub> . . . . .	XLI
E.10	Chlorite - (Mg,Fe <sup>2+</sup> ,Fe <sup>3+</sup> ,Mn,Al) <sub>12</sub> [(Si,Al) <sub>8</sub> O <sub>20</sub> ](OH) <sub>16</sub> . . . . .	XLII
E.11	The resulting EDS spectra for anhydrite - CaSO <sub>4</sub> . . . . .	XLII
E.12	The resulting EDS spectra for perchlorate salt - ClO <sub>4</sub> <sup>-</sup> . . . . .	XLIII
E.13	The resulting EDS spectra for calcite - CaCO <sub>3</sub> . . . . .	XLIII
E.14	The resulting EDS spectra for ankerite - Ca(Fe,Mg,Mn)(CO <sub>3</sub> ) <sub>2</sub> . . . . .	XLIV
E.15	The resulting EDS spectra for rutile - TiO <sub>2</sub> . . . . .	XLIV

E.16	The resulting EDS spectra for ilmenite - $\text{FeTiO}_3$ and Iron oxides - $\text{Fe}_x\text{O}_{x+1}$ . . . . .	XLV
E.17	The resulting EDS spectra for pyrope-almandine garnet - $\text{Mg}_3\text{Al}_2\text{Si}_3\text{O}_{12}$ - $\text{Fe}_3\text{Al}_2\text{Si}_3\text{O}_{12}$ . . . . .	XLV
E.18	The resulting EDS spectra for iron oxides - $\text{Fe}_x\text{O}_x$ . . . . .	XLVI

# List of tables

4.1	Eogenetic processes in sandstones and their impact on reservoir quality, modified from Morad et al., 2010 [9]. . . . .	27
4.2	Mesogenetic processes in sandstones and their impact on reservoir quality. From Morad et al. (with modifications) [9]. . . . .	29
4.3	Comparison of Meteoric water linked to telogenesis versus burial pore fluids linked to eogenesis and mesogenesis. . . . .	30
4.4	Diagenetic terms, modified from Worden and Burley, 2009 [10]. . . . .	31
7.1	20 wellbores from the Norwegian Sea. Wellbore 2, 5, 9 and 10 penetrates Precambrian basement. The column showing <i>oldest penetrated age</i> excludes the basement. *Informal name. . . . .	48
7.2	Nine wellbores from the Norwegian Sea selected according to availability of data. . . . .	49
7.3	Some of the applications for the log measurements used in the constructed logs. . . . .	50
7.4	Six wellbores from the Norwegian Sea selected for core sampling. . . . .	52
7.5	Wenworth (1922) grain size scale [11]. . . . .	53
7.6	14 samples from six different wellbores in the Norwegian Sea collected from Weatherford's core storage in Stavanger. Here, MD is short for measured depth, sst is short for sandstone, clst is short for claystone and lmst is short for limestone. . . . .	55
7.7	An overview of the methods used on the different samples. (X) means that the method is preformed, but not included among the results in this thesis. . . . .	63

8.1	Sedimentological facies found in cores from the six logged wells. . . . .	86
8.2	FA1-FA4 with their characteristics and depositional environment. Mudstone is a common term for claystone and siltstone combinations. The table is based on core findings and work by R. Müller et al., 2005 [3]. Mdst=mudstone. . . . .	94
8.3	14 samples from six different wellbores in the Norwegian Sea collected from Weatherford's core storage in Stavanger. S is short for sample, while sltst is short for siltstone. . . . .	96
B.1	An overview of the parameters used to calculate the geothermal gradients, $T(z)$ , by curve fitting methods. . . . .	XXIX
C.1	Thin section results from sample 1-5. . . . .	XXXI
C.2	Thin section results from sample 6-10. . . . .	XXXII
C.3	Thin section results from sample 11-14. . . . .	XXXII
C.4	Remarks to the thin section results from sample 1-14. . . . .	XXXIII
D.1	This table is used as a basis for constructing a QFL classification diagram. Quartz is the sum of monocrystalline and polycrystalline quartz, feldspar is the sum of feldspar, K-feldspar and plagioclase, rock fragment is the sum of muscovites, reworked biotites, anhydrite grains, chlorite grains, heavy minerals, rock fragments, sparite rock fragments, micrite rock fragments and opaque minerals. . . . .	XXXV
D.2	Overview of point counting results. . . . .	XXXVI
D.3	Matrix is the sum of sparite matrix and micrite matrix, cement is the sum of calcite cement and quartz cement, and diagenetic products is the sum of diagenetic anhydrite, chlorite and kaolinite. . . . .	XXXVI
F.1	Overview of the XRD results. . . . .	XLVII



# List of abbreviations

<b>A</b>	Artifact
<b>Ah</b>	Anhydrite
<b>APA</b>	Awards in predefined areas
<b>BCU</b>	Base Cretaceous Unconformity
<b>Ca</b>	Calcite
<b>CALI</b>	Caliper
<b>CBW</b>	Clay bound water
<b>Ch</b>	Chlorite
<b>Cl</b>	Clay
<b>cL</b>	Lower coarse
<b>Clst</b>	Claystone
<b>cU</b>	Upper coarse
<b>DRHO</b>	Bulk density correction
<b>DT</b>	Delta-T or interval transit time
<b>EDS</b>	Energy dispersive X-ray spectroscopy
<b>E&amp;P</b>	Exploration and production
<b>F</b>	Feldspar
<b>FA</b>	Facies association
<b>fL</b>	Lower fine
<b>fU</b>	Upper fine
<b>IGV</b>	Intergranular volume
<b>ILD</b>	Induction deep resistivity
<b>ILM</b>	Induction medium resistivity
<b>Kf</b>	K-feldspar
<b>L</b>	Lithic
<b>LLD</b>	Laterolog deep resistivity
<b>LLS</b>	Laterolog shallow resistivity
<b>Lmst</b>	Limestone
<b>Ma</b>	Mega-annum
<b>MCFL</b>	Microcylindrically focused log
<b>MD</b>	Measured depth
<b>Mdst</b>	Mudstone
<b>Mic</b>	Micrite



<b>mL</b>	Lower medium
<b>Mu</b>	Muscovite
<b>mU</b>	Upper medium
<b>MSFL</b>	Micro-spherically-focused resistivity
<b>MSL</b>	Mean sea level
<b>Mya</b>	Million years ago
<b>NCS</b>	Norwegian continental shelf
<b>NDR</b>	National Data Repository
<b>NGU</b>	Geological Survey of Norway
<b>NGU</b>	Geological Survey of Norway
<b>NPD</b>	Norwegian Petroleum Directorate
<b>NPHI</b>	Thermal neutron porosity
<b>O.e.</b>	Oil equivalents
<b>OM</b>	Organic material
<b>Pl</b>	Plagioclase
<b>Po</b>	Porosity
<b>PPL</b>	Plane-polarized light
<b>Py</b>	Pyrite
<b>Q</b>	Quartz
<b>REFL</b>	Reflected light
<b>RF</b>	Rock fragment
<b>RHOB</b>	Bulk density
<b>RKB</b>	Rotary kelly bushing
<b>Rpm</b>	Rounds per minute
<b>SEM</b>	Scanning electron microscope
<b>Slt</b>	Silt
<b>Sltst</b>	Siltstone
<b>Spa</b>	Sparite
<b>Sst</b>	Sandstone
<b>Sty</b>	Stylolite
<b>TD</b>	Total depth
<b>Tu</b>	Turmaline
<b>TVD</b>	True vertical depth
<b>vcL</b>	Lower very coarse
<b>vcU</b>	Upper very coarse
<b>vfL</b>	Lower very fine
<b>vfU</b>	Upper very fine
<b>XPL</b>	Cross-polarized light
<b>XRD</b>	X-ray diffraction
<b>Zi</b>	Zircon



# List of symbols

Symbol	Description
$\sim$	Approximately
$\rightarrow$	Chemical reaction arrow
$<$	Smaller than
$>$	Larger than
$C^\circ$	Degrees Celsius
$d$	Atom spacing
$d_{hkl}$	Distance between planes of atoms
$dT/dz$	Thermal gradient
$k$	Thermal conductivity
$\mu m$	Micrometer
$n$	Count
$\%$	Percentage
$\rho_b$	Bulk density
$\rho_f$	Fluid density
$\rho_{ma}$	Matrix density
$\phi_e$	Effective porosity
$\phi_{log}$	Log porosity
$\phi_t$	Total porosity
$Q$	Heat flow
$R_x$	Receiver
$\sigma_1$	Maximum stress
$Sm^3$	Standard cubic meter
$\theta$	Angle
$T_x$	Transmitter
$V_b$	Bulk volume
$\lambda$	Wavelength



# Chapter 1

## Introduction

The history of petroleum exploration in Norway goes back to the early 1960s. In February 1958, the Geological Survey of Norway (NGU) confirmed the absence of petroleum on the Norwegian continental shelf. In 1967, Phillips Petroleum proved this wrong by discovering the Balder field in the North Sea region. The Norwegian Sea region of the Norwegian continental shelf was first opened for petroleum exploration in 1979. The first exploration wellbore, penetrating the Triassic succession in the Norwegian Sea region, was wellbore 6507/12-1. It was spudded on the 1<sup>st</sup> of July 1980 by Saga Petroleum ASA. The wellbore was declared dry, plugged and abandoned about four months later, but started a series of over 80 exploration wellbores stratigraphically reaching the Triassic Period in the Norwegian Sea region.

The Petroleum System was defined by Leslie B. Magoon and Edward A. Beaumont in 1999 [12]. It consists of the four components; mature source rock, migration pathway, reservoir and a sealing trap. In addition, the relative timing of these components are necessary for hydrocarbon accumulation and preservation. The quality of the reservoir itself depends on the diagenetic evolution of the sediments from deposition in its respective depositional environment. Thus, the exploration and production (E&P) companies spend time and resources trying to generate the best possible models of the original depositional environment. Stating the correct depositional environment is a key factor of understanding the diagenetic evolution during burial of the sediments. The deeper the reservoir, the more important the diagenetic evolution becomes. These are some of the main driving forces for determining the reservoir quality in Petroleum Systems.

## 1.1 Motivation

Norwegian Sea fields are important contributors to the hydrocarbon production on the Norwegian continental shelf. In total 18 fields were producing in 2018. Aasta Hansteen, Draugen, Heidrun, Ormen Lange and Åsgard are some of the major fields from this area. Initially, before they started producing, they contained a combined volume of about 1470 million standard cubic metres of oil equivalents ( $\text{Sm}^3$  o.e.), or 9.25 billion barrels of oil [13]. The oldest reservoir is of Early Jurassic age, thus, younger than Triassic. One of the reasons for this, is the uncertainty that comes with the exploration of reservoirs close to major salt layers of Triassic age. Therefore, a major motivation for investigating the effect of the depositional environment and diagenesis on reservoir quality in Triassic units is to understand if Triassic salt affects the reservoir quality and if so, how does it affect the reservoir quality.

A better diagenetic understanding of evaporites is more important than ever, in terms of exploring new fields in abandoned and unexplored regions of the world. There are no such thing as a perfect model for a reservoir, but by improving the understanding of vital parts used to generate the model, the model will improve. Learning more about how diagenesis, especially of evaporitic environments, effects the reservoir quality is of great value. Therefore, this work will cover a simple approach to propose a model for the depositional environment, as well as the diagenetic evolution of the reservoir and how these affect the reservoir quality of the Triassic succession.

The idea behind this is to find evidence of mass solute transfer from the evaporite layers in the Triassic Upper and Lower Salt and how different evaporite minerals affect the porosity of the surrounding reservoirs in terms of compaction, authigenesis, cementation and clay mineral replacement among other processes.

## 1.2 Scope of work

The main goal of this work is to establish the depositional environment of the Triassic Unit Tr3 to Unit Tr5 and construct the respective diagenetic evolution of wellbores penetrating these formations. In addition, it is of great importance to understand how this affects the reservoir quality. The process of reaching a conclusion involves several steps. After an initial study of the theoretical concepts, a filtering process of Triassic exploration wells penetrating the relevant succession

will lead to the selection of a representative set of samples. Interpretation of the depositional environment will be based on core descriptions and analysis of petrophysical logs, as well as findings from optical microscopy, SEM and XRD analysis. Petrographical characterization from thin sections, as well as point counting, XRD and SEM analysis, will provide information for creation of diagenetic models. By constructing porosity models from petrophysical logs and combining the results from the depositional environment and diagenetic evolutions of the wells, the reservoir quality of the Triassic succession will be examined. Throughout this thesis, previous work by the NPD [14, 15, 16, 17, 18, 19], Müller et al. [3], Halland et al. [20], Blystad et al. [2], Dalland et al. [21], and others, will all contribute to the understanding of the various theoretical aspects of this work.

## 1.3 Outline

The remaining of this thesis is divided into nine chapters. Chapter 2 offers a theoretical background of the geological history of the Phanerozoic. The main focus is the Triassic evolution. Furthermore, Chapter 3 deals with the regional geology of the Norwegian Sea field area. Theory about diagenesis is presented in Chapter 4. It is divided into two parts, where first the conceptual regimes of diagenesis are established, and secondly, insights about geothermal gradients are given. Further on, Chapter 5 provides important lithologies and reservoir quality characteristics for the Norwegian Sea stratification. Chapter 6 is the final theoretical chapter of this thesis, and covers a theoretical background of mineralogical and petrographical tools used in this work. Then, Chapter 7 introduces the detailed workflow and methods of this thesis. At the end of the chapter, sources of error have been described. Applying the methodology gave different sets of results, such as mineral assemblages, geothermal gradients, sedimentological logs and structural appearance of minerals, which are given in Chapter 8. The results are discussed in Chapter 9 in relation to the interpreted depositional environment, diagenetic evolution and reservoir quality, which includes the examination of petrophysical porosity logs. Finally, Chapter 10 presents a conclusion which includes recommendations for further work at the very end.





## Chapter 2

# Geological History (Phanerozoic)

In this chapter the main geological events of the Phanerozoic Eon representative for the Norwegian Sea area are described. The mineral assemblage and spatial arrangement of the sediments, in addition to the structural setting of the Norwegian Sea structures, are controlled by main geological events during Phanerozoic times.

## 2.1 Pre Triassic (541-252 Ma)

### 2.1.1 Cambrian, Ordovician, Silurian (541-419 Ma)

By the transition from the Precambrian to Cambrian (541 mega-annum, hereafter Ma), Baltica (the continent of Norway) was completely surrounded by deep marine oceans. In addition, Müller et al. suggest that Baltica was flooded in the Cambrian Period due to a rise in the eustatic sea levels, and the continental plains slowly turned into a shallow marine environment [3]. During Cambrian-Silurian, the tectonic plates of Baltica and Laurentia (the continents of Greenland and North-America) drifted towards each other, closing the Iapetus Ocean by plate convergence. Laurentia and Baltica collided in Late Silurian (about 430 million years ago, hereafter Mya), deforming and folding the exposed rocks [3]. The collision gave birth to the 10 kilometer thick Caledonian orogeny.

### 2.1.2 Devonian, Carboniferous, Permian (419-252 Ma)

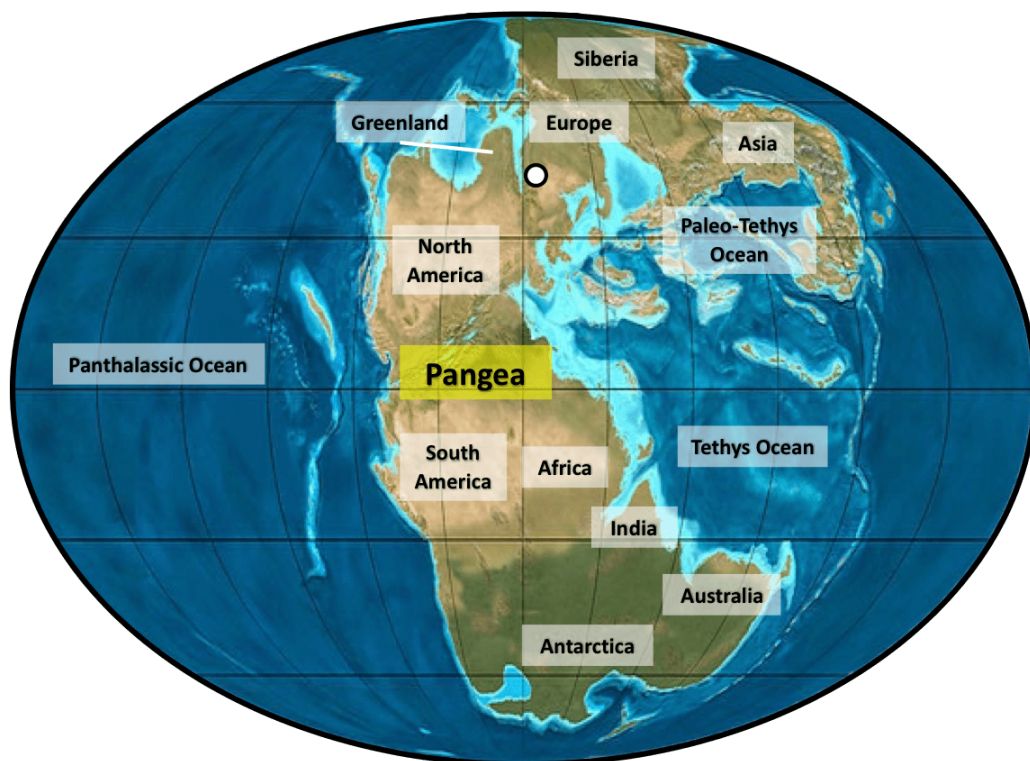
The closure of the Iapetus Ocean created the new continent Laurasia. Fossen et al. argue that the breakdown of the Caledonian orogeny started in Early Devonian

by a shift to extensional tectonic forces, and lasted the rest of the Devonian Period (405-359 Ma) [22]. At the end of the Devonian Period and the entrance of Carboniferous (359 Ma), the Caledonian orogeny was eroded down to continental plains [23].

During Carboniferous and Permian, Baltica drifted north from tropical, through arid and into the temperate climate zone. In Carboniferous, Laurasia in the north and Gondwana in the south collided and created the supercontinent Pangea. From ancient Greek "pan" means "all" and "gaia" means "earth". The creation of Pangea changed the global atmospheric circulation pattern and arid environment was widespread [23]. In the periods of Carboniferous and Permian, the eustatic sea level was slowly altered, probably due to the melting of the glaciers on Gondwana, until the end of Permian when a sudden fall of eustacy occurred. As a consequence, shallow marine sediments got exposed to erosion and weathering processes. Thick layers of sand with good reservoir qualities are deposited in marine basins along the Norwegian continental shelf (NCS) from the Permian Period. In 2013, Nøttvedt & Worsley proposed that growth of carbonates and possibly corals took place on the Nordland Ridge, these can be found analogously on the eastern part of Greenland [24]. In the Late Permian, thick salt-layers (the Zechstein Formation) was deposited in the North Sea and locally in the Norwegian Sea (e.g. in wellbore 6608/8-1). The end of the Permian Period is marked by the greatest mass extinction through out the history of the Earth [25].

## 2.2 The Triassic evolution (252-201 Ma)

The Permian-Triassic boundary marks the transition from the Paleozoic to the Mesozoic Era. Figure 2.1 shows a reconstruction of the Earth at Middle and Late Triassic. Referring to Nystuen et al., Norway was situated in the subtropical climatic zone in Early Triassic, between North America and Greenland in the west, and Europe and Siberia in the east [26]. The Late Permian continental fracturing of Pangea continued in the Triassic Period. The creation of the Tethys Ocean led to a change in the oceanic circulation pattern, which in turn changed the climate to the more humid. At the end of Triassic, Norway entered the temperate zone, prone to denser vegetation, thus more chemical weathering and higher deposition rates into the nearby basins [26].



**Figure 2.1:** Reconstruction of the continents placement on the supercontinent Pangea at Middle and Late Triassic times, about 240-220 Mya. Dark blue is oceanic crust while light blue is continental crust. The white dot is the suggested location of Norway [1].

In Early Triassic, the area between Greenland and Norway was an elongated marine basin. Mudstone deposits are therefore dominant. A transition to layered, continental floodplain deposits dominates the Middle Triassic succession. In Late Triassic, the Norwegian Sea was flooded and became a shallow marine basin with mud- and salt deposits. These layers are overlain by thick packages of mud indicating a marine depositional environment. At the very end of the Triassic succession, floodplain deposits dominate the Norwegian Sea basin, suggesting a continental environment [26].

As a result of the north-northeast to south-southwest (NNE-SSW) trending fault creations between Norway and Greenland in Early Triassic, deep marine basins were created. Basins developed as half grabens are common in the Triassic succession on the Trøndelag Platform (e.g. the Foran Basin and the Helgeland Basin).

Blystad et al. demonstrated that the Bremstein Fault complex, shown in Figure 3.1, separated the Nordland Ridge from the subsiding Helgeland Basin to the east during the Triassic Period [2]. As described by C. A. Baar, most major evaporites are directly precipitated from concentrated seawater [4]. Seawater that entered the Greenland-Norwegian basin evaporated due to the arid climate. Thus, precipitation of thick packages of salt and gypsum influence the Middle and Upper Triassic stratification [26].

## **2.3 Post Triassic (201-0 Ma)**

### **2.3.1 Jurassic (201-145 Ma)**

Johannessen & Nøttvedt concluded that Early and Middle Jurassic were influenced by a high level of erosion and transportation by large meandering rivers into the coastal basin as large delta systems [27]. A package of floodplain deposits rich in coal, mud and sandstone (the Åre Formation) is overlain by a thick package of beach and shallow marine sandstones (the Tilje Formation) and Late Jurassic marine mudstones (the Not Formation). During Late Jurassic, a great rift valley developed as a continuation from the Permian-Triassic rift structure. The Halten Terrace and the Dønna Terrace, observed in Figure 3.1, make the east flank of this rift valley. The rifting led to uplift, erosion and deposition of sediments on the Trøndelag Platform and Halten Terrace. Nøttvedt & Johannessen suggest that later subsidence led to marine mud depositions in the Norwegian Sea [28]. The stretching thinned the continental crust and led to subsidence of the rift valley. It also created characteristic rotated fault blocks often synonymously with hydrocarbon entrapment. Figure 3.6 provides a seismic line through the rotated fault blocks.

### **2.3.2 Cretaceous (145-66 Ma)**

Further stretching of Pangea in Cretaceous led to oceanic crust between Norway and Greenland. According to Brekke & Olaussen, the global temperature was falling and the mean sea level was up to 350 meters higher than today due to the low continental relief and ice free poles [29]. Deep Cretaceous basins were subsiding due to stretching and thermal subsidence. The basins were filled with

marine deposits from both the Scandinavian and Greenland side. Cretaceous ended with a mass extinction 65 Mya.

### **2.3.3 Cenozoic (66-0 Ma)**

Cretaceous to Paleogene marks the transition from the Mesozoic to Cenozoic Era. During the Cenozoic, creation of oceanic crust (55 Mya) by a middle ocean ridge led to the Greenland-Norwegian continental drift. In Late Cretaceous, the distance between Norway and Greenland was only 150 km, compared to a distance of 1600 km today. As described by Martinsen et al., thermal subsidence has led to an increase in water depth from about 900 to 4000 m [30]. Entering Pleistocene (2.6 Ma), Norway suffered a cooler climate that gave a cyclic variation of ice ages. Thus, moraines make the Quaternary succession on the NCS. According to Vorren & Mangerud, glaciers formed the landscape of Norway as we know it today [31]. As found by Vorren et al., the continental ice melted as a consequence of the Golf Stream, the mean sea level rose and the Norwegian continent experienced uplift in Holocene (11 700 years ago) [32].



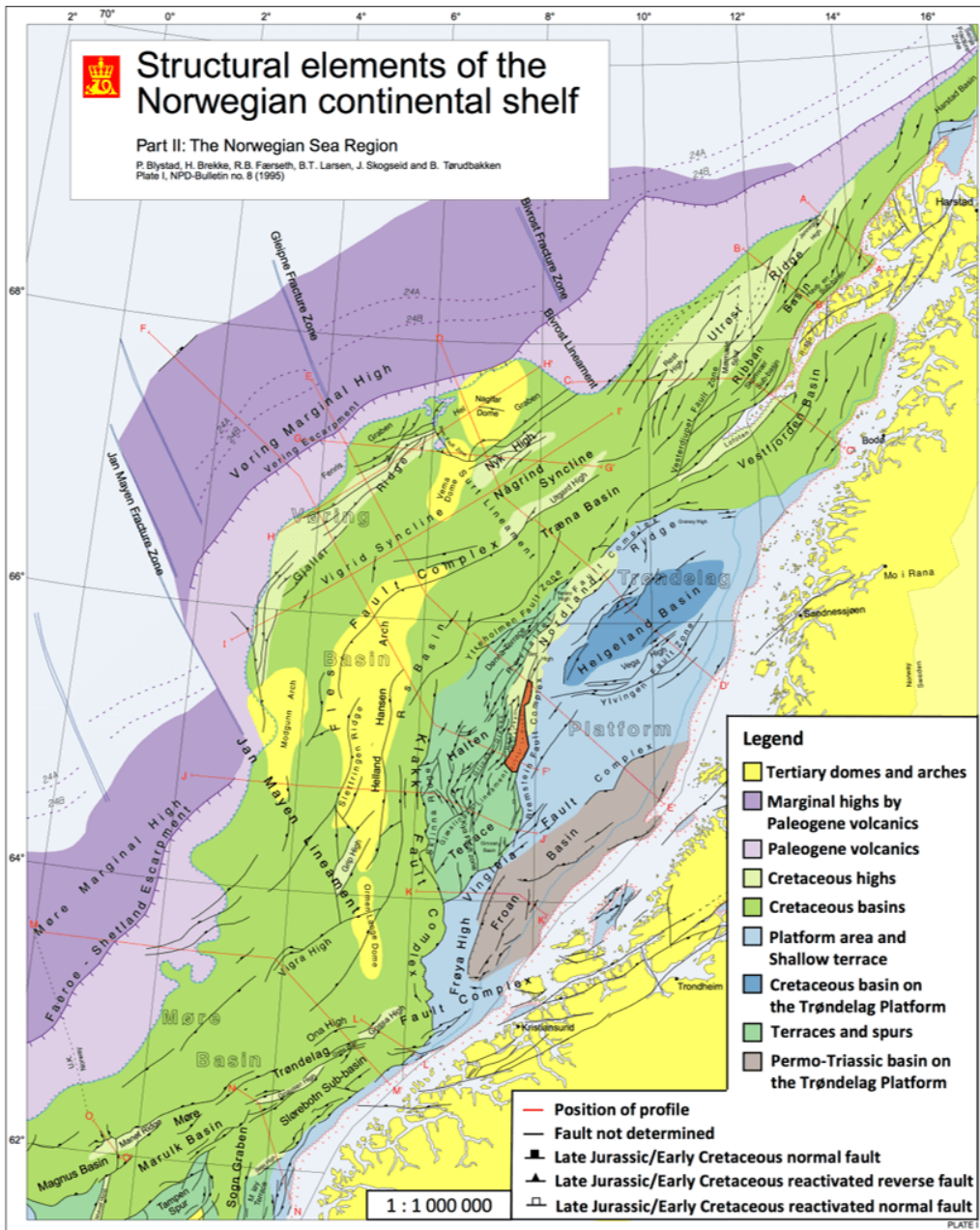
# Chapter 3

## Regional geology

The structural elements of the Norwegian Sea make the building blocks, while the tectonic history represents the framework in the understanding of the regional geology in the Norwegian Sea. The main purpose with this chapter is to get familiar with the area of investigation in three dimensions, both lateral, but also cross-sectional. Thus, a better understanding of the regional geology will improve the interpretation of the depositional environment, diagenetic evolution and reservoir quality of the studied wellbores. The Trøndelag Platform and Ellingråsa Graben will be in focus.

### 3.1 Norwegian Sea field area

The Norwegian Sea region of the NCS covers most of the continental margin between 62°N and 69°30'N (see Figure 3.1). As pointed out by Dalland et al., the area is described as a rifted passive continental margin [21]. As fairly mentioned in Chapter 2, two major plate tectonic episodes, the Caledonian orogeny and the North Atlantic break-up, divide the tectonic history of the Norwegian Sea into three major episodes, formulated by Dalland et al. [21].



**Figure 3.1:** Structural elements of the NCS showing the transect between the seismic lines EE' and FF' crossing the Ellingråsa Graben marked in orange. Edited from Blystad et al. [2].



### **3.2. Tectonic history and structural elements of the Norwegian Sea**

---

1. "The *pre-Late Devonian* epoch which ended with the final closure of the Iapetus Ocean during the Caledonian orogeny in Late Silurian and Early Devonian time."
2. "The *Late Devonian to Paleocene*, a period of extension culminating with the continental separation between Eurasia and Greenland at the Palaeocene-Eocene boundary."
3. "The *Earliest Eocene to Present*, a period of active seafloor spreading between Eurasia and Greenland."

The lithospheric plates were in compressional stress before the Late Devonian. This changed to extensional stress from Late Devonian until the continental separation in Eocene [2].

## **3.2 Tectonic history and structural elements of the Norwegian Sea**

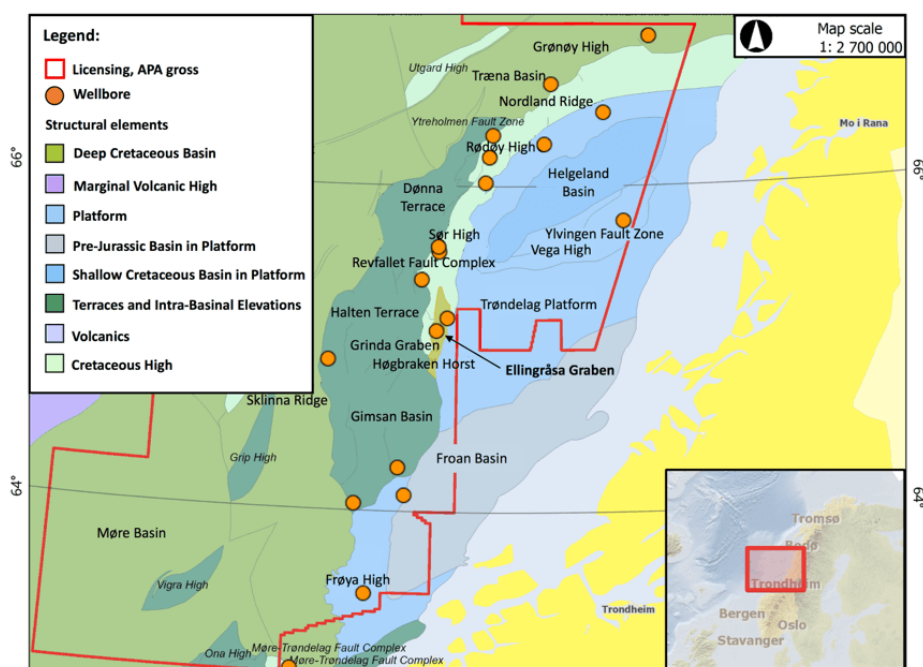
After a tranquil period since the Late Carboniferous and Early Permian rifting, new rifting led to NNE-SSW trending normal faults and rotated fault blocks on the Halten Terrace and the Trøndelag Platform in the Permian-Triassic transition, as observed from the seismic line in Figure 3.6. This was followed by deposition of continental Red and Grey beds, containing two Middle Triassic evaporites with thicknesses up to 400 m. The Triassic evaporites occur both as halite and anhydrite beds and no salt diapirs are observed. According to Jacobsen & Van Veen, the ages are thought to be latest Landinian (238 Ma) and latest Carnian (229 Ma) for the Lower and Upper Salt, respectively [33]. A chronostratigraphic table is given in Figure 3.7. These thick sequences are related to subsidence and deposition in a fluvial sabkha environment. The evaporite intervals are important detachments for normal and listric faults during subsequent episodes and later rifting episodes [2].

According to Halland et al., the Trøndelag Platform, Halten Terrace and Dønna Terrace were parts of a large north-south trending subsiding basin which was infilled by a deltaic to fluvial depositional system, during Early and Middle Jurassic [20]. Sediment input came both from the Norwegian side, but also from Greenland. Some of these faults were not reactivated during later tectonic episodes [2]. From Middle Jurassic to the Early Cretaceous, the Norwegian Sea underwent tectonic extension with major faulting and thinning of the upper crust. In relation

to the Trøndelag Platform, the Halten and Dønna terraces to the west were down-faulted, and further to the west, the Vøring Basin was subsiding. Both large-scale tectonic- and basement faults were active, affecting the Triassic salt. During Middle and Late Jurassic, the Nordland Ridge was uplifted, while the Helgeland Basin area was subsiding [20].

### 3.3 The Trøndelag Platform and Halten Terrace

The Trøndelag Platform contains the following structural elements; the Nordland Ridge, the Helgeland Basin, the Vega High, the Ylvingen Fault Zone, the Froan Basin and the Frøya High (see Figure 3.2). Frequent occurrence of oil, gas and condensate discoveries west of the Trøndelag Platform can be observed at Figure 3.3 and Figure 3.4.



**Figure 3.2:** An overview of 20 handpicked wellbores from the Norwegian Sea in relation to their structural elements. The Ellingråsa Graben is marked in yellow and the map was made using ArcGIS on NPD FactMaps.

Figure 3.2 is an overview of 20 handpicked wellbores in the field area, and their relation to the structural elements of the Norwegian Sea. The red line represents the APA (awards in predefined areas) gross and defines the licensing area for E&P companies in the Norwegian Sea. From the coastline towards west into the shelf, the structural elements roughly comprise of a Pre-Jurassic basin in platform (the Foran Basin), a platform (the Trøndelag Platform), a shallow Cretaceous basin in platform (the Helgeland Basin), a Cretaceous high (the Nordland Ridge), terraces and intra-basinal elevations (the Halten Terrace), a deep Cretaceous basin (the Vøring and Møre Basin) and a marginal volcanic high (the Møre Marginal High).

The Halten Terrace contains several lower-ranked structural elements; the Sklinna Ridge, the Grinda Graben, Kya Fault Zone, Gjæslingan Lineament and Gimsan Basin. During the late Middle Jurassic to Early Cretaceous rifting episode, there was a shift in the development in the master fault.

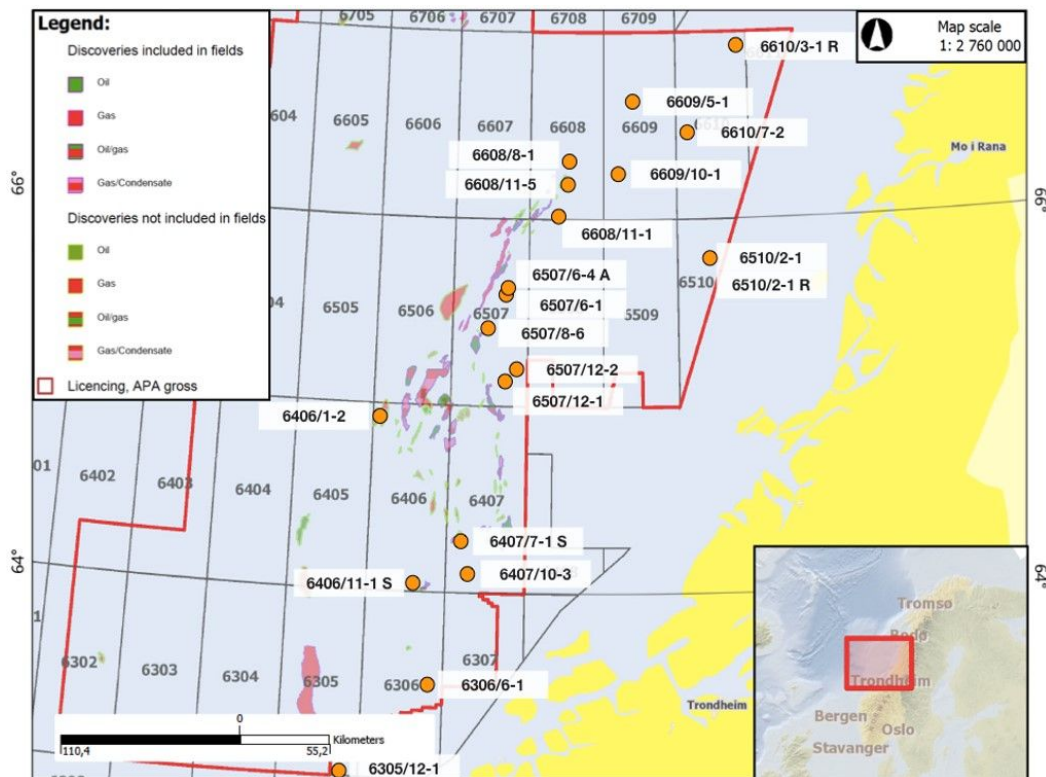


Figure 3.3: Relation of wellbores to discoveries in the Norwegian Sea area.

The first rifting phase took place along the Klakk Fault Complex to the west, while the second rifting phase took place along the Vingela Fault Complex in the south and the Bremstein Fault Complex in the east. This shift separated the Halten Terrace from the Trøndelag Platform, and the final separation stage occurred at Upper Cretaceous [2]. Figure 3.3 shows the names of the wells introduced in Figure 3.2 and illustrate their relative position to the oil, gas and condensate discoveries.

E&P companies started drilling offshore mid-Norway in 1980 with well 6507/12-1. This well provided the first detailed information about the lithology of the sedimentary succession [21]. Since then, more than 270 exploration wells have been drilled in the Norwegian Sea. The well data gives good coverage of the post-Triassic through the Tertiary sequence. The Triassic succession is present in over 80 wells, but is often incomplete. On the other hand, information on the pre-Triassic sequence and the Quaternary stratification is scarce due to erosional phases.

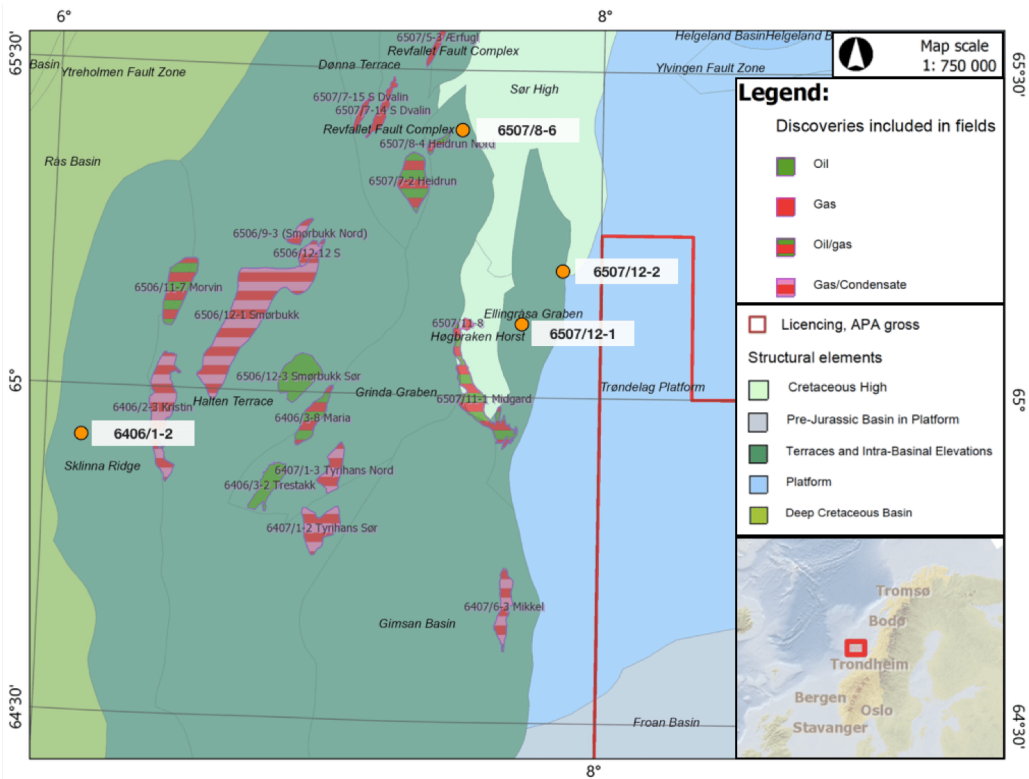


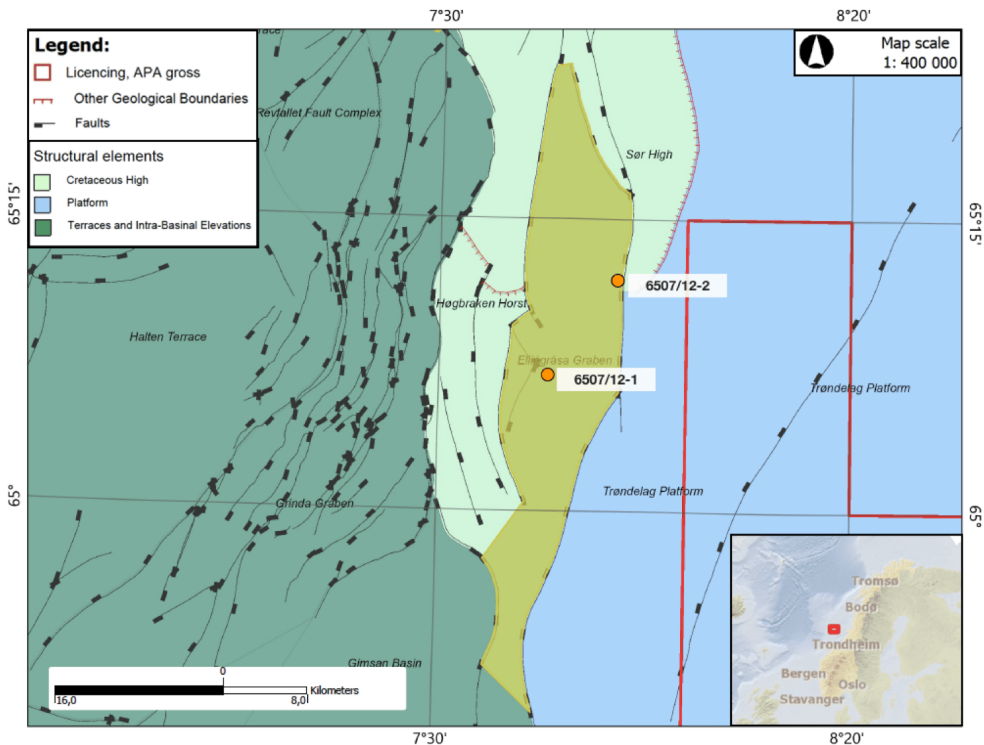
Figure 3.4: Hydrocarbon fields close to the Ellingråsa Graben.

It is clear that the Norwegian Sea hydrocarbon discoveries are important contributors to the petroleum industry of Norway. By having a closer look at the Halten Terrace, Dønna Terrace, Høgbraken Horst, Ellingråsa Graben and the Trøndelag Platform in Figure 3.4, one can see which discoveries are related to the nearby wells and structures. Wellbore 6406/1-2 is close to the Kristin field and wellbore 6507/8-6 is close to the Heidrun field, both on the Halten Terrace. Wellbore 6507/12-2 and 6507/12-1 on the Ellingråsa Graben are close to the oil and gas producing Midgard field. These four wellbores are linked to terraces and intra-basinal elevations. Wellbore 6507/12-2 is the deepest of the studied wells with a total depth (TD) of 5008 m. The TD includes a distance of 286 m from the rotary kelly bushing (RKB) to the sea floor.

## 3.4 The Ellingråsa Graben

The *Ellingråsa Graben* is a formal name after the Ellingråsa lighthouse west of Namsos in the county of Nord-Trøndelag [2]. Figure 3.5 shows the relative position of the graben in between the Halten Terrace and the Trøndelag Platform at about 65°00'N to 65°45'N and 7°40'E to 8°00'E. It occupies a downthrown area between the eastern master fault in the Bremstein Fault Complex and an easterly-dipping antithetic fault against the Høgbraken Horst [2].

The Ellingråsa Graben is elongated and has a north-south length of 65.4 km and a width of 3.2 km at the narrowest and 12 km at the widest. The graben is regarded as a subelement in the Bremstein Fault Complex. A number of almost north-south striking, mainly antithetic, faults are present within the graben. The domal shape of the grabens interior may be related to salt swells and can be observed on the seismic profiles EE' and FF' in Figure 3.6 [2].

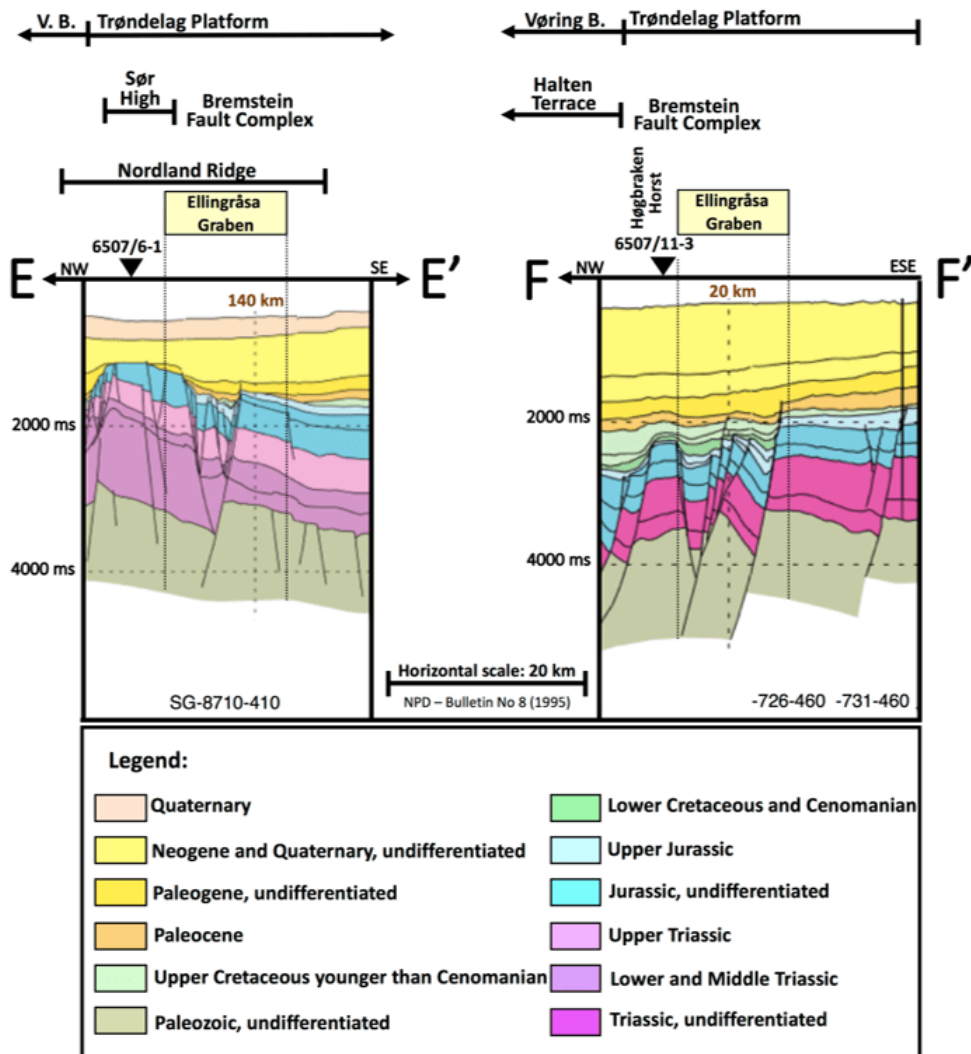


**Figure 3.5:** The Ellingråsa Graben, highlighted in yellow, is an area of intra-basinal elevations.

The Ellingråsa Graben is interpreted as an extensional structure formed in periods of crustal stretching. The earliest movement along the master fault forming the eastern side of the Ellingråsa Graben took place in Late Triassic, and the western boundary fault was activated shortly afterwards. The main periods of faulting and subsidence in the graben took place in the Late Triassic to Early Jurassic and the late Middle Jurassic to Early Cretaceous. After the rifting period in late Middle Jurassic-Early Cretaceous time, the boundary faults to the Ellingråsa Graben were reactivated during a Late Cretaceous tectonic phase [2].

Figure 3.6 is a cross section of the Ellingråsa Graben constructed from the seismic lines EE' and FF' in Figure 3.1. The profiles demonstrate the downthrown, domal shape of the structure as well as the chronostratigraphic content of the succession. By looking at this figure, it is clear that the Ellingråsa Graben is a highly faulted graben system with synthetic and antithetic faults from several tectonic events. Section EE' is crossing the Ellingråsa Graben at its northern part, while profile

FF' is cross-cutting the very south of the graben.



**Figure 3.6:** A reference section for the Ellingråsa Graben is given by the seismic lines SG-8710-410 in Profile EE', as well as 731-460 and 726-460 in Profile FF'. Edited from NPD - Bulletin No 8 [2].

## 3.5 Stratigraphic subdivision of the Permian-Triassic

Sediments of Triassic age beneath the Åre Formation of Early Jurassic age have been identified in several wells offshore Mid-Norway. The Triassic succession is the purple layers in Figure 3.6. Based on lithological color, the Triassic stratification in the Norwegian Sea has been informally divided into *Grey Beds* and *Red Beds*. The Red Beds represent continental clastics of red color deposited in an arid climate. The Grey Beds also represent continental clastics, but of semi-arid climate [21].

The left part of Figure 3.7 is an estimation of the dominating facies for the Triassic succession offshore Mid-Norway. The figure contains both a lithostratigraphic and a chronostratigraphic table. Also, a tectonic and a climatic overview are present, and on the right side, the eustatic- and relative sea-level curve are provided for the Late Permian and Triassic succession. In addition, a core column with respective wellbores is applied.

In 2005 Müller et al. redefined the Triassic lithostratigraphic names as the existing names were informal and roughly divided [3]. The Grey Beds and the Red Beds were replaced by the Unit Tr1 in Early Triassic to Unit Tr5 of Late Triassic age.

Throughout this thesis, the modified lithostratigraphic and chronostratigraphic overview in Figure 3.7 will be referred to. Including a few additions, mainly two important changes are made.

1. Chronostratigraphy - The previous subgroups Spathian, Smithian, Dienerian and Griesbach of the Early and Late Spathian are for this thesis replaced with Olenekian and Induan age. And the subgroups Tatarian and Utimian Kazanian of Late Permian are changed to Changhsingian and Wuchiapingian.
2. Lithostratigraphy - The Lower Turbedite Unit/Carbonate Unit, Anhydrite Unit and Shallow Marine Unit are replaced with the Zechstein Group.

These modifications are respectively based on the *International chronostratigraphic chart 2018* and the *End of Well Report* of wellbore 6608/8-1 and 6507/6-4 A. In this study, the pre-Unit Tr1 only occurs in these two wellbores. The well reports refer to them as the Zechstein Group and the Rotliegend Group of Late and Early Permian age respectively, which explains the second change.



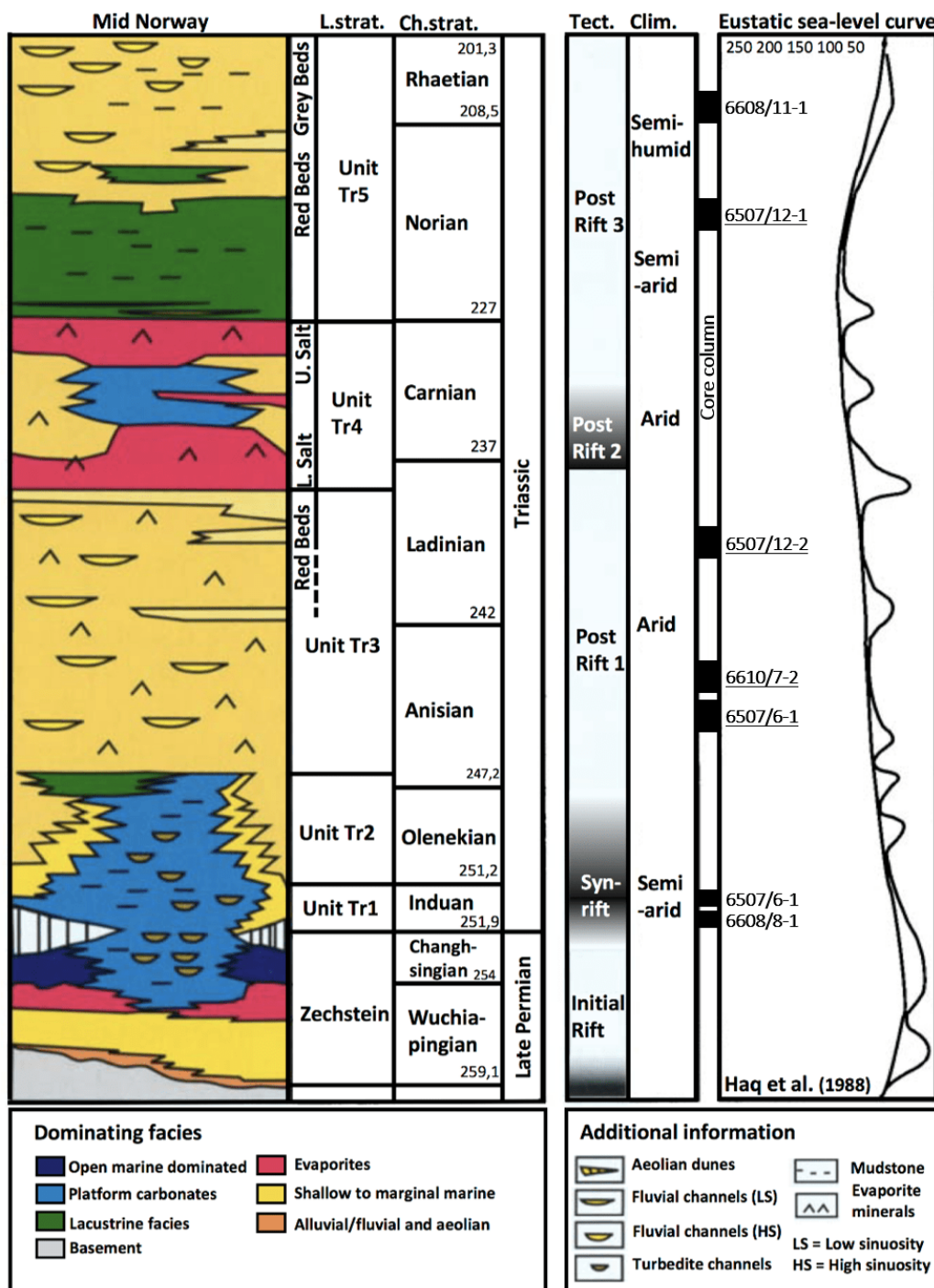


Figure 3.7: Stratigraphic overview of Late Permian and Triassic. Edited from Müller et al., 2005 [3].

The core section illustrates the relative position of the most important cores for this thesis. The well names are listed to the right of the respective cores, and the underlined well names are studied in detail in Chapter 8. The lithostratigraphic Unit Tr4 contains two thick salt layers. How reservoir quality of surrounding beds responds to these salt packages are investigated and discussed in the following chapters.

### 3.5.1 Lithostratigraphy of the Triassic, Mid-Norway

#### The Rotliegend and Zechstein Group

The Rotliegend Group of Early Permian age can be found in the deepest part in wellbore 6507/6-4 A, and is described by Glennie (2009) as red colored sedimentary rocks deposited in fluvial, aeolian, sabkha and lacustrine environments [34]. The overlying Late Permian Zechstein Group is found in wellbore 6508/8-1 in the Norwegian Sea. The Zechstein Group consists of evaporites and carbonates with local clastic rocks. The well report from the NPD fact page suggests a carbonate platform depositional environment [15]. The Zechstein Group of well 6508/8-1 consists of dolomite, and the group either rests on crystalline basement or the Rotliegend Group.

#### Unit Tr1

Unit Tr1 makes the base of Triassic, and 6608/8-1 is the only well that has drilled through the whole section. Nevertheless, Unit Tr1 is present in several wells, and Table 7.1 illustrates this. The succession mainly comprises of marginal marine deposits and submarine fan deposits [3].

#### Unit Tr2

Unit Tr2 from Olenekian times overlay Unit Tr1. A marginal-marine depositional environment dominates. Upward shallowing of the basin, indicated by brown to red-colored sediments, is proven by increased terrestrial polymorphs and reduced marine polymorphs compared to Unit Tr1 [3]. Müller et al., have studied wellbore 6507/6-1 and suggest a lacustrine and lagoonal sedimentary environment for Unit Tr2, with occasionally oxidation of the sediments as a result of exposure. Marine algae is however periodically appearing, indicating marine influence [3].

### Unit Tr3

In Unit Tr3 from Anisian and Ladinian age, alluvial deposits dominate. But for well 6610/7-2 in the northern part of the Helgeland Basin, marine algae indicate that the northern part of the Norwegian Sea was more influenced by the marine environment. However, the upper part of Unit Tr3 changes from red-brown to gray colors, thus a marginal marine environment [3].

### Unit Tr4

Unit Tr4 of Late Ladinian and Carnian time reflects a marine sabhka environment. The Lower and Upper Salt represent two thick packages of basin central halite deposits, while a thinner middle evaporite succession is composed of anhydrite. Marine algae suggest a marine origin of the halite beds [3]. From north to south, the evaporites are registered in well 6610/7-2 and 6510/2-1 on the Trøndelag Platform, but also in well 6507/12-2 on the Ellingråsa Graben.

### Unit Tr5

Unit Tr5 makes the upper part of the Triassic succession, and is chronostratigraphically dated to Norian and Rhaetian time. The depositional environment of Unit Tr5 is interpreted as shallow, lacustrine basin or playa. Thick green-gray and red-brown mudstones are typically interbedded with isolated sandstone units of 2-5 m thickness [3].



# Chapter 4

## Diagenesis

According to Worden & Burley, diagenesis can be considered as everything that contributes in the transformation from sediments to a sedimentary rock from weathering and deposition, until the onset of metamorphism [10]. It includes both physical and chemical changes. Diagenetic reactions change the pore fluid chemistry, temperature and pressure of the buried sediments. The rocks mineral assemblage undergoes water-rock interactions towards the ambient geochemical environment and diagenetic reactions cease with absence of aqueous pore fluids. Diagenesis is therefore a dynamic process that relates to the burial history of the basin [10]. The diagenetic history of a specific well can be used to determine the reservoir quality in the surrounding reservoirs. In addition, information about the diagenetic evolution can be used as qualified estimations for hydrocarbon exploration at unexplored depths. At about 300°C, diagenesis is replaced by metamorphic reactions.

### 4.1 Conceptual regimes

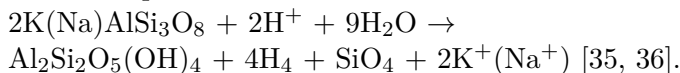
Worden & Burley have described three conceptual diagenetic regimes that relate diagenetic processes to the evolution of the sedimentary basin [10].

1. Early diagenesis - eogenesis.
2. Burial diagenesis - mesogenesis.
3. Uplift-related diagenesis - telogenesis.

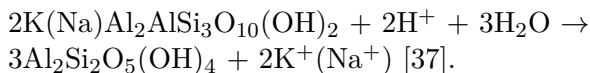
### 4.1.1 Eogenesis

Eogenesis is the regime where the original depositional pore water dominates. Hence, the higher the permeability of the rock, the deeper the impact of the eogenetic realm. It can vary from a few meters to the thousand meter scale, but a rule of thumb by Morad et al. (2000) suggest a limit of eogenesis at 70°C, i.e. a burial depth of 2 km for a Norwegian Sea geothermal gradient of 35°C/km [9]. Eogenesis can have both positive and negative impact on the later reservoir quality. The effects of eogenesis on reservoir quality is summed up in table 4.1. Positive effects include the counteraction of compaction and late quartz cementation by early pore lining cements. On the other hand, pore filling cements and early formed kaolinite, that later transforms into pore filling illite in presence of potassium, deteriorate the reservoir quality [9]. Kaolinite can be formed by several chemical reactions involving different minerals. Below, Bjørlykke, Lanson et al., and Stoch & Sikora, illustrate some of the most important reactions.

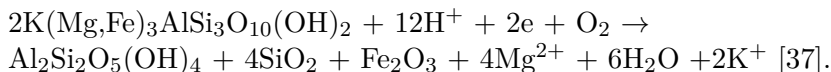
◇ From feldspar:



◇ From muscovite:



◇ From biotite:



Basin scale fluid includes aqueous (water or brine), non-hydrocarbon gases ( $\text{CO}_2$ ,  $\text{H}_2\text{S}$ ,  $\text{N}_2$  or the noble gases) and petroleum fluids (oil, gas or condensate). Oil-wet sandstone diagenesis is inhibited by the presence of oil, but can also lead to feldspar alteration and carbonate cementation if the oil undergoes oxidation and biodegradation [10]. Fluid pressure increases with depth and temperature.

One would expect that the resulting eogenetic pore water salinity is alkaline and dominated by  $\text{Ca}^{2+}$ ,  $\text{Mg}^{2+}$  and  $\text{HCO}_3^-$  in Triassic reservoirs due to the arid climate at the time. The hinterland underwent little chemical weathering due to

reduced rainfall. The Triassic climate is thus indicative of a low water table and an oxidizing environment. In such a climate the Triassic Red Beds were formed. Precipitation of authigenic cement is likely to occur for incoming highly saline water. In contrast, the influx of low salinity water may result in dissolution of feldspars and carbonates in sandstones [10].

**Table 4.1:** Eogenetic processes in sandstones and their impact on reservoir quality, modified from Morad et al., 2010 [9].

<b>Process</b>	<b>Controlling parameters</b>	<b>Reservoir impact</b>
Mechanical compaction and pseudomatrix formation	Ductile grains	Rapid loss of porosity and permeability during burial
Dissolution and kaolinization of framework feldspars	Feldspars and meteoric water	Formation of intragranular and moldic pores. Minor improvement of porosity and permeability
Cementation by K-feldspar overgrowths	K-feldspar	Permeability reducing
Formation of grain-coating Fe-clays	Sedimentation rates	Transformation into chlorite during mesodiagenesis. Deep porosity preservation by inhibition of quartz cementation
Formation of grain coating microquartz	Silica bioclasts	Inhibition of cementation by quartz overgrowth
Dissolution of carbonate grains	Meteoric water flux, enhanced by wet climate and high permeability	Increase in porosity due to formation of intragranular and moldic pores
Cementation by calcite, dolomite, siderite	Semiarid climate in fluvial sandstones and availability of carbonate grains	Destruction of porosity and permeability
Mechanical clay infiltration	Braided fluvial and alluvial fans or meandering fluvial and deltaic settings	May inhibit quartz overgrowth and preserve porosity during mesogenesis. Mesogenetic illitization of smectite may promote pressure dissolution

### 4.1.2 Mesogenesis

Mesogenesis takes place during burial and includes sediments at temperatures up to 300°C. It is defined by the processes affecting the sediments when passed the influence of the depositional environment until early metamorphism. Increasing the temperature leads to a series of diagenetic reactions as energy is added to the system [10]. Worden and Burley (2009) have listed a set of reactions during mesogenesis [10]. Some of them are included below.

1. The transformation of the clay mineral smectite to illite at temperatures greater than about 80°C.
2. The production of quartz arenites by K-feldspar dissolution, which occurs extensively at 2.5 km depth below the sea floor.
3. The production of illite and quartz from the reaction of K-feldspar and kaolinite at temperatures greater than 70°C.
4. Quartz cementation at the temperature range of 80-100°C.
5. Grain coating by chlorite at temperatures greater than 90°C.
6. Mesogenetic carbonate cementation at the temperature of ~100°C.
7. Recrystallization of calcite to cements of increased crystal size with increasing temperature.
8. For systems low in potassium, the transformation of kaolinite to chlorite (chloritization) at the expense of illite growth from kaolinite, occurs at the temperature range of 165-200°C.
9. Dependent on pressure and salinity, gypsum dehydrates to anhydrite at the temperature range of 50-120°C.

The transfer of dissolved species such as  $\text{Na}^+$ ,  $\text{K}^+$ ,  $\text{Ca}^{2+}$ ,  $\text{Mg}^{2+}$ ,  $\text{Fe}^{2+}$ ,  $\text{HCO}_3^-$ ,  $\text{SO}_4^{2-}$  and  $\text{Cl}^-$  in pore fluids, migrating from low permeable to high permeable rocks is known as *mass solute transfer*. Solute transfer tend to take place from mudstones, carbonates and evaporites rich in the above species, to porous sandstones and carbonates where reprecipitation and cementation are likely to occur. Their proportion affect the mineral stability, leading to albitization of K-feldspar and illitization of smectite, among other reactions. The mass solute transfer of aqueous fluids from mudstones rich in iron, magnesium, manganese and calcium are for example responsible for the growth of ankerite in sandstones [10].



The four processes; grain rearrangement, plastic deformation of ductile components, dissolution and brittle fracturing control the degree of compaction in sandstones [10]. Initial fluid movement during mesogenesis is a response to compactional processes. The fluids are seeking lower hydrostatic pressure, and move upwards and towards the basin margins, or sometimes downward if the fluid pressure decreases at higher depth. During deeper burial, thermal events such as those listed above become the dominant compactional processes. This includes gypsum dehydration, transformation of smectite to illite, pressure dissolution and source rock maturation, among others [10]. Mesogenetic reactions affecting the reservoir quality are summed up in Table 4.2.

**Table 4.2:** Mesogenetic processes in sandstones and their impact on reservoir quality. From Morad et al. (with modifications) [9].

Process	Controlling Parameters	Reservoir Impact
Illite formation	Availability of kaolinite and smectite	Permeability deterioration and increased water saturation. Enhancement of intergranular pressure dissolution
Chlorite formation	Availability of smectite and illite	Inhibits quartz overgrowth cementation in deep sandstone reservoirs
Albitization of K-feldspars	Abundance of K-feldspar, high $\text{Na}^+$ activities	Enhance illite formation supplying $\text{K}^+$ , permeability deterioration
Albitization of plagioclase	Abundance of Ca-rich plagioclase, high $\text{Na}^+$	Provides $\text{Ca}^{2+}$ and $\text{Al}^{3+}$ , prone to carbonate and clay cements
Quartz cementation and pressure dissolution of quartz grains	Availability of monocrystalline quartz, illite coatings or mica	Deterioration of porosity and permeability
Dissolution of unstable grains and calcite cement	Thermal maturation of organic matter which generates acids and $\text{CO}_2$	Creation of secondary intragranular and intergranular porosity
Cementation by ankerite, siderite and anhydrite	Flux of basinal fluids mainly along faults	Deterioration of reservoir quality

### 4.1.3 Telogenesis

Meteoric water is often highly oxidized and CO<sub>2</sub> saturated which cause an acidic pH. From Table 4.3, one can see that the salinity is low for meteoric water. Telogenesis is related to inverted rocks exposed to meteoric water, which is not related to the initial depositional environment with its eogenetic pore water neither the mesogenetic fluids. Most burial diagenetic waters are saline, reducing and with near neutral pH due to rock-limited CO<sub>2</sub> concentrations. The salinity varies from a few up to 30% dissolved solids. The inversion is related to uplift, seaward progradation of the coastline or sea level fall and thus sediment surface exposure [10]. Telogenesis is often related to outcropping sedimentary rocks, except where ancient unconformities are encountered. Influx of meteoric water may lead to oxidation of reduced iron-bearing cements, dissolution of feldspars and chert grains, as well as transformation of feldspar minerals to clay minerals. Influx of marine waters above ancient unconformities is associated with carbonate and sulphate cementation [10].

Although meteoric water can flow deep into the sediments, most geochemical reactions related to telogenesis take place at the first tens of meters from the surface. Modification of the subsurface sediment in response to the meteoric water is restricted to the soil or the exposed outcrop composition [10]. Newly formed mountain chains, such as the Ordovician-Devonian Caledonian orogeny, may cause mixing of meteoric water with deep formation water. This again can cause a range of diagenetic events in inverted basins [10].

**Table 4.3:** Comparison of Meteoric water linked to telogenesis versus burial pore fluids linked to eogenesis and mesogenesis.

Pore fluid	Meteoric water	Burial water
Salinity	Low	Often high
Agent	Oxidizing	Reducing
CO <sub>2</sub> saturation	High	Low
pH	Low	Neutral

The amount of compaction of the rock can relate diagenetic events to eogenetic, mesogenetic or telogenetic regimes. This can be determined using thin section analysis. Diagenetic events can also be dated. The most applied methods of absolute dating uses radiometric techniques with either K-Ar or Rb-Sr decay schemes on authigenic minerals. Table 4.4 is a list of diagenetic terms used in Chapter 4.

**Table 4.4:** Diagenetic terms, modified from Worden and Burley, 2009 [10].

Term	Definition
Authigenesis	In situ mineral growth
Cementation	Growth or precipitation of minerals in pore spaces
Compaction	Process causing reduced pore space
Dehydration	Loss of H <sub>2</sub> O as a result of increased temperature
Dissolution	Mineral interaction with fluid leaving behind cavity
Lithification	The process from loose sediment to solid rock by compactional and cementation processes
Neoformation	New growth of minerals during diagenesis
Precipitation	Crystallization of a mineral from solution
Recrystallization	Dissolution followed by precipitation involving changes of the mineral
Replacement	Growth of a chemically different authigenic mineral within the pre-existing mineral

## 4.2 Geothermal gradient

The geothermal gradient can be described as the temperature change relative to depth below the surface, and is about 35°C/km in the Norwegian Sea field area. Sandstones in active rift basins or basins with high amounts of accommodation space, high in sediment supply, are more likely to be far from equilibrium than those in stable and slowly subsiding basins [10]. This will influence the formation temperature and thus the timing of diagenetic reactions.

### 4.2.1 Heat flow

The flow of heat through a substance is described by Fourier's law:

$$Q = -k \frac{dT}{dz}, \quad (4.1)$$

where

$$\begin{aligned} Q &= \text{Heat flow } \left[ \frac{W}{m^2} \right], \\ k &= \text{Thermal conductivity } \left[ \frac{W}{mK} \right], \\ dT/dz &= \text{Thermal gradient } \left[ \frac{K}{m} \right]. \end{aligned}$$

The negative sign of Equation 4.1 appears as heat flows out of the system. Ocean heat flow measurements are relatively reliable because the temperature on the ocean floor has remained constant for long periods. According to Spear, the temperature within a volume element will vary as a function of heat conduction, heat production and heat advection [38]. Heat conduction follows from the law of conservation of energy, while heat production at diagenetic scale mainly depends on radioactive decay of potassium, uranium and thorium, but also on dehydration reactions, heat of fusion and shear heating. Depths of the diagenetic realm are relative shallow. Radioactive decay, dehydration reactions and shear heating are therefore the main controlling factors of heat production. Burial depth, on the other hand, is the controlling parameter for heat advection. Heat advection is the temperature change at a point in space by movement through a thermal gradient [38].

# Chapter 5

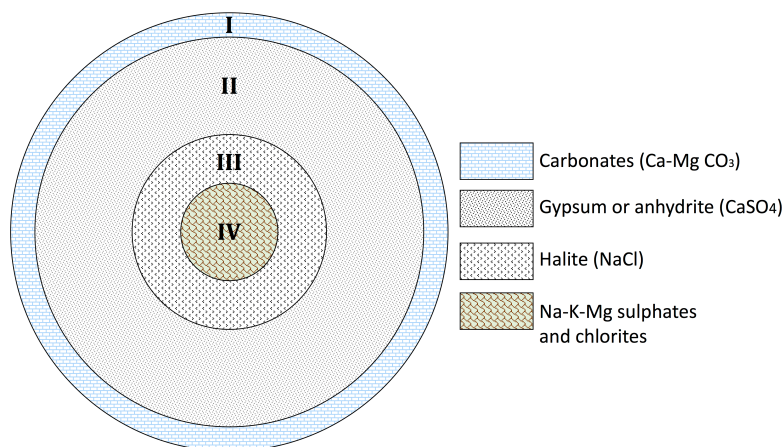
## Lithology and reservoir quality

This chapter provides the basic theory to support the investigations on reservoir potential of the Triassic stratification from the Trøndelag Platform and Ellingråsa Graben. The first section focuses on important lithologies of the Norwegian Sea and the classification of these. It includes an in-depth investigation of salts, sandstones, shales and clays. In addition, the following sections will deal with porosity and reservoir quality.

### 5.1 Lithology

#### 5.1.1 Evaporites

Evaporites, often referred to as salt rock, is a sedimentary rock made from evaporation of seawater and enclosed lakes. If an isolated lake or basin of seawater undergoes complete evaporation, so-called isothermal evaporation, the deposition takes a shape with a characteristic bull's eye pattern, as illustrated in Figure 5.1. Only 1% of the total solids are made of carbonate precipitation. This is phase I. Phase II consists of calcium-sulphate (gypsum or anhydrite) and makes 3% of the total precipitation. 69% of the total volume is halite precipitation. This is phase III. The resulting 27% of the bull's eye pattern is phase IV and consist of Na-K-Mg sulphates and chlorides [4]. In reality, a complete and consistent drying of a basin generating this salt-pattern is unlikely to occur. Influx of water from rainfall, external rivers, or any other source would recharge the system with water, resulting in drawback to a lower phase. As a consequence of this, reality is often much more complex. For instance, a salt succession can hold tens of meters of anhydrite and halite without precipitation of sulphates.



**Figure 5.1:** Successive phases of complete evaporation of seawater with the characteristic bull's eye pattern. Based on work from C.A Baar, 1977 [4].

Salt diagenesis behaves very differently compared to other sedimentary rocks. Salt is almost incompressible and has a low density of about  $2.17 \text{ g/cm}^3$ . While typical siliciclastic sediments increase their density with depth, the density of salt is constant or decreasing. This is because salt has the ability to expand at elevated temperatures.

Salt is diamagnetic. This feature, together with the low density, makes salt easily detectable on gravimetric and magnetic surveys. Salt absorbs much of the acoustic energy in seismic surveys. This characteristic differentiates it from the surroundings, but as a consequence, it can be difficult to interpret strata underneath salt on seismic images. Finally, salt has a very distinct signature on petrophysical resistivity logs.

Salt has a low viscosity, which makes it behave like a fluid. Salt flows slowly, but continuously. The process is referred to as salt creep. According to Li et al., the deeper the salt is located, the higher the creep tends to be [39]. Hydrocarbon traps are often formed as a consequence of salt creep. Salt is impermeable and makes a good cap rock.

In addition, salt is readily dissolved in water. Mass solute transferred salt may affect the reservoir quality of surrounding reservoirs. Special attention is therefore given to the Upper and Lower Salt in Unit Tr4 at the Halten Banken and Trøndelag Platform area. See Figure 3.7 for the lithostratigraphic overview.

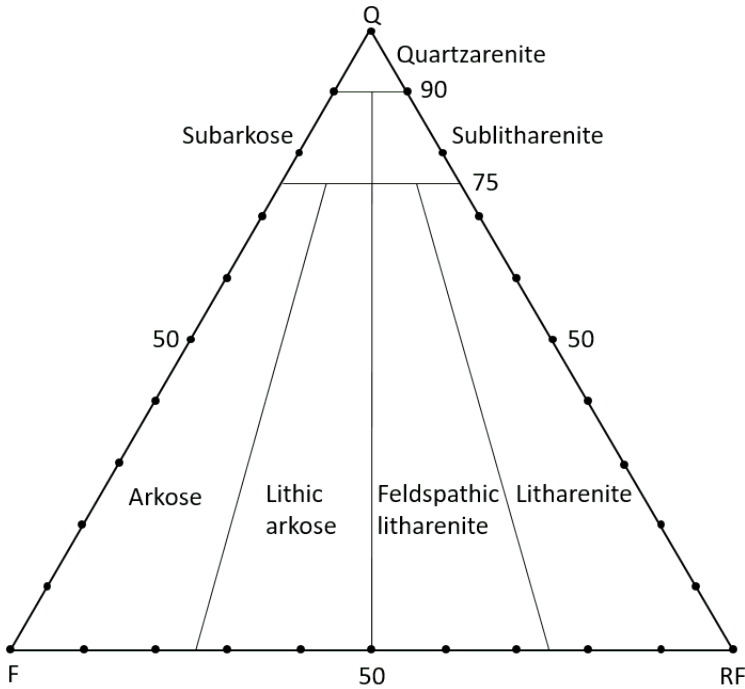
Anhydrite ( $\text{CaSO}_4$ ) and gypsum ( $\text{CaSO}_4 + 2\text{H}_2\text{O}$ ) have the same chemical formula, but gypsum is hydrated. Introducing water to anhydrites may start a chemical reaction creating gypsum. During burial of gypsum, reaching temperatures of  $200^\circ\text{C}$ , gypsum tend to dehydrate into anhydrite [39]. Worden and Burley suggest that this reaction can occur at lower temperatures [10]. In contrast to salt, the anhydrite density is high. This gives characteristic anomalies that can be detected on petrophysical logs.

### 5.1.2 Sandstone, claystone and shale

#### Sandstone

Figure 5.2 is a diagram called the QFL sandstone classification diagram, and is made to illustrate the relative proportion of the contents in the sandstone. A sandstone is described by its relative proportion of quartz ( $\text{SiO}_2$ ), lithic grains (i.e. rock fragments) and feldspar. Quartz grains occur as monocrystalline, polycrystalline and chert which are distinctly different when observed under the microscope. Lithic grains are grains from a pre-existing rock. There are three feldspar end members that behave differently in terms of chemical diagenesis, being the K-feldspar minerals orthoclase and microcline (I:  $\text{KAlSi}_3\text{O}_8$ ), and the plagioclase feldspar minerals albite and anorthite (II:  $\text{NaAlSi}_3\text{O}_8$  and III:  $\text{CaAl}_2\text{Si}_2\text{O}_8$  respectively). Feldspar rapidly transforms into clay and calcite and is prone to dissolution and possibly precipitation at a later stage. This will most certainly affect the reservoir quality.

In addition, sandstones can be classified in terms of matrix content. By progressively adding clay and silt to the matrix, the sandstone will be classified as a wacke lithotype or a sandy mudstone when 50% or more of the matrix is occupied by clay and silt. The sandstone quality in a reservoir context depends on the source rock, transport distance and climate, and can be further described in terms of rounding and angularity, maturity, hardness, color, sorting, grain size, porosity, permeability and fluid content.



**Figure 5.2:** QFL sandstone classification diagram. From Folk, 1970 [5].

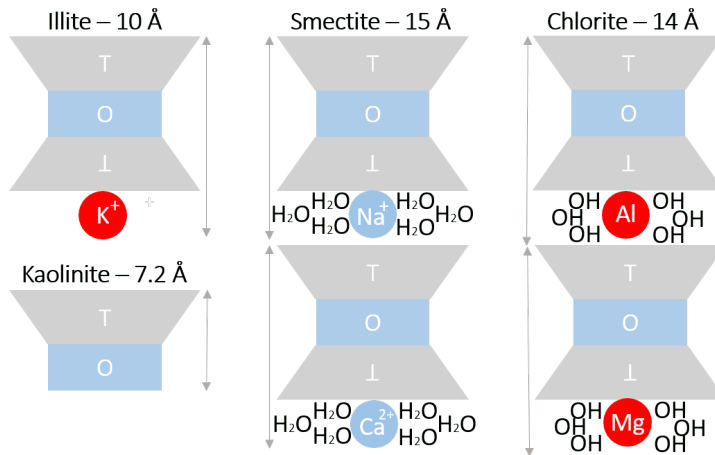
## Claystone and shale

Shale is a sedimentary rock composed of silt and clay-sized grains smaller than  $62\ \mu\text{m}$ . Shale is distinguished from other mudstones because it is fissile and laminated with a high degree of anisotropy. Measuring anisotropic minerals with logging tools will give different values dependent on direction of the measurements. Shale has a very high compaction rate due to the occurrence of high microporosity values, soft rock fragments and organic grains. The essential environments for shale deposition are river floodplains, lakes, deltas, basin slopes and deep marine settings.

The main building blocks of clay minerals are silica tetrahedra and aluminum octahedra sheets. Clay grain size is smaller than  $4\ \mu\text{m}$  regardless of mineral composition and can be detected and classified by scanning electron microscope (SEM) and X-ray diffraction (XRD) analysis. The most common diagenetic clay minerals are kaolinite, illite and chlorite. In addition, smectite also occurs [10]. Clays are



hydrous sheet minerals rich in aluminum with variable amounts of iron, magnesium, calcium, potassium and sodium. The radioactive species uranium, thorium and potassium are associated with clay, attached to the clay surface. As described by Ellis & Singer, in terms of reservoir properties, the type of authigenic (born in place) clay will play a controlling factor for porosity and permeability [6]. Reaching above 300°C, metamorphosed clay minerals transform into chlorite and mica.



**Figure 5.3:** Illustration of clay building blocks. Based on Ellis & Singer’s work on *Well Logging for Earth Scientists*, 2008 [6].

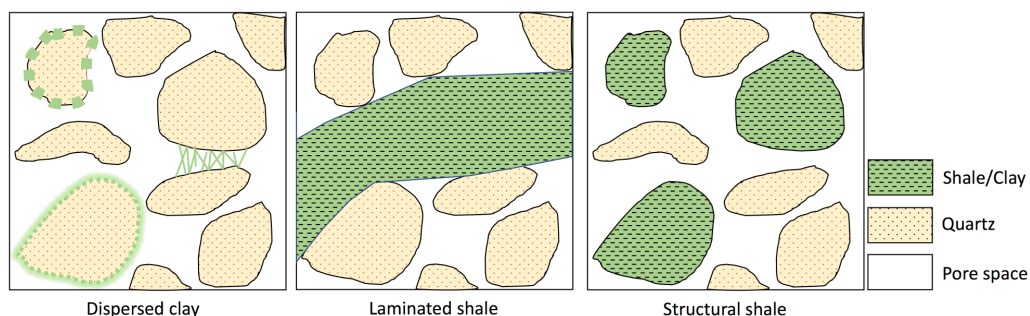
The four most common clay minerals are shortly described in the following list and is based on work by Morad et al. [9].

- ◇ **Kaolinite**  $\text{Al}_4[\text{Si}_4\text{O}_{10}](\text{OH})_8$  is the simplest clay consisting of silica tetrahedra and aluminum octahedra. It originates from feldspars and muscovite.
- ◇ **Smectite**  $(\text{OH})_4\text{Si}_8\text{Al}_4\text{O}_{20}\cdot n\text{H}_2\text{O}$  is common at shallow depths. Smectite is a swelling clay type that contains interlayer water that can collapse through compaction or heating. Smectite transforms into illite above 100°C. This leads to 30% volume reduction due to expulsion of ionized water. Smectite can also transform into kaolinite, and montmorillonite is a common type of swelling smectite.
- ◇ **Illite**  $\text{K}_{1.5}(\text{Si}_8\text{Al}_{1.5}(\text{Al}_4\text{Fe}_4\text{Mg}_4)\text{O}_{20})(\text{OH})_4$  is the most common clay type. While smectite has interlayer water, illite has interlayer potassium ions. The

transformation of smectite to illite can cause a reduction in porosity of 1-10%. Illite can transform into chlorite with increased temperature.

- ◇ **Chlorite**  $(\text{MgFe}^{2+}\text{Fe}^{3+}\text{MnAl})_{12}[(\text{SiAl})_8\text{O}_{20}](\text{OH})_{16}$  is a stable mineral at high temperatures. It contains interlayer brucite  $(\text{Mg}(\text{OH})_2)$  at every other octahedron. Chlorite preserves reservoir quality through preventing cementation. Chlorite crystals are smaller than illite and cause less severe occlusion of pores in coarse grained sandstones.

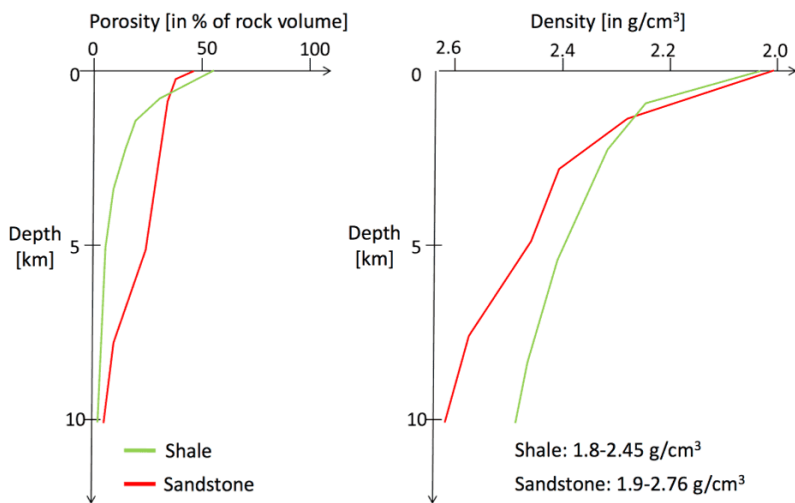
A combination of different clay types is called *mixed layer clays* and is common in the transition phase from one clay mineral to another. Shale and clay can be distributed as laminated shale, dispersed clay or structural shale, as illustrated in Figure 5.4. Dispersed clay has the most devastating effect on the porosity and permeability as the clay is occupying the intergranular pore space and severely reduces the fluids ability to flow. While kaolinite tend to be pore filling, illite tend to be pore bridging and will significantly target the permeability. High amounts of microporosity will maintain some of the porosity [6]. Chlorite is typically pore lining. Laminated shale will alter the anisotropic properties of the rock, reducing flow perpendicular to the bedding. Laminated shale will thus reduce the porosity where present, and preserve porosity between the shale beds. Not occupying any intergranular pore space, structural shale will not reduce the reservoir quality, if not heavily compacted and deformed between harder quartz grains.



**Figure 5.4:** Illustration of shale and clay distribution in a sandstone. The dispersed clay show pore filling, lining and bridging clay. Based on work from Ellis & Singer, 2007 [6].

## 5.2 Porosity

Porosity is a term that has slightly different meaning, depending on the setting it is used in. For a petrophysicist, total porosity is defined as the available pore space not occupied by the rock matrix or dry solids. The effective porosity excludes clay bound water and water trapped in the shale matrix, but includes capillary bound water (see Figure 5.6). In terms of diagenesis, porosity can be divided into primary porosity and secondary porosity. Primary porosity is the porosity that occurs at deposition (intergranular for sandstones). Sorting is the prominent property affecting depositional porosity. Unsorted grains tend to have low porosity because smaller grains occupies the pore space between the larger grains. Sandstones tend to have a primary porosity of about 40% while the primary shale porosity tend to be higher, above 50% (see Figure 5.5). When buried, mechanical compaction reduces the porosity the first 2-3 kilometers. A general rule of thumb for porosity loss during burial is that 1% of the porosity is lost per 100 m of burial. At higher depths, temperature rises and chemical compaction takes over. Figure 5.5 indicates that the sandstone retains its porosity at deeper depth compared to the shale which is highly affected by mechanical compaction during the initial burial. The rock density rises with mechanical and chemical compaction.



**Figure 5.5:** A model showing the development of porosity and density with depth for shale (green) and sandstone (red).

Secondary porosity is porosity that develops during diagenetic processes. It includes dissolution of matrix, solids and authigenic cements, as well as removal of the dissolved products. Porosity of sandstone divides into several types, such as intergranular porosity, microporosity (smaller than the sand grains), fracture porosity (porosity developed during brittle deformation) and dissolution or vuggy porosity (macroporosity). As described by Choquette & Pray, other porosity types like intragranular, moldic and fenestral exist for carbonates [40]. The resulting reservoir porosity is a function of primary porosity, depth and compaction, cementation and other diagenetic processes either destroying, creating or preserving porosity [10].

### 5.2.1 Petrophysical porosity curve

Density porosity curves can be applied to petrophysical logs to estimate the porosity throughout the drilled succession. The equation used for calculation of the density porosity curve is as follows:

$$\phi_{log} = \frac{\rho_{ma} - \rho_b}{\rho_{ma} - \rho_f}, \quad (5.1)$$

where  $\phi_{log}$  is log porosity and  $\rho_{ma}$ ,  $\rho_b$  and  $\rho_f$  are matrix density, bulk density and fluid density, respectively.

### 5.2.2 Intergranular volume

Intergranular volume (IGV) is the sum of the matrix, cement and porosity between the detrital grains. IGV decreases with burial due to mechanical compaction, which depends on the amount of overburden. Grain size, sorting, grain shape and mineral type are important factors affecting the amount of compaction and IGV.

$$IGV [\%] = V_{porosity} + V_{cement} + V_{matrix} \quad (5.2)$$

### 5.2.3 Volumetric rock model

For a shaly sand, the bulk volume ( $V_b$ ) of the rock can be divided into porosity, shale and rock matrix (see Figure 5.6), where effective porosity ( $\phi_e$ ) is defined

as the mobile and capillary bound water and hydrocarbons in the pores. Total porosity ( $\phi_t$ ) includes clay bound water (CBW) from shale. Thus, the difference between  $\phi_e$  and  $\phi_t$  is the CBW trapped in the shale matrix, attached to the clay surface and related to the clay molecules. The rock matrix is composed of all the minerals except silt and clay solids.

<b>Porosity</b>	$\phi_t$	$\phi_e$	Oil and/or Gas	Mobile	} $V_b$
				Residual/capillary bound	
<b>Free Water</b>		Free Water	Mobile		
			Irreducible/capillary bound		
<b>Shale</b>	$V_{shale}$ (wet)	Bound Water	Trapped in the shale matrix		
			Attached to the clay surface		
			Constituent of clay molecules		
$V_{clay}$	$V_{silt}$	Dry Solids	Dry clay (Clay 1, Clay 2, Clay 3)		
$V_{silt}$			Silt		
<b>Rock Matrix (non-clay)</b>	$1 - (V_{shale} + \phi_e)$	Mineral 1			
		Mineral 2			
		Mineral 3			
		Mineral 4			

**Figure 5.6:** Indicates the components for the bulk volume of the rock. The figure is based on work by Ellis and Singer, 2008, and the Petrophysics Advanced course by Erik Skogen, 2018 [6].

### 5.3 Reservoir quality

In terms of petroleum exploration, the porosity and permeability are highly important for the reservoir quality. The effective porosity of the bulk volume is the storage capacity, while permeability is the transmittability of fluids, which combined defines the reservoir quality. Porosity values higher than 15% are preferred for high quality reservoir zones. Moreover, important reservoir quality controlling factors are the type of depositional environment, the diagenetic evolution, mechanical and chemical compaction, cementation, dissolution, recrystallization, structural deformation, wettability and capillary pressure among others. Mass solute transfer from evaporites are important for the reservoir quality of sandstones.

It gives high salinity water which may prevent albitization of K-feldspar, anhydrite cementation, illitization of kaolinite, and sulphide mineralization in presence of hydrocarbons [10]. For the Trøndelag Platform and Ellingråsa Graben, the reservoir quality in the Norian, Carnian and Ladinian Triassic sandstones may be affected by mass solute transfer from the Unit Tr4 Upper and Lower Salt. This is one of the key questions that will be investigated in later chapters. The loss of porosity as a result of compaction and cementation are also of importance.

## Chapter 6

# Mineralogy and petrography

In order to fully understand the results obtained from optical microscopy, SEM and XRD analysis, a chapter of fundamental theory on these methods is included. Understanding the capacity of the apparatuses and how they generate results will not only create better results, but also determine abnormal results and sources of error.

### 6.1 Optical microscopy

Optical microscopy uses petrographic microscopes to determine the nature of rock minerals. A light source, sent through the thin section and the objective, generates a magnified image of the sample detectable in the oculars. By letting all the light waves to pass through, the thin section is observed at plane polarized light. By applying a polarizer lens over the objective lens, only certain light waves are allowed to pass through the filter. Thus, the thin section sample is observed in cross polarized light. In addition, the thin sections can be observed at reflected light. The light source of reflected light microscopes originates from a light house above the objectives.

### 6.2 Scanning electron microscope

In a SEM apparatus, a thin beam of electrons scans the sample while a detector records the scattered electrons from each point of the sample. The detector signal is proportional to the amount of scattered electrons. Fjellvåg explains that by synchronising the electron beams, the sample points are depicted [41]. Due to the high velocity of the scanning, a picture of the whole sample is generated. The

resolution of SEM is able to detect particles at a size of 2 nm, and is therefore a powerful tool for clay structure investigations [41]. The configuration of the software used for interpreting the signals displays heavy minerals as light colors, while light minerals are dark colored. Dispersive X-Ray spectroscopy (EDS) is a method from SEM that measures the X-ray signals from a sample point. The given X-ray signal is characteristic for the atomic number. The sum of X-ray signals generates a spectra characteristic for the respective mineral. Thus, the EDS spectra makes it possible to determine the mineral composition at a desired point during SEM.

### 6.3 X-ray diffraction

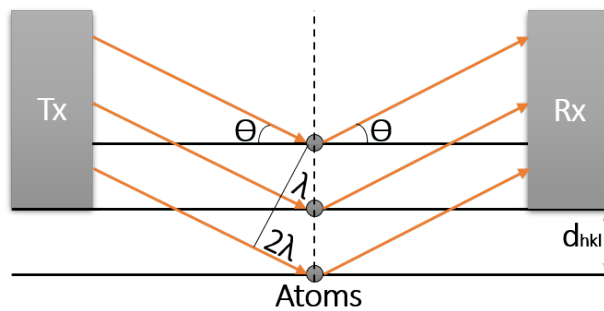
XRD methods use the signal from diffracted X-rays to determine the composition of the targeted mineral. Based on the frequency of emitted X-rays of a specific wavelength, XRD can estimate the proportion of the mineral assemblage. XRD follows Bragg's law:

$$\lambda = 2d_{hkl}\sin\theta \quad (6.1)$$

Figure 6.1 shows an X-ray transmitting beam on three sets of parallel planes of atoms. The beam is sent from the transmitter ( $T_x$ ). The distance between the planes is  $d_{hkl}$ . The incident angle is equal to the diffracted angle and reaches the receiver ( $R_x$ ). This is called constructive interference and can only occur if Bragg's law is fulfilled:

1. The emitting X-ray wavelength  $\lambda$  is fixed.
2. Diffraction peaks only occur at the specific angle  $\theta$ .
3. A plane of atoms must be perpendicular to the vector that bisects the incident and diffracted beam angle.





**Figure 6.1:** Simplified sketch of the conditions required for the transmitting X-rays to diffract from a two-dimensional crystal lattice to the receiver.

As explained by Mani, the peak position is determined by the distance  $d_{hkl}$  and the peak intensity by the specific atom in the specific position [42]. The resulting signal is transformed to XRD patterns of the specific minerals which are plotted with the X-ray intensity against the diffraction angle. The mineral XRD patterns show what crystal plane that gives the specific peak.



# Chapter 7

## Methodology

The methodology of this thesis gives the detailed procedure of generating the results. The first section of Chapter 7 will in short deal with the approach used for gathering the data and how the data have been used in this work. The method of determining geothermal gradients is described in the second section. Furthermore, Section 7.3 shows the approach of the mineralogical and petrographical analyses. At the end of this section, an overview of the applied methods for each of the samples can be found. The final section includes the sources of error for the different applied methods.

### 7.1 Data set

Initially, the data set was chosen by sorting wellbores at the Norwegian Petroleum Directorate's fact page, hereafter referred to as the NPD fact page. The sorting criteria are covered in Section 7.1.1. Additional data and samples were collected from the Diskos National Data Repository (NDR) and from Weatherford's core storage in Stavanger, respectively.

#### 7.1.1 Wellbores

Starting with 1874 exploration wellbores on the Norwegian continental shelf, the sorting criteria filtered out wellbores based on their main area, oldest penetrated age and publication date, ending up with 85 public domain wellbores from the Norwegian Sea older than the Åre formation. By investigating bulletins and papers by Blystad et al. [2], Dalland et al. [21], Müller et al. [3], Brekke and Riis [43], Bugge et al. [44], Jongepier et al. [45], Oftedal et al. [46], Mørk and Johnsen [47] and others, it was decided to investigate 20 exploration wellbores

in more detail. Data on wellbore history, chronostratigraphy, lithostratigraphy and penetration depths, in addition to wellbore information such as grid position, penetration depth, temperature at TD, available core and cutting descriptions for these 20 wellbores were collected from the NPD fact page to form a database. The filtered wellbores can be observed in Table 7.1.

**Table 7.1:** 20 wellbores from the Norwegian Sea. Wellbore 2, 5, 9 and 10 penetrates Precambrian basement. The column showing *oldest penetrated age* excludes the basement. \*Informal name.

Number	Wellbore name	Oldest penetrated age	Oldest formation
1	6305/12-1	Pre-Noran	Uint Tr4-1
2	6306/6-1	Rhaetian or older	Uint Tr5-1
3	6406/1-2	Rhaetian-Induan	Red Beds*
4	6406/11-1	Rhaetian	Uint Tr5
5	6407/10-3	Ladinian	Uint Tr3
6	6407/7-1 S	Norian	Uint Tr5
7	6507/12-1	Rhaetian	Uint Tr5
8	6507/12-2	Anisian	Uint Tr3
9	6507/6-1	Induan	Uint Tr1
10	6507/6-4 A	Pre-Wuchiapingian	Rotliegend GP
11	6507/8-6	Rhaetian	Uint Tr5
12	6510/2-1	Late Carnian	Uint Tr4
13	6510/2-1 R	Olenekian	Unit Tr2
14	6608/11-1	Rhaetian	Uint Tr5
15	6608/11-5	Late Triassic	Red Beds*
16	6608/8-1	Wuchiapingian	Zechstein GP
17	6609/10-1	Rhaetian	Uint Tr5
18	6609/5-1	Olenekian	Uint Tr2
19	6610/3-1 R	Norian	Uint Tr5
20	6610/7-2	Anisian	Uint Tr3

In the database, the wellbores were sorted in relation to the international chronostratigraphic chart and the lithostratigraphic chart from the Trøndelag Platform, Halten Terrace, Vøring Basin and the Møre Basin in the Norwegian Sea. The arrangement was based on reported penetrated formations from the NPD fact page. By including the depth of the formation horizons, the scheme was able to discover erosional surfaces, unconformities and hiatuses, as well as formation depths. The side wall cores and recovered cores from the respective wells were identified and marked in the scheme. Based on availability of cores, sidewall cores, existing core

pictures, completion logs and reports, nine wellbores were selected for further investigation of their petrophysical characteristics. These are listed in Table 7.2. A map showing the location of these wellbores can be found in Figure 3.3.

**Table 7.2:** Nine wellbores from the Norwegian Sea selected according to availability of data.

Number	Wellbore name
5	6407/10-3
7	6507/12-1
8	6507/12-2
9	6507/6-1
10	6507/6-4 A
12	6510/2-1
14	6608/11-1
16	6608/8-1
20	6610/7-2

### 7.1.2 Petrophysical logging

The petrophysical investigation of the wellbores was done using Techlog, a Schlumberger tool for petrophysical investigations. The idea was to investigate the lithology in the respective wellbores, trying to say something about the reservoir quality and where the salt is located, which in turn were the key arguments for deciding on where to collect the samples from. The data gathering for the Techlog analysis was done downloading LAS-files from the NDR. This is a database controlled by the NPD, where copies of all the seismic and drilling raw data from the NCS are collected and stored [14]. These files were imported to Techlog, for construction and interpretation of well logs.

The well logs are designed with a header that contains general information about the specific well, such as the well name, loggers name, data set, various type of elevations, total depth, a reference grid, the spud and completion date, as well as the field and survey company. It is further divided into a number of columns depending on what measurements the company conducted during the survey. The upper log of well 6507/6-1 can be found in Figure 7.1 to demonstrate the log design. Some applications concerned all the wells; the gamma ray (GR) and the caliper (CALI) on the left column, and to the right; the resistivity (LLD, LLS, ILD, ILM, MSFL, MCFL) column with various coverage of the drilled section, the

sonic (DT) column, the density (DRHO, RHOB) and neutron porosity (NPHI) column with density correction and sand/shale crossover. Below, in Table 7.3, the main applications for the different log measurements are displayed.

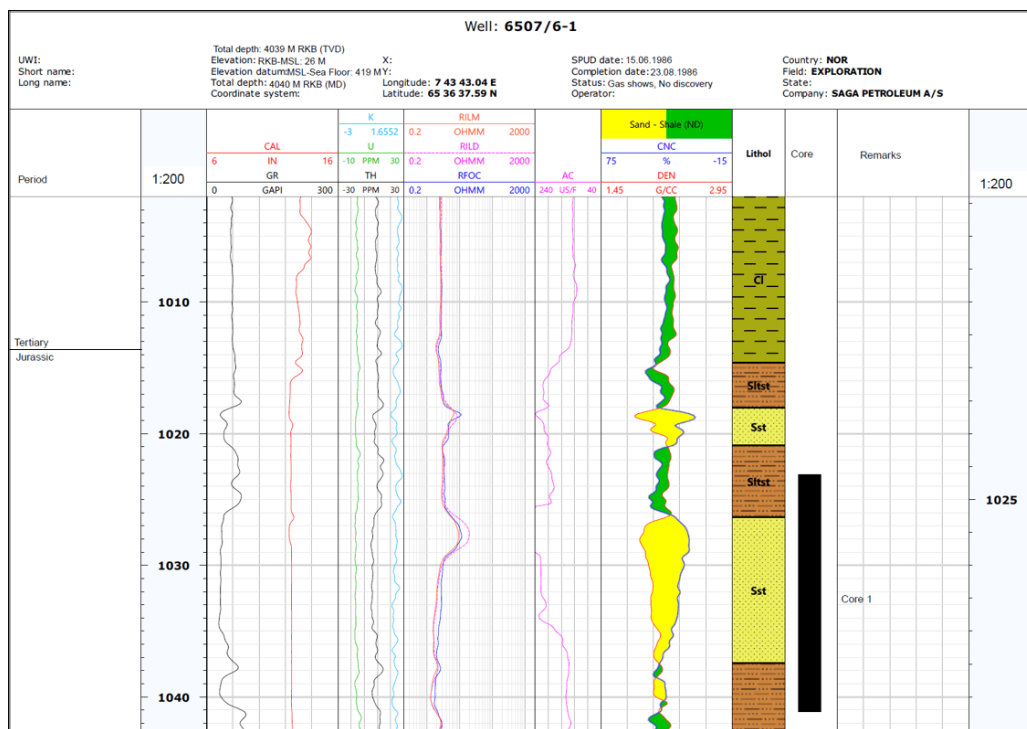
**Table 7.3:** Some of the applications for the log measurements used in the constructed logs.

<b>Log measurement</b>	<b>Main applications</b>
Gamma Ray	Lithology, shale volume
Caliper	Permeability, borehole condition
Resistivity	Fluid type, permeability
Sonic	Porosity, lithology, fractures
Density	Bulk density, lithology, porosity
Neutron	Porosity, lithology, gas

The logs also contain a column for chronostratigraphic and lithostratigraphic information, a column that shows the presence of side wall cores and conventional cores, a reference depth curve, a column for remarks and a column for lithology interpretation. The lithology interpretation curve is based on the different curve values as well as the existing interpretation from the completion report and completion log at the NPD factpage.

In addition, some logs contain a potassium, uranium and thorium concentration curve which can give an indication of mineralogy. Others contain an automatically generated shale volume estimation curve, and a coal-, limestone- and coal-flag curve for lithological suggestions. The different features in the well logs were used to get an overview of the different wellbores and to prepare for the core sampling stage at Weatherford's core storage in Stavanger. In addition, the well logs were used for comparison with the results from sedimentary logging.

The logs were constructed in three different scales; 1:50, 1:200 and 1:2000. The depth interval covered for the different logs vary depending on the scale. For the 1:50 scale, only the cored interval is covered, for the 1:200 scale, the Base Cretaceous Unconformity (BCU) and down to TD is covered, and for the 1:2000 scale, the whole log section is covered. The 1:50 scale was made for detailed investigation on site, 1:2000 for overview and comparison between the wells, while 1:200 was the ideal scale to work with in Techlog. For each of the nine wells, three logs were created and brought to the core view storage as support for sedimentological logging and sampling.



**Figure 7.1:** The upper part of the log for well 6507/6-1 at a scale of 1:200. The log is generated using Techlog on raw data from the Diskos NDR.

## Density porosity curve

The density porosity curve was calculated on the petrophysical logs to indicate the porosity throughout the Triassic succession of wellbore 6610/7-2, 6507/6-1, 6507/12-2 and 6507/12-1. For Equation 5.1 in Section 5.2.1,  $\rho_f$  is set to 1.02 (slightly saline solution),  $\rho_{ma}$  assumes a sandstone density of 2.65 g/cm<sup>3</sup>, while the bulk density is a measure from the logging tool along the wellbore. Thus, the curve is valid for sandstone reservoir zones and should be applied to other lithology zones with caution. An overestimation of the porosity can therefore be observed in salt- and coal zones on the lithology column. It should be noticed that  $\rho_{ma}$  in Equation 5.1 is set to 2.75 g/cm<sup>3</sup> for well 6507/12-2, as 2.65 g/cm<sup>3</sup> would cause negative values of the porosity. This will give slightly higher porosity values, and might generate an overestimation of porosity at shallower depths where the cementation rates are lower. In addition, a Gaussian smoothed density porosity curve which is based on the primary density porosity curve, was established to

reduce noise for selected wells.

### 7.1.3 Sedimentological logging

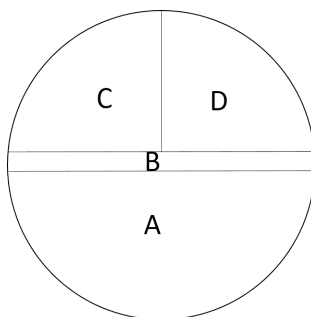
Sedimentological logging was done on cores at the scale of 1:20 using core photos and sedimentological interpretation available at the NPD fact page, as well as observations of the A-cut and B-cut (see Figure 7.2) at the core storage. Also, additional core photos were taken on site and used for logging. The sedimentary logging of the cores from the nine wells covered a range of 181.5 m in total. After reviewing the quality of the available core cuts, as well as limitations in cores available for sampling, nine wellbores were reduced to six (see Table 7.4). The logging of these six wells covers a range of 102 m. A handpicked collection of the logged cores can be found in Chapter 8 at a scale of 1:100 and in Appendix A at a scale of 1:20.

**Table 7.4:** Six wellbores from the Norwegian Sea selected for core sampling.

Number	Wellbore name
7	6507/12-1
8	6507/12-2
9	6507/6-1
14	6608/11-1
16	6608/8-1
20	6610/7-2

The sedimentological logging of the cores was carried out prior to and during the visit at Weatherford's laboratory in Stavanger, under the supervision of Professor and Geologist Arve Næss (NTNU and Equinor). In the storage, cores were displayed in one meter sections, except for core 6507/12-1 which was displayed in 90 cm sections. The width of the cores varied from 8-13 cm.





**Figure 7.2:** An illustration of how the core is cut. The different cuts A through D are used for different purposes.

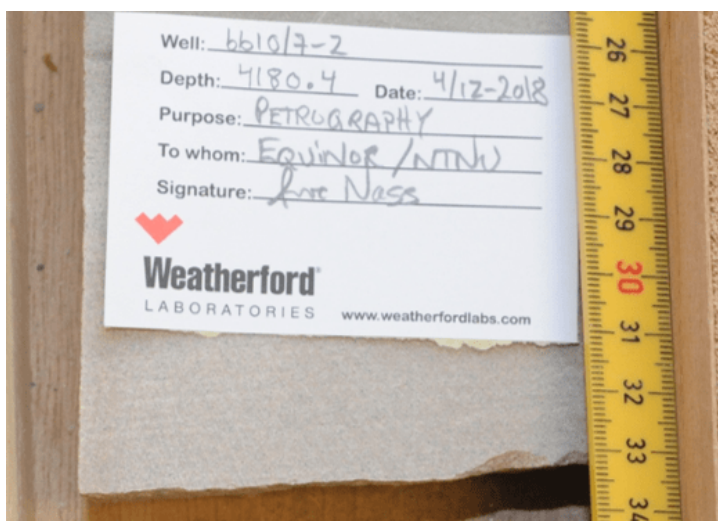
The A-cut was tested with acid to confirm the presence of carbonates and both the A- and B-cuts were sprayed with water for a clearer view before they were studied with a hand lens. Core 6608/11-1 contains a swelling clay type and could not be sprayed with water. In addition, core 6507/12-1 and 6507/12-2 were brushed clear from core dust. The different cores were logged following the geological evolution in time, starting with the deepest part. Classification of grain size was done according to Wentworth's grain size scale, which is shown in Table 7.5.

**Table 7.5:** Wenworth (1922) grain size scale [11].

Size Class	Abbreviation	Grain Diameter [mm]
Gravel		>2.0
Upper very coarse	vcU	2.0-1.41
Lower very coarse	vcL	1.41-1.0
Upper coarse	cU	1.0-0.71
Lower coarse	cL	0.71-0.5
Upper medium	mU	0.5-0.35
Lower medium	mL	0.35-0.25
Upper fine	fU	0.25-0.177
Lower fine	fL	0.177-0.125
Upper very fine	vfU	0.125-0.088
Lower very fine	vfL	0.088-0.0625
Silt		0.0625-0.002
Clay		<0.002

### 7.1.4 Sampling

An overview of the collected samples from Weatherford's core storage in Stavanger can be found in Table 7.6. 14 samples were collected for further analyses using a hammer on the A-cut. The weight of each sample was 50 g or less. The samples were named according to depth at their respective core names, as shown in Figure 7.3. These 14 samples were chosen to represent a varied collection of different lithofacies and reservoir properties. Both color, grain size, sorting, lithology, sedimentary structures, bedding, microfossils as well as collected data, depositional environment and the relative position of the sample to the Triassic salt layers were discussed prior to collection of the samples. The samples were sealed and carefully transported back to Trondheim for preparation of thin sections at NTNU.



**Figure 7.3:** Shows the naming method of the collected samples from Weatherford's core storage.

**Table 7.6:** 14 samples from six different wellbores in the Norwegian Sea collected from Weatherford's core storage in Stavanger. Here, MD is short for measured depth, sst is short for sandstone, clst is short for claystone and lmst is short for limestone.

Sample	Well	MD [m]	Lithology	Ch.strat.	L.strat.
1	6507/6-1	3044.45	Sst	Anisian	Unit Tr3
2	6507/6-1	4011.75	Sst	Induan	Unit Tr1
3	6507/12-1	3711.70	Clst	Norian	Unit Tr5
4	6507/12-1	3717.00	Sst	Norian	Unit Tr5
5	6507/12-2	4982.30	Clst	Ladinian	Unit Tr3
6	6608/8-1	1839.05	Sst	Induan	Unit Tr1
7	6608/8-1	1839.47	Clst	Induan	Unit Tr1
8	6608/11-1	1376.60	Lmst	Early Rhaetian	Unit Tr5
9	6608/11-1	1376.00	Clst	Early Rhaetian	Unit Tr5
10	6610/7-2	4180.40	Sst	Anisian	Unit Tr3
11	6610/7-2	4184.65	Sst	Anisian	Unit Tr3
12	6610/7-2	4194.05	Sst	Anisian	Unit Tr3
13	6507/12-2	4983.90	Clst	Ladinian	Unit Tr3
14	6610/7-2	4187.15	Sst	Anisian	Unit Tr3

### 7.1.5 Facies description and facies association

The facies description is based on physical characteristics of the rock samples observed from the samples themselves, thin sections, core pictures and core logs. The samples are divided into different sedimentary facies depending on sedimentary structures, lithology and other characteristics unique for the specific facies. Sedimentary facies can be further grouped into facies associations, used to define a particular depositional environment. The facies and facies association are further described in Chapter 8.

## 7.2 Geothermal gradient

The geothermal gradient was calculated using the bottom hole temperature at TD stated in *End of well reports* from the NPD fact page. The penetrated thickness was calculated subtracting the distance between 1) *RKB* and *MSL*, and 2) the *MSL* and *sea floor* from the true vertical depth. A temperature of 5°C at the sea

floor was assumed. To produce the geothermal gradient, the temperature formula in Frank S. Spear's book was used [38].

$$T(z) = \frac{-Az^2}{2k} + \left(\frac{Q}{k} + \frac{AD}{k}\right)z \quad (7.1)$$

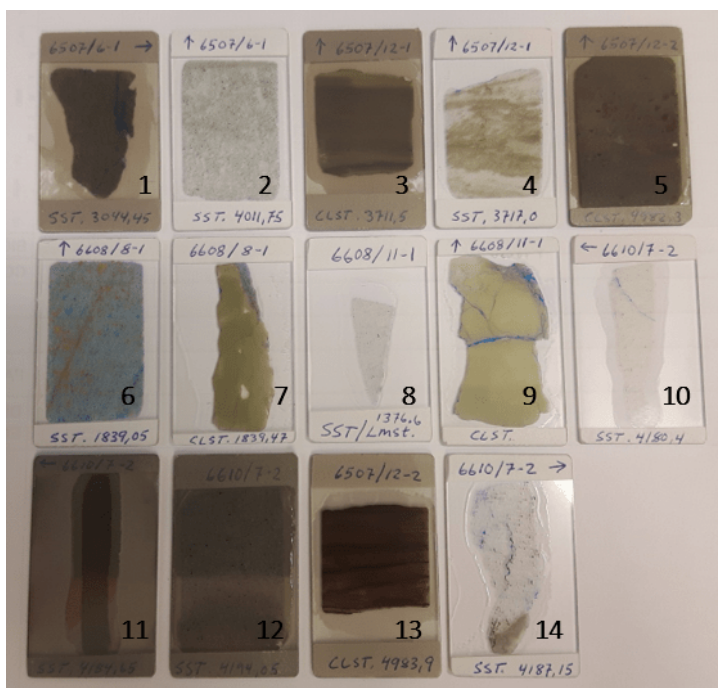
The parameters applied in this equation ( $A$ ,  $k$ ,  $Q$  and  $D$ ) are obtained by curve fitting on the measured temperature values from the NPD fact page. Here,  $A$  is the heat produced from radioactive decay,  $k$  is the thermal conductivity,  $Q$  is the heat flow,  $D$  is the crustal thickness and  $z$  is the depth. A detailed overview of the parameters used for the different wellbores can be found in Table B.1 in Appendix B. By plotting the resulting temperature versus the given depth, the geothermal gradients were determined. According to Spear, the average value of  $A$ ,  $k$  and  $Q$  is  $0.75 \text{ W/m}^3$ ,  $2.25 \text{ W/mK}$  and  $78 \text{ W/m}^2$ , respectively [38].

## 7.3 Mineralogical and petrographical analyses

Mineralogical and petrographical analyses were done in laboratories at NTNU in Trondheim. Petrological and SEM analyses were performed using thin section samples, and XRD analysis was performed using rock samples.

### 7.3.1 Thin section analysis

On the 6<sup>th</sup> of December 2018, the samples were sent to the lab for preparing the thin sections. An overview of the included samples can be found in Table 7.6 and in Figure 7.4. They were prepared by the Engineers Arild Edin Monsøy and Kjetil Eriksen. The samples were impregnated with blue epoxy, dried and glued onto a 25 x 45 mm wide glass slide.

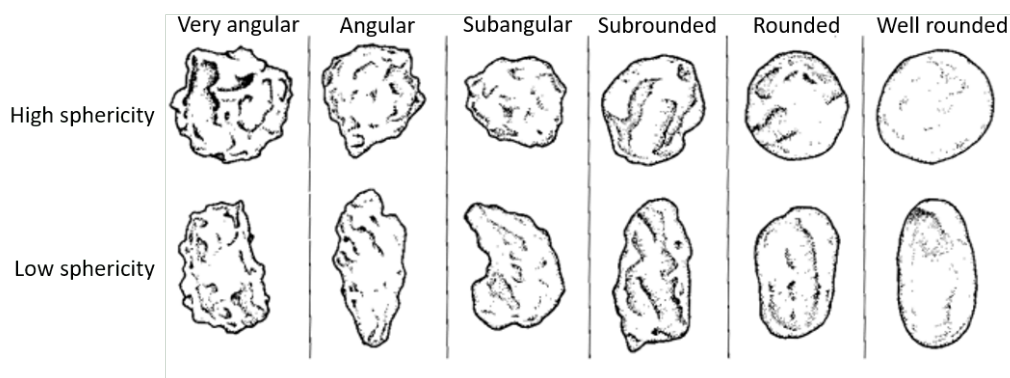


**Figure 7.4:** The resulting thin sections numbered from sample 1 to 14. Dark colored glass (e.g. sample 1) have been carbon coated for SEM analysis.

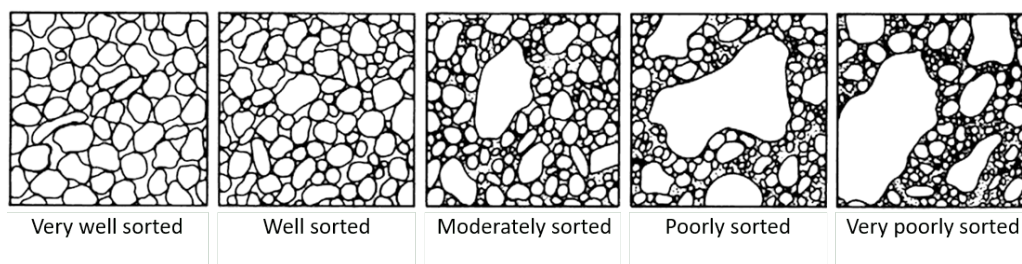
The samples were cut perpendicular to the bedding and polished down to 30  $\mu\text{m}$ , and on the 15<sup>th</sup> of January 2019 they were handed over to the author. Sample 9 from well 6608/11-1 broke in pieces during preparation due to a swelling clay type. A new version of the same sample was polished and reworked with alcohol to counteract the swelling.

A *Leica DM 2500 P* microscope was used during the study of the thin sections. The microscope is connected to a television screen, and has the capacity of a total magnification of 25 to 500x. During the study, the thin sections were investigated in plane polarized light (PPL), cross polarized light (XPL) and reflected light (REFL) at different magnifications. The microscope is also connected to a computer which is set up with *ProgRes Capture Pro*, a software that makes it possible to take pictures of the thin sections at desired scale. The thin sections gave detailed information about grain size, grain shape, sorting, mineralogy and lithology. They also provided information about internal structures and molluscs that was used to construct a model of the depositional environment for the investigated areas. Table 7.5, Figure 7.5 and Figure 7.6 were used to describe the

grain size, rounding and sorting, respectively, during the thin section analysis.



**Figure 7.5:** Grain shape terminology sorted from very angular to well rounded. From Powers (1953) [7].



**Figure 7.6:** Sorting terminology sorted from very well sorted to very poorly sorted. From Compton, 1962 [8].

## Point counting

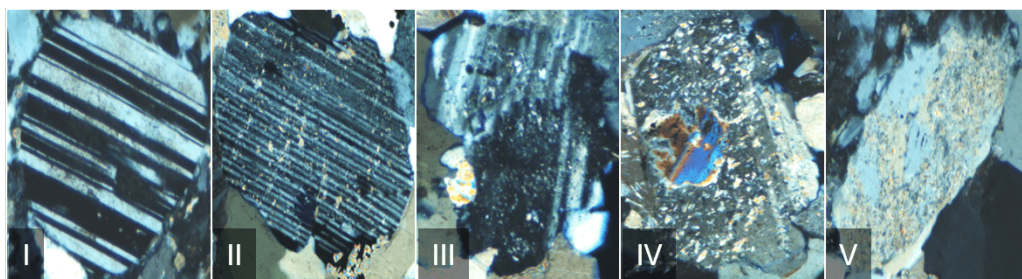
The Pelcon point counter setup on a *Nikon Optiphot* microscope was used performing point counting on sample 1, 4, 10, 11, 12 and 14. Point counting was not done for samples 3, 5 and 13 as the grain size was too small for the microscope to classify the minerals. Because of this, these samples were found to be good candidates for XRD and SEM analysis. 300 counts were performed on each of the thin sections to get representative results. When a point count fell on the border between grains, the grain on the right hand side of the border was systematically chosen. The point counting results are listed in Table D.2 in Appendix D. In

addition to classifying the grains present in the sample, point counting was also used for estimating the porosity of the samples.

After point counting, the counts were grouped so that the quartz end-member comprises of monocrystalline quartz and polycrystalline quartz, the feldspar end member consists of feldspar, K-feldspar and plagioclase, and the rock-fragment end-member contains muscovite, reworked biotite, anhydrite grains, chlorite grains, heavy minerals, opaque minerals, rock fragments, sparite rock fragments and micrite rock fragments.

Figure 7.7 shows the feldspar preservation grades from I to V. Grade I appears clean and has not been subjected to weathering. Grade II has been introduced to weathering and sericitization. The twinning is still easy to detect. At grade III the twins start to disappear, but still the feldspar type can be identified. The sericitization grade is increasing. At grade IV the twins are difficult to detect and sericitization is widespread over the mineral. Grade V is the most weathered and dissolved feldspar grade. At this stage, the twins are absent and only parts of the feldspar are preserved. Plagioclase cannot be distinguished from K-feldspar at category V.

The feldspars observed during point counting were classified either as K-feldspars, plagioclase or feldspars based on twinning type. The feldspar minerals that were too weathered to be classified as plagioclase or K-feldspar were classified as feldspar. This was typical for feldspars of preservation grade IV and V.



**Figure 7.7:** Feldspar preservation grades from I to V. Pictures are taken of thin sections from wellbore 6610/7-2.

### 7.3.2 Scanning electron microscope (SEM)

A *Hitachi SU6600 Scanning Electron Microscope* was used during the SEM analysis under supervision of the Department Engineer Kjetil Eriksen at the Department of Geoscience and Petroleum. SEM was used to identify and confirm minerals that was detected upon visual inspection of the thin sections. Thus, the main focus was to investigate authigenic minerals and therefore, samples 1, 3, 5, 11, 12 and 13 were chosen for SEM analysis. The thin sections were coated with carbon to prevent the accumulation of electrons which would have reduced the resolution of the result. The thin section was placed in a vacuum chamber in the apparatus, and scanned (bombarded) with an electron beam. The backscattered values were converted to a picture that was analysed. In this picture, lighter color signals higher atomic number, while black color signals porosity. When an interesting area was detected on the backscattered picture, EDS was performed on the thin section. The atomic composition of the resulting spectra was used to interpret the minerals of the investigated area.

### 7.3.3 X-ray diffraction (XRD)

Bulk XRD was performed on sample 1, 3, 5, 11, 12 and 13 under supervision of Chief Engineer Laurentius Tjihuis. One by one, the samples of about 20-30 g were crushed by a fly press rock into fragments of smaller diameters than 0.5 cm. Between each sample, the machine was cleaned with a vacuum cleaner, ethanol and compressed air. Afterwards, the samples were milled with a *Seibtechnik* (SiO<sub>2</sub>) agate mill down to particle sizes of about 30 µm. The samples were milled for 90 seconds at 710 rounds per minute (rpm). Between each run, the mills were cleaned and dried with water, ethanol and compressed air. As the mica minerals tend to form elongated grains during the second crushing process, the grains were put through a third crushing process to produce round grains. Stoke's law is based on an assumption of round grains, and therefore, rounding the grains produces more accurate results when applying Stoke's law. Stokes' law can be used for determination of an unknown distribution of spherical particles at desired grain size. According to CPS Instruments Europe, this is done by measuring the time required for the grains to settle a known distance in a fluid of known properties [48]. For a solution that settles for 1 hour and 46 minutes, the upper 20 cm will contain particles equal or smaller than 6 µm. The sample particles were placed in a *McCRONE Micronising Mill* machine and micronized with a SiO<sub>2</sub> agate. 10 mL of ethanol were added and the machine was running for 1 minute and 30



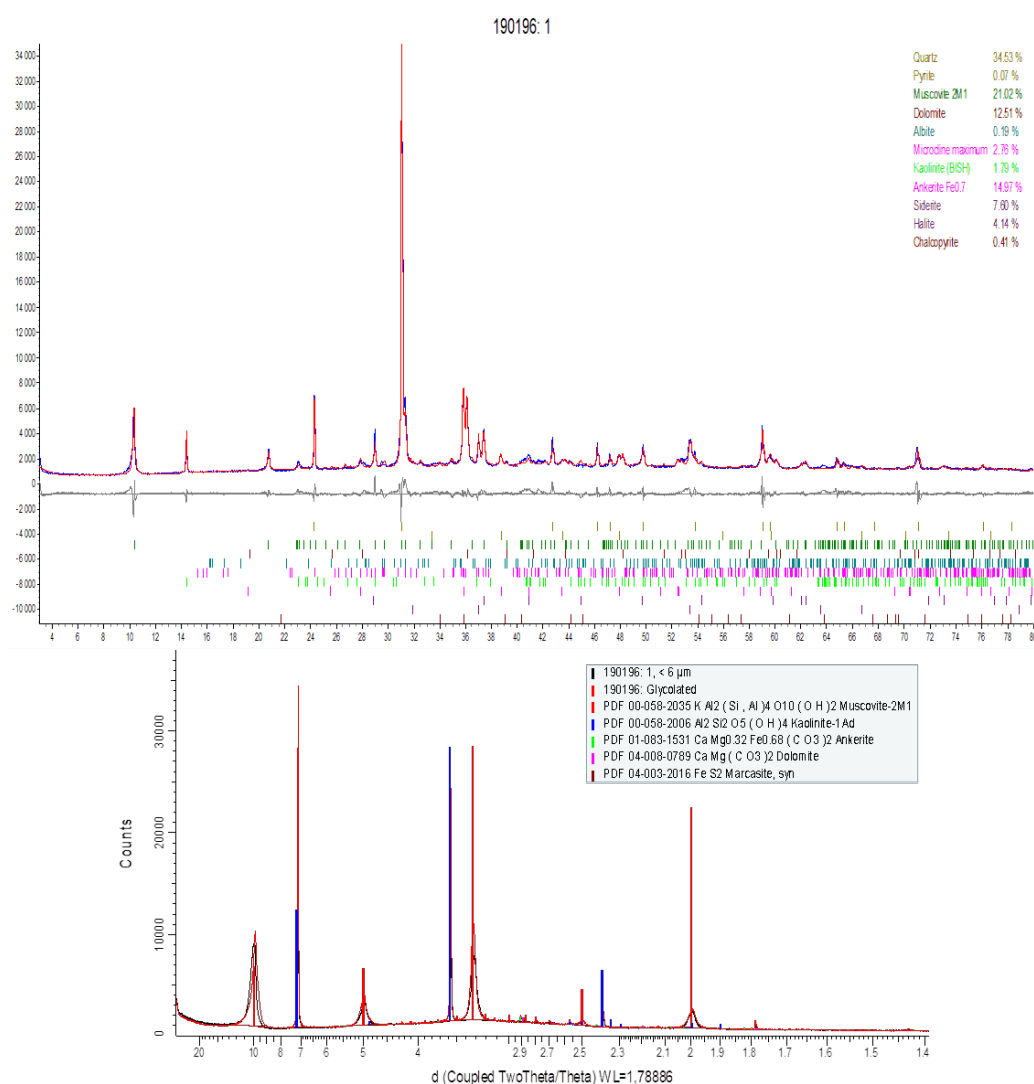
seconds per sample. Between each run, the equipment was rinsed with water and ethanol and dried. The resulting solutions were put in individual petri dishes and dried in the oven for 1 hour at a temperature of 105°C. Further, the sample powder was cooled and prepared for the XRD machine, a *Bruker - D8 Advance* apparatus. One part of the preparation was to mix the sample powder, as the particles tend to stratify in terms of grain size during the drying process. The apparatus scanned the individual samples and then, an attached software program produced the XRD results.

Fine fraction XRD was performed on sample 1, 11 and 12. One by one, the samples of about 20-30 g were gently crushed by a fly press rock crusher smaller than 0.5 cm. The samples were crushed gently to separate the finer material from the larger grains without contamination of feldspar and quartz particles. Between each sample, the apparatus was cleaned as mentioned above. The samples were placed in their own beaker filled with 200 mL elix water and placed in an ultrasonic bath for 5 minutes to separate the finer material from the larger grains. The resulting solutions were poured into graduated cylinders and settled for 1 hour and 46 minutes so that the particles above the 20 cm mark was smaller than 6 µm, based on Stokes' law. 20 cm was separated from the graduated cylinders by a vacuum suction into new beakers. The vacuum suction machine was cleaned with elix water between each run. The new solution was filtered through a paper filter that let through particles smaller than 0.45 µm. The remaining particles between 6 and 0.45 µm were placed on a glass plate. Two samples were created for each solution, one sample was placed in a glycol bath and placed in an oven of 60°C for 20 hours. If the source material is not homogeneous, the two samples can give slightly different diffractograms. If this was the case, the unglycolated sample was glycolated and run through the XRD apparatus again to compare the results. Glycol creates extra space between the atoms which may give a slightly different end result due to Bragg's law. This is done to identify swelling clay. If the sample contains swelling clay, the sample containing glycol will shift to the left in the diffractogram due to the increased atom spacing. If swelling clay is absent, the glycolated- and unglycolated-diffractogram curves will overlap. See the exemplified diffractogram in Figure 7.8. The other sample, for each of the three solutions, was placed directly into the oven. Further, the sample powder was cooled and prepared for the same XRD machine in the same manner as mentioned above. After the XRD apparatus had worked through the samples, the software (*Diffrac Plus XRD Commander*) used two methods to investigate the samples.

1. *XRD DIFFRAC.EVA* was used to identify the minerals in the samples. In

the diffractogram, the red line is supposed to match the observed blue line.

2. While *Topas* was used for quantification of the given minerals. The program uses a database of 45497 variations of minerals.



**Figure 7.8:** Example of a bulk and fine fraction XRD diffractogram. The upper plot is the bulk XRD diffractogram, while the lower shows the fine fraction diffractogram.

For a bulk XRD analysis, the resulting table is a diffractogram measuring how the intensity of diffracted radiation reaching the detector varies with the angle of diffraction,  $2\theta$ .  $2\theta$  is the sum of the incident angle and the reflected angle, which are both equal and denoted  $\theta$ . One mineral has many reflection peaks (tops) at different angles depending on which crystal surface that is reflected. The primary reflection tops fall within the d-value intervals of 2.6-3.5 and above 7.0. This can be observed in the lower fine fraction diffractogram of Figure 7.8. The d-values can be calculated by Bragg's Law, Equation 6.1. As seen from Figure 7.8, the fine fraction XRD analysis gives a diffractogram that measures how the intensity of diffracted radiation varies with the distance between the atoms (d).

### 7.3.4 Applied methods

During this work, the collected samples have been investigated using several different methods. Therefore, Table 7.7 shows an overview of the methods used on the different samples. The wellbore that each respective sample have been taken from is given in the lower row of the table. It can be observed that wellbore 6507/6-1, 6507/12-1, 6507/12-2 and 6610/7-2 were studied in more detail, compared to wellbore 6608/8-1 and 6608/11-1.

**Table 7.7:** An overview of the methods used on the different samples. (X) means that the method is performed, but not included among the results in this thesis.

Sample →	1	2	3	4	5	6	7	8	9	10	11	12	13	14
Thin section analysis	X	X	X	X	X	X	X	X	X	X	X	X	X	X
Point counting	X			X						X	X	X		X
SEM EDS	X		X		X						X	X	X	
SEM Backscattered	X		X		X						X	X	X	
SEM Topography	X										X		(X)	
XRD Bulk	X		X		X						X	X	X	
XRD Fine fraction	X										X	X		
<b>Sample wellbore</b>	6507/6-1	6507/6-1	6507/12-1	6507/12-1	6507/12-2	6608/8-1	6608/8-1	6608/11-1	6608/11-1	6610/7-2	6610/7-2	6610/7-2	6607/12-2	6610/7-2

## 7.4 Sources of error

### 7.4.1 Data set

#### NPD

As the investigated wellbores in the Norwegian Sea are very old, it is uncertain whether the information used on the Norwegian Petroleum Directorate is updated. Post well results for dry wells may also be less prioritized for the company performing the survey.

#### Techlog

Using the survey company's raw data files may have affected the logs. The resolution of the files used may be relatively low as the surveys were conducted with an old generation of logging tools.

#### Diskos Database

One cannot be certain that all of the desired data are present and distributed in the Diskos Database. There are laws facilitating the companies to hold on to their information for a given period of time in order to protect a competitive advantage. In addition, one cannot be certain that the distributed files are of good condition. Wells tend to be re-evaluated by the survey companies, and these re-evaluations are often not shared in the Diskos Database.

#### Sedimentological logging

When the cores are stored, they are divided into slices of about 1 meter each. It can occur that a core slice is marked wrong and therefore stored upside down (180° wrong). Sedimentological logging on core pictures from the NPD might also give unrealistic colors or contrasts that influence the interpretation. Old cores stored over several decades may start to produce a layer of core dust onto the core, which makes it difficult to get a clear picture of the core material.

## 7.4.2 Mineralogical and petrographical analysis

### Thin section microscopy

During the optical microscopy, the production of microscopy images using *ProgRes CapturePro* caused a slightly reduced resolution of the generated pictures. In addition, during the production of the thin sections, artifacts like air bubbles and dust grains occasionally occur.

### SEM

Due to the epoxy and the carbon coating applied to the thin section surface, the SEM results contain minor artificial chlorite and carbon traces that influence the results to some degree. In addition, the SEM apparatus cannot resolve atoms equal to or of lower atomic number than Nitrogen.

### XRD

For mineral groups like mica, plagioclase and k-feldspar (among others), the software *Topas* can give an indication of the specific mineral composition. But the software will not always manage to separate muscovite from biotite or illite, microcline from orthoclase, or dolomite from ankerite due to the shoulder-effect on the signal. This is the effect where minor signals are lost as a consequence of more dominating signals. XRD analysis will therefore not always give a complete picture of the mineral composition.



# Chapter 8

## Results

The first part of the current chapter, which describes the results from this study, highlights some of the petrophysical signals observed from the constructed well logs. The second part is assessing the sedimentary logs. This part includes interpretation of the depositional setting for the logged cores. Furthermore, the observed facies and facies associations are presented, before mineralogical and petrographical descriptions of the core samples are given. Finally, the results from thin section, XRD and SEM analyses are shown in Section 8.5.

### 8.1 Petrophysical results

Figure 8.1 correlates the Triassic succession (Unit Tr1 - Unit Tr5) for four wellbores from the Norwegian Sea with locations shown in Figure 8.2. From left to right, Figure 8.1 gives the succession of well 6610/7-2 in the northern part of the Trøndelag Platform before it moves south-westwards through 6507/6-1 at the Nordland Ridge and ends up with 6507/12-2 and 6507/12-1 at the Ellingråsa Graben. The formation top of Unit Tr5 is set as the reference baseline for the wells. The marker is placed at the base of the Åre Formation. The resulting figure gives information of the topography and relative facies thickness between the wells at the time of deposition. It should be noticed that there is a significant difference in the lateral thickness between well 6507/6-1 and the other wells. From Figure 8.1 it is clear that the relative position of sample 3 and 4 are supra-salt, in contrast to sample 1, 5, 10, 11, 12, 13 and 14 which are sub-salt.

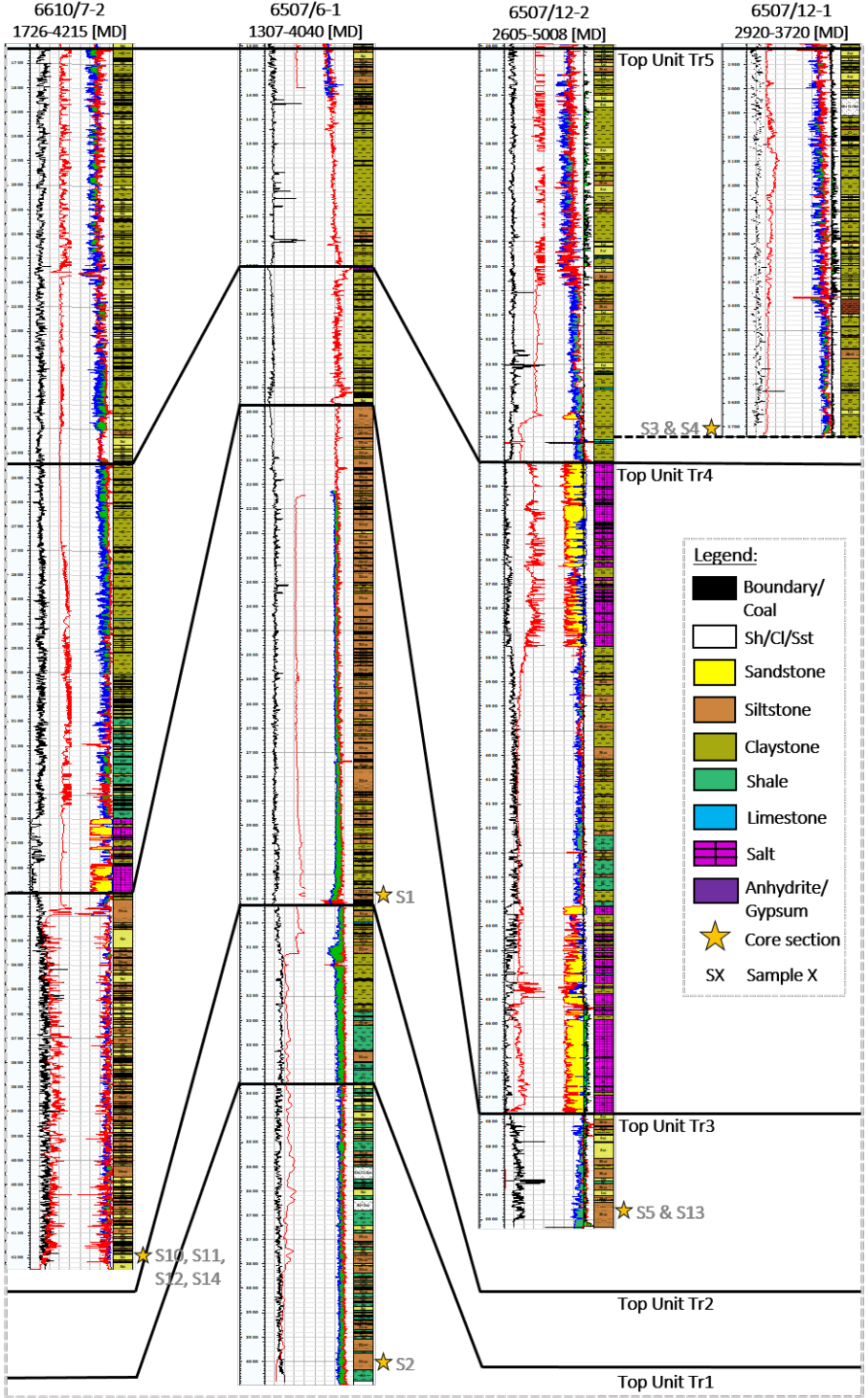
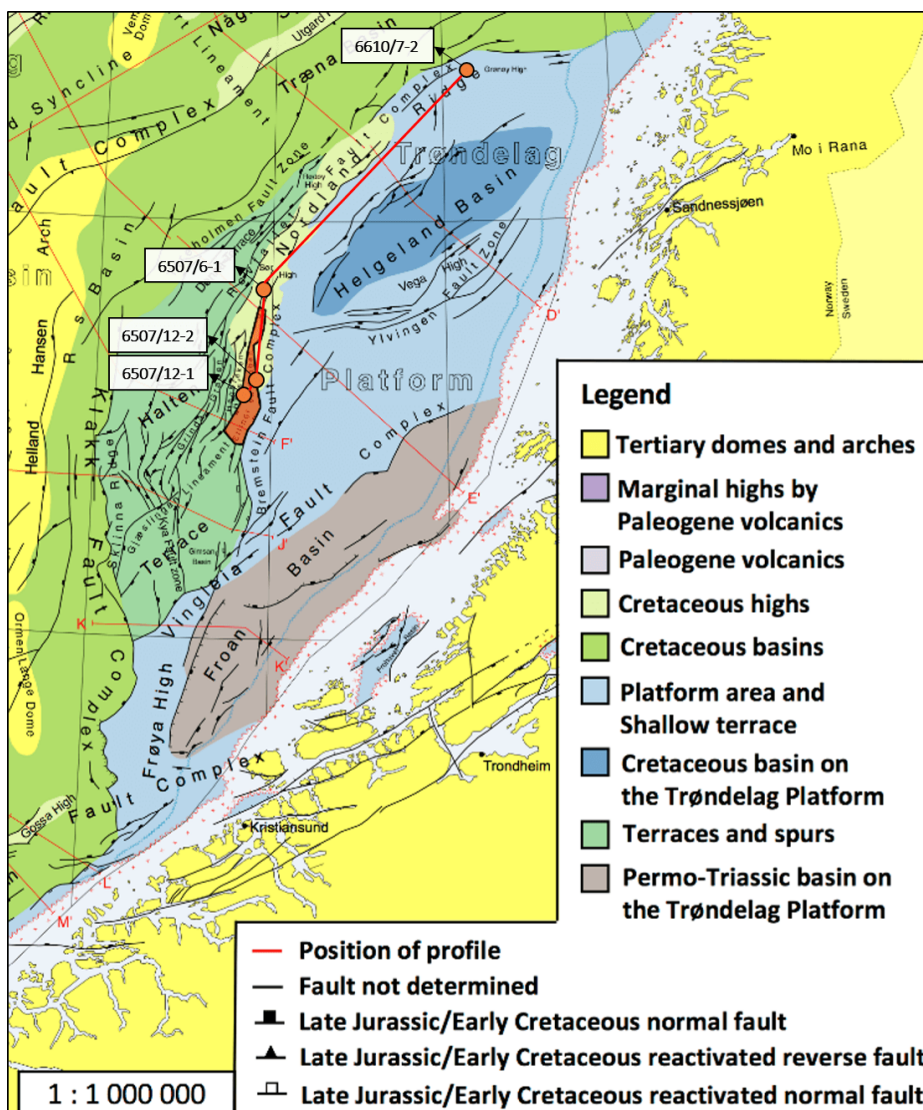


Figure 8.1: Wellbore correlation of Triassic Unit Tr1 to Unit Tr5.

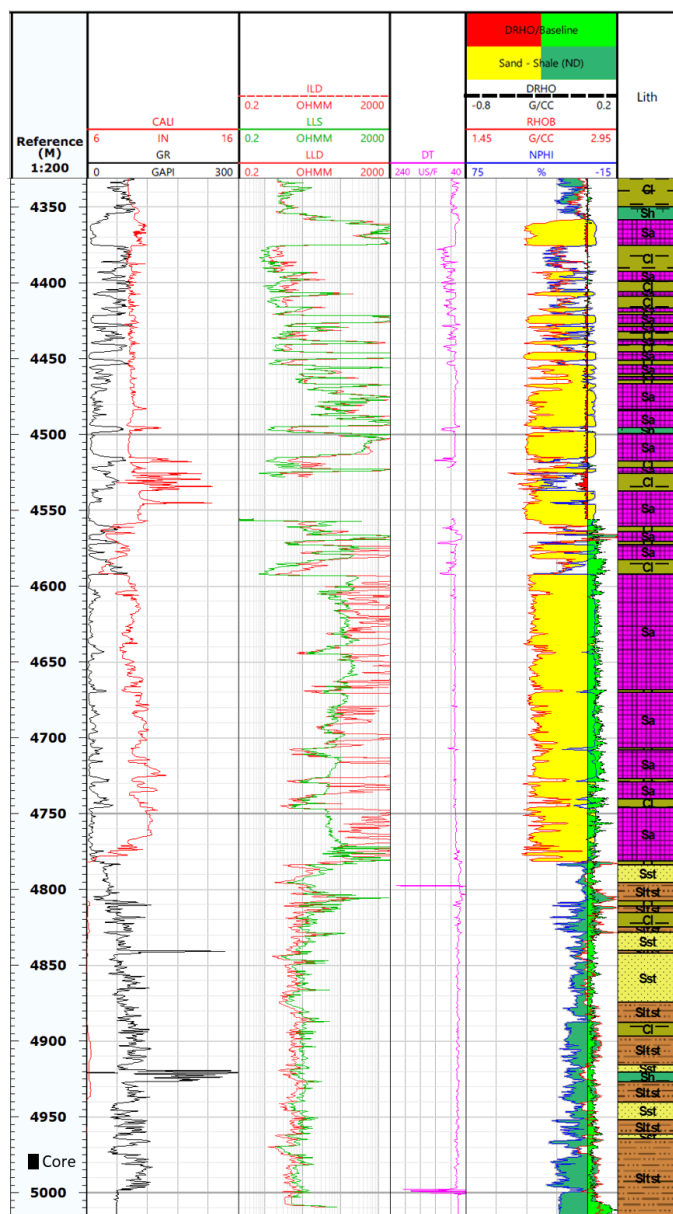




**Figure 8.2:** Structural elements of the NCS with the position of the wells investigated in Figure 8.1. This is an edited version of a figure from [2].

Exploration well 6507/12-2 was drilled June 9<sup>th</sup>, 1981 by Saga Petroleum A/S. The TD was 5008 m RKB, which includes 25 m between the RKB and MSL and 261 m between the MSL and the sea floor. The end status of the well was dry, but traces of hydrocarbons were observed in the Upper Triassic Red Bed sequence [16]. Figure 8.3 gives the petrophysical log showing 700 m of the Triassic succession in

wellbore 6507/12-2. The total penetrated thickness of the Triassic succession in this wellbore is about 2550 m, starting at a depth of 2450 m.

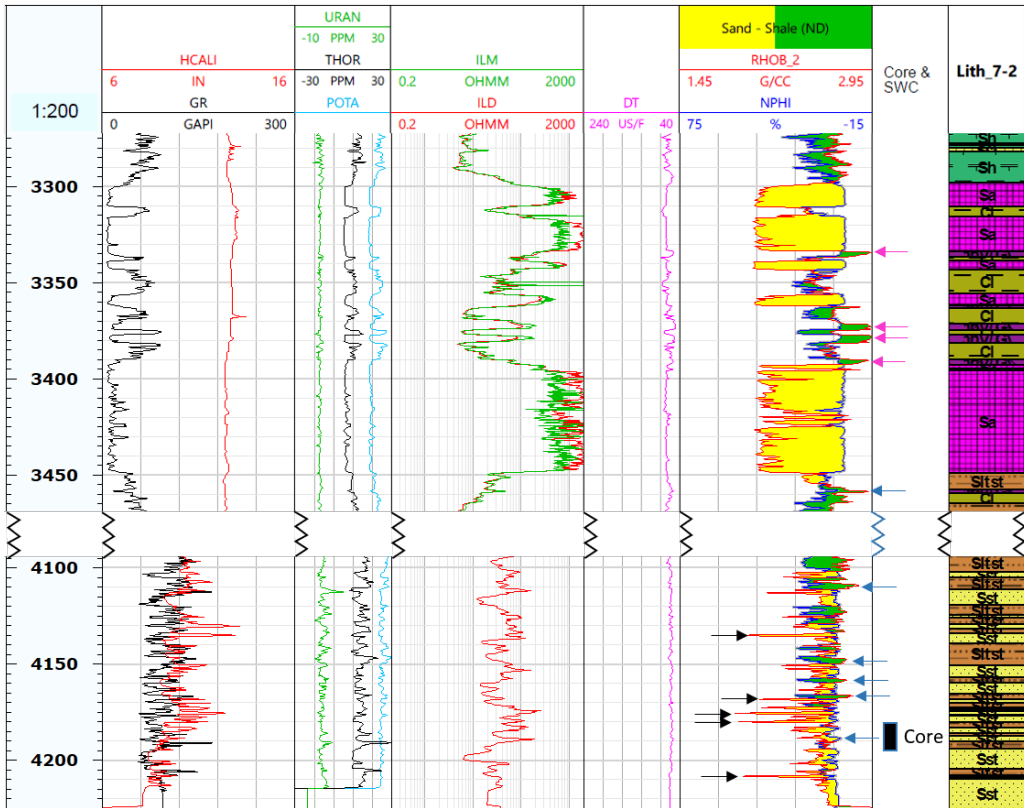


**Figure 8.3:** Petrophysical log of wellbore 6507/12-2 showing Lower Salt and core from the respective well, constructed using Techlog.

The violet color on the lithology curve is salt, and the salt is interpreted as the Lower Salt from Unit Tr4 because the Upper Salt was detected at depths between 3450-3830 m. The signal is characterized by low gamma ray readings, high resistivity readings, density values of  $2.05 \text{ g/cm}^3$  and very low neutron porosity readings. The cored section at 4975-4985 m is interpreted as siltstones based on well log readings and investigations of the core itself.

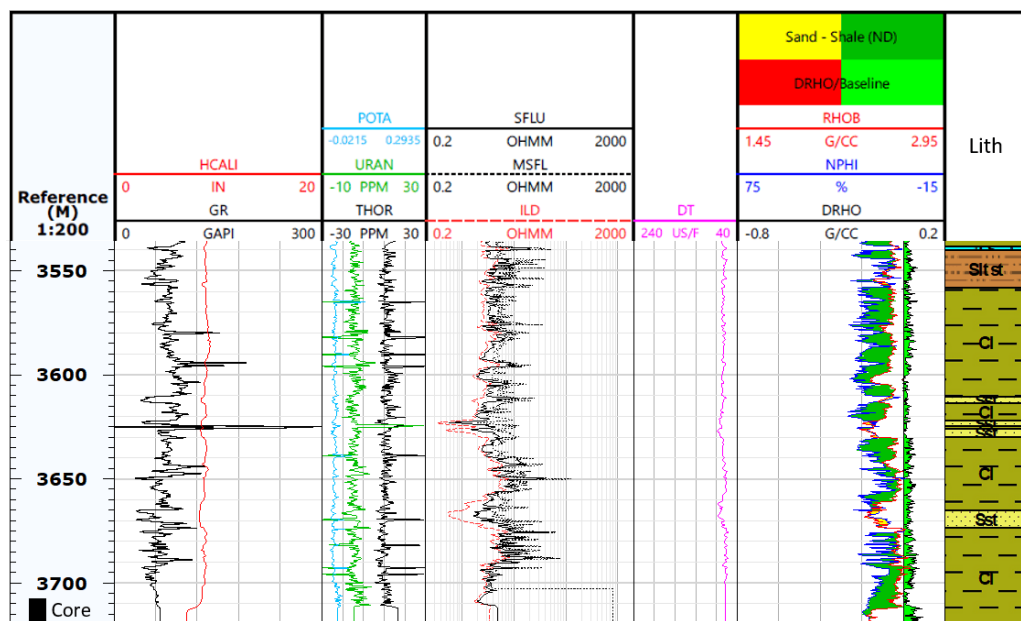
The spud date of the exploration wellbore 6610/7-2 was 28.09.1983 and the completion date was 14.03.1984. The owner company was Statoil and the end status of the well was dry [17]. The TD was 4215 m RKB (MD) and 4213 m RKB (TVD), the RKB elevation was 22 m and the distance between MSL to the sea floor was 235 m. The total penetrated thickness of the Triassic succession in wellbore 6610/7-2 is about 2595 m starting at a depth of 1630 m RKB. The cored section from wellbore 6610/7-2 consist of an alternation of thin layers of sandstones and siltstones, observed in Figure 8.4. In addition to salt signatures, spikes can be observed in between the salt layers. These have significant higher density values and are interpreted as anhydrite or gypsum. They are marked with violet colored arrows in Figure 8.4.

In the lower part of the log, the density curve shows spikes in both directions. When the density curve spikes towards lower density values (marked by black arrows), the signal may represent coal or salt. When the density curve spikes towards higher density values (blue arrows), the signal could indicate calcite cementation or diagenetic anhydrite. As this environment consists of evaporites, it can be problematic interpreting lithology based on petrophysical logs alone. Calcite cemented sandstones can be taken for siltstones as authigenic calcite alters the density value in the sandstone.



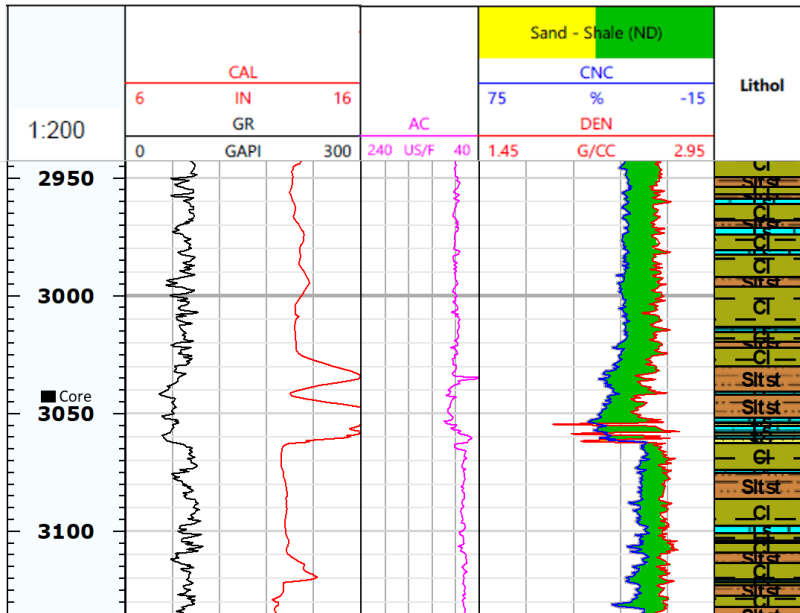
**Figure 8.4:** Petrophysical log of wellbore 6610/7-2 showing the cored section in relation to the salt observed in the well. The figure was constructed using Techlog.

Wellbore 6507/12-1 was drilled by Saga Petroleum A.S. with spud date of 01.07.1980 and completion date of 26.10.1980. This is the first exploration well drilled in the Norwegian Sea. The TD of the well was 3720 m RKB and the well status was dry [18]. Figure 8.5 shows the lower part of the logged wellbore. The cored section at depths of 3708-3720 m is located in an area dominated by claystone. The logged section is situated supra-salt.



**Figure 8.5:** Petrophysical log of wellbore 6507/12-1 showing the cored section. The figure was constructed using Techlog.

The exploration well 6507/6-1 was spudded on 15.06.1986 by Saga Petroleum A/S and completed 23.08.1986 with gas shows, but the findings were not extensive enough to be considered a discovery [19]. A TD of 4040 m RKB (MD) with a water depth of 419 m was measured. Figure 8.6 shows the constructed well log from the well. The Triassic succession starts at a depth of 1130 m RKB, and is present at TD, which gives a Triassic succession of at least 2910 m at this site. The log lacks information about resistivity at this depth, but contains enough information to develop a lithological interpretation. On the lithological column it is possible to see thin layers of calcite cement (blue color), represented by high density values and low gamma ray readings. At shallower depths of 1755-2025 m, thin dense layers were interpreted as anhydrite.



**Figure 8.6:** Petrophysical log of wellbore 6507/6-1 showing the cored section. The figure was constructed using Techlog.

### 8.1.1 Density porosity curves

The following section shows the results from applying Equation 5.1 on the petrophysical logs on well 6507/12-2, 6507/12-1, 6507/6-1 and 6610/7-2. As this equation assumes a sandstone matrix density, the curves give too high porosity values for rocks of low density, while rocks of high density may be given too low porosity values. Figure 8.7 shows the density porosity curve of well 6507/12-2 in the *DENSPOR* column. Notice that the porosity interval header ranges from 0-60%. The Gaussian smoothed density porosity curve in the *DENSPOR\** column was established to reduce noise. For this column, the red dashed line reflects the rule of thumb of 1% porosity loss per 100 m of burial. Furthermore, Figure 8.8 presents the density porosity curve for well 6507/12-1, while Figure 8.9 reflects the density porosity curve for well 6507/6-1. Finally, Figure 8.10 shows the density porosity curve for well 6610/7-2. In addition to density porosity curves, the logs have a lithology column, indicating the rock type along the well section. In general, the porosity curve values increase moving upward in the stratigraphy. The individual curves will be discussed in Section 9.3.1 of Chapter 9.3, which will focus on the relation between the reservoir quality and the observed porosity.

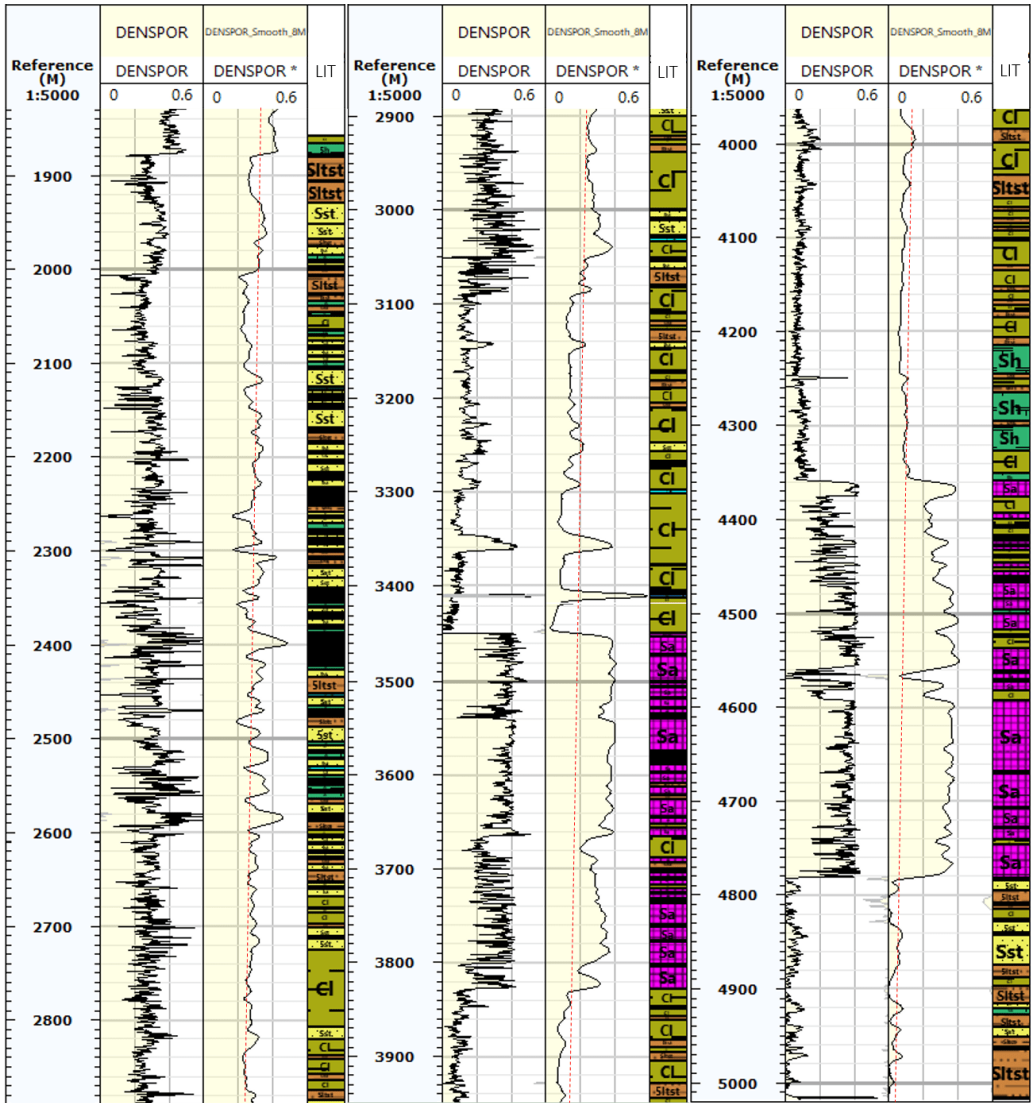


Figure 8.7: Density porosity curves for wellbore 6507/12-2. The log depth is MD.

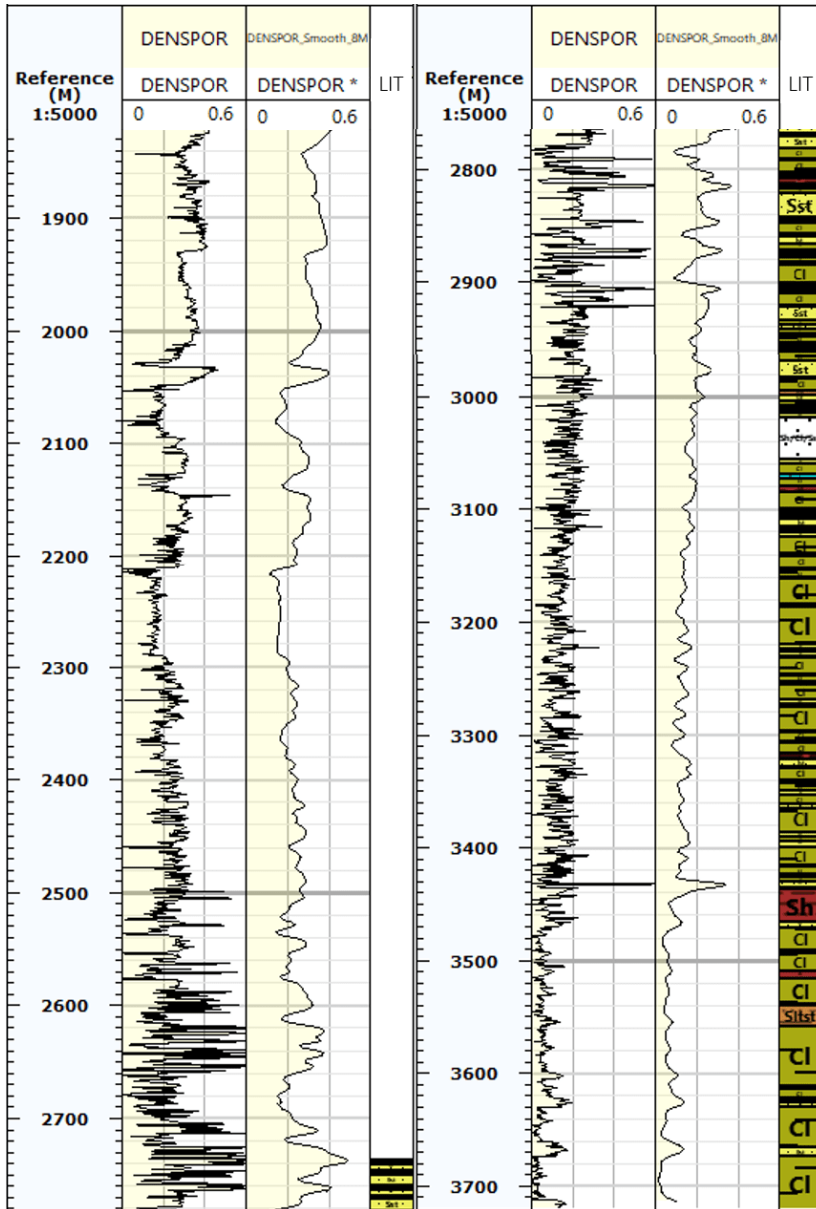


Figure 8.8: Density porosity curves for wellbore 6507/12-1.



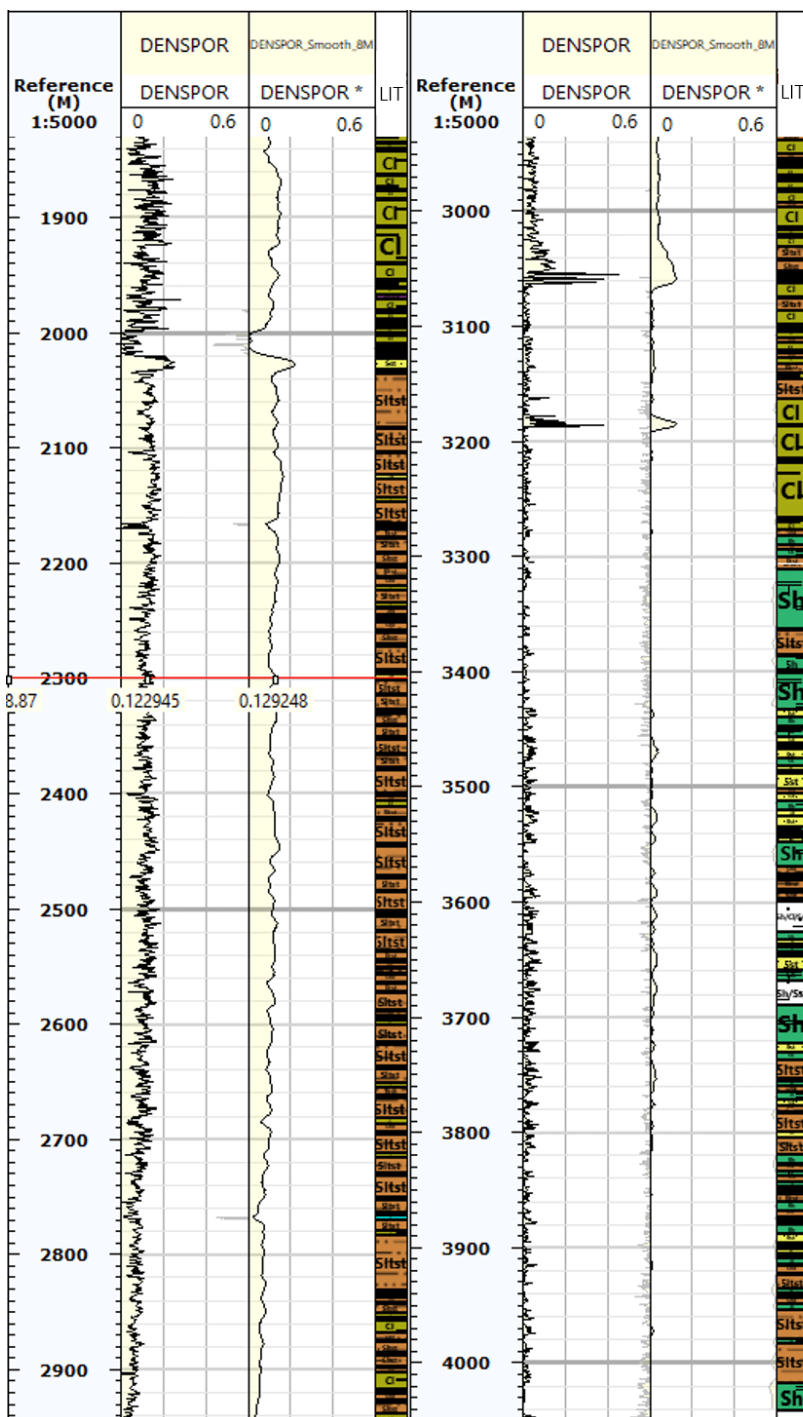


Figure 8.9: Density porosity curves for wellbore 6507/6-1.

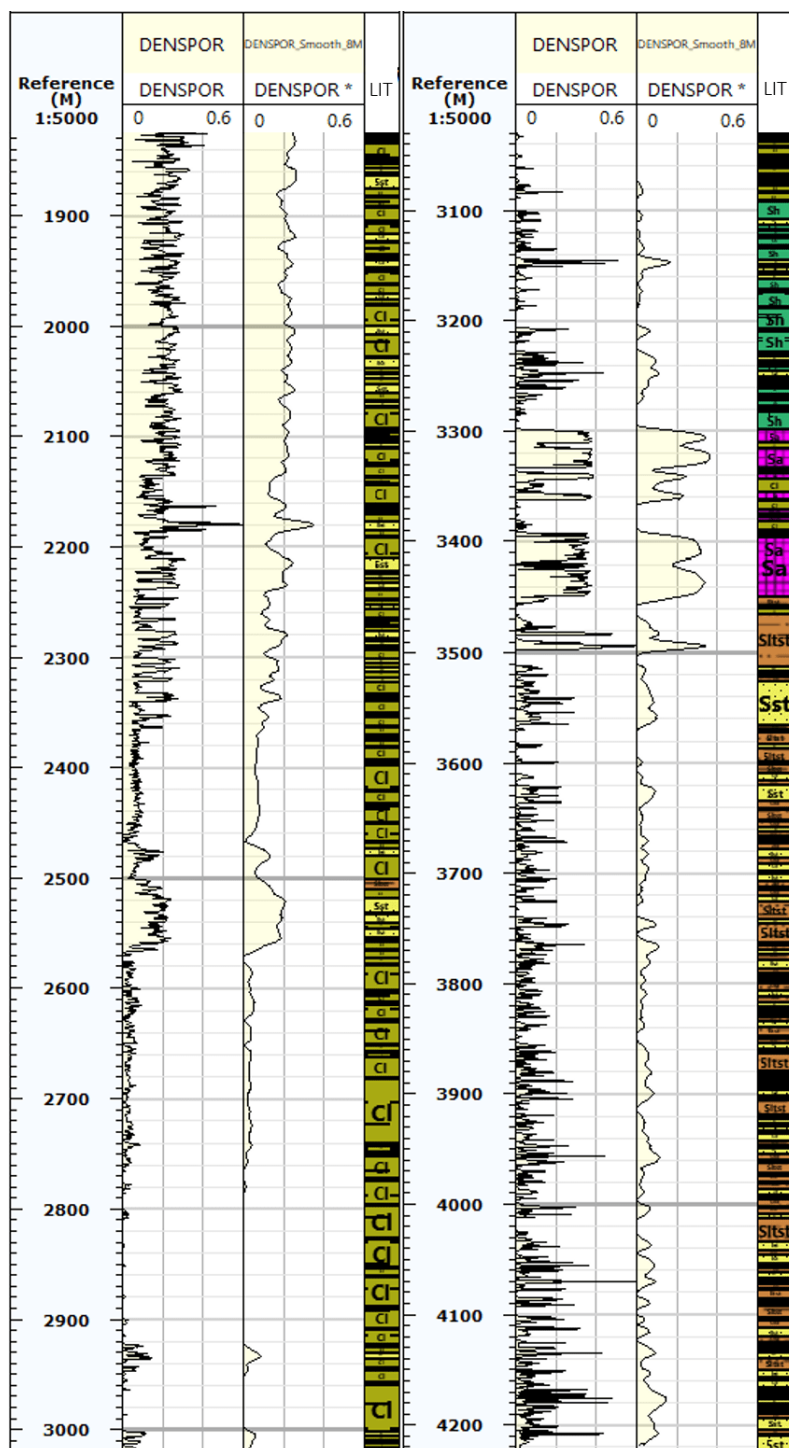


Figure 8.10: Density porosity curves for wellbore 6610/7-2.

## 8.2 Sedimentological logging

The six wells given in Table 7.4 make an important assemblage of Triassic strata from the Trøndelag Platform in the central Norwegian Sea (see Figures 3.2 and 3.3). The different cores were logged at the scale of 1:20, and can be found in Appendix A. It was decided to continue with four core sections, one core each from well 6507/12-1, 6507/12-2, 6610/7-2 and 6507/6-1. These cores were logged at a scale of 1:100, and are displayed in Figure 8.16. The core from well 6507/12-1 represents a shallow lacustrine basin to a playa lake depositional environment. The core is situated in Unit Tr5, which is supra-salt. The depositional environment for the core from well 6507/12-2 is somewhat similar to the core from well 6507/12-1, and represents non-channelized fluvial deposits to a playa lake type of depositional environment. The core from well 6507/12-2 is situated in Unit Tr3, which is sub-salt. These two wells are included among the four chosen wells as they contain important information on how the Triassic Salt in Unit Tr4 influence the surrounding rocks and their diagenetic evolution. Cores from well 6610/7-2 and 6507/6-1 are included among the chosen wells to reveal information on reservoir properties from Unit Tr3 in a marginal marine and fluvial to tide influenced mouthbars depositional setting. The spatial arrangement between the wells also plays an important role for the depositional variations. This will be further discussed in Chapter 9.

Figure 8.11 is the lithological and structural legend for the four sedimentary logs at a scale of 1:100. Figure 8.12 shows the log of core 4 from well 6507/12-1. These 11 m of core represent Unit Tr5 which is of Norian age. Dark red to brown matrix is the dominating facies. Siltstones with micro mud flasers, carbonate nodules, desiccation- and syneresis cracks occur. The sand bodies appear at a thickness of 1.7 m with a sand grain size of vFL to fU. Thin white limestone and marl layers occasionally occur in the upper half of the sedimentary log. In addition, other structures like rootlets and current ripples are represented in the logged section. Playa lake or shallow lacustrine basin and channelized fluvial deposits are suggested for the depositional environment of the core from well 6507/12-1.

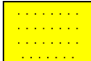

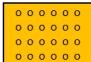


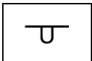

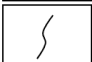

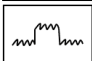




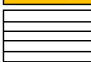


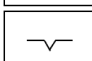



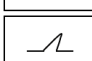
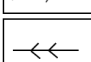


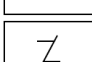

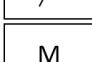

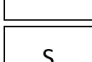

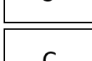
	Sandstone		Fossil fragment
	Conglomerate		Rootlets
	Limestone		Boring
	Siltstone		Bioturbation
	Claystone		Stylolite
	Dolomite		Light nodule
	Breccia		Dark nodule
	Horizontal lamination		Mud drape
	Wavy bedding		Mud/desiccation crack
	Current ripple		Synaeresis crack
	Climbing ripple		Flame structure
	Herringbone		Mud flasers
	Low angle x-bedding		Micro fracture
	High angle x-bedding		Mica
	Unconformity		Sample
	Not exposed		Coaly fragments

Figure 8.11: Lithological and structural legend for the sedimentary logs.

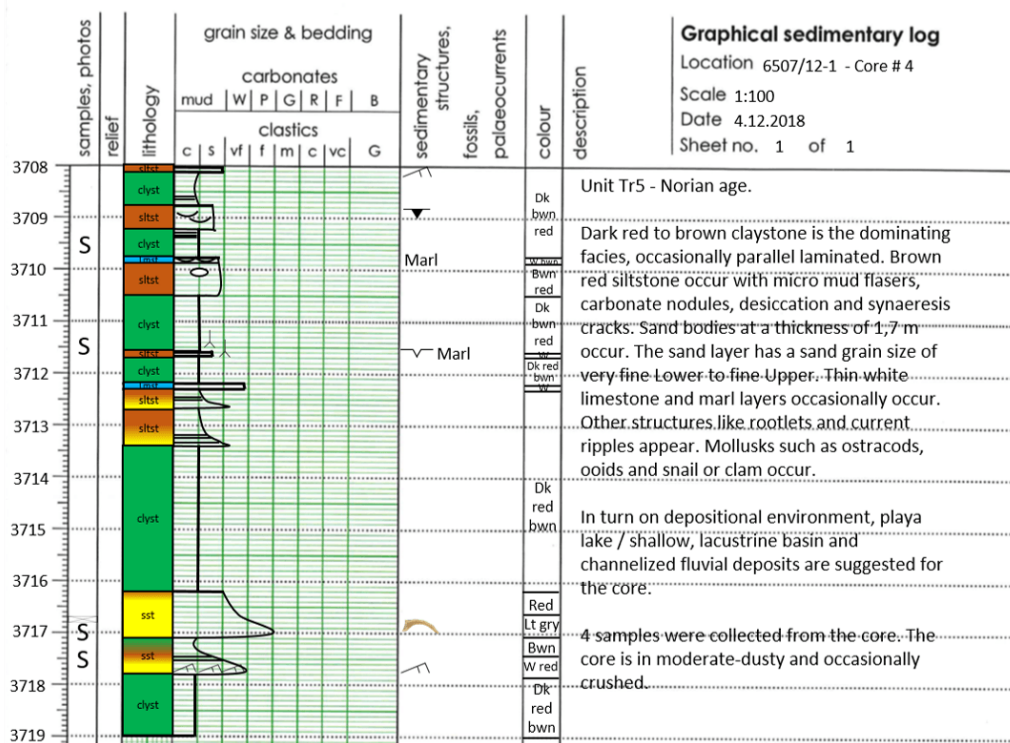
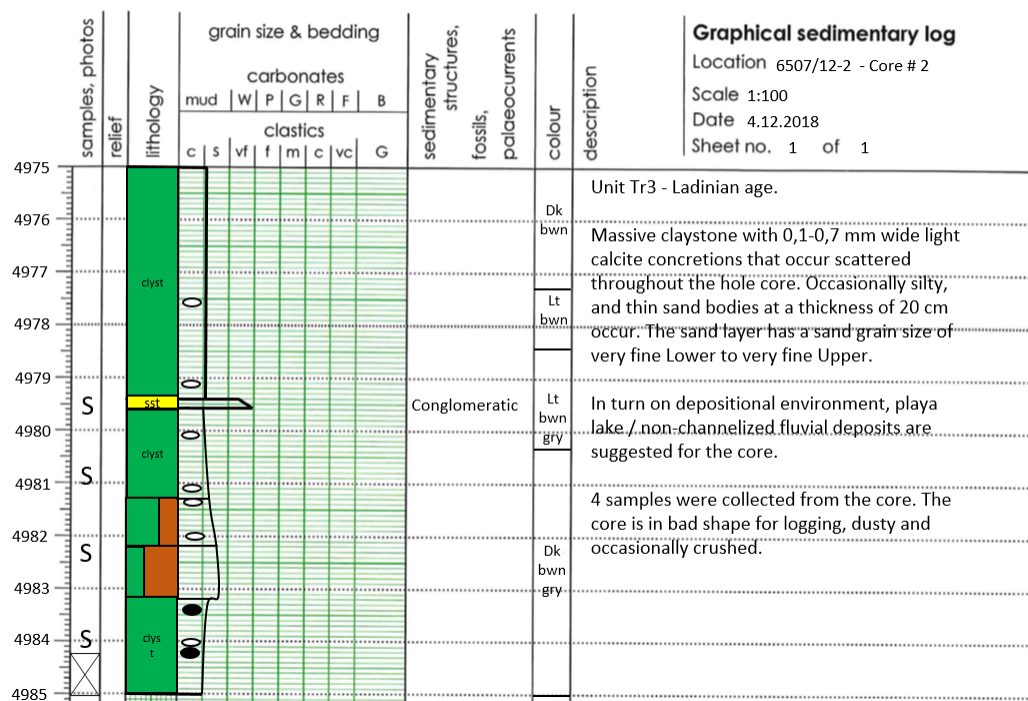


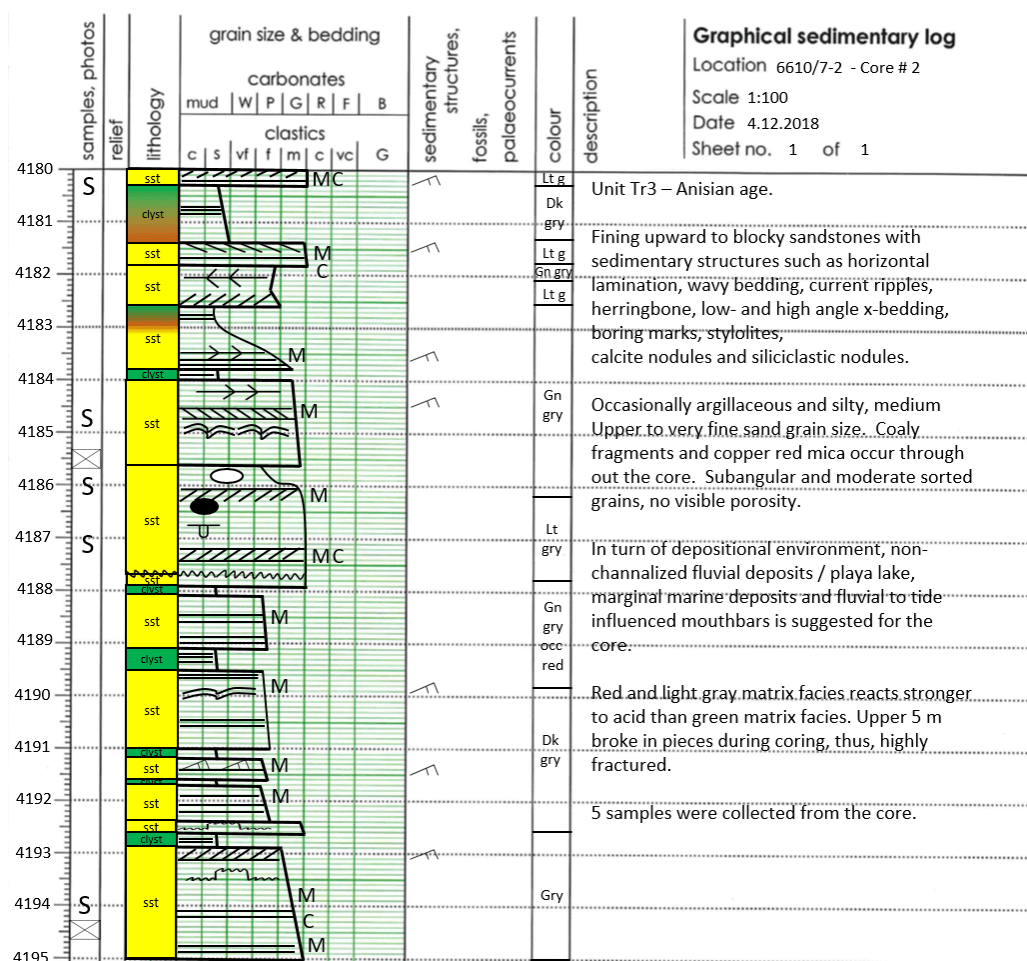
Figure 8.12: Sedimentary log of core 4 from well 6507/12-1 at a scale of 1:100, including core description.

Figure 8.13 is the log of core 2 from well 6507/12-2. These 9-10 m of core represent the Upper Unit Tr3 of Ladinian age. The core is logged as a massive claystone with 0.1-0.7 mm wide light calcite concretions that occur scattered throughout the whole section. Therefore, calcite nodule facies makes the dominating facies in this core. The logged section is occasionally silty and thin sandstone beds of vFL to vfU sand grain size at a thickness of 20 cm occur. The core is dusty and occasionally crushed. The depositional environment is suggested to be playa lake to non-channelized fluvial deposits.



**Figure 8.13:** Sedimentary log of core 2 from well 6507/12-2 at a scale of 1:100, including core description.

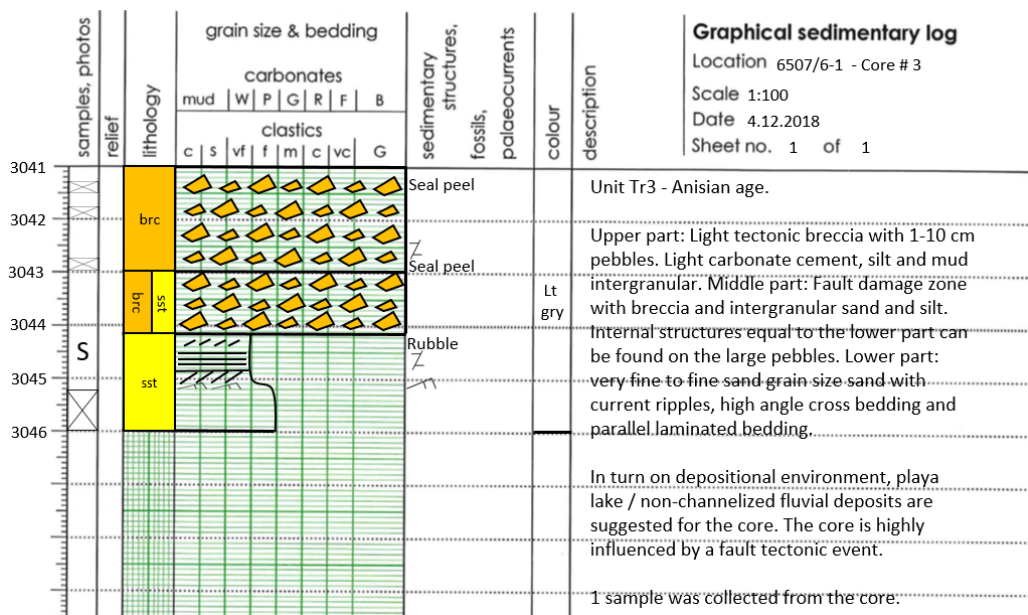
Figure 8.14 is the sedimentary log of core 2 from well 6610/7-2. The 15 m of core represents the Lower Unit Tr3 of Anisian age. The logged section is logged as sequences of blocky to fining upward sandstones with sedimentary structures such as horizontal lamination, wavy bedding, current ripples, herringbone, low- and high angle cross-bedding, boring marks, stylolites and calcite- and siliclastic nodules. The logged section is occasionally argillaceous and silty, and the sand grain size is vfU to mU. Coaly fragments and copper red mica occur throughout the whole core. The grains are subangular and moderately sorted and shows no visible porosity. There are three matrix facies in the core, where the pinkish-gray and the light gray matrix facies react stronger in contact with acid than the green matrix facies. The well report informs that the upper five meters broke in pieces during coring. This is also confirmed upon visual inspection, as the core is highly fractured in the upper part. In terms of depositional environment, marginal marine deposits and fluvial to tide influenced mouthbars are the suggested ones.



**Figure 8.14:** Sedimentary log of core 2 from well 6610/7-2 at a scale of 1:100, including core description.

Figure 8.15 is the sedimentary log of core 3 from well 6507/6-1 and represents Unit Tr3 of Anisian age. The upper part is a light tectonic breccia with 1-10 cm pebbles. Light carbonate cement, silt and mud make the intergranular fill. The middle part of the core indicates a fault damage zone with both breccia and intergranular sand and silt. Internal structures like current ripples, laminated bedding and cross-bedding can be found in the pebbles. The lower part represents a vfL to fU sand grain size sandstone with current ripples, high angle cross-bedding and parallel laminated bedding. Core 4 from the same well, at depths of around 4000 m is interpreted to result from a marine turbidite depositional environment with

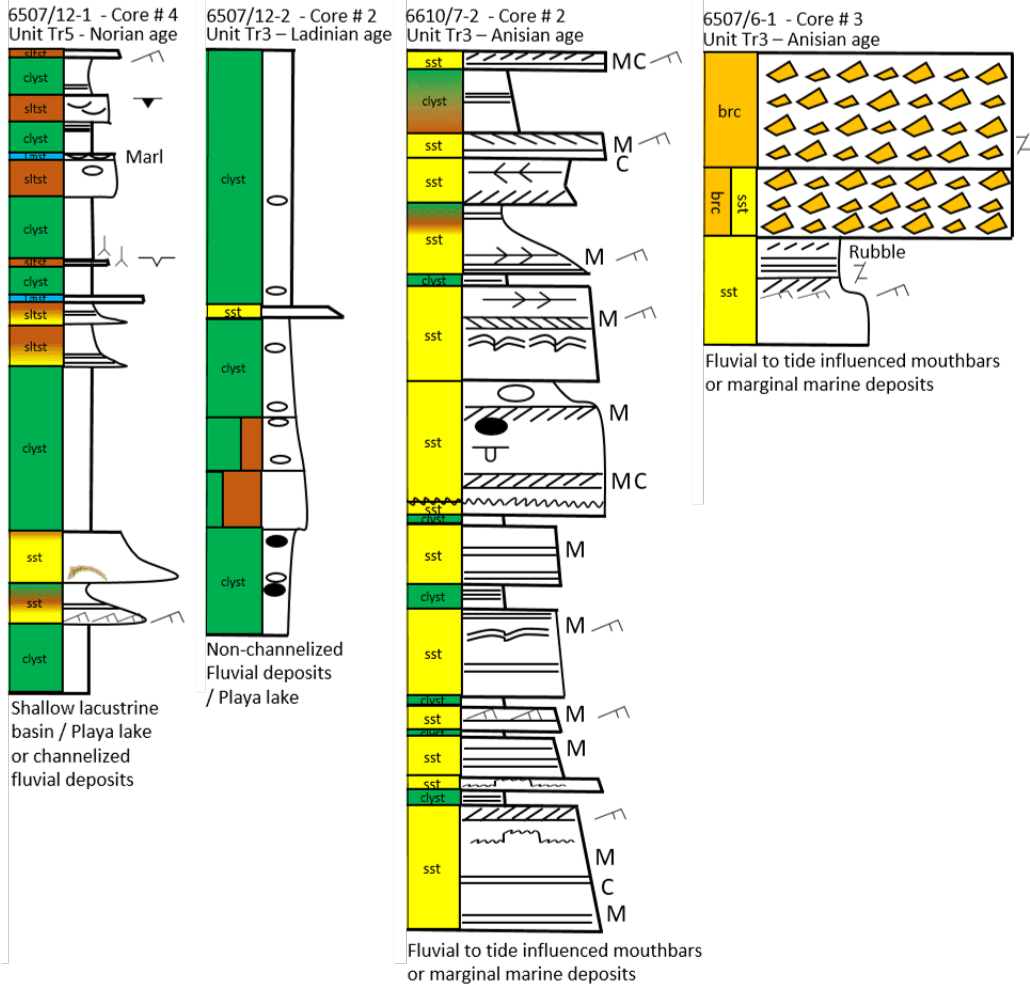
upwards fining Bouma-sequences. Entering core 3 of well 6507/6-1 at depths from 3041 to 3046 m, the depositional environment has changed to marginal marine deposits or fluvial to tide influenced mouthbars. Furthermore, the core is highly influenced by a fault tectonic event.



**Figure 8.15:** Sedimentary log of core 3 from well 6507/6-1 at a scale of 1:100, including core description.

The four sedimentary core logs given above, are displayed in Figure 8.16 in an overview focusing on the key information. It gives an impression of the relative differences from one core to the others, both in terms of depositional environment, grain size, structures, lithology and dimensions.





**Figure 8.16:** Sedimentary log overview that compare the four chosen wells at a scale of 1:100.

### 8.3 Facies and facies association

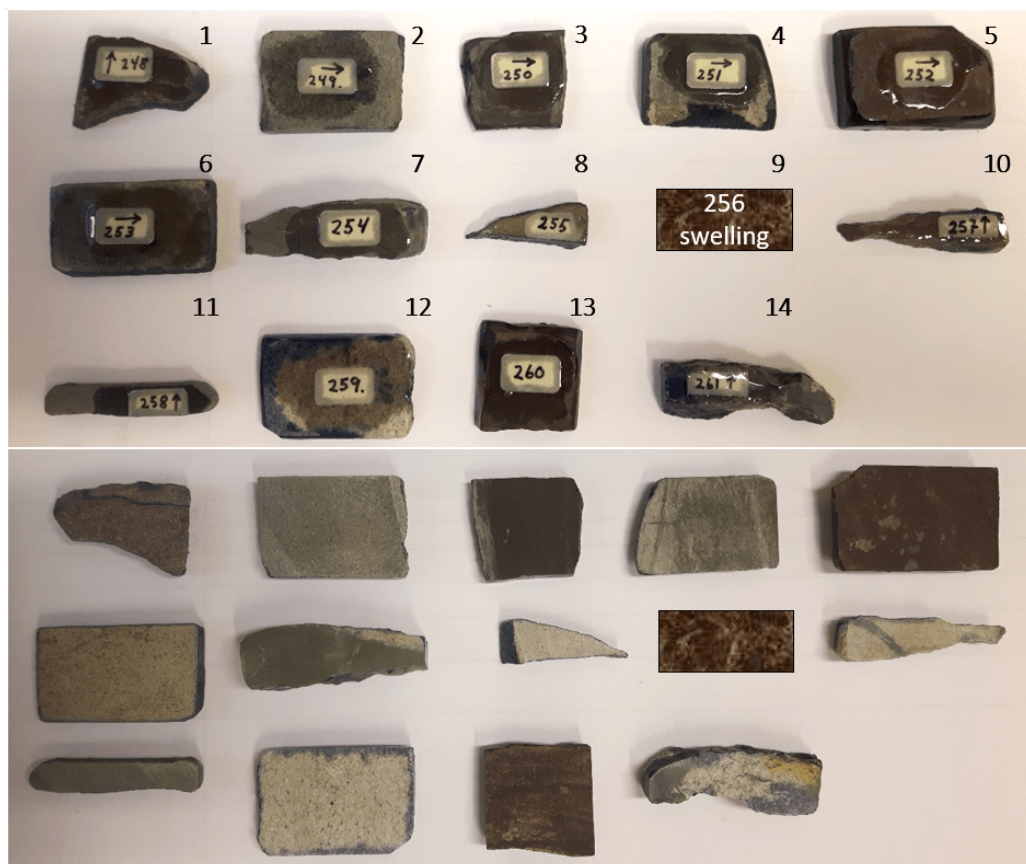
With 6507/12-2 and 6507/12-1 situated on the Ellingråsa Graben, 6608/11-1, 6608/8-1 and 6507/6-1 on structural highs, and 6610/7-2 on the Trøndelag Platform, they are all sedimentary Mesozoic deposits mainly consisting of sandstones, claystones, siltstones, limestones, evaporites and occasionally marl and tectonic

breccia. Twelve different facies and four different facies associations have been identified from the logged section. These are described in Section 8.3.1 and 8.3.2.

### 8.3.1 Facies description

**Table 8.1:** Sedimentological facies found in cores from the six logged wells.

Number	Facies	Physical appearance
F1	Light gray matrix	Calcite cemented matrix, from fine to medium sand grain size.
F2	Red to brown matrix	Partly oxidised, calcite cemented. Occasionally mica. Both clay, silt and up to fine sand grain size.
F3	Pinkish-gray matrix	K-feldspar rich matrix, calcite cemented. Often fine to medium sand grain size.
F4	Green matrix	Partly reduced, less calcite cemented. Chlorite in the pore structure. Clay to medium sand grain size.
F5	Stylolite facies	Appears in light gray facies rich in calcite. Black planar stylolite rims.
F6	Breccia	Intergranular calcite cement, mud, silt and sand. Pebble sized clasts are dominating.
F7	Wavy lamination	Grades into parallel and cross-bedded facies. Occurs mostly in siltstones.
F8	Carbonate nodules	0.1-0.5 mm white calcite nodules. Occur in clay to sandstones. Larger nodules and thin calcite beds also appear.
F9	Swelling facies	Massive fine grained greenish gray color, swells in contact with water. Clay size.
F10	Parallel planar laminated	Thin horizontal lamination, often silty, but occurs in clay to medium sand grain size. Low energy system.
F11	Cross-bedded	Low to high angle, indicative of a system of higher energy. Silt to medium sand grain size.
F12	Structureless	No sedimentary structures are visible. Massive, hard, occasionally argillaceous and calcite cemented. Clay to medium sand grain size.



**Figure 8.17:** The thin section sample cuts give an indication of which facies number (F1-F12) that belongs to the given sample number (1-14). The lower pictures shows the thin section sample cuts from the back side. Numbering of samples at the lower picture follows the method used in the upper picture. Sample 9 is a swelling clay type, and did not make it to the wall of fame.

### F1. Light gray matrix facies

The light gray matrix facies that can be seen in Figure 8.18 (1), is one of the dominating facies in core number 2 from well 6610/7-2 and core number 3 of well 6507/6-1. The facies is prominent in core sample 8, 12 and 14 (see Figure 8.17). It can vary from whitish gray to gray dependent on the amount of carbonate minerals, which are prone to white color. The facies tends to occur in sandstones from fine to medium sand grain size. Both cross beds, current ripples, stylolites,

breccia and planar lamination can be observed in this facies.

## **F2. Red to brown matrix facies**

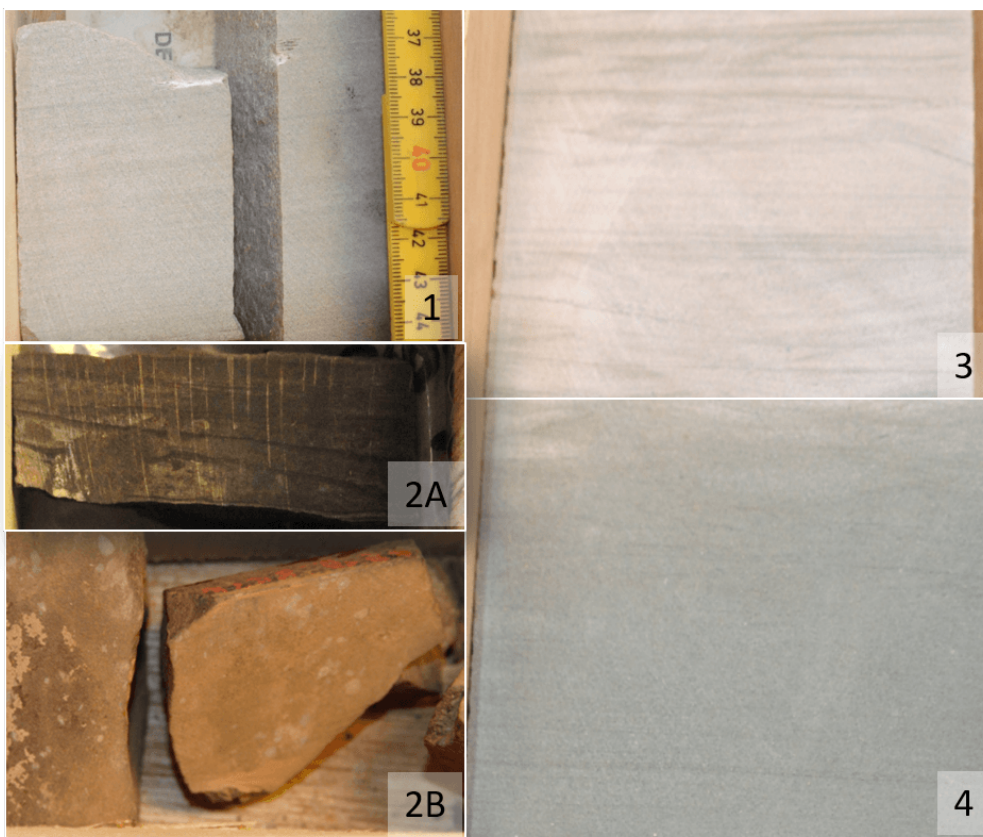
The red to brown matrix facies tend to be dark in color for claystones and siltstones. Lighter versions appear in larger grain size sandstones. The facies appears oxidized or with mica and micro-mica, and is calcite cemented as it reacts to acid. This facies can be observed in Figure 8.18 (2A and 2B) and is the prominent facies in core 4 from well 6507/12-1 and core 2, well 6507/12-2.

## **F3. Pinkish-gray matrix facies**

Pinkish-gray matrix facies is mostly applicable for fine to medium sized sandstones with high levels of K-feldspar and can be observed in the upper part of core number 2 of well 6610/7-2. The facies is calcite cemented and is related to the light gray matrix facies. This can be seen in Figure 8.18 (3).

## **F4. Green matrix facies**

The green matrix facies in Figure 8.18 (4) is both applicable for sandstones and mudstones. The facies represents a reduced environment or a less arid climate, with chlorite in the pores and reduced calcite cementation. This facies can be observed in the middle and upper part of core 2 from well 6610/7-2, but also in the lower part of core 1, well 6608/11-1.



**Figure 8.18:** Facies number 1 (sample 10, see Table 8.1 and 8.3) is the light gray matrix facies, F2 (A and B - sample 13 and 5) is the red to brown matrix facies, F3 is the pinkish-gray matrix facies, F4 (sample 11) is the green matrix facies.

### F5. Stylolite facies

The stylolite facies observed in Figure 8.19 (5) from core 2 of well 6610/7-2 appears as a light gray facies rich in calcite. The facies contains black horizontally planar rims of stylolite. The stylolite facies is also observed in the thin section of sample 14.

## **F6. Breccia facies**

The breccia facies is composed of pebble sized angular clasts, and is shown in Figure 8.19 (6). The color is commonly green and the pebbles often contain internal structures. Gray sand, silt and mud make the intergranular mass of the breccia. The breccia is most likely tectonic in origin and can be related to faulting. This facies can be observed in the upper part of core number 3 in well 6507/6-1 and in the lower part of core 2 in well 6608/8-1.

## **F7. Wavy laminated facies**

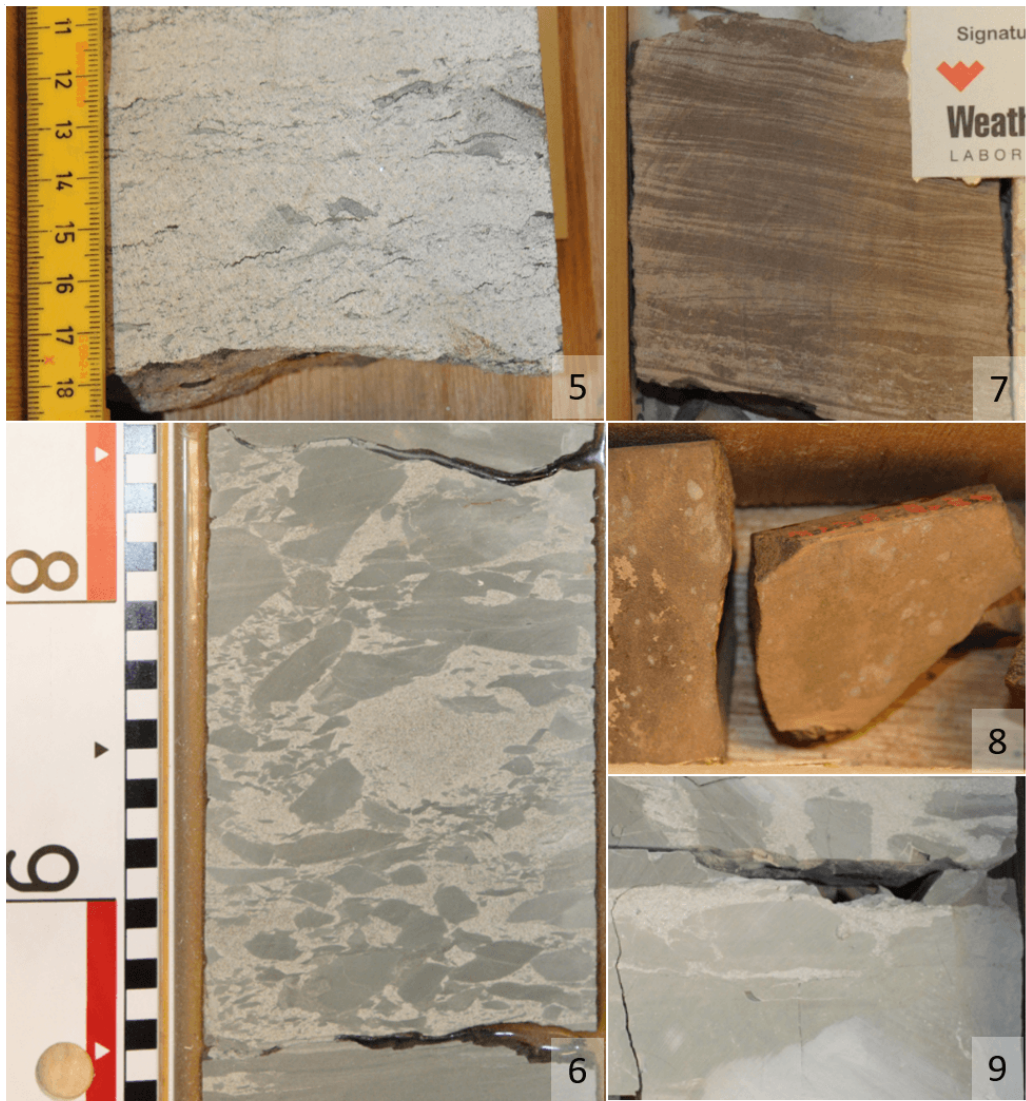
As seen from Figure 8.19 (7), the wavy laminated facies appears in siltstones and can be observed in core 4 from well 6507/12-1. The structure tend to grade into horizontal lamination and current ripples. The facies can also be interpreted as lenticular bedding, which is the alternation of very fine sand and clay.

## **F8. Calcite nodule facies**

The calcite nodule facies appears both in fine and coarser layers. In claystones, the typical nodule size is 0.1-0.5 mm, while in sandstones they typically appear as larger pebble size nodules or up to 10 cm thick layers of carbonate. The nodules are white in color and can be observed in Figure 8.19 (8). They are spatially distributed throughout the core of well 6507/12-1, but more prominent in the core of well 6507/12-2.

## **F9. Swelling facies**

The swelling facies can be observed in core 1 of well 6608/11-1 and in Figure 8.19 (9) as a green clay type. The facies swells in contact with water and may contain smectite, which is a swelling clay type.



**Figure 8.19:** Facies number 5 (sample 14) is the stylolite facies, F6 is the breccia facies, F7 is the wavy laminated facies, F8 (sample 5) is the calcite nodule facies and F9 (sample 9) is the swelling facies.

### **F10. Parallel planar laminated facies**

The parallel horizontal laminated facies occurs both in claystones as very thin laminae, but also in siltstones and sandstones. Often, larger grain size of the hosting rock implies higher frequency of laminated beds. This can be observed in well 6507/12-1 and 6507/6-1 among others, but are highlighted in Figure 8.20 (10A and 10B) from well 6610/7-2. This facies originate from an environment of low energy.

### **F11. Cross-bedded facies**

The cross-bedded facies tend to occur in sandstones of fine to medium sand grain size. The environment of this facies is indicated by high energy, and can be observed in well 6610/7-2 and 6507/6-1, and in Figure 8.20 (11A and 11B) from well 6608/8-1. 11A also contains micro-mica and some minor fractures that may be related to drilling of the horizontal side wall cores.

### **F12. Structureless facies**

In the structureless facies, no sedimentary structures are present. The facies is calcite cemented, massive, hard, occasionally argillaceous and blocky for sandstones. The facies also occurs in claystones.

### **Additional facies**

Each of the observed lithologies have not been interpreted as a facies on their own, as many of the facies occur for several lithologies and because the present lithologies are all sedimentary rocks. In addition several structures observed were not grouped into individual facies. Some of these were syneresis cracks observed in claystones, boring marks, micro fractures, coaly fragments, mud flasers and rootlets.





**Figure 8.20:** 10A is a proposed interpretation of 10B (sample 11) and illustrate both the planar laminated and the cross-bedded facies. 11A and 11B show the cross-bedded facies. 11A is an interpretation of 11B (sample 6).

### 8.3.2 Facies association

The twelve described facies are grouped into four different facies associations (FA1-FA4) in order to place them into a specific depositional environment based on their facies characteristics. This section will describe each of FA1-FA4, while Table 8.2 and Table 8.3 give a short overview of the findings.

**Table 8.2:** FA1-FA4 with their characteristics and depositional environment. Mudstone is a common term for claystone and siltstone combinations. The table is based on core findings and work by R. Müller et al., 2005 [3]. Mdst=mudstone.

FA	Facies characteristics	Depositional environment
FA1	1-5 m blocky sst beds interbedded with pale brown mudstones from stacked channel units. Mdst; extensive bioturbation, scattered root horizons, desiccation cracks and carbonate nodules.	Non-channelized fluvial deposits /playa lake
FA2	Fining upward units and upper laminated greenish gray mudstones. slumping, flame and water-escape structures.	Submarine fan deposits /turbidites
FA3	Thick greenish-gray interbedded with brown-red mudstones. Occurrence of mud cracks, root structures and small carbonate nodules. Interbedded isolated, blocky sst units of 2-5 m and thin carbonate beds.	Shallow, lacustrine basin /playa lake
FA4	Up to 10 m thick sst intervals with cross-bedding and parallel lamination. Occasionally convolute lamination, climbing ripples, and flame structures. Interbedded fine laminated mudstones.	Marginal marine deposits /fluvial to tide influenced mouthbars

#### FA1

FA1 is composed of 1-5 m blocky to fining upward sandstone beds, interbedded with brown mudstones from stacked channel units. Extensive bioturbation, scattered root horizons, desiccation cracks and carbonate nodules can be observed

in the claystones. The desiccation cracks tend to be filled with white carbonate deposits. FA1 is composed of F1, F2, F8, F10, F11 and F12. Hence, a light gray matrix is characteristic for the sand intervals, and red to brown matrix facies is characteristic for the finer materials. The sandstones tend to be both parallel planar laminated, cross-bedded and structureless. FA1 is found in well 6507/12-2 and the uppermost part in core 2 of well 6610/7-2 and is described as non-channelized fluvial deposits to a playa lake depositional environment. This is a type of environment with arid climate, both warm and dry. An analogue of this depositional environment from modern time can be found on the west coast of Mexico and on the west coast of Australia. This comparison will be described in more detail in Chapter 9.

### FA2

FA2 consists of upward fining sequences of sandstones, siltstones and claystones which make turbidite sequences. The turbidite sandstones are light gray in color, while the fine clay materials on top of a sequence are greenish gray and laminated. One can clearly see the full Bouma-sequence or parts of it throughout core 4 in well 6507/6-1. In cases where only parts of the Bouma-sequence is present, erosion from one turbidite deposit to another may be implied. The sandy parts are gradually shifting between massive structureless areas, to current ripples, wavy lamination and planar lamination. FA2 indicates a deep marine depositional environment with claystones and sandstones as the dominating lithologies. F1, F4, F7, F10, F11 and F12 can be observed in FA2, see Table 8.1 for the physical appearance of F1-F12.

### FA3

FA3 is composed of thick packages of greenish gray or red-brown claystones and siltstones. Occurrence of mud cracks, root structures, carbonate nodules and planar bedding is normal. Isolated, interbedded and blocky sandstone units of 1 to 5 m in thickness tend to take place, in addition to thin carbonate beds. This is the prominent facies association for well 6507/12-1 and 6608/11-1 and is interpreted to be a shallow lacustrine basin to a playa lake type of depositional environment. FA3 is therefore highly related to FA1. F2, F4, F7, F8, F9, F10 and F12 can be observed in FA3.

## FA4

FA4 comprises of up to 10 m thick sandstone intervals with cross-bedding and parallel lamination. Occasional convolute lamination, climbing ripples and flame structures occur. Interbedded fine laminated mudstones between the sandstone layers are typical. FA4 makes the marginal marine deposits or fluvial to tide influenced mouthbars type of depositional environment. The facies association is observed in well 6610/7-2, core 3 of well 6507/6-1 and in well 6608/8-1. Both F1, F3, F4, F5, F6, F7, F10, F11 and F12 can be observed in FA4.

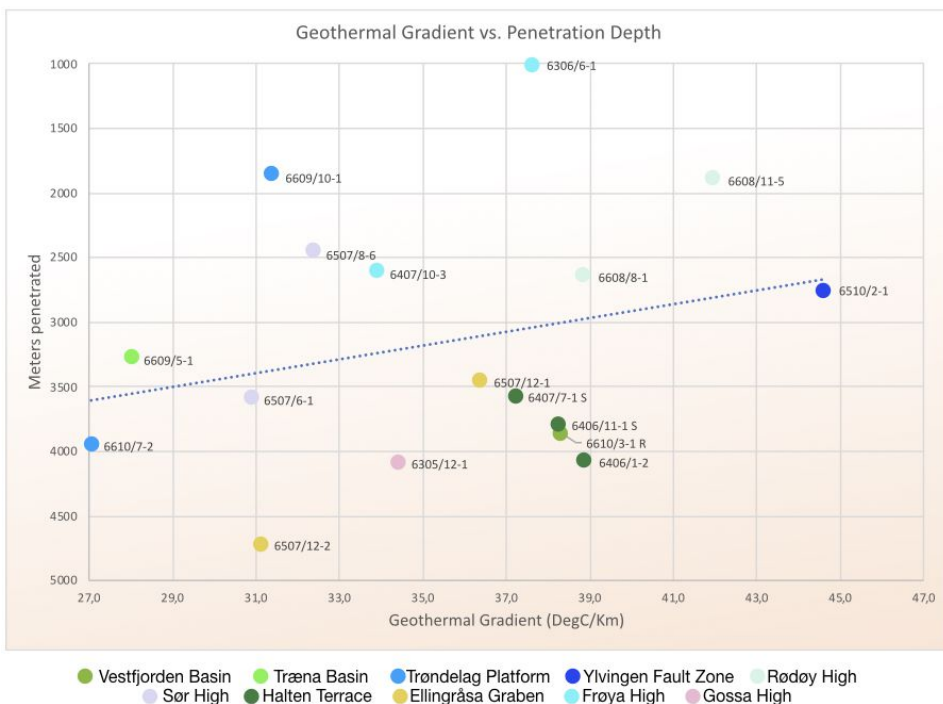
**Table 8.3:** 14 samples from six different wellbores in the Norwegian Sea collected from Weatherford's core storage in Stavanger. S is short for sample, while sltst is short for siltstone.

S	Well	MD [m]	Lith.	Ch.strat.	Unit	FA	Cores
1	6507/6-1	3044.45	Sst	Anisian	Unit Tr3	FA4	3041-3045
2	6507/6-1	4011.75	Sst	Induan	Unit Tr1	FA2	3995-4013
3	6507/12-1	3711.50	Sltst	Norian	Unit Tr5	FA3	3708-3720
4	6507/12-1	3717.00	Sst	Norian	Unit Tr5	FA3	3708-3720
5	6507/12-2	4982.30	Sltst	Ladinian	Unit Tr3	FA1	4975-4985
6	6608/8-1	1839.05	Sst	Induan	Unit Tr1	FA4	1833-1842
7	6608/8-1	1839.47	Clst	Induan	Unit Tr1	FA4	1833-1842
8	6608/11-1	1376.60	Lmst	Early Rhaetian	Unit Tr5	FA3	1372-1398
9	6608/11-1	1376.00	Clst	Early Rhaetian	Unit Tr5	FA3	1372-1398
10	6610/7-2	4180.40	Sst	Anisian	Unit Tr3	FA1	4180-4195
11	6610/7-2	4184.65	Sst	Anisian	Unit Tr3	FA4	4180-4195
12	6610/7-2	4194.05	Sst	Anisian	Unit Tr3	FA4	4180-4195
13	6507/12-2	4983.90	Sltst	Ladinian	Unit Tr3	FA1	4975-4985
14	6610/7-2	4187.15	Sst	Anisian	Unit Tr3	FA4	4180-4195

## 8.4 Geothermal gradient

Figure 8.21 shows the geothermal gradient plotted against the penetration depth of the respective wells from the field area. The blue line indicates a trend of higher geothermal gradient with reduced penetration depth. This is explained by a progressive reduction of radioactive minerals with burial causing a higher heat production relative to penetration depth for shallow depth readings. The highest geothermal gradient is observed on the Ylvingen Fault Zone and is of about 44.8°C/km, ending up near the regression line. The wells on the Halten Terrace shows a reverse trend compared to the other wells, with increased geothermal

gradient with increased penetration depth. It should be noticed that the wells 6610/7-2, 6507/6-1, 6507/12-1 plot closely below the regression line and that 6507/12-2 has the lowest geothermal gradient given its penetration depth.



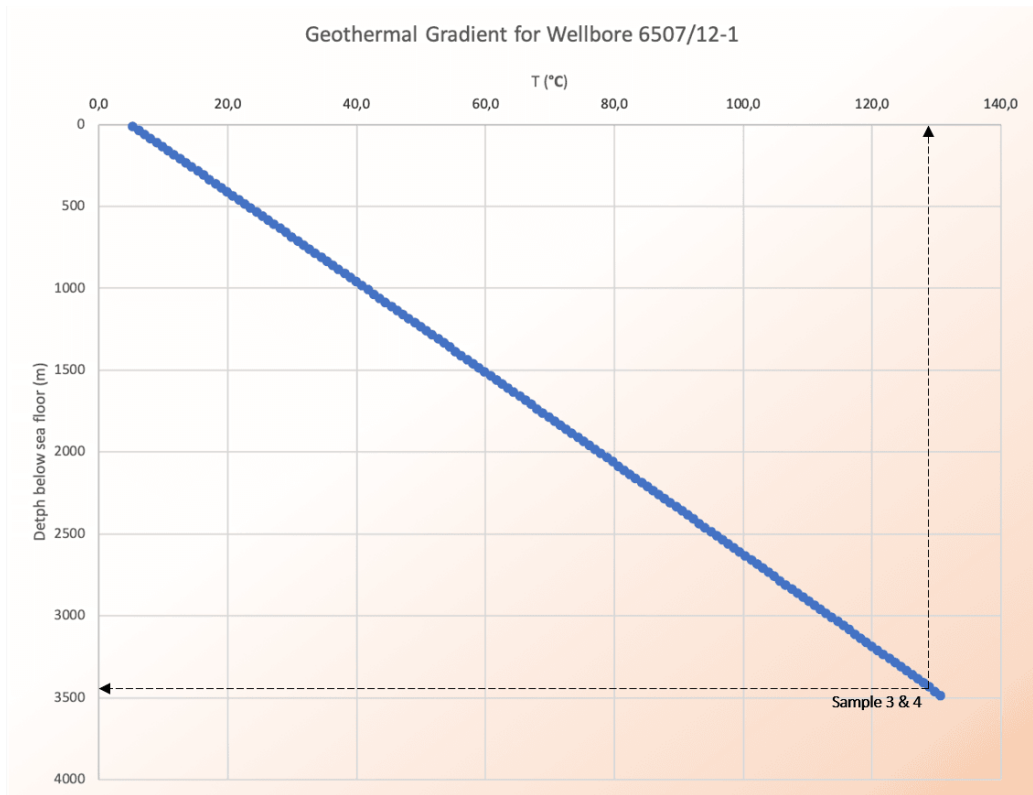
**Figure 8.21:** A plot showing geothermal gradients and penetration depth for the individual wells.

Figure 8.22 shows the geothermal gradient for wellbore 6507/12-2 based on Equation 7.1. It assumes a sea floor temperature of 5°C and a TD temperature of 152°C stated from the well report at the NPD fact page [16]. The plot is used for estimating the temperature for the collected samples. By plotting the depth of samples 5 and 13, the resulting temperature is found to be ~151°C.



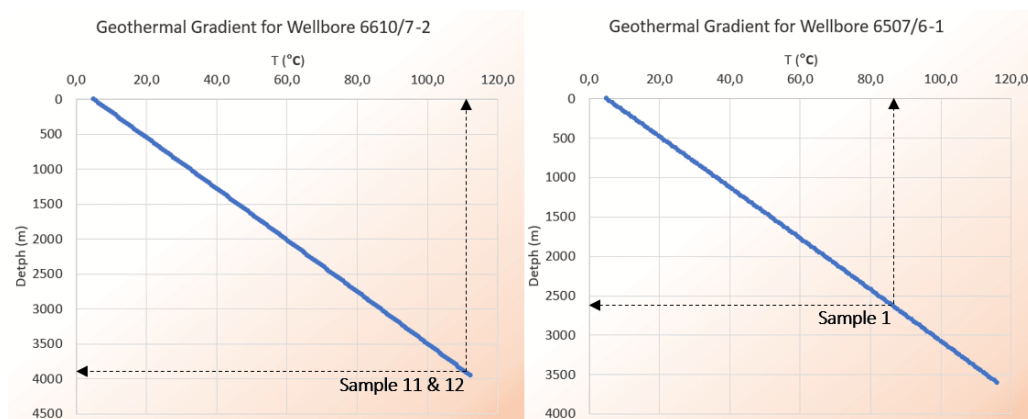
**Figure 8.22:** Geothermal gradient for well 6507/12-2. The depth from RKB to the sea floor is 286 m, and has to be added to the depth to get the MD.

Figure 8.23 assumes a sea floor temperature of  $5^{\circ}$  and a TD temperature of  $131^{\circ}\text{C}$  for wellbore 6507/12-1, as stated in the well report at the NPD fact page [18]. The resulting temperature for samples 3 and 4 is therefore  $\sim 128^{\circ}\text{C}$ .



**Figure 8.23:** Geothermal gradient for well 6507/12-1. The depth from RKB to the sea floor is 250 m, and has to be added to the depth to get the MD.

Figure 8.24 shows the geothermal gradient for wells 6610/7-2 and 6507/6-1. At TD the temperatures are  $112^{\circ}\text{C}$  and  $116^{\circ}\text{C}$ , respectively [17, 19]. The temperature of samples 11 and 12 is  $\sim 111^{\circ}\text{C}$ , while the temperature of sample 1 is  $\sim 88^{\circ}\text{C}$ .



**Figure 8.24:** Geothermal gradient for well 6610/7-2 and well 6507/6-1.

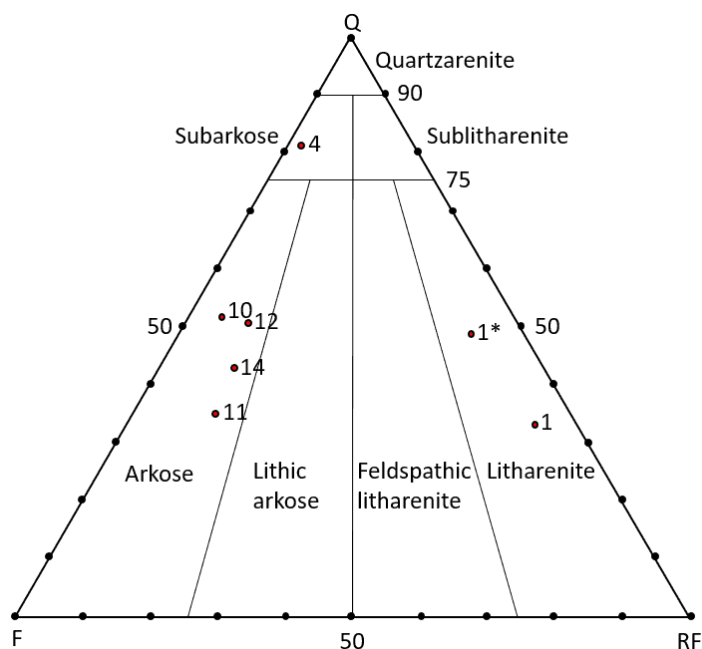
## 8.5 Mineralogical and petrographical description

Section 8.5 is divided into three main parts. The first part shows the thin section and point counting results, the second and third part, Section 8.5.2 and 8.5.3, present the SEM and XRD results.

### 8.5.1 Thin section and point counting results

The QFL sandstone classification diagram in Figure 8.25 uses Table D.1 from Appendix D to plot the samples according to their point counting results. Sample 1 ends up under the litharenite category. Reworked biotite could be grouped as a diagenetic product. Sample 1\* is a version of sample 1 that excludes the reworked biotite minerals as a contributor to the total counts of rock fragments. Sample 1\* still plots as a litharenite. Sample 4 plots as a subarkose and can be regarded as the most mature sandstone. Sample 10, 11, 12 and 14 plot very close to each other in the realm of arkose. This is because they all originate from the same wellbore (6610/7-2). Sample 1 originates from wellbore 6507/6-1 and sample 4 from 6507/12-1. Tables which are based on the point counting results, showing the mineral assemblage and IGV, can be found in Appendix D.



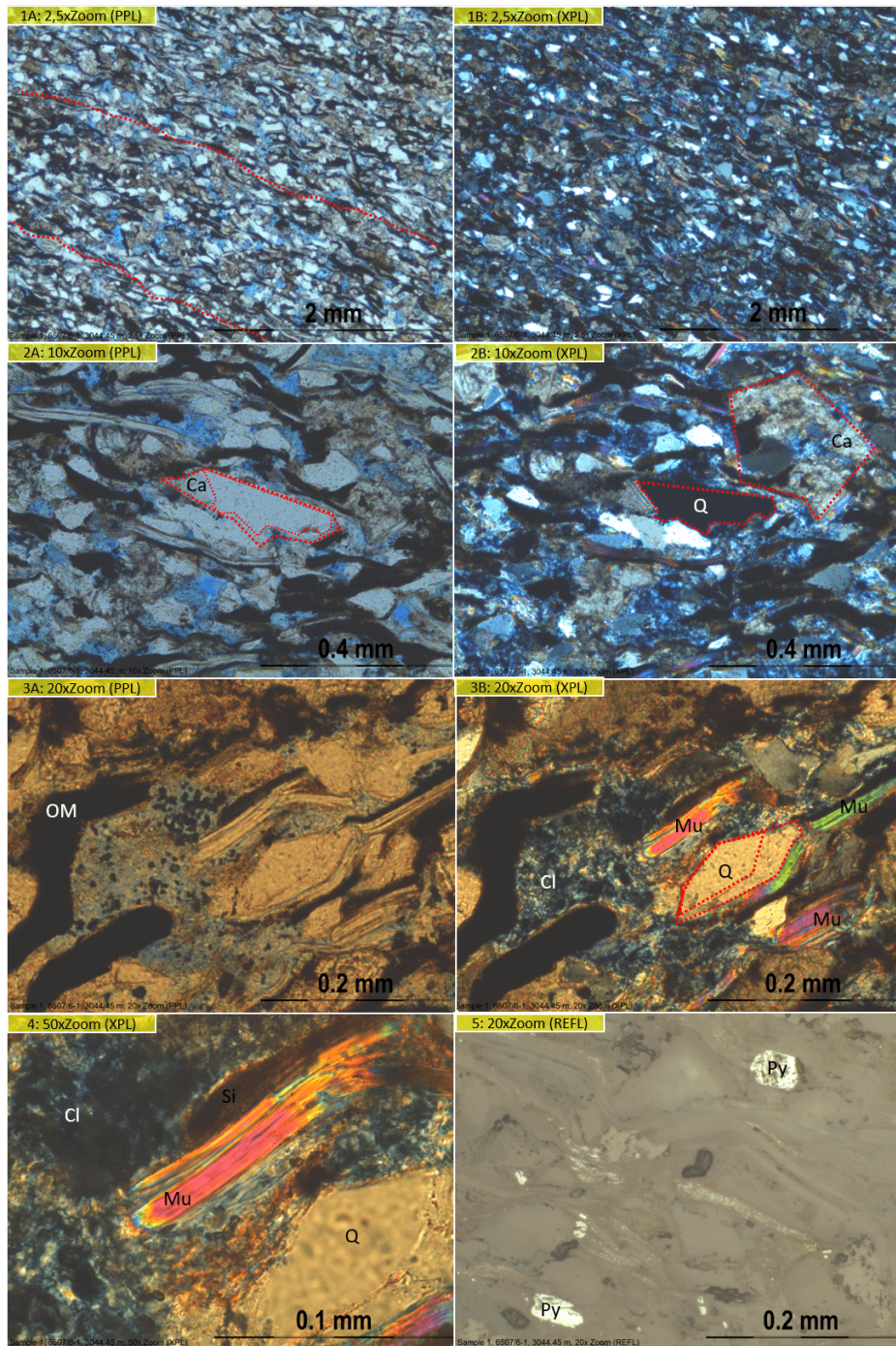


**Figure 8.25:** Sample plot in the QFL sandstone classification diagram.

### Sample 1, 6507/6-1, 3044.45 m MD

The majority of the grains are 0.08 mm in diameter, which is a grain size defined as vfl sand. Using the information from the QFL plot in Figure 8.25, sample 1 can be classified as a litharenite. The sample is subangular and moderately to poorly sorted. Figure 8.26 (1A and 1B) shows an overview of sample 1 in PPL and XPL at an objective magnification of 2.5x. With an eyepiece magnification of 10x, the total magnification is 25x. A list of mineral acronyms can be found in Figure 8.30. The sample has a lineation indicated by the red lines. This lineation indicates the bedding and is best illustrated by the quartz and mica minerals. The elongated minerals tend to be oriented perpendicularly to the maximum stress,  $\sigma_1$ . The mica mineral muscovite is present with second order interference colors. Muscovite is more resistant to weathering compared to biotite. 3A, 3B and 4 presents deformed muscovite grains that bends around quartz grains. The lineation and deformed muscovite grains suggest that the rock has suffered a great amount of deformation. The sandstone has a schist-like structure, which is typical for low-grade metamorphic rocks.

Even though sample 1 contains 21% calcite cement, the rock contains 12% porosity illustrated by the blue epoxy in 1A and 2A. The quartz grains and mica flakes are surrounded by numerous small crystals with low relief of first order gray interference colors, illustrated in picture 3B and 4. These are probably the clay mineral kaolinite. According to Adams et al., an electron microscope is needed to demonstrate the shape of the clay minerals, and X-ray diffraction to identify the minerals [49]. 2A and 2B show a subhedral quartz grain of first order interference colors with overgrowth of authigenic calcite of high interference colors observed in XPL. Grain coating calcite reduces porosity of the rock. The calcite cemented area in the upper right corner shows some intragranular porosity. This porosity can occur as a consequence of calcite dissolution. The quartz grain in 3A and 3B shows the overgrowth of authigenic quartz cement. The quartz cement has deformed the underlying muscovite flake and contributes to the reduction of total porosity.



**Figure 8.26:** Sample 1, 6507/6-1, 3044.45 m. Objective magnification marked in yellow. Multiplying by the eyepiece magnification of 10 gives the correct zoom.

The black parts on the left hand side of picture 3A and 3B are interpreted as organic material and the brown parts in picture 4 (at a total magnification of 500x) are interpreted as sideritized biotite. The brown color is typical for oxidized iron. For this sample, the feldspars are not present, which is probably due to dissolution and kaolinization of the feldspar. Picture 5 shows white sulfide grains in reflected light. These are isotropic, thus they are dark in transmitted light and are interpreted to be cubic pyrite minerals.

### **Sample 3, 6507/12-1, 3711.5 m MD**

Sample 3 is a fine grained rock with alternating beds of clay and silt sized grains. The dominating grain diameter is about 5 micrometers which makes it a siltstone, but larger sparitic grains occur. The grains are well sorted and has a subangular grain shape. Picture 1A (PPL) and 1B (XPL) of Figure 8.27 are 25 times enlargements of the thin section. They show planar lamination of dark clay, argillaceous silt and bright micrite (see the red lines of 1B in Figure 8.27). The lamination is cross-cut by a boring mark, syneresis- or desiccation crack of sparitic fill. An arrow showing the orientation of the thin section can be found in the upper right corner. 1A is likely a boring mark as the orientation of a desiccation crack would be upside-down. 2A and 2B present a bed of sparitic material connected to a syneresis crack or a root structure. The bright second- and third-ordered interference colored grains in 3A, 3B and 4A, 4B are interpreted as anhydrite. The micritic grain marked with the red dashed line in 3B also contains scattered anhydrite grains. The grains have a moderate relief in PPL and shows two cleavages perpendicular to each other. Desiccation crack structures and evaporitic gypsum minerals typically form in an arid climate zone.

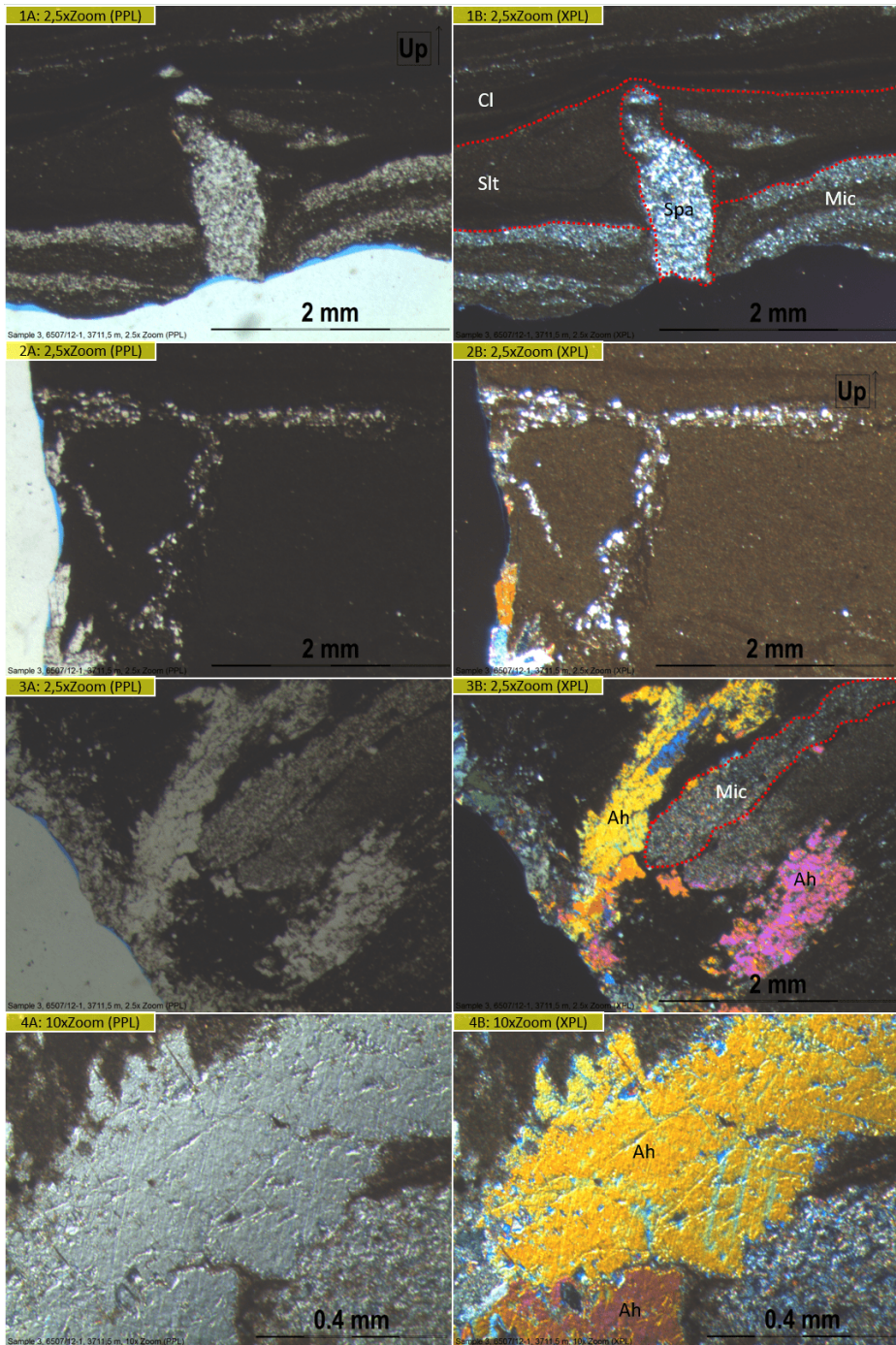


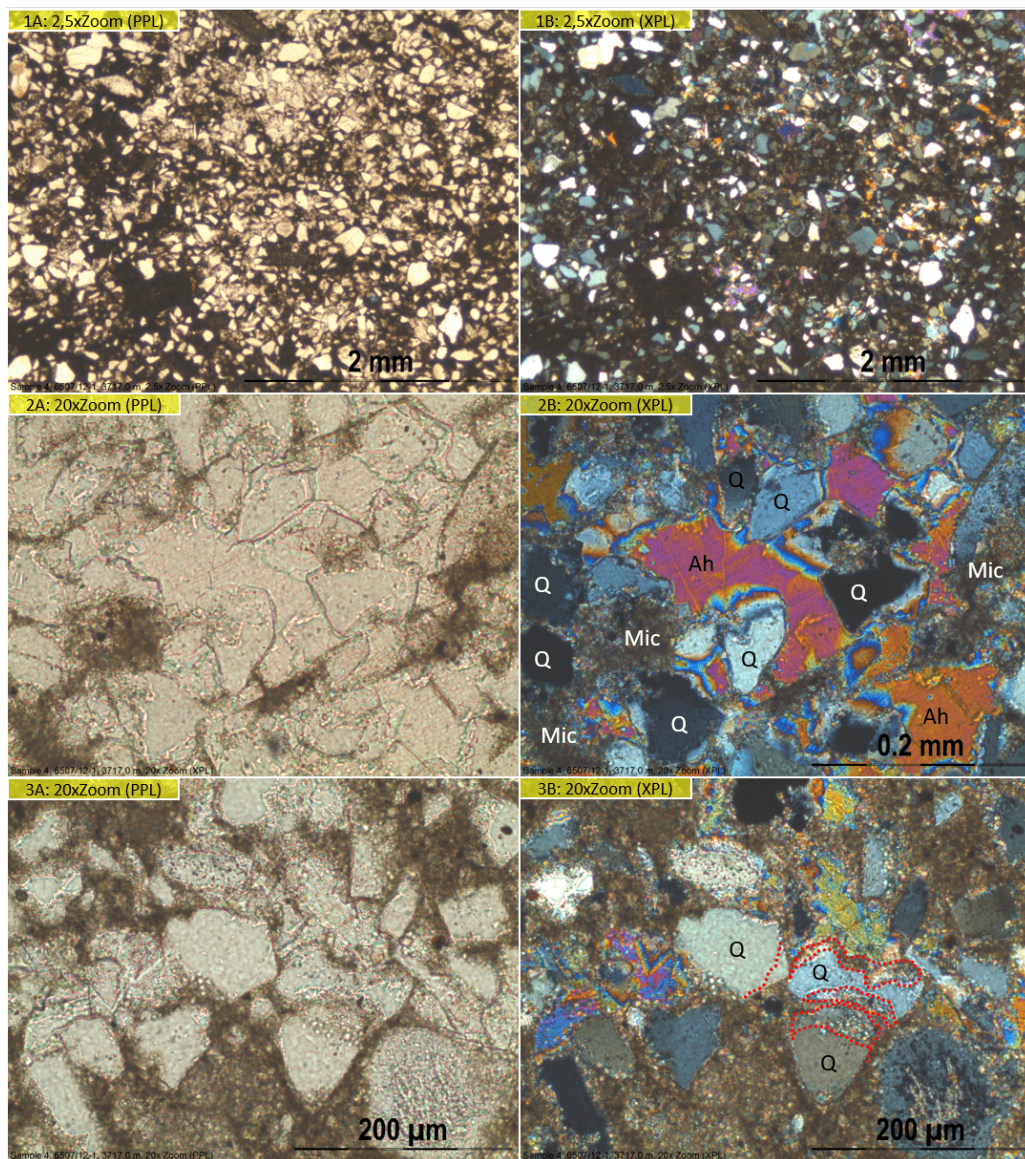
Figure 8.27: Thin section images of sample 3, 6507/12-1, 3711.5 m

### Sample 4, 6507/12-1, 3717.0 m MD

Picture 1A and 1B from Figure 8.28 at a total magnification of 25x show that the dominating grain size is 0.1 mm in diameter, which makes it a vfU sized sandstone. The sample is moderately to poorly sorted with subangular to sub-rounded grains and is classified as a subarkose. The rock is matrix supported, and the matrix mainly consists of micrite, sparite and anhydrite, which makes 65% of the bulk rock. The anhydrite is a diagenetic product surrounding the detrital grains. Additional 3% calcite cement is detected. As a consequence, the porosity is non-existent in sample 4. 2A and 2B at a total magnification of 200x, show scattered anhydrite crystals of higher order interference colors in the micrite matrix. The anhydrite also occurs as undisturbed clean intergranular diagenetic products. Quartz grains are the dominating mineral in the sample and make 25% of the bulk volume. In 3A and 3B, three quartz grains are marked. The upper left shows a subhedral grain with authigenic quartz cement. The upper right and lower right quartz grains are intergrown. They both have their own dust rim indicated by the red line, as well as overgrowth of quartz cement. The dust rim typically appears in arid environments where smaller clay particles attach themselves to quartz grain surfaces. In this sample, the clay dust rims may have been substituted with calcite, indicated by the high order interference colors. The dust rims could also originate from a carbonate mud source.

Sample 4 is situated in Unit Tr5 of Norian age. Figure 8.29, presenting pictures of sample 4, shows four fossil fragments from the Mollusca phylum. The interpretations on the kind and origin of these fossils was made with the help from Professor Atle Mørk from Department of Geoscience and Petroleum (NTNU). Rows 5 and 6 are interpreted to be molluscs from ostracods, while row 4 is believed to be a calcite ooid. The ooid is interpreted to be an extraclast, an older carbonate clast transported from outside of the depositional basin, due to the low amount of ooid observations. The ooid growth has evolved during several separate episodes. The inner layer is replaced by a fine grained rock fragment. Afterwards, the ooid has been growing in two separate episodes. This implies a shift between periods of growth and erosion. The ostracods in row 5 and 6 show a microstructure of parallel calcite crystals perpendicular to the surface, which is typical for ostracods. The ostracods are also known for the shadow observed at the centre of the fragment in 5B and 6B when polars are crossed. The shadow progress through the fragment as the microscope rotates. The fragment in row 6 is articulated with the shell still arranged in the proper order. Row 7 illustrates an abraded fragment showing pressure dissolution to the upper right. Pressure dissolution, indicated by the sutured intergranular contact, is consequentially created due to localized

stress and compaction. Overall, the size of the molluscs are about 0.4 mm in diameter, meaning that they are larger than the dominating grain size. A snail or clam fragment was also observed in sample 4. In addition, clams and ostracods are present in sample 8, also situated in Unit Tr5, but rather of Rhaetian age.



**Figure 8.28:** Thin section images of sample 4, 6507/12-1, 3717.0 m

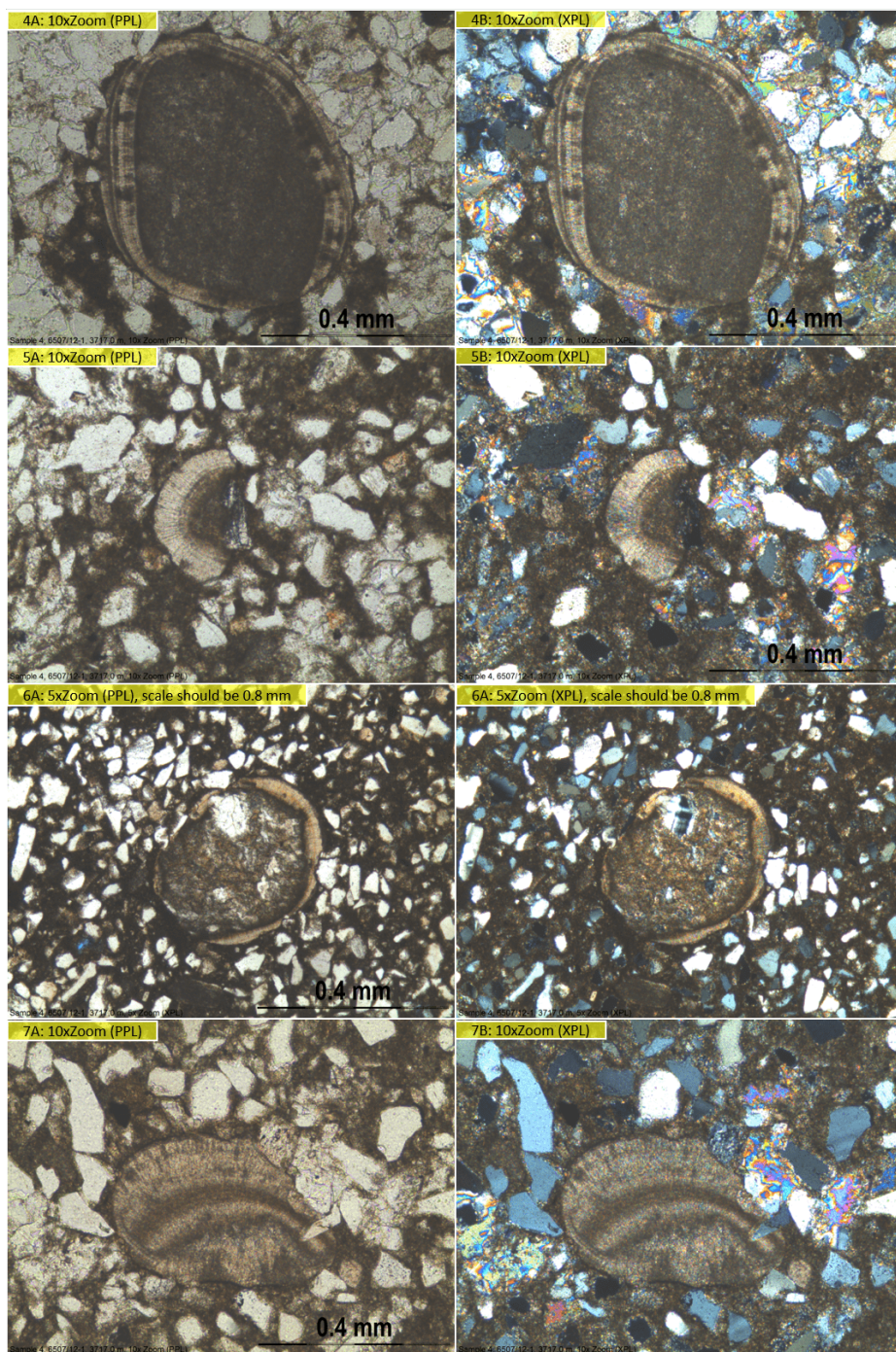


Figure 8.29: Molluscs from sample 4, 6507/12-1, 3717.0 m



**Sample 5, 6507/12-2, 4982.3 m MD**

As illustrated in Figure 8.30, the majority of grains from sample 5 have a diameter of 0.05 mm. This is indicative of silt sized grains. Sample 5 is therefore classified as a siltstone. The grains are moderately to poorly sorted and subangular with calcite nodules of 0.4 to 2 mm in diameter. The calcite nodules are detectable by the naked eye. 2A and 2B show a calcite nodule with intragranular grains, an euhedral plagioclase grain with albite twinning (multiple twinning) and a quartz grain (upper right) with undulose extinction. This is an indication of compaction and strain deformation of the quartz grain. The black and brown fine grained matrix contains organic material and sideritized biotite (precipitation of  $\text{FeCO}_3$ ). 3A shows that the sample contains some micro sulfide minerals in the form of pyrite. Picture 4, at a total magnification of 100x, is a close up view of a calcite nodule with sparitic recrystallized calcite inside the grain. The calcite nodule also contains some organic material occupying intragranular porosity. This porosity type is likely to have formed as a consequence of calcite dissolution.

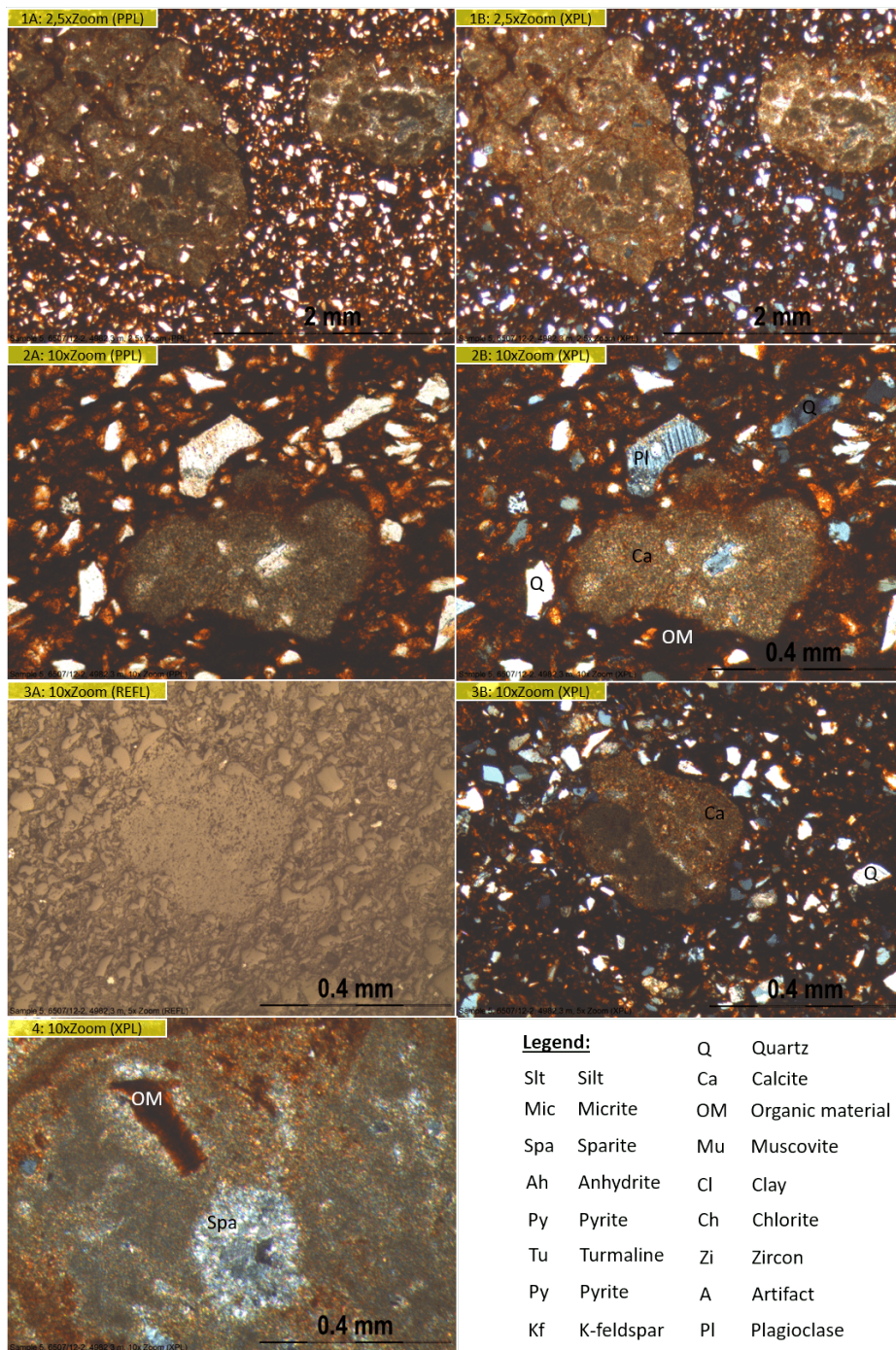
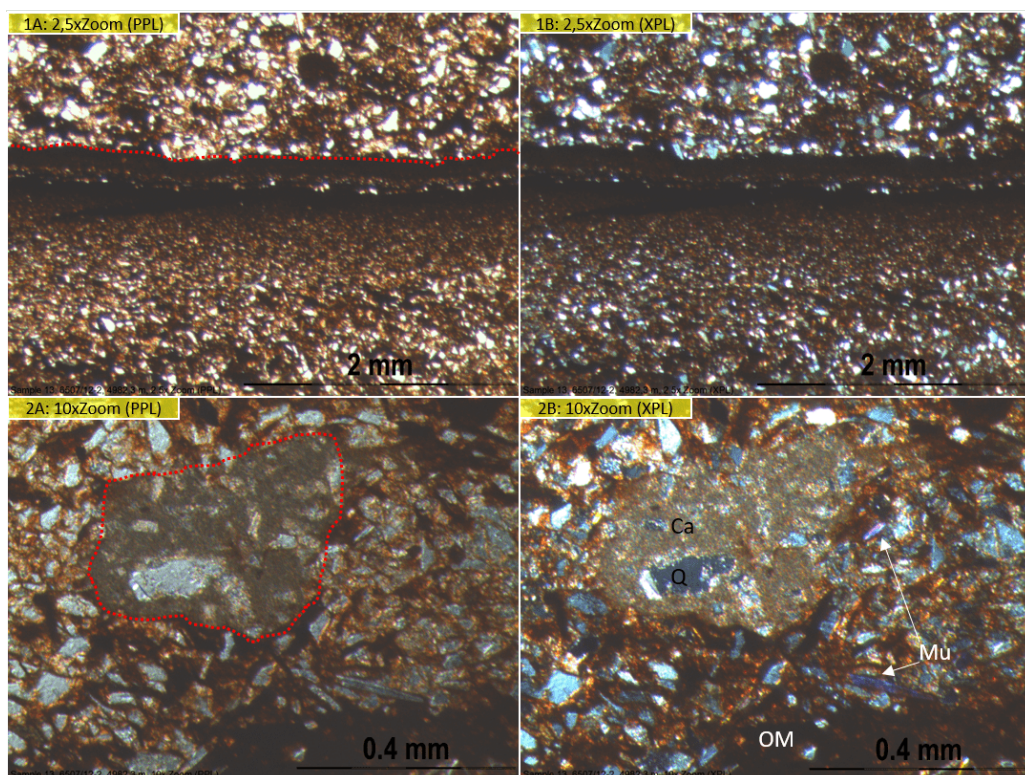


Figure 8.30: Sample 5, 6507/12-2, 4982.3 m

**Sample 13, 6507/12-2, 4983.9 m**

Sample 13 (Figure 8.31) is a planar laminated siltstone with the majority of the grains at a grain size of 0.04 mm, which implies a silt grain size. This sample is collected 1.6 m below sample 5 from the same wellbore. The grains are well sorted and has a subangular grain shape. In addition, the grains mainly consist of quartz, but muscovite also occurs. The grains are subangular and moderately sorted, and the matrix consists of clay, calcite, organic material and sideritized/reworked biotite. 1A and 1B illustrate how the siltstone layers are fining upward to clay size up until the red dotted line. Above this line, a new upward fining sequence from silt to clay sized grains begins. This may indicate that the beds are deposited in pulses or within an environment with gradually decreasing energy from one bed to the other. 2A and 2B show that the calcite nodules are present in this sample too, this time with intragranular quartz among other minerals.



**Figure 8.31:** Thin section images of sample 13, 6507/12-2, 4983.9 m

### Sample 10, 6610/7-2, 4180.4 m MD

Figure 8.32 shows thin section images of sample 10 which has a subangular grain shape and moderately sorted grains. The sample originates from well 6610/7-2 and is classified as an arkose with approximately equal amounts of plagioclase and K-feldspar. More than half of the feldspars were impossible to quantify as plagioclase or K-feldspar grains as a consequence of weathered grains. The majority of the grains have a sand grain size of 0.12 mm, which makes it a vfU arkose. The sample is moderately sorted, subangular and contains 24% intergranular calcite cement. There is no porosity in sample 10, very likely due to the high amount of diagenetic calcite cement. 1A and 1B at a magnification of 25x show the overview of the thin section, and in the lower right corner, a thin rim of fracture porosity is detectable. 2A and 2B at higher magnification reveals some diagenetic chlorite and detrital chlorite grains, which are green colored in PPL. Quartz grains and intergranular calcite can also be observed.

3A and 3B show a plagioclase grain in the lower left corner with the characteristic albite twinning. In the upper right corner, a K-feldspar grain is detected by its cross-hatched twinning. The upper left corner is occupied by intergranular calcite cement. In the center of 3B, a quartz grain is captured with some quartz overgrowth (quartz cement marked by the red dashed line), which gives the characteristic euhedral shape of the grain. In 4B, a quartz grain is highlighted with two red dashed lines. The innermost line demonstrates the original quartz grain and is surrounded by a dust rim that is most easily observed in 4A. The dust rim is overgrowth by quartz cement to the outer red dashed line. The lower quartz grain, marked with a red dashed line in PPL in 4A, shows a polycrystalline quartz grain. The origin of this grain is probably metamorphic as the boundaries between the crystals are sutured. It may be argued that the grain has suffered from strain and that the observed variation in interference colors is a result of undulose extinction.

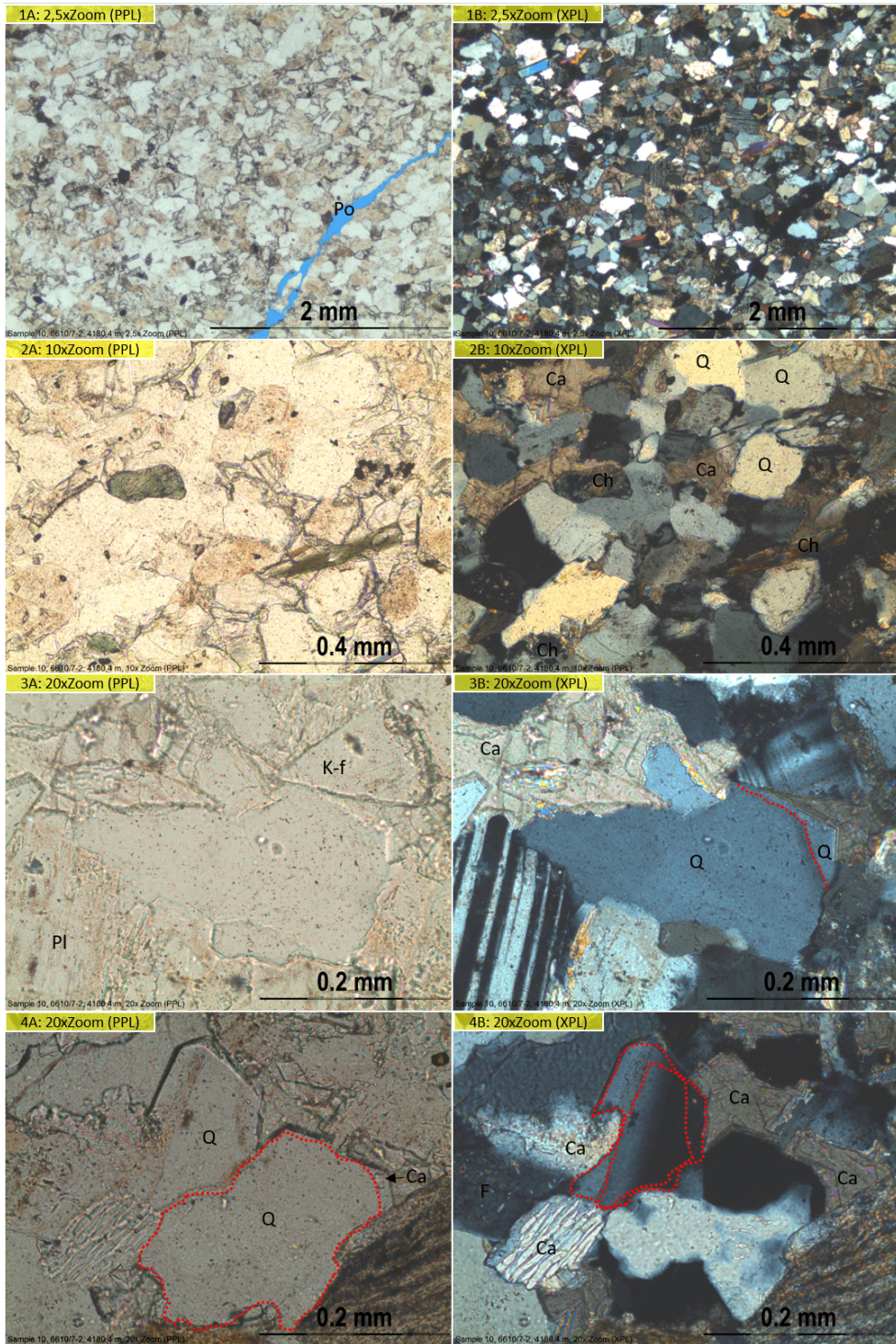


Figure 8.32: Thin section images of sample 10, 6610/7-2, 4180.4 m

### Sample 11, 6610/7-2, 4184.65 m MD

Sample 11 is situated 4.2 meters below sample 10 in the same well. Figure 8.33 shows thin section images of sample 11. The sample is moderately sorted and has a subangular shape. It is classified as an arkose from the QFL diagram. The dominating grain size is 0.1 mm and makes it a vfU arkose. 1A and 1B indicate that the grain size is a bit smaller than for sample 10 at a total magnification of 25x. 2A and 2B show that feldspar, plagioclase, quartz, calcite cement, muscovite and chlorite make the dominating mineralogy. This is also illustrated in 3A and 3B at a magnification of 200x. The chlorite tend to be intergranular and is most likely a diagenetic product. Diagenetic chlorite makes 19% of the bulk rock volume. In addition, calcite cement makes 8%, which in turn reduces the porosity to only 1%.

For most of the feldspar grains, the twins are difficult to recognize and sericitization is visible. The feldspar grains have been subjected to diagenetic effects, such as weathering and sericitization. Therefore, it is difficult to distinguish plagioclase from K-feldspar. 27% of the bulk volume is feldspar that could not be classified as plagioclase or K-feldspar. Of the bulk rock volume, 5% K-feldspar and 6% plagioclase could be detected and grouped. It shows that the sample contains approximately equal amounts of the two feldspar groups. At a total magnification of 500x, shown in 4A and 4B, a zircon mineral with its high order interference colors, was captured. Table D.2 from the Appendix D states that this sample contains minor amounts of organic material (1%). The organic material was observed intergranularly with a dark brown color on the thin section.

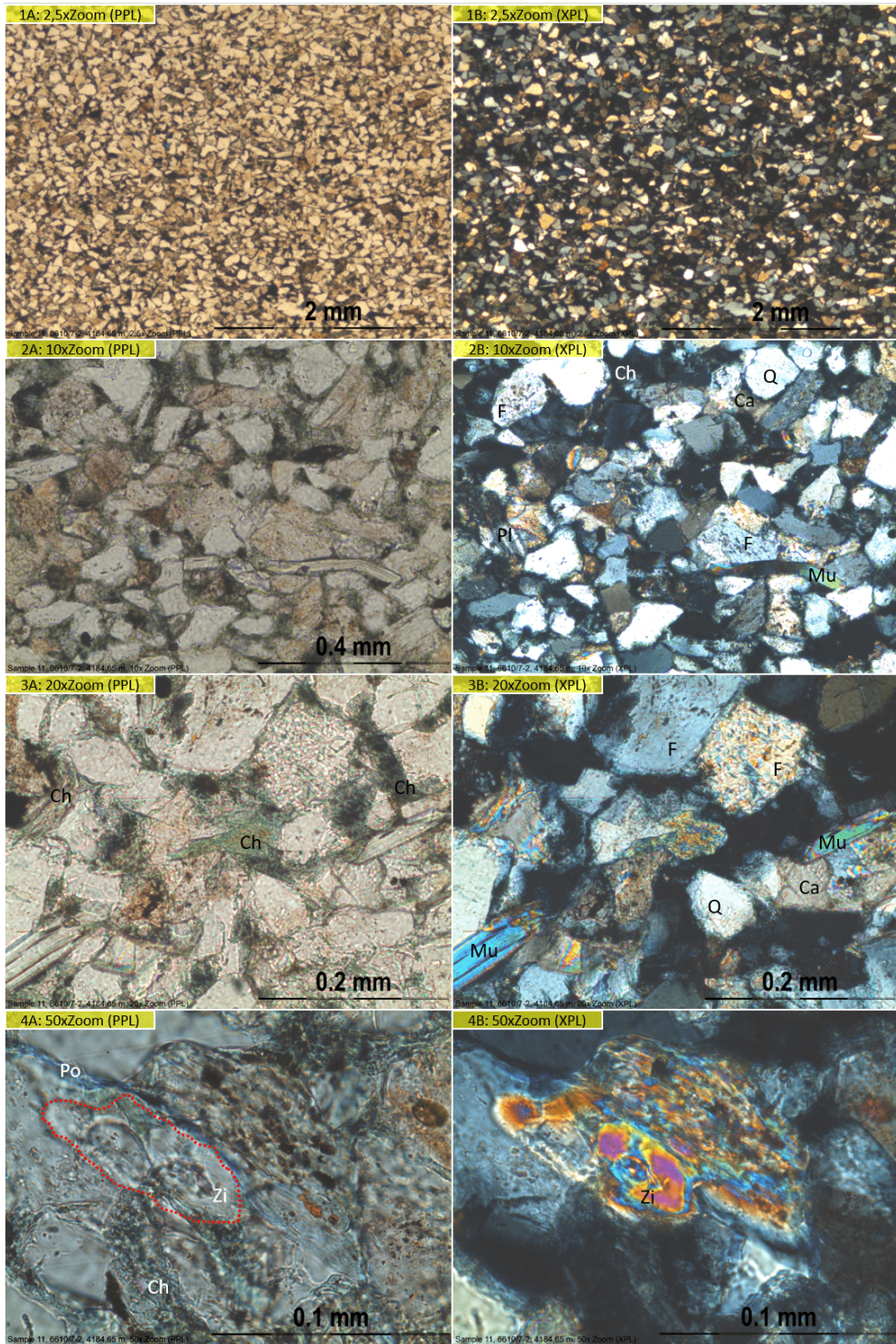


Figure 8.33: Thin section images of sample 11, 6610/7-2, 4184.65 m

### Sample 14, 6610/7-2, 4187.15 m MD

The thin section of sample 14 is cut at the border between an arkose with a dominating sand grain size of 0.45 mm, and a siltstone with a dominating grain diameter of 0.03 mm. In the point counting process, the arkosic part of the sample was focused on. This part had a sand size class of mU. Sample 14 is moderately sorted and the detrital grains are subangular. In Figure 8.34, 1B shows a rock fragment of silt sized particles where the source is the adjacent siltstone. Further down, a stylolite can be detected in picture 2, 3A and 3B. The stylolite consists of muscovite grains oriented along the direction of the stylolite, and also of opaque minerals. The stylolite continues into the arkosic part of the sample (4A and 4B), and pressure has been applied to both the siltstone and the arkose. 4% of the bulk volume is polycrystalline quartz with sutured crystal boundaries, which is typical for a metamorphic source. 35% of the bulk rock volume comprises of feldspars, and the ratio between the amount of K-feldspar and plagioclase is approximately 1:3.

In Figure 8.35, 5A, 5B and 5C show a cluster of heavy minerals on a calcite grain in both PPL, XPL and reflected light. The minerals that are white in the reflected light may be sulfide minerals (e.g. pyrite). The dark heavy minerals that is light brown in reflected light may be phosphate minerals (e.g. apatite). 7A and 7B show a tourmaline grain, which is another type of heavy mineral quite resistant to diagenetic processes. 6A and 6B shows a quartz grain with calcite cement overgrowth. 19% of the bulk volume is calcite cement, combined with 2% quartz cement and 2% sparite matrix. The remaining porosity is 1%.



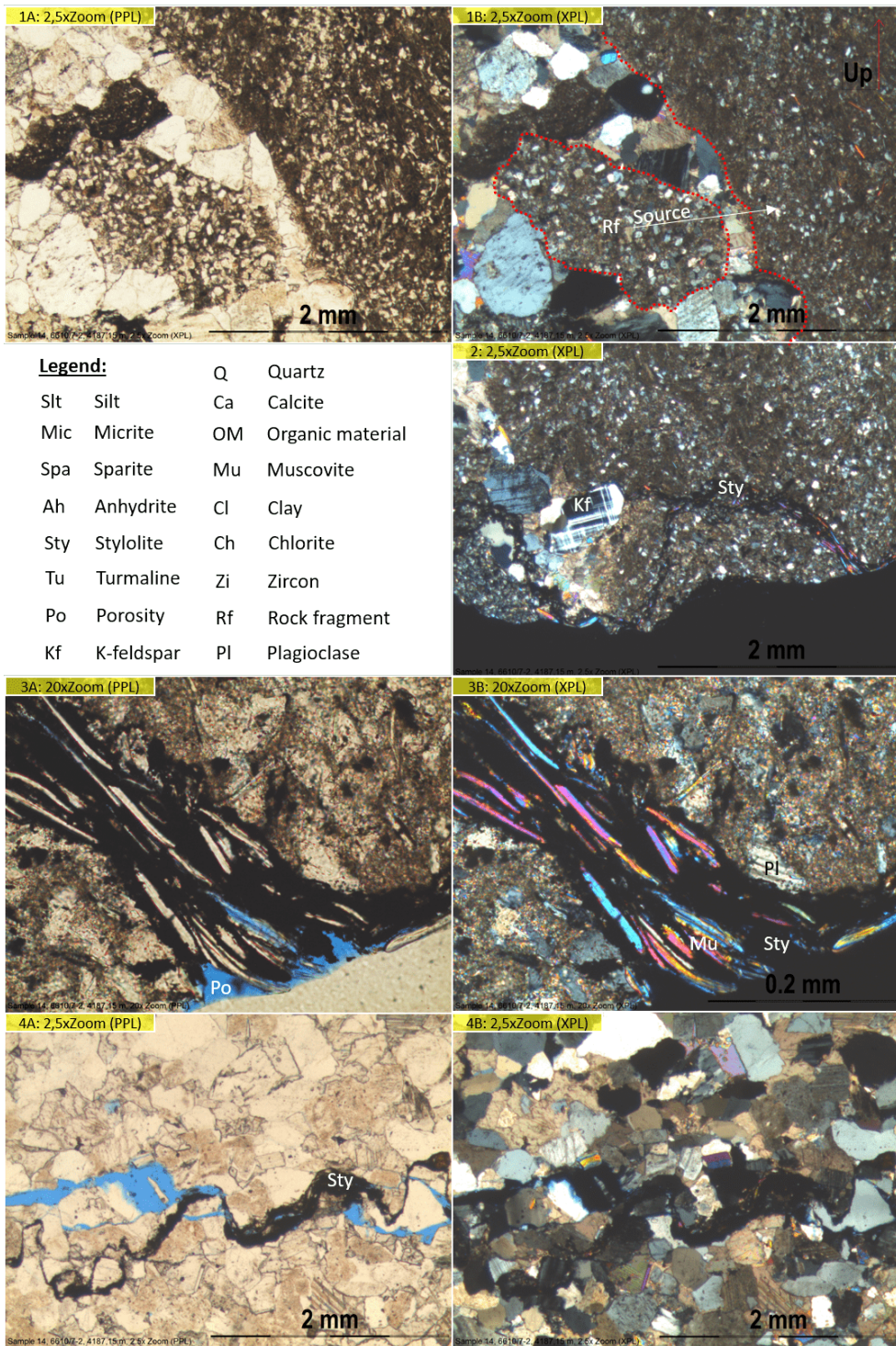


Figure 8.34: Thin section images of sample 14, 6610/7-2, 4187.15 m

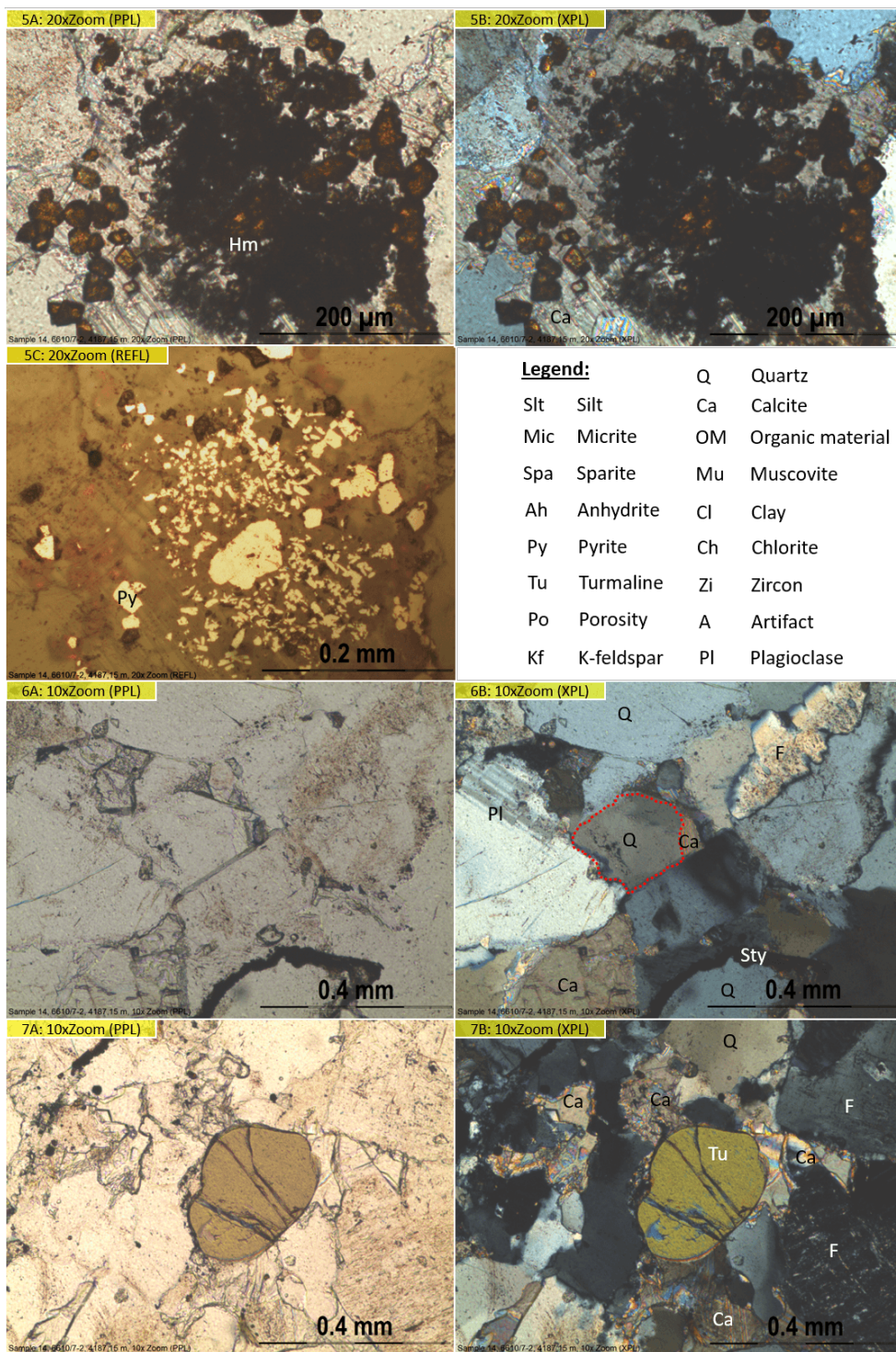


Figure 8.35: Thin section images of sample 14, 6610/7-2, 4187.15 m

**Sample 12, 6610/7-2, 4194.05 m MD**

Sample 12 is the lowermost sample from well 6610/7-2 at a depth of 4194 m. Figure 8.36 shows that the dominating grain size is 0.4 mm, which makes it a mU sized arkose. 1A and 1B shows that sample 12 still contain some porosity. It can be seen from Table D.3 in Appendix D that the porosity is found to be 11%. It should be noted that calcite cement makes 12% of the bulk rock volume. At the centre of 2A and 2B, a detrital anhydrite grain can be observed with high order interference colors and two cleavages perpendicular to each other. This observation is important as it adds information about the type of depositional environment at this location. 3A and 3B presents a weathered feldspar grain subjected to sericitization. The surrounding calcite is filling in the intergranular pore space between the feldspar and the quartz grains. Intragranular calcite cement also occupies some of the pore space within the feldspar grains. 4A and 4B captured a bent muscovite grain suffering from mechanical strain from the surrounding grains. This may suggest that the feldspars where weathered prior to calcite cementation. On the upper part of 4A and 4B, a green detrital chlorite grain can be observed. To the lower right of this grain, one can see a feldspar grain subjected to sericitization (replacement by sericite, a fine grained muscovite). Only parts of the grain is preserved and the twinning is undetectable. 12% of the bulk rock consists of feldspar, 6% of K-feldspar and 13% of plagioclase. Thus, there is more plagioclase relative to K-feldspar in sample 12.

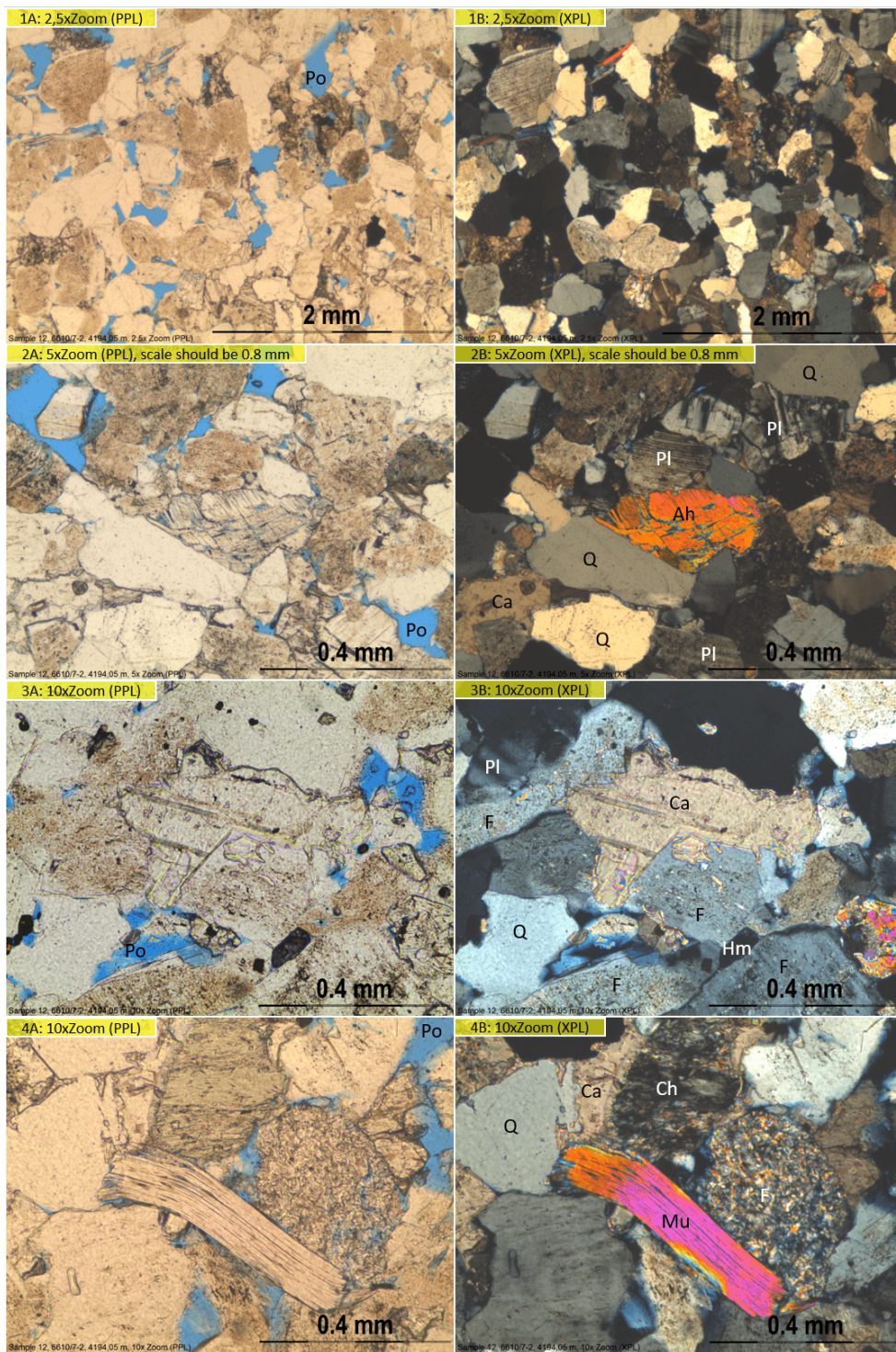
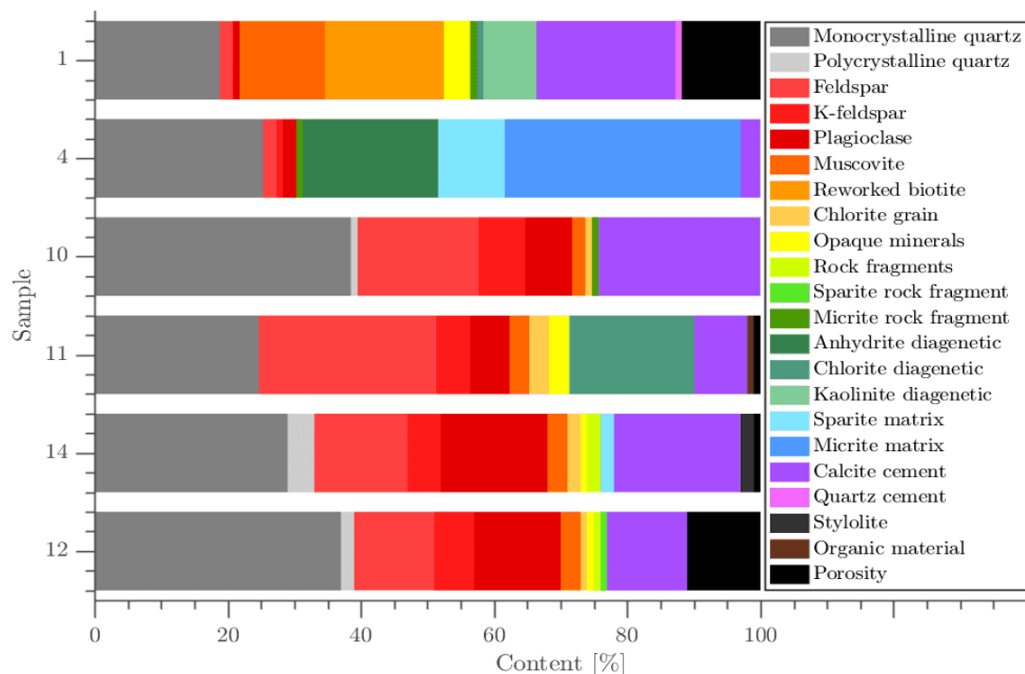


Figure 8.36: Thin section images of sample 12, 6610/7-2, 4194.05 m

In Figure 8.37, an overview of the point counting results for all the samples is given. The well name, sample number and sample depth, can be found in Table 8.3, while the mineralogy determined by point counting is covered by Table D.2 in Appendix D. In this figure, the samples are sorted in terms of their respective depths. Sample 1 from wellbore 6507/6-1 on the Sør High is taken from a depth of 3044 m. It has one of the highest porosity values, even though the cement values are very high. Sample 1 also has some diagenetic kaolinite which has a negative effect on the porosity. Sample 4 from wellbore 6507/12-1 on the Ellingråsa Graben is taken from a depth of 3717 m. It has a high portion of micrite and sparite matrix, and together with diagenetic anhydrite and calcite cement nearly 70% of the bulk volume is covered. Sample 10, 11, 14 and 12 from wellbore 6610/7-2 on the northern part of the Trøndelag Platform are taken from depths of 4180, 4185, 4187 and 4194 m, respectively. The porosity seems to be better sustained in the deepest part of this well. By comparing sample 10 and 12, it is convincing that some of the calcite cement is replaced by porosity in sample 12. A trend of increasing porosity with depth can be observed for the core location of wellbore 6610/7-2. This will be discussed in Chapter 9.



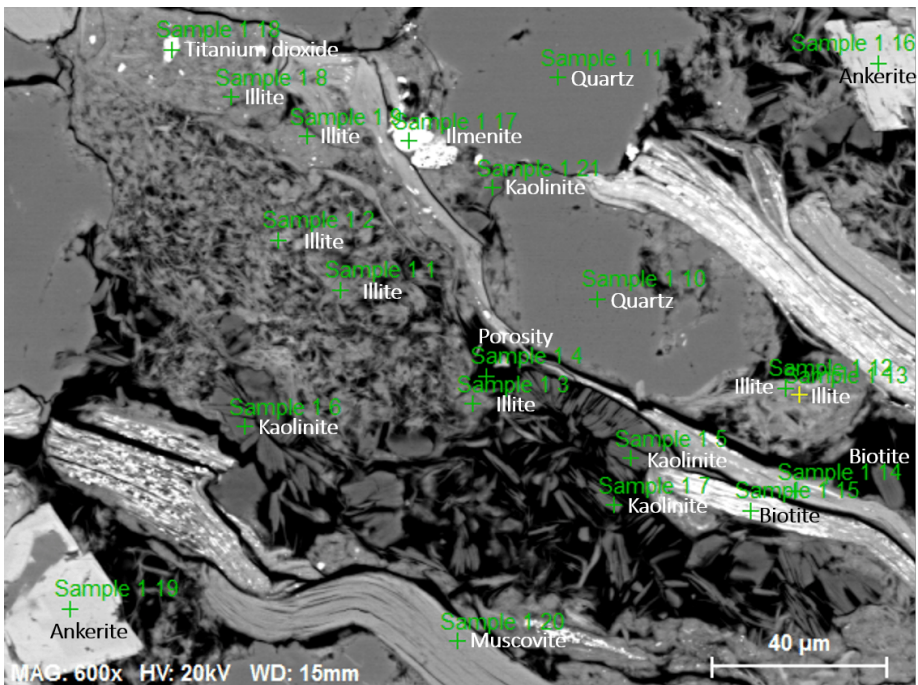
**Figure 8.37:** A bar plot visualizing the point counting results. The samples are sorted with respect to depth, with the shallowest sample in the top.

## 8.5.2 SEM results

The purpose of performing the SEM analysis was to highlight the presence of intergranular authigenic minerals, especially the clay minerals; kaolinite, illite and chlorite, but also the evaporite and cement minerals; anhydrite and calcite cement. To some degree feldspar, quartz, mica and heavy minerals were also identified using SEM. Due to the small grain size, point counting was not performed on sample 3, 5 and 13. During SEM analysis, sample 1, 3, 5, 11, 12 and 13 were used to investigate the desired features.

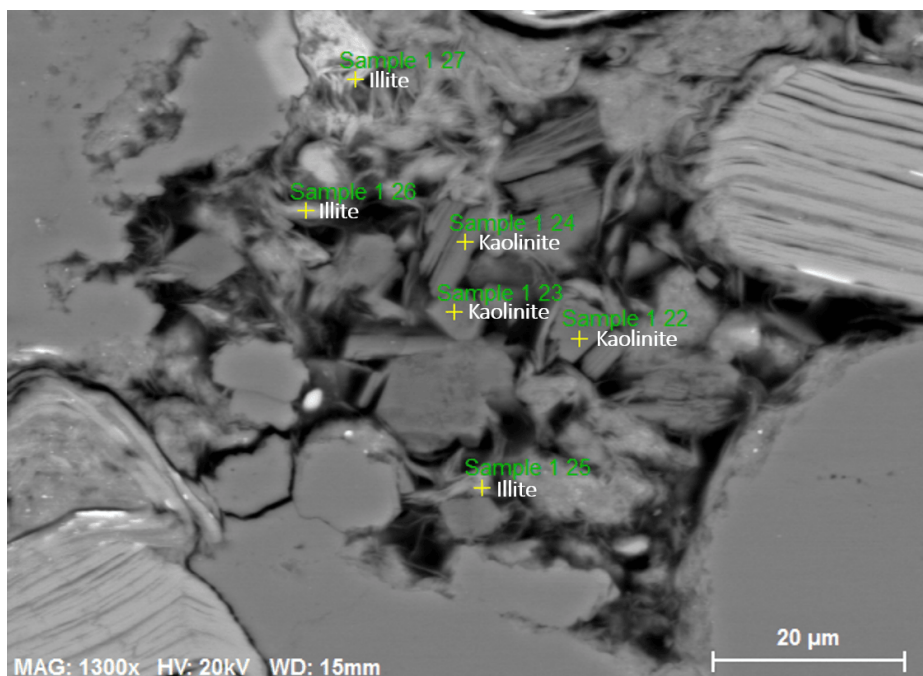
### Sample 1, well 6507/6-1, 3044.45 m MD

The goal for SEM analysis on sample sample 1 was to investigate the pore filling structures. As observed in Figure 8.38, kaolinite and illite are the dominating pore filling structures.



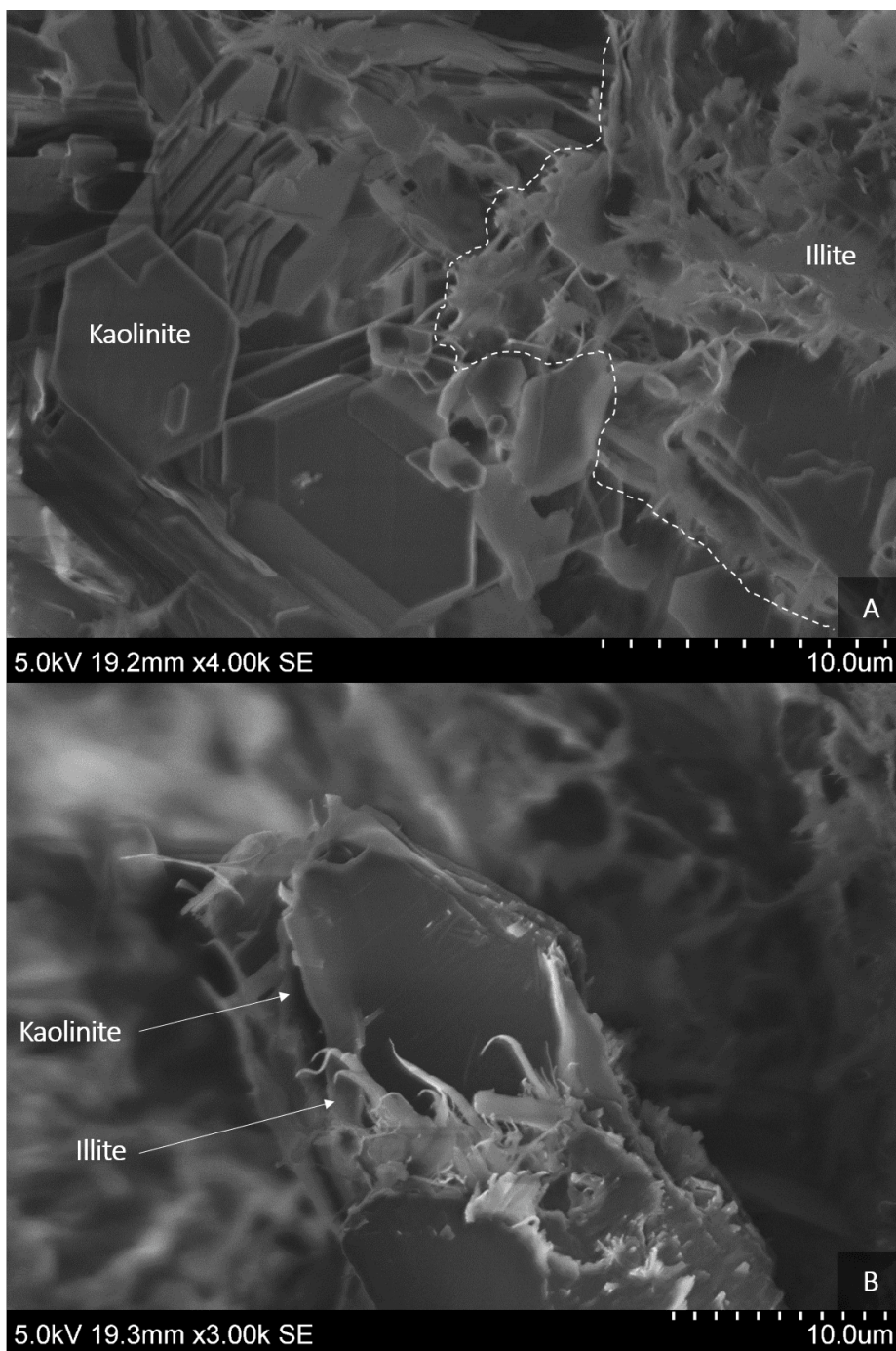
**Figure 8.38:** Results from SEM analysis performed on sample 1 at a magnification of 600x.

A close up view of the kaolinite and illite structure can be seen in Figure 8.39 at a magnification of 1300x. The kaolinite has a stacked blocky structure, while illite appears in a network structure as a pore bridging clay mineral. The illite is also occupying some of the pore space between the kaolinite clay minerals.



**Figure 8.39:** Results from SEM analysis performed on sample 1 at a magnification of 1300x.

The morphology was also studied on selected samples. The procedure was carried out by carbon coating an open fracture surface on the sample hand specimens. For sample 1, kaolinite and illite (as described above) can be found in Figure 8.40, which shows the SEM results for the sample, 3000 and 4000 times magnified. For part A of the figure, the white dashed line roughly makes the border between kaolinite and illite minerals. Kaolinite form a characteristic structure of stacked hexagonal minerals. In part B of the figure, needle shaped illite can be observed growing into the pore space, most likely transformed from kaolinite.

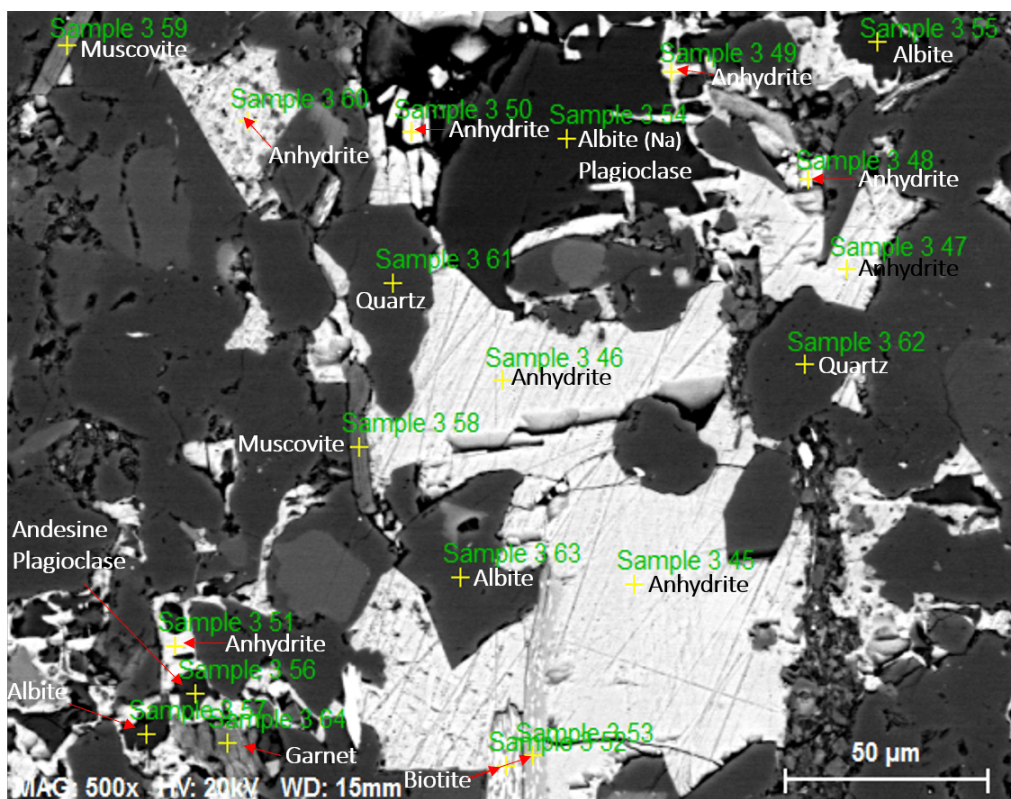


**Figure 8.40:** Results from SEM morphology of sample 1 at a magnification of 4000x in A, and 3000x in B.



### Sample 3, well 6507/12-1, 3711.50 m MD

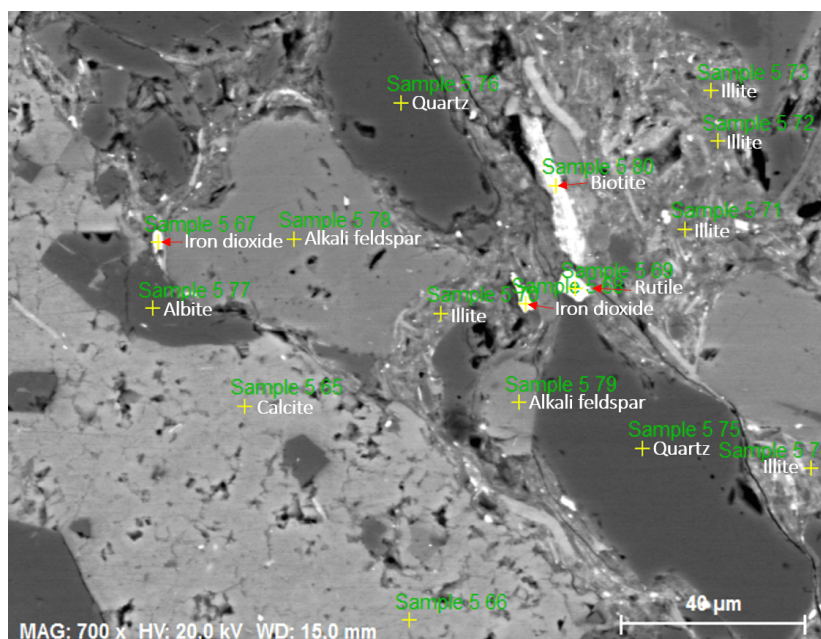
The goal of SEM analysis on sample 3 was to verify the authigenic anhydrite mineral. The EDS spectra of anhydrite, attached in Appendix E.1, confirmed the presence of the mineral. The characteristic perpendicular anhydrite cleavages can be observed in Figure 8.41. It can also be observed that the anhydrite mineral is filling the pore space both between large and small grains. Plagioclase is the dominating feldspar mineral observed in this sample.



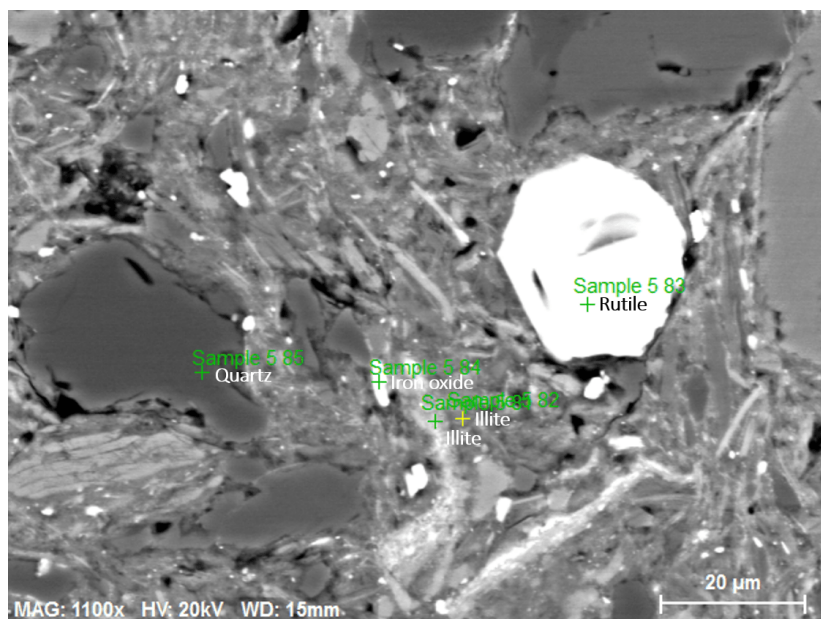
**Figure 8.41:** Results from SEM analysis of sample 3 at a magnification of 500x.

### Sample 5, well 6507/12-2, 4982.30 m MD

SEM analysis was conducted on sample 5 to identify the mineral composition of the matrix and the light nodules.



**Figure 8.42:** Results from SEM analysis of sample 5 at a magnification of 700x.

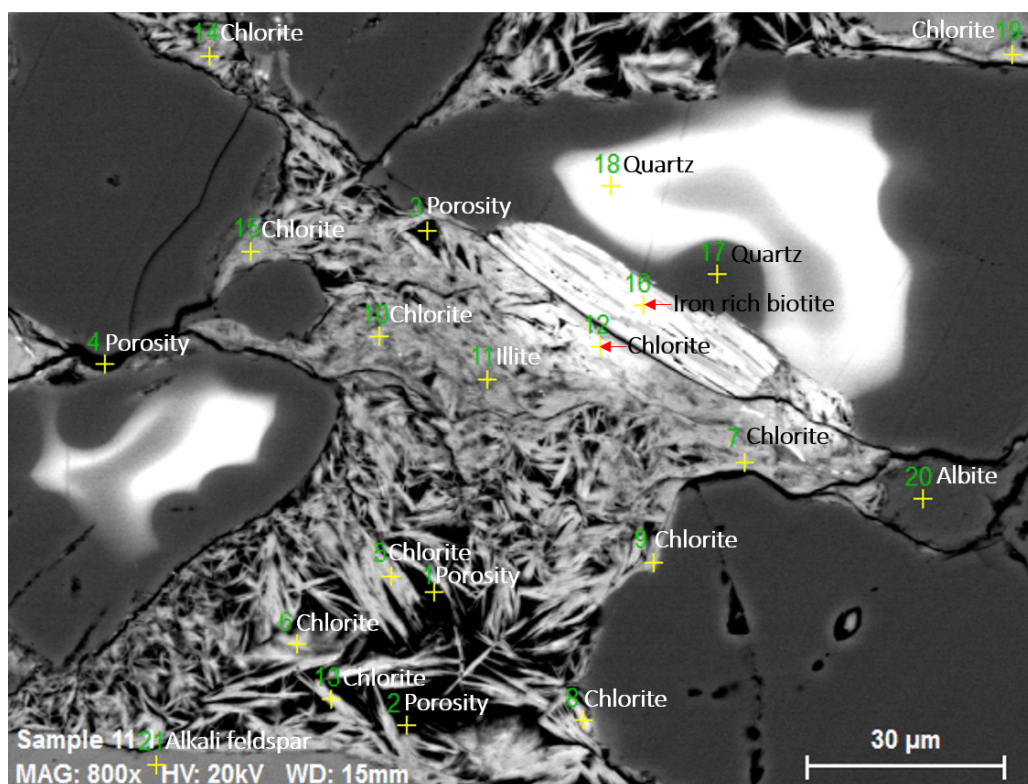


**Figure 8.43:** Results from SEM analysis of sample 5 at a magnification of 1100x.

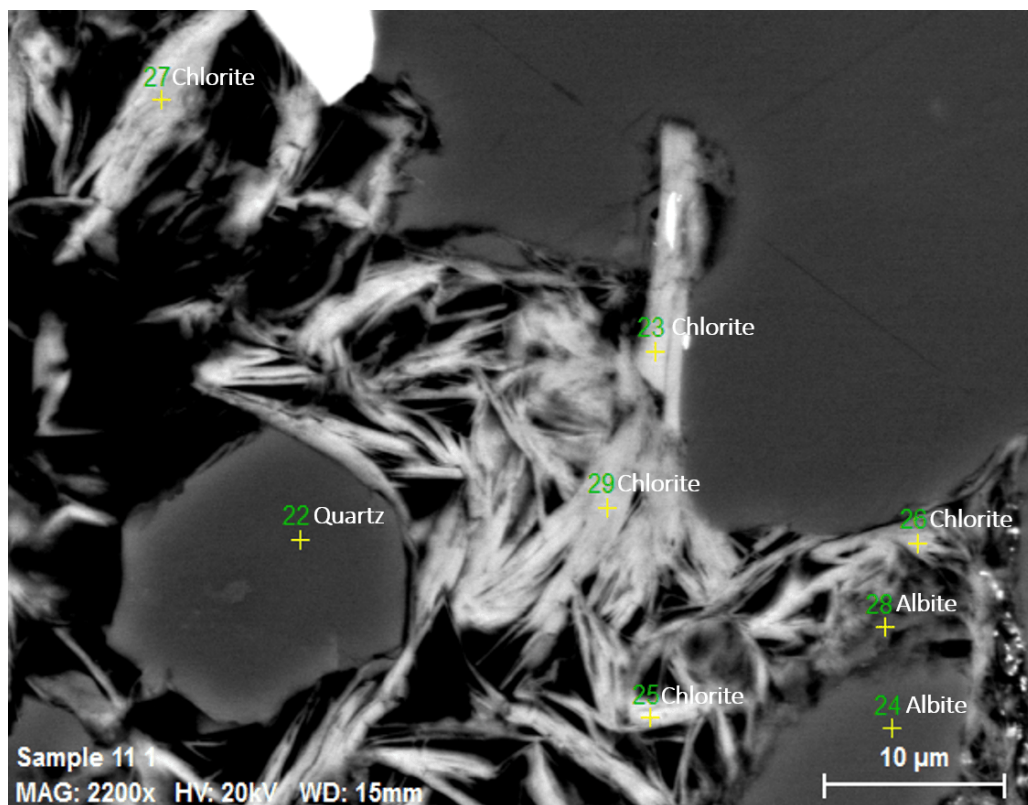
Figure 8.42 shows that the light nodule is a calcite nodule and that the brown matrix is composed of illite, micro mica and heavy micro minerals. This can also be observed in Figure 8.43 at a magnification of 1100x. The heavy minerals observed are rutile and iron oxides.

### Sample 11, well 6610/7-2, 4184.65 m MD

Sample 11 is an Anisian arkose from well 6610/7-2. From Table D.2 in Appendix D, it can be seen that diagenetic chlorite is present by 19% of the bulk volume. By looking at Figure 8.44, it is clear that chlorite and partly illite is filling the pore space of this arkose. At a magnification of 2200x, a close up view of chlorite minerals can be seen in Figure 8.45. Rather small amounts of calcite cement was observed in this sample, while chlorite is filling most of the IGV.

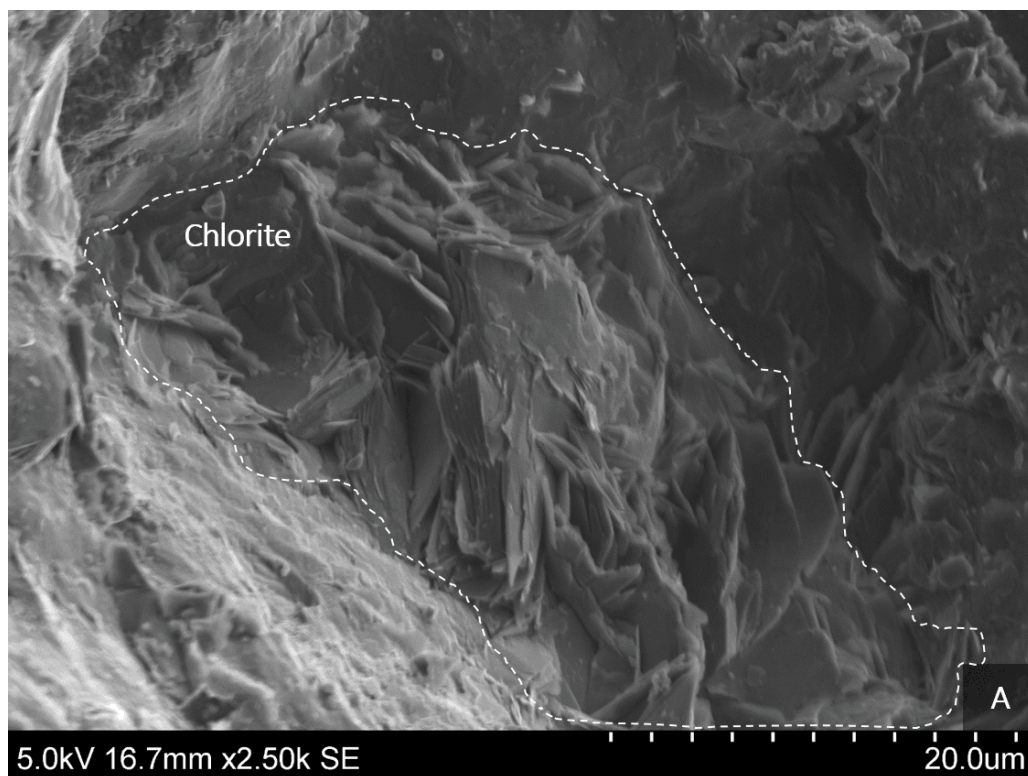


**Figure 8.44:** Results from SEM analysis performed on sample 11 at a magnification of 800x.



**Figure 8.45:** Results from SEM analysis performed on sample 11 at a magnification of 2200x.

The morphology of sample 11 can be found in Figure 8.46. Grain coating chlorite minerals can be observed within the white dashed line in the figure. The chlorite minerals tend to form rose structures along the detrital grains, with restrained growth into the pore space.



**Figure 8.46:** Results from SEM morphology of sample 11 at a magnification of 2500x.

### **Sample 12, well 6610/7-2, 4194.05 m MD**

Point 31 in Figure 8.47 represents perchlorate ( $\text{ClO}_4^-$ ) salt within a feldspar grain. This is a moderately weathered feldspar grain, where salt have precipitated and filled in the intragranular pore space. The sample represents an arkose of mU sand grain size from well 6610/7-2 and has a porosity of 11%. The observed salt is not occupying free intergranular pore space. In this sample, clay minerals were not observed during SEM. See Appendix E, Section E.1 for the respective EDS spectra. Figure 8.48 shows a grain rock aggregate of quartz and muscovite. Intragranular porosity can also be observed. In general, sample 12 is rich in feldspars (albite and alkali feldspar), muscovite, quartz and calcite.

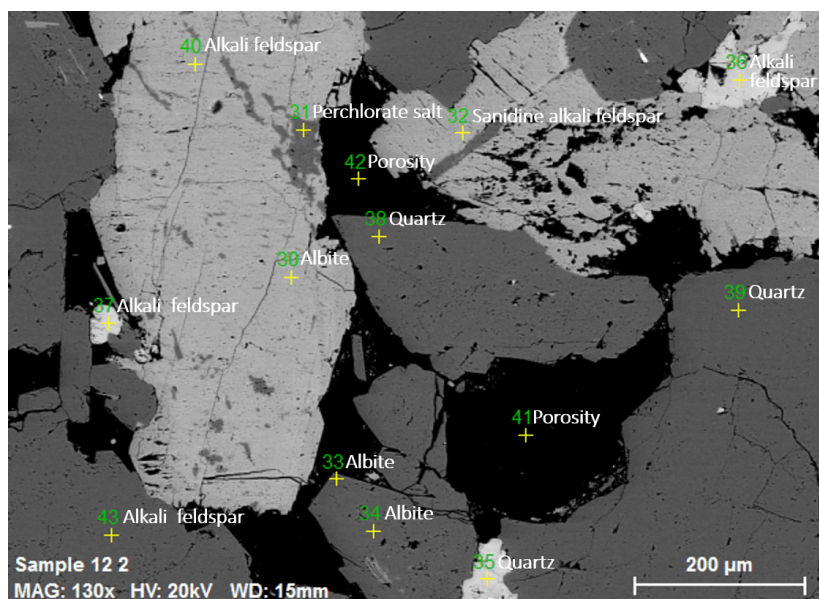


Figure 8.47: Results from SEM analysis of sample 12 at a magnification of 130x.

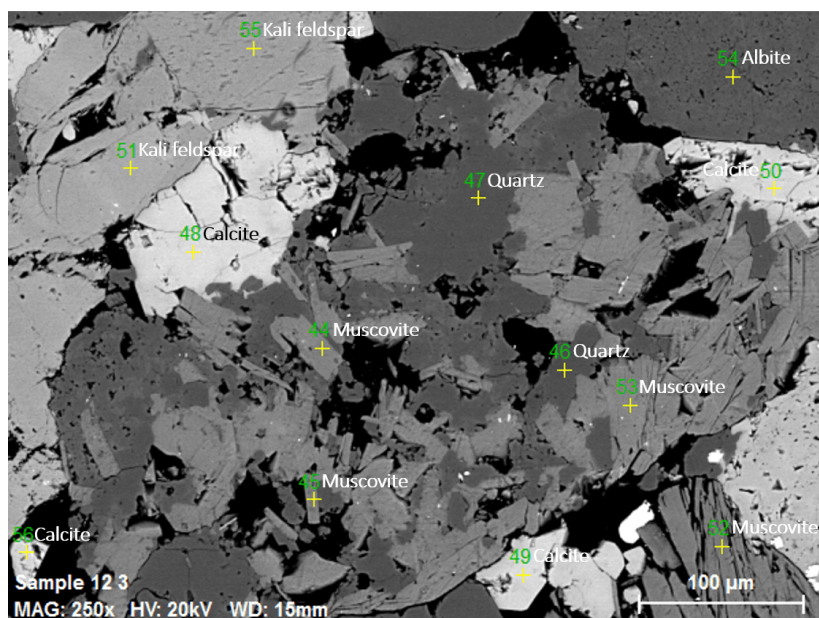
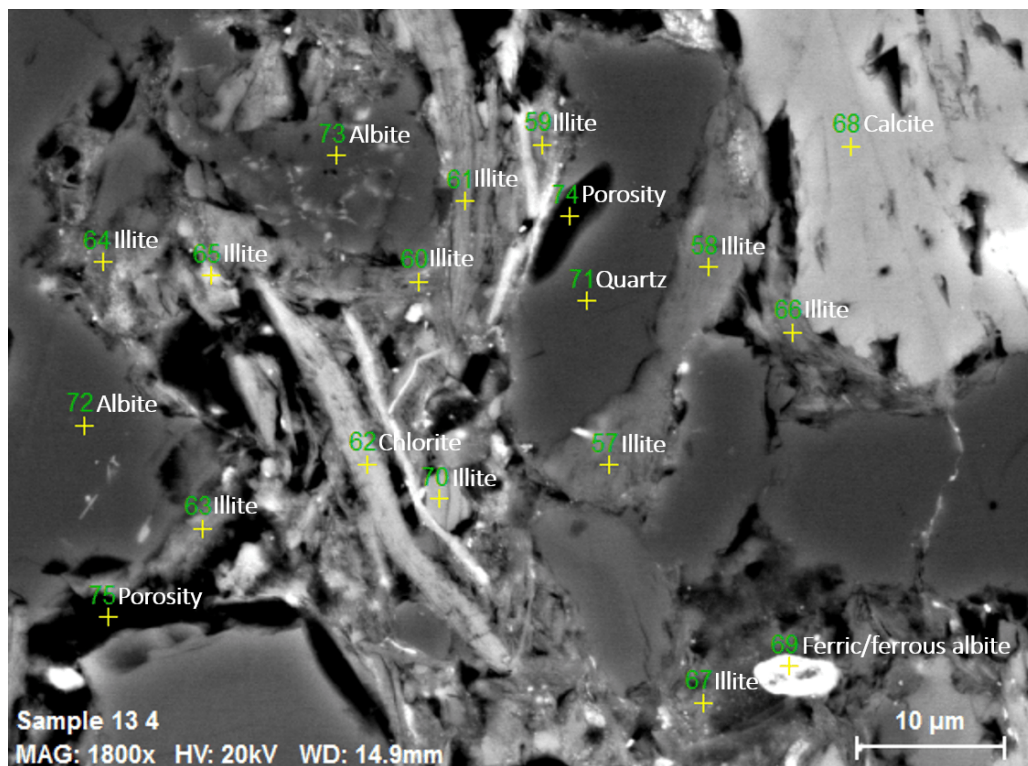


Figure 8.48: Results from SEM analysis of sample 12 at a magnification of 250x.

**Sample 13, well 6507/12-2, 4983.90 m MD**

The idea behind performing SEM analysis on sample 13 was to investigate the red-brown matrix of the siltstone located in well 6507/12-2 at a depth of 4984 m (MD). In Figure 8.49, the intergranular matrix can be observed at a magnification of 1800x. It consists of quartz, feldspars and calcite, in addition to intergranular illite, microporosity and occasionally chlorite and heavy minerals.



**Figure 8.49:** Results from SEM analysis performed on sample 13 at a magnification of 1800x.

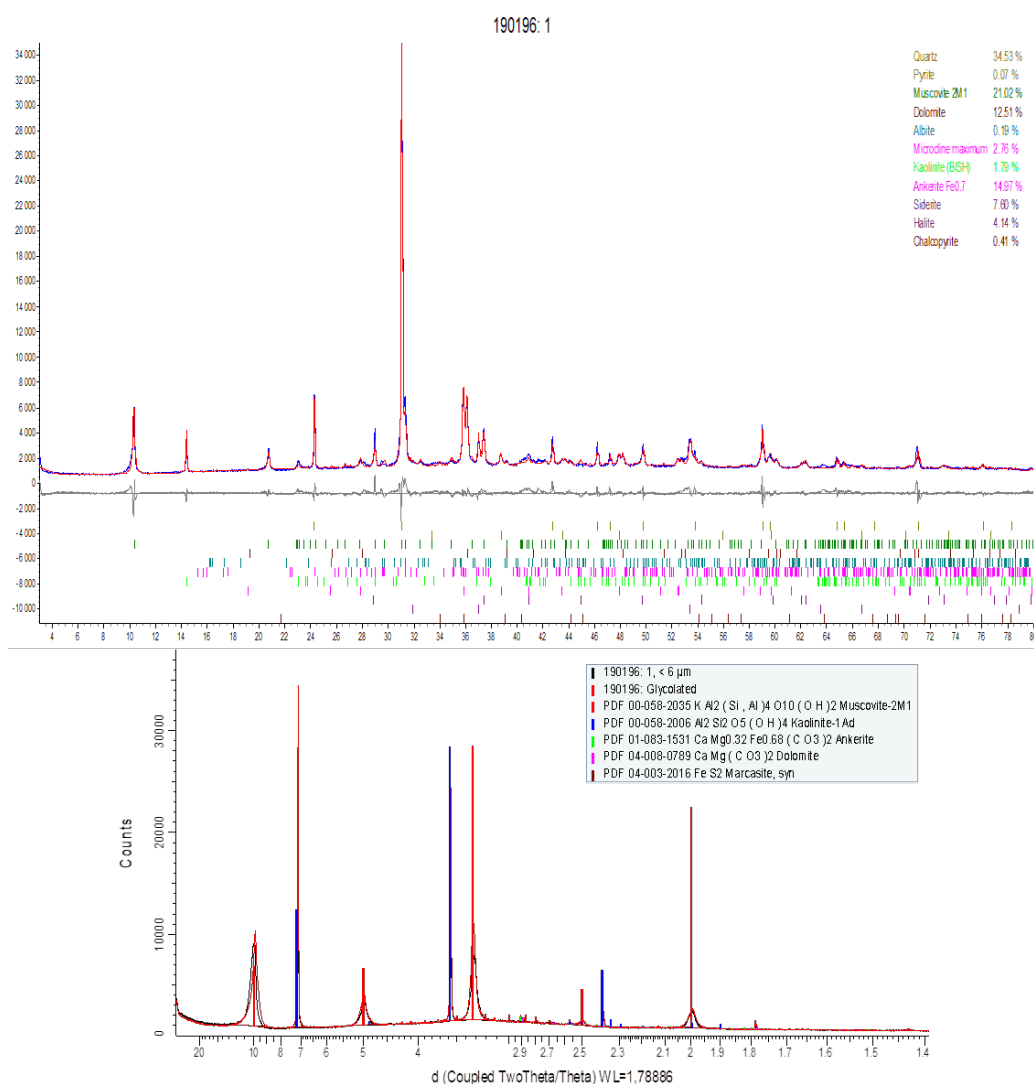
### 8.5.3 XRD results

In this section, the XRD results will be in focus. Bulk XRD has been conducted on sample 1, 3, 5, 11, 12 and 13, while fine fraction XRD was performed on sample 1, 11 and 12.

#### Sample 1, well 6507/6-1, 3044.45 m MD

In the bulk diffractogram in Figure 8.50, 11 minerals were identified. The mineral proportions are listed in Appendix F, Table F.1. An overview of the mineral proportions are visualized at the end of Section 8.5.3 (Figure 8.56). 35% quartz and 29% mica are present in sample 1. For mica, about 1/4 of the minerals are sideritized. Ankerite and dolomite make 15% and 13% of the bulk volume, respectively. The structures of these two minerals show similar characteristics and are difficult to separate in the diffractogram. Sample 1 shows a halite proportion of 4% of the bulk volume even though the sample is taken 1000 meters below Unit Tr4. K-feldspar makes 3% of the bulk volume, and 2% is occupied by the clay mineral kaolinite. The illite observed in SEM analysis falls within the mica group during XRD analysis. Traces of chalcopyrite (copper iron sulfide), pyrite and albite were also observed. The lower part of Figure 8.50 shows the fine fraction results. The particle size is smaller than 6  $\mu\text{m}$ . There is no sign of swelling clay in the diffractogram as the mineral curve of the glycolated sample overlaps with the unglycolated sample. The illite/mica peak at  $d=9.97$  indicates the presence of the illite observed from SEM. Kaolinite is present at a  $d$ -value of 7.17, while chlorite is absent in this sample. In addition, ankerite, dolomite and marcacite (iron sulfide) were found. In comparison to the isometric crystal structure of pyrite, marcacite is orthorhombic. It should be noticed that the halite mineral is not present in the fine fraction. A natural explanation might be that the halite is intragranular and not intergranular, as observed in sample 12 during SEM analysis (see Figure 8.47). Other explanations will be discussed in the following chapter.





**Figure 8.50:** Bulk- and fine fraction XRD diffractograms of the subarkosic sample 1 from Unit Tr3.

### Sample 3, well 6507/12-1, 3711.50 m MD

The bulk diffractogram of sample 3 is given in Figure 8.51. 11 minerals were identified and the calculated red line matches the blue observed sample line except for one peak at a  $2\theta$ -value of about 7.9. This gives a d-value of 14 Å by applying

Bragg's Law:

$$\begin{aligned} n\lambda &= 2d \cdot \sin \theta, \\ d &= \frac{n \cdot \lambda}{2 \sin \theta}, \end{aligned} \tag{8.1}$$

where

$$\begin{aligned} \theta \text{ (angle)} &= 3.95, \\ \lambda \text{ (wavelength)} &= 1.79 \text{ \AA}, \\ n \text{ (counts)} &= 406, \\ d \text{ (atom spacing)} &= 14 \text{ \AA}. \end{aligned}$$

A d-value of 14 Å indicates the presence of smectite. Fine fraction XRD was not performed on sample 3, thus in order to verify the hypothesis, a swelling clay test was performed using some of the remaining material. For this test, one sample was glycolated while the other was not, before they both ran through the XRD apparatus. The glycolated diffractogram was shifted to a higher d-value, thus confirmed the presence of smectite in sample 3. Another clay mineral observed is chlorite, occupying 5% of the bulk volume. Further on, sample 3 contains 46% dolomite, 10% calcite and 1% anhydrite. 11% quartz, 6% albite and 2% K-feldspar were also identified. In addition, 10% mica minerals were observed. 8% of the bulk volume consists of analcime with the chemical formula  $\text{NaAlSi}_2\text{O}_6 \cdot \text{H}_2\text{O}$ . Traces of pyrite and siderite occur in sample 3. Note that sample 3 is situated supra-salt and that halite is not present here.

### Sample 5, well 6507/12-2, 4982.30 m MD

In sample 5, eight minerals can be observed in the diffractogram shown in Figure 8.52. The diffractogram indicates that the sample contains 22% quartz, 22% plagioclase and 7% K-feldspar. Calcite represents 8% of the bulk volume, while mica minerals make 32%. From the SEM results, it is clear that the illite is disguised as a part of the mica content. In the absence of kaolinite and smectite, chlorite occupies 9% of the bulk volume. Traces of pyrrhotite (iron sulfate) and pyrite (iron sulfide) occur in sample 5.

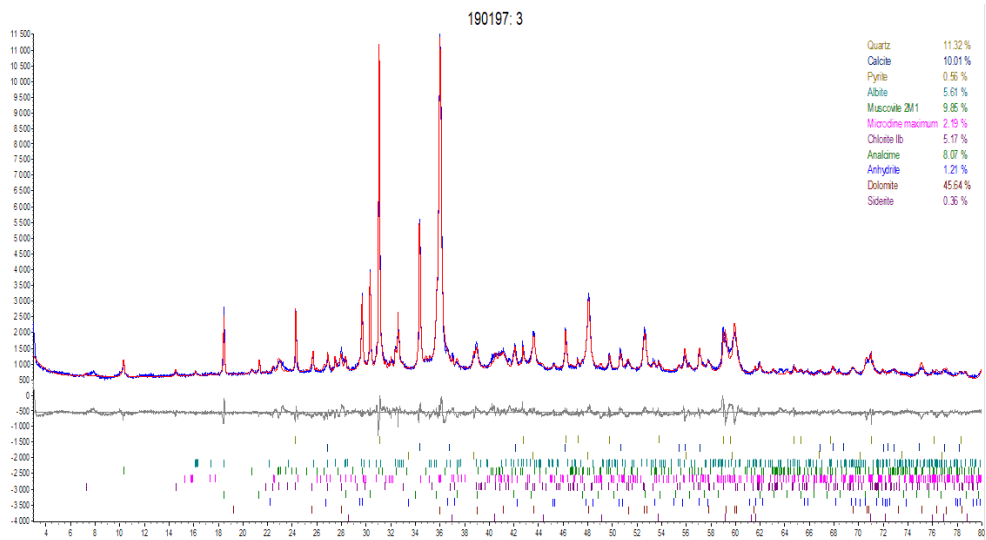


Figure 8.51: Bulk XRD diffractograms of sample 3 (siltstone) from Unit Tr5.

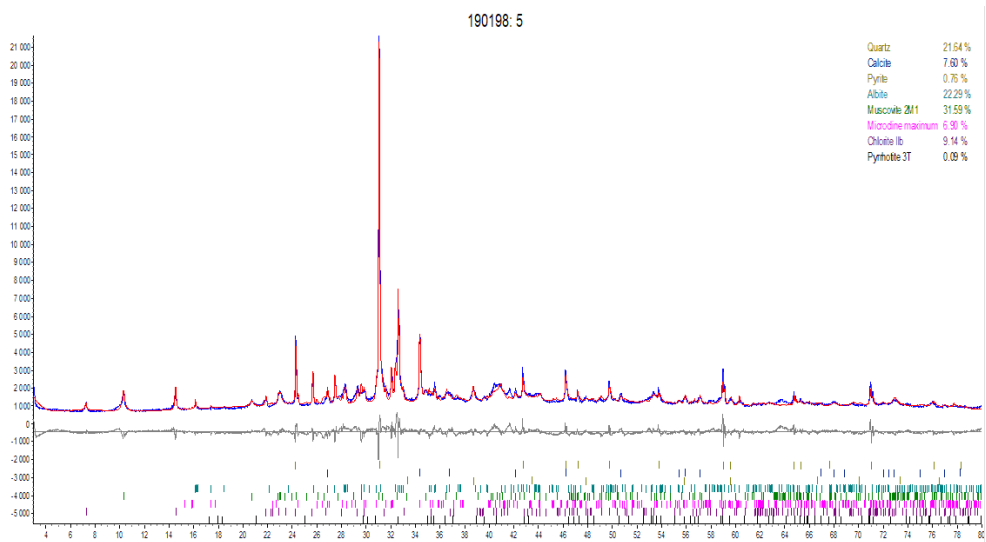


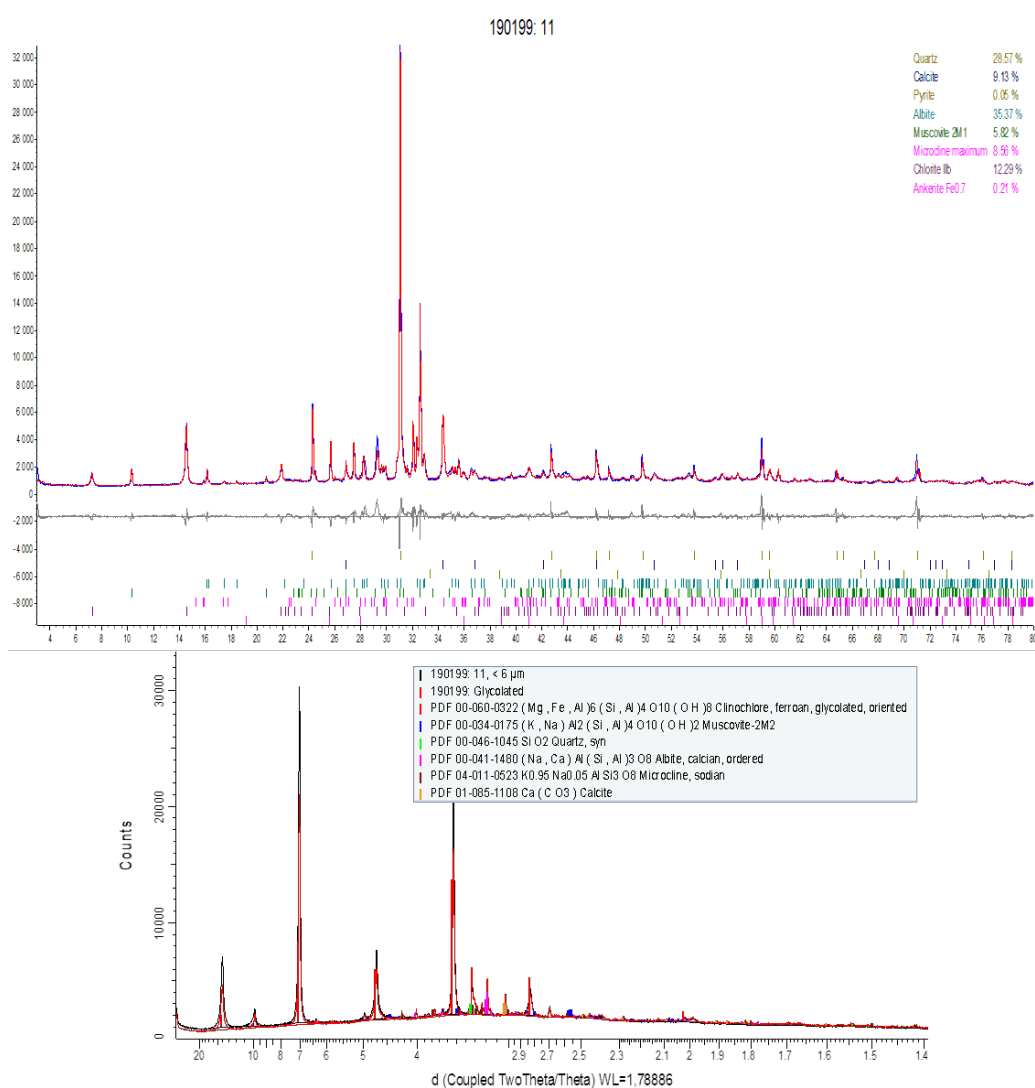
Figure 8.52: Bulk XRD diffractograms of sample 5 (siltstone) from Unit Tr3.

### **Sample 11, well 6610/7-2, 4184.65 m MD**

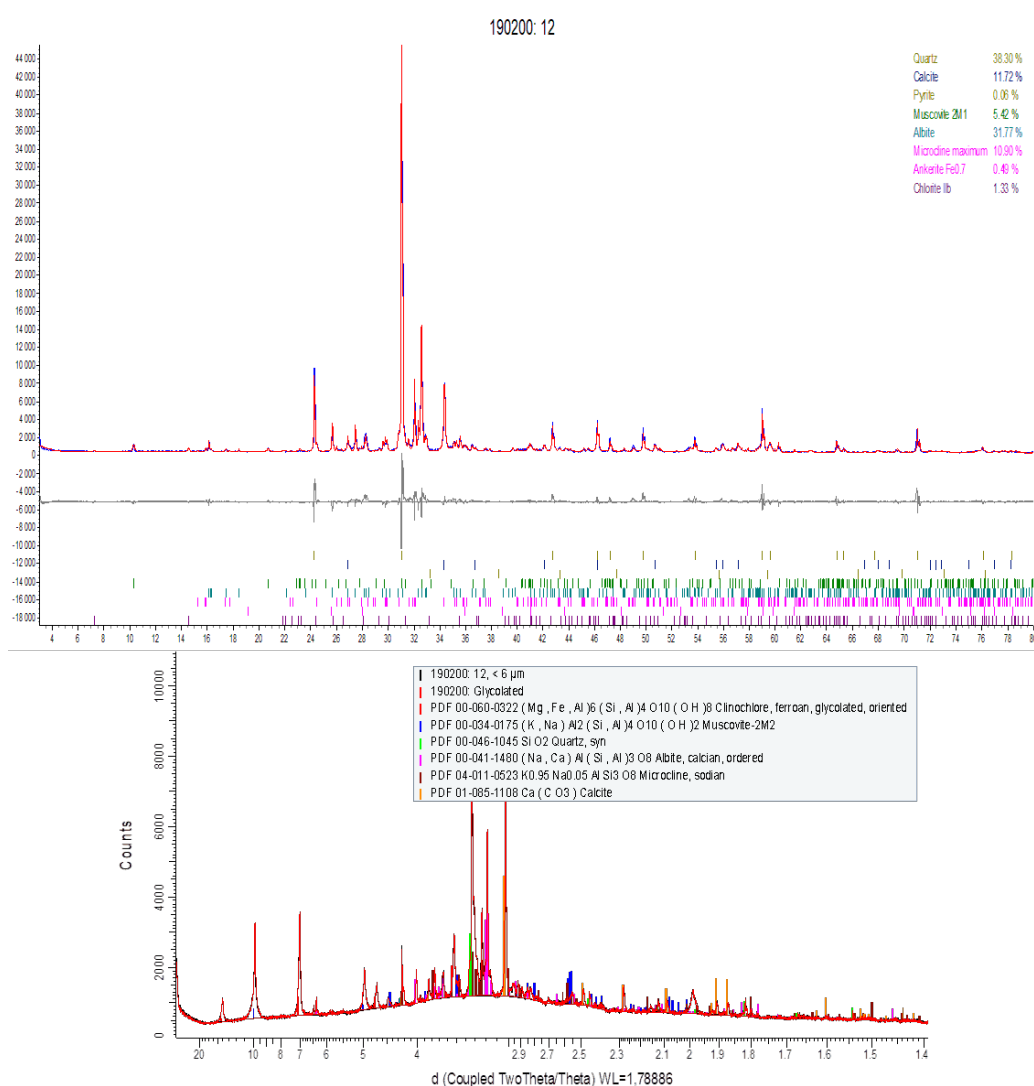
In the bulk diffractogram of sample 11, shown in Figure 8.53, eight minerals appear. Quartz makes 29% of the bulk volume, while feldspar is present by 44%. Albite is the dominating feldspar mineral. Furthermore, 9% calcite and 6% mica are present. Chlorite is the dominating clay mineral in sample 11 and occupies 12% of the bulk volume. Traces of ankerite and pyrite were also found. For the fine fraction XRD diffractogram, the glycolated and non-glycolated sample overlap perfectly. Thus, swelling clay is not present in sample 11. The d-spike at 4.73 represents clinocllore, which is a chlorite mineral.

### **Sample 12, well 6610/7-2, 4194.05 m MD**

As seen from Figure 8.54, the bulk diffractogram of sample 12 shows that quartz makes 38% of the bulk volume. Feldspars are present by 43% and albite is dominating. In addition, 12% calcite and 5% mica are found. For the clay minerals, chlorite is detectable in sample 12 by 1%. Traces of ankerite and pyrite were observed. Notice that the fine fraction diffractogram for sample 12 contains a lot of noise. This is due to high levels of quartz and feldspar in the solution. When the minerals are crushed too hard during preparation of the sample, more quartz and feldspar minerals get mixed into the fine fraction powder. This will disturb the signal of the clay minerals. For this sample, the clay minerals are still detectable and the chlorite d-spike at 4.73 confirms its presence.



**Figure 8.53:** Bulk- and fine fraction XRD diffractograms for sample 11 (arkose) from Unit Tr3.

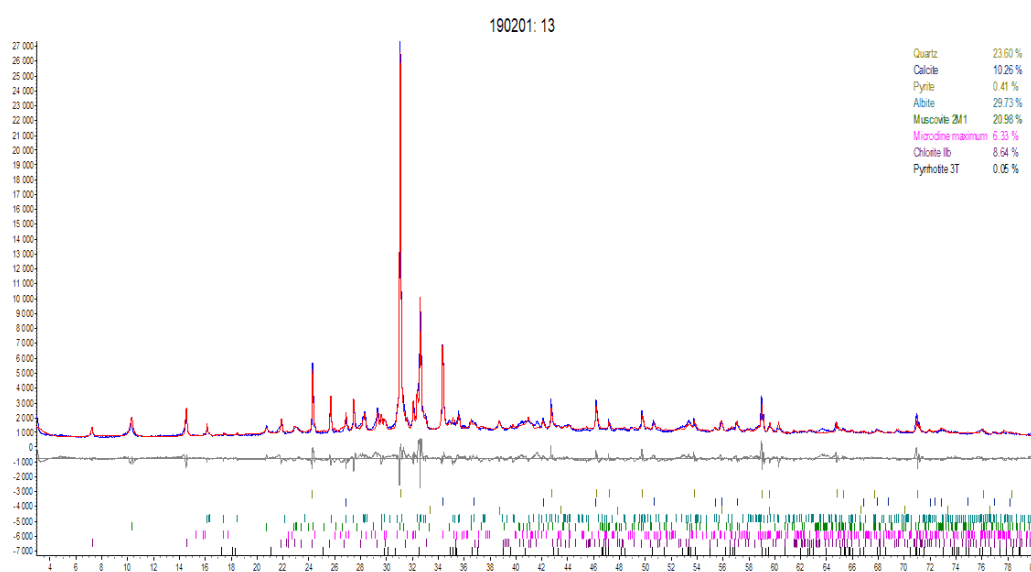


**Figure 8.54:** Bulk- and fine fraction XRD diffractograms for sample 12 (arkose) from Unit Tr3.

### Sample 13, well 6507/12-2, 4983.90 m MD

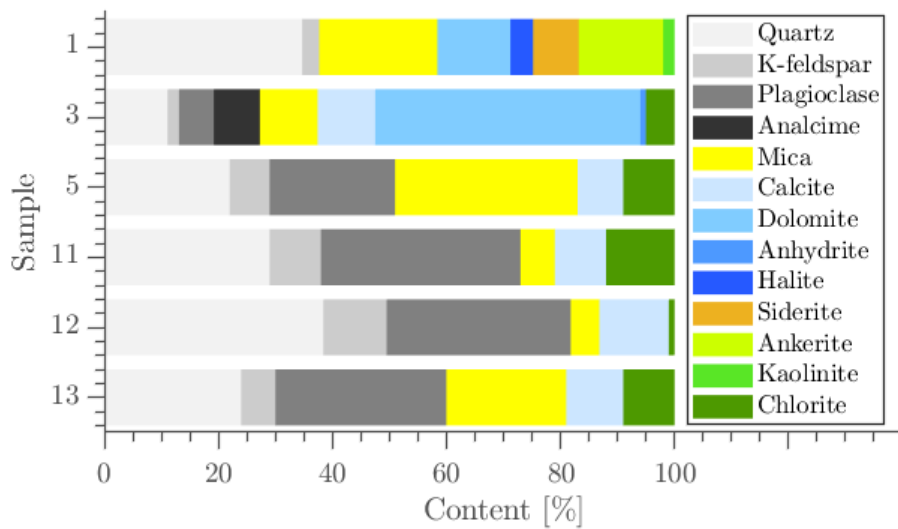
Figure 8.55 shows the bulk diffractogram of sample 13. The calculated red line overlaps with the observed sample curve. Thus, the main mineral assemblage is included and the results are reliable. Quartz makes 24% of the bulk volume, while

feldspar makes 36% and is dominated by albite. 21% of the bulk volume is made up of mica minerals. From SEM analysis it is obvious that a fair portion of this is illite. A bulk portion of 10% consists of calcite. Furthermore, chlorite is the only clay mineral present in sample 13 with a bulk portion of 9%. Finally, traces of pyrrhotite and pyrite were also observed.



**Figure 8.55:** Bulk XRD diffractograms for sample 13 (claystone) situated in Unit Tr3.

The mineral assemblage from the different samples analysed by XRD (see Appendix F, Table F.1) are visualized in Figure 8.56. The figure shows that sample 5 and 13, both from wellbore 6507/12-2, show mineralogical similarities. Of importance, the figure presents what feldspar-, evaporite- and clay-minerals that dominate the respective samples. The well name, sample number and sample depth, can be found in Table 8.3.



**Figure 8.56:** A bar plot showing the bulk XRD mineral composition from the six examined samples.



# Chapter 9

## Discussion

In this chapter, the depositional environment, diagenetic evolution and reservoir quality of the studied stratification will be discussed in the light of the results presented in Chapter 8. The first part of the discussion (Section 9.1) is assessing the depositional environment of Unit Tr3 to Unit Tr5. Then, the diagenetic evolution of the collected samples is argued in Section 9.2. Finally, the third part of Chapter 9 will highlight the reservoir quality throughout the studied wellbores in relation to porosity curves obtained from petrophysical logs. At the end of this section, the impact of compaction, mineralogical maturity and evaporites on reservoir quality is examined.

### 9.1 Depositional environment

In the process of defining the depositional environments, mainly six themes have been examined. Those are the theoretical aspects, as well as the petrophysical logs, sedimentological logs, facies association, mineralogy and petrography, and at last, the provenance of the individual depositional environments. Combing the information from these topics gives a strong indication of the depositional environments.

#### 9.1.1 Theory to be addressed

As mentioned in Section 2.2, the area between Norway and Greenland was an elongated marine basin in Triassic. As the Bremstein Fault Complex separated the uplifted Nordland Ridge from the subsiding Helgeland Basin, it is likely that a lacustrine basin was created. As further stated, seawater that entered the Greenland-Norwegian basin evaporated due to the arid climate. This is sup-

ported by the fact that continental and evaporitic deposits dominate the Middle Triassic succession, as mentioned in Section 2.2. The fluctuation of marginal marine, lacustrine, continental and evaporitic deposits indicates that the lacustrine basin was occasionally enclosed and at times open for influx from the Panthalassic Ocean.

### 9.1.2 Petrophysical logs

The log correlation baseline and correlation lines in Figure 8.1 are in accordance with existing models, among others described by Müller et al. [3]. These demonstrate that the topography on the Trøndelag Platform was dominated by a very low relief during deposition of Unit Tr3, Unit Tr4 and Unit Tr5. The exception is the Nordland Ridge, penetrated by well 6507/6-1. It was an elevated ridge surrounding the Trøndelag Platform flats to the east. Lateral thickness variations between wells may be a consequence of local tectonic uplift and erosion in addition to subsidence and deposition. The topographic variations observed may have been influenced by the extensional Bremstein-, Revfallet- and Ytreholmen (normal) Fault Complex. The orientation and dimension of these NNE-SSW trending faults generated local basins and highs in the area. As the Nordland Ridge stood out as a topographic high, it was continuously eroded. This is why the lithological succession is shortened in the location of well 6507/6-1. The erosional products from the Nordland Ridge deposited on the Trøndelag Platform, but also on the Halten and Dønna Terrace to the west.

Moreover, observing the petrophysical log correlation, the present succession of Unit Tr3 represents a thick package of claystones and sandstones, but mostly siltstones. These packages are likely to be a result of shallow to marginal marine deposits. By observing the eustatic sea-level curve in Figure 3.7, the sea level is rising throughout the Anisian-Carnian time. However, the relative sea-level curve localized in the Norwegian Sea area shows several falls in the sea level. Entering Unit Tr4, a drastic relative sea level reduction gives rise to the deposition of the Lower Salt. The Lower Salt unit is observed at Lower Unit Tr4. At this time, the influence of the Panthalassic Ocean on the Trøndelag Platform was cut off by the uplift of the Nordland Ridge. The seismic cross-section in Figure 3.6 (E-E') provides evidence of uplift of the Nordland Ridge, while Figure 2.1 indicates that the Panthalassic Ocean influences the NCS during the Triassic Period. The only influx of external water came from rainfall and rivers at times of complete enclosure. As a consequence of the arid climate, the lacustrine basin rapidly dried out. In Late Ladinian and Early Carnian times, over 500 m of Lower Salt evaporites

deposited, as observed from the salt package on the petrophysical logs in Figure 8.1. As the eustatic sea level continued to rise, seawater entered the Trøndelag Platform and influx of ocean became the dominant factor controlling the relative sea level. Shallow to marginal marine deposits influenced this stratification. The isolation of the Trøndelag Platform repeated itself twice more during Carnian times, giving fluctuations between evaporites and marginal marine deposits. This is observed from the petrophysical log in Figure 8.1, showing deposition of two more salt packages in Middle and Upper Unit Tr4. During the local regressions, deposition and preservation of evaporites on the Nordland Ridge was minimal. During transgressions, the Nordland Ridge stood up as an elongated island and was therefore exposed to erosion. The vertical thickness of Unit Tr4 at the Nordland Ridge is less than one third of the succession on the Trøndelag Platform. During Unit Tr5, the eustatic sea level reached its highest before it dropped during the Late Norian and Rhaetian times. The relative curve follows the eustatic, suggesting influence of ocean seawater on the Trøndelag Platform. As indicated by Figure 8.1, the erosion of the uplifted Nordland Ridge and deposition in the surrounding basins continued during Late Triassic times, as the stratigraphy of Unit Tr5 still is reduced.

### 9.1.3 Sedimentological logs

Figure 8.16 shows the graphically logged sections, their respective wells, age and depositional environment. Samples 3 and 4 are both situated in well 6507/12-1 from Norian times. The cored section shows thick packages of claystones inter-layered by meter thick packages of sandstones fining upward to siltstones. Additionally, thin layers of limestone occur. The sandy-silty units show an energy decrease moving upwards. This is indicated by a transition from current ripples at the lower part, to horizontal lamination at the upper part of the individual units. This is typical for fluvial deposits.

Fossil fragments of ooids, clams and ostracods are detected in sample 3. The occurrence of ooid and ostracod may suggest a shallow marine environment. Ostracods were tolerant organisms, and survived in many different environments. Their presence can therefore not be used as an indicator for the depositional environment. The exception is the case where only Ostracods, and no other fossils, can be found. This is an evidence of a rough environment, such as lagoons with high salinity or tidal flats.

Besides the mentioned layering structure and presence of fossils, rootlets and desiccation cracks were also observed. This suggests a continental setting of tidal

flats and a semi-arid climate, which is supported by Müller et al., 2005 [3]. In addition, flaser bedding and synaeresis cracks were detected at the upper part of the cored section. Flaser bedding is created during intermittent flows, where the sand ripples are infilled by mud at quieter flow periods. Syneeresis cracks, on the other hand, form by contraction of clay in response to a change of the water salinity. The observed syneeresis cracks are filled with white evaporite or calcite deposits. As several limestone beds can be observed in the cored section, limestone is most likely filling in the syneeresis cracks. The change of water salinity effecting the playa lake of Unit Tr5, may be explained by erosion and influx of the Upper Salt formation. Thus, the sedimentological investigations also indicate that the Triassic environment is most likely fluctuating between a shallow marine and an exposed arid setting.

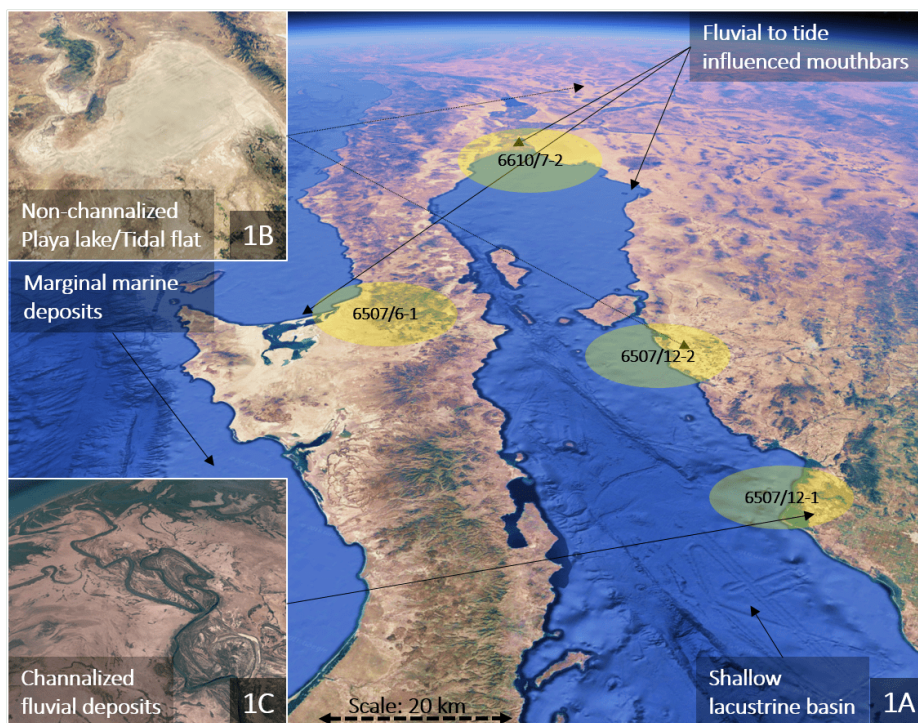
For well 6507/12-1 at Unit Tr5, the depositional environment is most probably a playa lake dominated by channelized fluvial deposits. The environment is highly influenced by the shallow basin with elevated salt values due to the restricted influence of the Panthalassic Ocean. In 1C of Figure 9.1, a visualization of the suggested depositional environment is shown. The figure is based on a Google Earth map view at the northwest coast of Mexico, which is located in the arid climate zone. It should be noticed that the shallow lacustrine basin in the Norwegian Sea was nearly completely evaporated during Late Ladinian, Early- and Late Carnian.

In the cored section of 6507/12-2 representing Unit Tr3, syneeresis cracks were not observed. This is explained by the absence of a salt-rich source to produce fluctuations in the water salinity. During deposition of Unit Tr3, the salt layers in Unit Tr4 were not yet created. Furthermore, the water salinity was stable and low due to the impact from the Panthalassic Ocean. Thick packages of claystones with light calcite nodules dominate the succession. Few structures were observed, meaning that the energy level of the depositional environment is lower than for that observed in Unit Tr5. As the topography is still flat, the depositional environment is interpreted to be a playa lake not influenced by channelized fluvial deposits, as illustrated in 1B of Figure 9.1.

The cored section of well 6610/7-2 of Anisian age shows packages of blocky to upward fining sandstone sequences interlayered with thin claystones. The energy of the system is high, indicated by the sedimentary structures like wavy bedding, current ripples, low- and high-angle cross bedding and herringbone deposition. Boring marks also influence Unit Tr3 sandstones in the northern part of the Trøndelag Platform. Furthermore, coaly fragments occur occasionally. Thus, the depositional environment is likely based in a fluvial and tide influenced mouth-

bars to marginal marine setting. The northern part of Figure 9.1 (1A) shows a proposed positioning of the cored section of well 6610/7-2, marked in yellow.

In contrast to the three mentioned wells from the Trøndelag Platform and the Ellingråsa Graben, well 6507/6-1 is drilled through the Nordland Ridge. The cored section shows an upward fining sandstone unit at the lower half influenced by current ripples, high angle cross-bedding, horizontal lamination and low angle cross-bedding. This indicates that the depositional environment is dominated by fluvial to tide influenced mouth bars or a marginal marine depositional setting. The upper half, however, is dominated by breccia interfilled with sand, silt and clay, suggesting that Unit Tr3 in well 6507/6-1 is situated in a fault zone. From the relative location of the wellbore in Figure 8.2, it is reasonable that this fault zone is related to the Bremstein Fault Complex.



**Figure 9.1:** Proposed depositional environment of described wells during the Triassic Period.

This is the normal fault complex that causes uplift of the Nordland Ridge and subsidence of the Trøndelag Platform, as illustrated by the seismic line stratig-

raphy in Figure 3.6, cross section E-E'. In Figure 9.1 (1A), an elevated, mostly continental, depositional environment for Unit Tr3 in well 6507/6-1 is suggested.

#### 9.1.4 Facies association

FA3 dominates the cored section in well 6507/12-1, which indicates a shallow lacustrine basin to a playa lake type of depositional environment. The physical appearance of the grains are shifting between the red to brown matrix facies and the green matrix facies. This indicates shifts in the exposure of the sediments. The red to brown facies suggests an environment exposed to oxidization, while the green facies suggests a less exposed and more reducing environment. These findings strengthens the theory of the depositional setting suggested in Section 9.1.3. It can also be argued that the facies shift may represent a local shift of climate, varying between a dry arid and a semi-humid continental setting. For the cored interval of well 6507/12-2, FA1 dominates. From Section 8.3.2, FA1 is described as a non-channelized fluvial or playa lake depositional environment. The physical appearance of the grains shifts between light gray and red to brown matrix facies. The light gray matrix facies reacts in contact with acid, thus contains carbonate minerals. The red to brown matrix facies is found in the finer materials. FA1 in 6507/12-2 lacks some of the high energy structures observed in FA3, and is interpreted to exist in a system of lower energy. In addition, only one sandstone unit is present between the mudstones, which also suggests that the energy of the depositional setting is low. The main part of the cored section of well 6610/7-2 is dominated by FA4, which points towards a marginal marine to fluvial and tide influenced mouth bar depositional environment. The physical appearance of the sediments lacks the red to brown matrix facies and suggests a more marine dominated setting. The upper part of the core shows a transition to FA1 and may signify a local sea level fall. While FA2 dominated core 4 of well 6507/6-1, FA4 dominates core 3. Thus, the depositional setting reflected in well 6507/6-1 shows similarities to core 2 of well 6610/7-2.

#### 9.1.5 Mineralogy and petrography

During the study of quartz cement using optical microscopy of sample 4, dust rims were found at the border between the detrital grain and the authigenic cement. The dust rim is typical for dry environments where small clay particles attach themselves to sand grains. From Figure 8.28, it is obvious that the dust rim is made of carbonate minerals due to the high interference colors. Carbonate might

be the original detrital clay sized mineral. Another option is that during later diagenesis, the original siliciclastic clay dust rim has recrystallised to form authigenic carbonate minerals. Furthermore, this suggests that the supra-salt sample 4 was deposited in a continental setting. The molluscs discovered in sample 4 and described in Section 9.1.3 were discovered during optical thin section analysis. This finding indicates that the depositional environment was rough and that the salinity of the water was high. Several minerals observed during microscopy, SEM and XRD analysis supports this hypothesis. Anhydrite was discovered in samples 3 and 4 in wellbore 6507/12-1, supra-salt in Unit Tr5. Halite was found in sample 1, in wellbore 6507/6-1, sub-salt in Lower Unit Tr3. In addition, small amounts of intragranular perchlorate minerals were observed in sample 12 at wellbore 6610/7-2, sub-salt in Unit Tr3. The perchlorate mineral was identified with SEM, but was not detected during the XRD analysis. There might be several conceivable reasons, and some of them are mentioned below.

- ◇ The bulk amount of perchlorate minerals was much less than 1%,
- ◇ Overlapping d-value- or  $2\theta$ -peaks can make different minerals indistinguishable,
- ◇ The salt mineral was dissolved during micronization,
- ◇ An incorrect perchlorate mineral was suggested during the interpretation. This is possible, as the database contains about 700 variations of perchlorate.

In conclusion, the findings of evaporitic minerals throughout the Triassic succession, not only in Unit Tr4, but also in Unit Tr3 and Unit Tr5, give the impression of an inhospitable environment with elevated salt values in the nearby water and a warm and dry arid climate on the continent. However, the important question to answer is whether or not all of these evaporitic minerals are in-situ authigenic, or transported from the salt units in Unit Tr4. This question will be discussed in Section 9.2.

### 9.1.6 Provenance

As mentioned in Section 3.5, red deposits of Middle and Late Triassic share the informal name Red Beds. The color of these deposits may suggest that the sediments were exposed to oxidation causing the creation of red colored hematite, or that the provenance of the sediments was oxidized. Likewise, the informal name

Grey Beds is used for the Upper Unit Tr5 gray colored sandstones. The same reasoning suggests that these beds originate from a reduced environment or from provenance of gray sandstones. It can also be argued that the facies shift from the Red Beds to the Grey Beds symbolizes a shift from an arid climate, through a semi-arid setting, entering a semi-humid climate. To the east of the elongated basin, the former mountain chain was eroded down to continental plains in Triassic. For the Triassic succession on the Trøndelag Platform, the provenance is most likely from the European side of the basin between Greenland and Europe, as the Nordland Ridge acted as a barrier for provenance from Greenland. In addition, the uplifted Nordland Ridge was continuously being eroded, depositing its sediments on both sides of the ridge. Müller et al. suggest that platform carbonates were present on the Nordland Ridge during Triassic [3]. The findings of carbonate rocks, anhydrites and fossil fragments in some of the wells supports that the Nordland Ridge was a source of sediments for the Trøndelag Platform. Therefore, the provenance of the Trøndelag Platform is most likely a combination of sediments from the Nordland Ridge to the west and from the European continental plains in the east.

## 9.2 Diagenetic history

In this section, the diagenetic evolution of wellbore 6610/7-2, 6507/6-1, 6507/12-2 and 6507/12-1 are investigated in terms of the findings from sample 1, 3, 4, 5, 11, 12 and 13. The porosity and mineral assemblage of the samples in relation to their respective depth and temperature are used to generate the diagenetic history.

### 9.2.1 Feldspar

As mentioned in Section 4.1.1, dissolution and kaolinization of framework feldspar are eogenetic processes controlled by the presence of meteoric water and feldspar. The reactions may result in minor improvements to the reservoir porosity and permeability as they may create intragranular and moldic pores. As known from Section 4.1.2, K-feldspar dissolution, producing quartz arenites, occurs extensively at 2.5 km depth below the sea floor, at temperatures greater than 70°C. The plagioclase content, mainly dominated by albite, is 22% and 30% for sample 5 and 13, respectively. Albitization of Ca-rich plagioclase provides  $\text{Ca}^{2+}$  and  $\text{Al}^{3+}$  to the solution, and makes it prone to carbonate cementation and precipitation of clay minerals. The albitization of K-feldspars observed in samples 1, 5 and 13,



enhance illite formation by supplying  $K^+$  to the solution. This reaction reduces permeability and porosity of the reservoir, as observed in numerous images from Chapter 8. Even though dissolution of feldspar may create secondary porosity, precipitation of cement and neof ormation of clay minerals deteriorates the reservoir quality for the studied samples. Grain coating clay may also restrict further dissolution of feldspars preventing generation to quartz arenites. This process was very distinct for sample 1, 5 and 13.

### 9.2.2 Clay minerals

#### Smectite

Smectite is common at shallow depths and was observed in sample 3 (well 6507/12-1) during fine fraction XRD analysis. The mineral typically form during eogenesis in presence of meteoric water saturated by sodium and calcium cations. From the geothermal gradient in Figure 8.23, the temperature at depths of 3460 m below the sea floor is  $\sim 130^\circ\text{C}$ . At this temperature, most of the smectite minerals are replaced by kaolinite, illite or chlorite. Smectite transforms into illite above  $100^\circ\text{C}$  and leads to 30% volume reduction due to expulsion of ionized water. The absence of illite and kaolinite in sample 3 suggests that the smectite is replaced by chlorite or that the transformation has stepwise (through kaolinite or illite) transformed smectite to chlorite. According to Weaver, smectite is abundant in warm climatic zones at low rainfall levels, which promotes the theory of an arid to semi-arid climate during Triassic [50].

#### Kaolinite

Section 4.1.1 shows that kaolinite can be formed by chemical reactions involving feldspar, muscovite and biotite. The stacked booklet shape of kaolinite observed during optical microscopy, SEM and in Figure 5.4 argues in the direction of an authigenic origin of the mineral. Kaolinite is a dispersed clay type which is pore filling and was observed in sample 1 (well 6507/6-1) at a depth of 2600 m below the sea floor. The geothermal gradient for well 6507/6-1 indicates a temperature of  $\sim 90^\circ\text{C}$  at this depth. If kaolinite is allowed to grow in open space, the mineral will form hexagonal shapes. As observed from Figures 8.38 and 8.39, the hexagonal shape is not totally preserved. This may indicate that the pore space available for kaolinite growth was restricted or that replacement of kaolinite has taken place. The prominent porosity of sample 1 is 12%, and as kaolinite tend to form prior to

illite, the presence of illite signifies that illite is replacing kaolinite. Additionally, the production of illite from the reaction of K-feldspar and kaolinite takes place at temperatures greater than 70°C [10]. Furthermore, the presence of feldspar is less than 4%, while mica makes about 20% of the bulk mineral assemblage. Most of the present feldspar was of category IV or V, thus heavily weathered and sericitized. This implies that feldspar is a source for production of kaolinite, but that the main source is more likely to be mica minerals.

## Illite

The properties of the most common clay type, illite, can be found in Section 4.1.2. The mineral was discovered in sample 1 at a depth of 2600 m, but also in sample 5 and 13 at a depth of about 4700 m below the sea floor. The calculated temperatures were 90°C and 152°C for the samples from well 6507/6-1 and 6507/12-2, respectively. For sample 1, the illite replaces kaolinite and causes a porosity reduction, while the illite is being replaced by chlorite in sample 5 and 13 due to the increased temperature. Illite can be observed in the SEM photographs in Figures 8.38, 8.39, 8.42, 8.43 and 8.49, and the pore bridging structure can be recognized in Figure 5.4. Illite forms by transformation of smectite or kaolinite and may be a component of sericite. The exact bulk volume of illite cannot be quantified from SEM or XRD analysis, but a qualified estimation can be acquired from the results. When performing XRD analysis, the illite mineral falls within the mica group. The highest amount of mica in the other samples where illite was not found, was 10%. Subtracting 10% from the mica group for the illite containing samples, a rough estimate of the amount of illite present is obtained. This gives a bulk illite content of 11% for sample 1, 22% of sample 5 and 11% for sample 13. The illite observed in sample 1 is pore bridging and fills the pore space between the kaolinite grains. The minerals bend around the kaolinite grains, suggesting that the illite mineral is of a younger authigenic age compared to kaolinite. In sample 5 and 13, kaolinite is absent, and has been completely replaced by illite. For these samples, it can be observed that the chlorite minerals form elongated grains that bend around illite grains. This interaction can be observed in Figure 8.49. It indicates that the illite minerals have grown prior to the younger chlorite grains. The illite minerals are most likely being replaced by the authigenic chlorite minerals.

## Chlorite

As observed from the clay structures in Figure 5.4, chlorite is a dispersed clay type often forming pore lining structures in the pore space. Chlorite was observed in various amounts in sample 3 (5%), 5 (9%), 11 (12%), 12 (1%) and 13 (9%), but was not observed in sample 1 at a temperature of about 90°C. Sample 11 and 12 are both from the same well and depth, but differs in chlorite content. This is a result of the facies variation, which can be observed from the sample cuts in Figure 8.17. Sample 11 is categorized as green matrix facies, while sample 12 is categorized as light gray matrix facies. Furthermore, from the SEM photographs of Figure 8.44 and Figure 8.39, the structural appearance of chlorite can be investigated. Near the grain boarder of detrital grains, the chlorite mineral particles are smaller compared to chlorite particles closer to the center of the pore space. Two different textures of chlorite were observed. The first texture appears as needle shaped, with elongated grains that show a tendency of pore bridging. In addition, micro porosity is present. This texture shows similarities to the illite texture. The second texture appears as a carpet of fine grained minerals filling the pore space. Therefore, this texture has low values of micro porosity. Some illite was present in this texture, detected as lighter material indicated by a darker color on SEM. A border between these two textures can be observed at the center of Figure 8.44. The elongated minerals in the first texture bend in relation to the texture border. The findings may suggest that the first texture is younger than the second texture and that illite is being replaced by chlorite in the second texture. The controlling parameters of chlorite growth is the availability of smectite, illite and kaolinite. In systems low in potassium, transformation of kaolinite to chlorite happens directly at the expense of the kaolinite-illite-chlorite transformation. This occurs at temperatures of about 165-200°C [10]. In sample 5, the authigenic chlorite also transforms from illite, while the transformation of smectite to chlorite most likely occurs in sample 3. Chlorite is stable at high temperatures and preserves reservoir quality through preventing cementation. In addition, chlorite crystals are smaller than crystals of illite and causes less severe occlusion of pores in coarse grained sandstones. Nevertheless, in reservoirs of low grain size, extensive chlorite mineral growth may destroy the reservoir quality in terms of porosity and permeability reduction. This is applicable for sample 11, as shown from the porosity and mineral assemblage overview in Figure 8.37. From optical microscopy, detrital chlorite grains were found in sample 10, 11, 12 and 14 (about 1-3%). Some of the authigenic chlorite may have been derived from recrystallization of these detrital grains.

### 9.2.3 Authigenic cements and evaporite minerals

#### Anhydrite

As stated in Section 2.2, gypsum is commonly formed by slow evaporation of water with high calcium and sulphate levels. Dependent on pressure and salinity, gypsum dehydrates to anhydrite in the temperature range of 50-120°C [10]. Anhydrite is present in sample 3 and 4 from well 6507/12-1 of Norian age (Unit Tr5). In addition, a detrital anhydrite grain was observed in Figure 8.36 (2B), representing sample 12. As the temperature has reached ~130°C, all the gypsum minerals are dehydrated and replaced by anhydrite. The chemical bonds to H<sub>2</sub>O in the gypsum structure are broken due to the increased temperature 3700 meters below the sea floor. In Figure 8.28 (2A and 2B) from optical microscopy, the anhydrite fills the entire intergranular pore space in sample 4. Thus, there is no porosity in the sample. From the SEM analysis of sample 3, illustrated by Figure 8.41, the anhydrite is occupying both the large and small intergranular pore space, thus reducing the porosity. The anhydrite mineral appears as an authigenic cement as it forms around the detrital grains. The mineral may have been transported as mass solute transfer from the Upper Salt in Unit Tr4 and reprecipitated in Lower Unit Tr5. This hypothesis assumes that Unit Tr4 is present beneath Unit Tr5 for well 6507/12-1 (e.g. Unit Tr5 is supra-salt) and that during the mass solute transfer, permeability values were still high in Unit Tr5. The transfer of dissolved species such as SO<sub>4</sub><sup>2-</sup>, Ca<sup>2+</sup> and HCO<sub>3</sub><sup>-</sup> from low permeable zones in Unit Tr4 to high permeable zones of Unit Tr5 may have caused precipitation of CaSO<sub>4</sub> (anhydrite). In addition, dolomite and calcite are present in samples 3 and 4. When the mass solute transfer of SO<sub>4</sub><sup>2-</sup> species enters a reservoir that contains carbonates, anhydrite cementation is likely to occur. On the other hand, the occurrence of anhydrite in the pore space could simply be a result of replacement of in situ gypsum minerals. As gypsum have not been discovered in this study, it is difficult to conclude whether the present anhydrite is a result of mass solute transfer or in situ replacement of gypsum. If gypsum was identified, it would have been possible to determine the latter based on how the gypsum deposits in relation to other grains.

#### Salt

Halite (NaCl) is the most common type of salt and was detected in sample 1 at Lower Unit Tr3 by bulk XRD analysis. This is the same salt mineral as observed in

the Lower and Upper Salt formations in Unit Tr4. However, the raising question is how halite has precipitated here, 1000 m below Lower Salt, as observed from the petrophysical logs in Figure 8.1. As the salt layers in Unit Tr4 was not yet created during deposition of sample 1 in Unit Tr5, it is likely that the present halite is a result of later mass solute transfer from the salt formation in Unit Tr4. Having a closer look at the surrounding lithology of sample 1 at the petrophysical log in Figure 8.6, it is clear that the frequent appearance of impermeable limestone beds make the mass solute transfer from the above salt in Unit Tr4 less likely. Two other possible scenarios can explain the presence of salt in sample 1. Scenario 1 assumes that the mass solute transfer of halite from the above salt formation occurred before calcite cementation. Scenario 2, on the other hand, is built upon a theory of a lateral mass solute transfer along the permeable zones from the Trøndelag Platform. This hypothesis is derived by the investigation of Figure 8.1. Well 6507/6-1 is positioned on the Nordland Ridge, which have been uplifted relative to the Trøndelag Platform in the east. The transfer of mass solute salt from the subsiding Trøndelag Platform to the uplifted Nordland Ridge may have been increased by leaching, permeable faults from the Bremstein Fault Complex.

Perchlorate salt,  $\text{ClO}_4^-$ , is identified in sample 12 at Unit Tr3 during SEM analysis. Figure 8.47 shows the SEM image of sample 12 where the salt was observed. The related EDS spectra can be found in Appendix E, Figure E.12. As mentioned in Section 9.1.5, the perchlorate salt mineral was not detected in the XRD results. The salt mineral appears as an intragranular replacement mineral in feldspar minerals, both in highly weathered K-feldspars and in albites. On SEM images, the salt mineral appears with a darker color than the host feldspar grain. Thus, the feldspar grain is denser than the salt. It should be noticed that the salt minerals are not observed intergranularly, and are therefore not occupying any of the intergranular porosity. It may be claimed that the authigenic perchlorate salt observed sub-salt is not reducing the reservoir quality.

### Calcite, dolomite and ankerite cement

From point counting during optical microscopy, calcite cement was found in sample 1, 4, 10, 11, 12 and 14. From bulk XRD analysis, it was found that calcite makes about 10% of the bulk volume in sample 3, 5, 11, 12 and 13, but was not detected in sample 1 at a temperature of  $\sim 90^\circ\text{C}$ . Figures 8.56 and 8.37 are bar plots generated from XRD and point counting analysis, showing the calcite composition for the samples. Instead, a bulk volume of 13% dolomite ( $\text{CaMg}(\text{CO}_3)_2$ ), as well as siderite ( $\text{FeCO}_3$ ) and ankerite ( $\text{Ca}(\text{Fe},\text{Mg},\text{Mn})(\text{CO}_3)_2$ ) were prominent in sam-

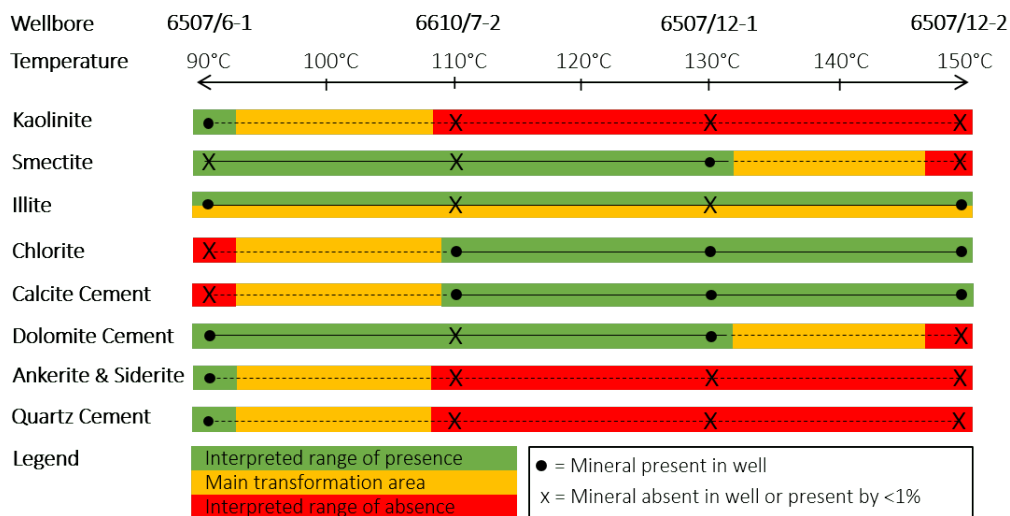
ple 1. Mesogenetic carbonate cementation starts at temperatures of  $\sim 100^{\circ}\text{C}$  [10]. Having determined calcite cement at temperatures of  $\sim 110^{\circ}\text{C}$ , but not at  $\sim 90^{\circ}\text{C}$ , it can be argued that production of authigenic calcite cementation occurs in the interval of 90 to  $110^{\circ}\text{C}$ . Cementation by calcite, dolomite and siderite is promoted by a semi-arid climate in fluvial sandstones and controlled by the availability of carbonate grains [9]. The cementation destroys porosity and permeability of the reservoir by precipitation in the available pore space. Dolomite was observed at temperatures of  $130^{\circ}\text{C}$ , at the highest. 46% dolomite was observed in sample 3 during XRD analysis. From optical microscopy on sample 4, 35% micrite matrix was discovered. As both samples originate from the same layer in the same well, it is likely that the micrite matrix observed in sample 4 is made of dolomite. Likewise, it is reasonable that the observed dolomite in sample 3 is structurally precipitated as micrite and sparite matrix. This can be observed in PPL and XPL by the bright and brown matrix colors in Figure 8.27 and 8.28. Furthermore, as mentioned in Section 4.1.2, mass solute transfer of aqueous fluids from mudstones rich in iron, magnesium, manganese and calcium are responsible for the growth of ankerite and siderite in sandstones. The latter mass solute transfer is therefore applicable for sample 1, rich in ankerite and siderite minerals.

### Quartz cement

As mentioned in Section 4.1.2, quartz cementation occurs in the temperature range of  $80\text{-}100^{\circ}\text{C}$ . Furthermore, the same section states that quartz cementation and pressure dissolution of quartz grains is controlled by availability of monocrySTALLINE quartz or illite coatings. In terms of reservoir impact, quartz cement causes deterioration of porosity and permeability. However, quartz cement was present at very low quantities in the analyzed samples. The largest amounts of quartz cement were found in sample 1, measured to represent 1% of the total volume. Figure 8.26 shows the optical microscopy images of sample 1 where the quartz cement can be observed. Occasionally, quartz cementation was also observed in sample 4 with the presence of dust rims. The fact that quartz cementation values are low in the studied samples could possibly be due to the occurrence of illite coatings, as availability of monocrySTALLINE quartz is not the limiting factor. Coating illite is observed at temperatures as low as  $90^{\circ}\text{C}$ .

### 9.2.4 Visualization of the diagenetic history

Figure 9.2 shows what minerals are present in the different wells and the given temperature at the sample locations. As the considered samples in this study are not from the same well, Figure 9.2 does not necessarily give a fully representative picture, but rather an indication of the diagenetic evolution. To get a better model for the diagenetic evolution, samples from the same well at different depth should have been collected and studied, as the diagenetic evolution may vary across the different wells. Based on the sample locations and temperatures of the different wells, in addition to the discussion from Section 9.2.1 to Section 9.2.3, an interpretation of the diagenetic evolution for the minerals was carried out. For well 6507/6-1 at 90°C, kaolinite is present and is transforming into illite. Moreover, the illite coating restricts massive quartz cementation. Furthermore, mass solute transfer causes precipitation of halite, followed by cementation of ankerite, siderite and dolomite cement. For well 6610/7-2 at 110°C, chlorite has transformed from either kaolinite, smectite or illite. Precipitation of calcite cement most certainly starts at a temperature range of 95-105°C. Moreover, intragranular feldspar replacement by perchlorate salt minerals may be a response to a change in salt content of the encircling fluids.



**Figure 9.2:** Interpretation showing diagenetic stable intervals, diagenetic unstable intervals and intervals of absence for the respective minerals listed to the left, in terms of temperature in the respective wellbores.

In well 6507/12-1 at 130°C, smectite is probably transforming into chlorite due to the absence of illite. Smectite is not observed in well 6507/6-1 or 6610/7-2, but is likely to be present at shallower depths in well 6507/12-1. Furthermore, mass solute transfer from Unit Tr4 causes cementation of anhydrite. In addition, calcite and dolomite cement have precipitated in the remaining pore space. Increasing the depth in well 6507/12-2 at a temperature of ~150°C, illite is being replaced by chlorite, which is stable at high temperatures. Finally, calcite cement, presumably precipitated in the interval of 95-105°C, occupies the remaining pore space.

## 9.3 Reservoir quality

As mentioned in Section 5.3, the reservoir quality is defined by its effective storage capacity (porosity) and deliverability (permeability). In this section, the reservoir quality of the Triassic succession in wellbore 6507/6-1, 6610/7-2, 6507/12-1 and 6507/12-2 will be discussed. The clay and evaporite mineral assemblage as well as porosity values from the studied samples will be in focus. At what depth, regarding the diagenetic evolution, will the intergranular volume give reasonable porosity values? And do the authigenic salt and anhydrite minerals affect the IGV? These are some of the questions that will be discussed in the following section.

### 9.3.1 Porosity

As mentioned in Section 5.2, a rule of thumb for porosity loss during burial is that 1% of the porosity is lost per 100 meter of burial. This rule is incorporated in Figure 8.7 by a red dashed line. The density porosity log in Figure 8.10 clearly indicates that reality is much more complicated, and that porosity with burial greatly depends on lithology. Sample 10, 11, 12 and 14 are sampled from cores ranging in depth from 4180 to 4194 m. At this depth, the log porosity is approximately 5-13%, while the porosity found from point counting was 0-11%. Variation in intergranular calcite cementation volume, which in this case is ranging from 10 to 20%, may cause the porosity fluctuation. In areas of high calcite cementation rates,  $\rho_b$  will be higher than for areas of low cementation rates. Thus, high cementation rates will reduce  $\phi_{log}$  more than zones of low cementation rates. High  $\phi_{log}$  values will therefore indicate areas of less cementation. As mentioned in Section 5.3, porosity values higher than 15% are preferred for high quality reservoir zones. As observed from the density porosity curve in Figure 8.10 for well 6610/7-2, a 10



meter thick reservoir zone of about 25% porosity is observed sub-salt, at a depth range of 3490-3500 m. The distance from the Lower Salt formation is only 40 m, and the reservoir quality is most likely preserved. This may indicate that the reservoir potential is present also in Unit Tr3, with the salt package acting as a cap rock for a potential petroleum play. One would have to search 1000 meters shallower to find the next prominent reservoir zone, supra-salt at Lower Unit Tr5. Here, a 50 meter thick sandstone package of about 20% porosity is identified. Throughout the rest of Unit Tr5, from a depth of about 2300 m, porosity seems to be reasonable in terms of the reservoir potential. Unfortunately, no clean sandstone zones can be identified looking at the lithology interpretation. Thus, one would have to evaluate the risk of producing from a shaly-sand reservoir zone.

From point counting of sample 1 (3045 m depth), a porosity of 12% is demonstrated. Looking at the density porosity log of well 6507/6-1 in Figure 8.9, the porosity is about 12% for the same depth. During optical microscopy, SEM and XRD, it is obvious that the reservoir potential for this zone is reduced by cementation of dolomite, ankerite and siderite, but also by authigenic kaolinite growth. As seen from the well log in Figure 8.9, the deeper reservoir zones are even more affected by the diagenetic effects. One would therefore have to investigate zones of shallower depth for reservoir potential. A siltstone package with interbedded sandstones can be observed with porosity values of about 15% at the depth of 2020-2160 m. This is most likely the zone located on the Nordland Ridge with the most promising reservoir quality in terms of porosity. Surprisingly, this interval is also situated in Upper Unit Tr3 with a potential seal from anhydrite of Lower Unit Tr4.

Shifting over to wellbore 6507/12-2 at Ellingråsa Graben, the siltstones of samples 5 and 13 at a depth of 4983 m, do not show promising porosity values from Figure 8.7. The highest porosity of Unit Tr3 is ~7% in a sandstone zone 60 m below Unit Tr4. The reservoir is therefore of low quality, likely caused by calcite cementation and authigenic chlorite. At shallower depths, several high porosity reservoir zones are identified. The most interesting reservoir units are observed at depths of 3340-3355 m, 3000-3030 m, 2700-2720 m, 2100-2165 m and 1925-1980 m. The porosity range between 20 and 30% for these zones. The first of the mentioned reservoir zones is located in a claystone. Frequent calcite beds surrounds the zone and may indicate that calcite cementation affects the reservoir quality. The same applies throughout the rest of the reservoir. Thin layers of calcite, observed as peaks towards lower porosity, reduces the vertical permeability of the sandstone reservoirs. Nevertheless, as porosity is high above depths of 3100 m (Upper Unit Tr5), cementation and authigenic clay minerals may not deteriorate the reservoirs

above this depth. Therefore, in terms of porosity and diagenetic evolution, the reservoir quality is possibly reasonable in sandstone zones above 3100 m depth. Additionally, the red dashed line showing the porosity rule of thumb, illustrates the compactional effect that sandstone intervals sustain porosity far better than the siltstones, shales and claystones during burial.

The density porosity curve of wellbore 6507/12-1 can be observed in Figure 8.8. From thin section analysis, samples 3 and 4 at a depth of about 3715 m do not show promising porosity in terms of reservoir characteristics. The petrophysical log confirms a low porosity of about 3% at this depth. Dolomite and chlorite deteriorates the intergranular volume for this well at Lower Unit Tr5. As for well 6507/12-2, the porosity is significantly higher at depths shallower than 3100 m. The sandstones at 2970-2980 and 2920-2940 are the most promising reservoirs of Unit Tr5, with a porosity of around 20-25%.

### 9.3.2 Compaction, mineralogical maturity and evaporites

Evidence of compaction can be observed in terms of undulose quartz grains and broken mica minerals (e.g. in Figure 8.26, Figure 8.33 2A and 2B and Figure 8.36 4A and 4B). Another piece of evidence is the stylolite observed in Figure 8.34 (row 3 and 4). Moreover, pressure dissolution can be observed along the molluscs in Figure 8.29. In addition, the grain orientation observed in Figure 8.26 is a vital indication of sediment load and compaction. Including the porosity reduction observed from the petrophysical density porosity logs, these are essential signs of diagenetic compaction reducing the intergranular porosity of the Triassic strata.

In terms of mineralogical maturity, sample 4 is taken from the most mature sandstone collected, having a subarkosic texture, as pointed out by the QFL-diagram in Figure 8.25. On the other hand, samples collected from well 6610/7-2 are classified as arkoses, while those from 6507/12-1 are categorized as litharenites. These are immature sandstones and reduces the probability of preserving porosity. The rounding of the grains also reveals that the rocks are immature, having a subangular shape. In addition, most of the samples tend to be moderately sorted. The high feldspar content is consistently reducing the reservoir quality during burial, as the feldspar reacts with the pore fluid, generating authigenic clay minerals. As sample 4 is mature, it does not contain extensive amounts of feldspar minerals, and the clay minerals are almost absent for this sample. The porosity should therefore be preserved during burial, compared to the immature rocks. Unfortu-

nately for the reservoir quality, its close relation to the anhydrite source of Upper Unit Tr4 has caused a mass solute transfer of intergranular authigenic anhydrite cement, heavily reducing the porosity.

In contrast, the halite observed in sample 1 at a depth of 3045 m may have a positive effect on the reservoir quality, as the porosity remains higher than for the surrounding layers. The same occurs in sample 12 at a depth of 4194 m. For this case, the observation of intragranular perchlorate salt minerals in feldspar minerals may be the key to explain the reservoir quality preservation. A reasonable theory is that intergranular salt have reduced the likelihood of extensive authigenic clay mineral growth. Instead of reacting with the pore fluid, creating clay minerals, weathered feldspar minerals are replaced with salt. This prevents clay minerals from growing into the intergranular pore space, which would reduce the porosity. Unfortunately, preventing growth of authigenic clay will not prevent calcite cementation. Sample 10 is very similar to sample 12 in terms of mineral assemblage, but is sampled 10 meter shallower. This sample is also low in clay minerals, but calcite cement has occupied all of the observed porosity. Thus, for areas low in calcite cement, intragranular salt may have a positive effect on the reservoir quality.



# Chapter 10

## Conclusions and recommendations for further work

### 10.1 Conclusions

The work with this thesis has involved an extensive literature review of Triassic reservoir units on the Trøndelag Platform and Ellingråsa Graben in the Norwegian Sea on the Norwegian continental shelf. With this, the fundamentals for understanding the Triassic stratification have been established, focusing on geological history, regional geology, depositional environment, diagenesis and reservoir quality. Following this, a wide range of scientific methods, including petrophysical, mineralogical and petrographical methods, have been applied both to data and core samples from the Norwegian Sea area. The objective behind these investigations was to establish the depositional environment and to gain knowledge on how the diagenetic evolution for the mineral assemblage affects reservoir quality.

The provenance for the Triassic sedimentary stratification of the Trøndelag Platform and Ellingråsa Graben combines sediment input from the elevated Nordland Ridge in the west and from European continental plains in the east. Petrophysical log correlation demonstrates that the topography on the Trøndelag Platform was dominated by a very low relief during deposition of Unit Tr3, Unit Tr4 and Unit Tr5. However, the Nordland Ridge stood out as a topographic high and erosional products from the Nordland Ridge were redeposited on the Trøndelag Platform during Unit Tr3 to Unit Tr5. An extensional regime in the Norwegian Sea activated the Bremstein Fault Complex which gave rise to tectonic uplift of the Nordland Ridge and subsidence of the inner platform. Furthermore, at three occasions during deposition of Unit Tr4, the Trøndelag Platform basin was completely enclosed by the Nordland Ridge. At times of enclosure, the lacustrine basin evaporated, depositing layers of salt and gypsum. During later burial, dehydration of

gypsum transformed the gypsum to anhydrite layers. Periodic breakthroughs by the Panthalassic Ocean led to influx of seawater and deposition of shallow marine sediments. Thus, in accordance with the changing facies associations, the sediments have periodically been exposed to oxidizing surface environments as well as reducing marine environments. As the Triassic climate zone is gradually changing from an arid towards a semi-humid environment during deposition of Unit Tr3 to Unit Tr5, an elevated water salinity dominated the partially enclosed Trøndelag Platform and Ellingråsa Graben basin. From mineralogical and petrographical methods, evaporitic minerals have been observed throughout the Triassic succession, not only in Unit Tr4, but also in Unit Tr3 and Unit Tr5. In Unit Tr4, the evaporitic minerals are in situ deposits, while some of the evaporitic minerals in Unit Tr3 and Unit Tr5 are mass solute transferred deposits from Unit Tr4.

On sedimentological logs of Unit Tr5 from the Ellingråsa Graben, one can observe upward fining sequences with current ripples and horizontal lamination, containing fossil fragments of ooids, clams and ostracods, in addition to dust rims along quartz grain borders, rootlets, desiccation cracks, flaser bedding and syneresis cracks. At this location, the depositional environment of Unit Tr5 is a playa lake dominated by channelized fluvial deposits, which is closely influenced by fluctuations in relative sea level and varying water salinity. In contrast, the depositional environment of Unit Tr3 in the Ellingråsa Graben represents a playa lake which is not influenced by channelized fluvial deposits nor a salt-rich source to produce fluctuations in the water salinity. Unit Tr3 in the northern part of the Trøndelag Platform is situated in a marginal marine to fluvial and tide mouth bars influenced depositional environment. Finally, the depositional environment for Unit Tr3 on the Nordland Ridge is marginal marine to fluvial and tide, influenced by mouth bars.

The diagenetic evolution is unique for each well location, but general trends explaining the observed reservoir quality are discovered. The number of sub-salt zones with preserved reservoir quality are limited in Unit Tr3 and Unit Tr5. The main reducing reservoir quality factors are compaction, mineralogical immaturity, authigenic clay minerals, calcite and dolomite cements and mass solute transferred anhydrite. In general, compaction follows the general rule of thumb of 1% porosity loss per 100 m of burial. Thus, at the great depth of Unit Tr3 and Unit Tr5, most of the stratified sedimentary layers contain severely reduced porosity values. Furthermore, mineralogical immature samples from Unit Tr3 and Unit Tr5 have a high feldspar content, which is poorly to moderately sorted with subangular grain shapes. The high feldspar content reduces the probability of preserving the porosity during burial. Weathered feldspar minerals are replaced by authigenic

kaolinite and illite during eogenesis and mesogenesis. For the authigenic clay minerals, intergranular kaolinite dominates at shallow depths, while pore bridging illite and pore lining chlorite dominates at higher depths. At a temperature of 110°C, kaolinite is completely replaced by illite and chlorite. Moreover, growth of calcite cement starts at temperatures of ~100°C. At this temperature ankerite and siderite are replaced by calcite and dolomite. At the highest temperatures, illite is being replaced by stable chlorite minerals. Finally, mass solute transferred anhydrite from Unit Tr4, is reducing the reservoir quality of supra-salt reservoir units.

For layers of preserved reservoir quality in Unit Tr3 and Unit Tr5, clay mineral coating have restricted massive quartz cementation. Moreover, intragranular precipitation of perchlorate salt within feldspar minerals have restricted extensive growth of authigenic clay minerals. In addition, the cementation rates are low relative to the surrounding units for layers of preserved reservoir quality. Finally, for reservoir units of depths shallower than 2300 m MD, the high porosity values promotes a high reservoir quality for well 6610/7-2 in the northern part of the Trøndelag Platform. At depths shallower than 2160 m, the reservoir quality seems reasonable for well 6507/6-1 located on the Nordland Ridge. For well 6507/12-1 and 6507/12-2 located on the Ellingråsa Graben, reservoir units of depths shallower than 3100 m show promising reservoir quality in terms of the observed high porosity values.

## 10.2 Further work

A natural next step in terms of investigating the depositional environment, diagenetic evolution and reservoir quality of Triassic units on the Trøndelag Platform and Ellingråsa Graben, would be to extend the data basis using more samples from the investigated wells, along with samples from unexplored wells. Furthermore, the findings from this work could be strengthened by applying other experimental methods, such as seismic interpretation, X-ray fluorescence and radiometric dating. By comparing this work with the E&P companies re-evaluated data sets, the sources of error could be significantly reduced. In addition, the larger E&P companies have access to information from wellbores of high reservoir quality. Including these wells in this work would improve the geological understanding of the diagenetic effects on reservoir quality. By expanding the investigation to other areas of the world with a similar geological setting, the understanding of the Norwegian Sea can be further enhanced. For instance, the impact of eogenesis on reservoir quality in basins of elevated salinity can be explored from the Cenozoic stratification in the Mediterranean Sea. Thus, this area could contribute to the understanding of diagenetic impact on reservoir quality in the Trøndelag Platform and Ellingråsa Graben reservoir units. Finally, it could also be of value to construct the structural geological development from the observed depositional environments and diagenetic histories.



# Bibliography

- [1] R. Blakey, “Triassic Period.”  
<http://www.geologypage.com/2014/04/triassic-period.html>, April 2014. [Accessed 10.04.2019].
- [2] P. Blystad, H. Brekke, R. B. Færseth, B. T. Larsen, J. Skogseid, and B. Tørudbakken, “NPD Bulletin no 8, structural elements of the Norwegian continental shelf. Part II: The Norwegian Sea region,” 1995.  
<http://www.npd.no/Global/Norsk/3-Publikasjoner/NPD-Bulletin/Bulletinnr8.pdf>, Accessed 20.08.2018.
- [3] R. Müller, J. P. Nystuen, F. Eide, and H. Lie, “8.7.2.4 Unit Tr4 (Carnian),” in *Onshore-Offshore Relationships on the North Atlantic Margin*, pp. 165–189, Elsevier, 2005.
- [4] C. A. Baar, *Applied salt-rock mechanics - The in-situ behavior of salt rocks*, vol. 1. Amsterdam: Elsevier, 1977.
- [5] R. L. Folk, P. B. Andrews, and D. W. Lewis, “Detrital sedimentary rock classification and nomenclature for use in New Zealand,” *New Zealand Journal of Geology and Geophysics*, vol. 13, no. 4, pp. 937–968, 1970.
- [6] D. V. Ellis and J. M. Singer, “21 - Clay quantification,” in *Well Logging for Earth Scientists*, pp. 597–624, Springer, Dordrecht, 2007.
- [7] M. C. Powers, “A new roundness scale for sedimentary particles,” *Journal of Sedimentary Research*, vol. 23, pp. 117–119, 06 1953.
- [8] B. McKee and R. R. W. Compton, “Manual of field geology,” *Science*, vol. 135, no. 3509, pp. 1122–1123, 1962.
- [9] S. Morad, K. Al-Ramadan, M. Ketzer, and L. De Ros, “The impact of diagenesis on the heterogeneity of sandstone reservoirs: A review of the role of depositional fades and sequence stratigraphy,” *The American Association of Petroleum Geologists*, vol. 94, pp. 1267–1309, 08 2010.

- [10] R. Worden and S. Burley, "Sandstone diagenesis: The evolution of sand to stone," in *Sandstone Diagenesis: Recent and Ancient*, vol. 4, pp. 1–44, University of Liverpool, University of Keele, 03 2009.
- [11] C. K. Wentworth, "A scale of grade and class terms for clastic sediments," *The Journal of Geology*, vol. 30, no. 5, pp. 377–392, 1922.
- [12] B. L. Magoon and A. E. Beaumont, "Petroleum Systems," *Online Journal for E&P Geoscientists*, pp. 1–34, 2003.
- [13] Norsk Petroleum, "Felt." <https://www.norskpetroleum.no/fakta/felt/>, 2019. [Accessed 09.04.2019].
- [14] Oljedirektoratet, "Kort om Diskos." <http://www.npd.no/no/Publikasjoner/Presentasjoner/DISKOS/Kort-om-Diskos/>, 2015. [Accessed 08.01.2019].
- [15] NPD, "NPD fact page, wellbore 6508/8-1." [http://factpages.npd.no/ReportServer?/FactPages/PageView/strat\\_Litho\\_level1\\_group\\_formation&rs:Command=Render&rc:Toolbar=false&rc:Parameters=f&NpdId=194&IpAddress=129.241.65.155&CultureCode=nb-no](http://factpages.npd.no/ReportServer?/FactPages/PageView/strat_Litho_level1_group_formation&rs:Command=Render&rc:Toolbar=false&rc:Parameters=f&NpdId=194&IpAddress=129.241.65.155&CultureCode=nb-no). Accessed 11.01.2019.
- [16] NPD, "NPD fact page, wellbore 6507/12-2." <http://factpages.npd.no/FactPages/Default.aspx?nav1=wellbore&nav2=PageView%7CExploration%7CA11&nav3=8655>. Accessed 11.01.2019.
- [17] NPD, "NPD fact page, wellbore 6610/7-2." <http://factpages.npd.no/FactPages/Default.aspx?nav1=wellbore&nav2=PageView%7CExploration%7CA11&nav3=8655>. Accessed 11.01.2019.
- [18] NPD, "NPD fact page, wellbore 6507/12-1." <http://factpages.npd.no/FactPages/Default.aspx?nav1=wellbore&nav2=PageView%7CExploration%7CA11&nav3=8655>. Accessed 11.01.2019.
- [19] NPD, "NPD fact page, wellbore 6507/6-1." <http://factpages.npd.no/FactPages/Default.aspx?nav1=wellbore&nav2=PageView%7CExploration%7CA11&nav3=8655>. Accessed 11.01.2019.
- [20] E. Halland, A. Bjørnestad, C. Magnus, F. Riis, I. M. Gjeldsvik, I. M. Tappel, J. Mujezinovic, M. Bjørheim, R. S. Rød, and V. T. H. Pham, "CO<sub>2</sub> samleatlas for norsk kontinentalsokkel," in *CO<sub>2</sub> Storage Atlas*, Oljedirektoratet, 2014.

- [21] A. Dalland, D. Worsley, and K. Ofstad, “NPD Bulletin no 4, A Lithostratigraphic scheme for the Mesozoic and Cenozoic succession offshore mid- and northern Norway,” 1988. [http://www.npd.no/Global/Norsk/3-Publikasjoner/NPD-Bulletin/NPD\\_BulletinNo4.pdf](http://www.npd.no/Global/Norsk/3-Publikasjoner/NPD-Bulletin/NPD_BulletinNo4.pdf), Accessed 23.08.2018.
- [22] H. Fossen, R. B. Pedersen, S. Bergh, and A. Andresen, “En fjellkjede blir til,” in *Landet blir til: Norges geologi*, ch. 6, pp. 180–233, Trondheim: Norsk geologisk forening, 2. ed., 2013.
- [23] H. Fossen, W. Dallman, and T. B. Andersen, “Fjellkjeden går til grunne,” in *Landet blir til: Norges geologi*, ch. 7, pp. 234–261, Trondheim: Norsk geologisk forening, 2. ed., 2013.
- [24] A. Nøttvedt and D. Worsley, “Vidstrakte sletter, kull og salt,” in *Landet blir til: Norges geologi*, ch. 8, pp. 262–287, Trondheim: Norsk geologisk forening, 2. ed., 2013.
- [25] K. C. Condie, “Great Events in Earth History,” in *Earth as an evolving planetary system*, pp. 357–435, Amsterdam: Elsevier, 2nd ed., 2011.
- [26] P. A. Nystuen, A. Mørk, R. Müller, and A. Nøttvedt, “Fra ørken til elveslette - fra land til hav,” in *Landet blir til: Norges geologi*, ch. 10, pp. 333–357, Trondheim: Norsk geologisk forening, 2. ed., 2013.
- [27] E. P. Johannessen and A. Nøttvedt, “Norge omkranses av kystsletter og deltaer,” in *Landet blir til: Norges geologi*, ch. 11, pp. 338–385, Trondheim: Norsk geologisk forening, 2. ed., 2013.
- [28] A. Nøttvedt and E. P. Johannessen, “Grunnlaget for Norges oljerikdom,” in *Landet blir til: Norges geologi*, ch. 12, pp. 386–421, Trondheim: Norsk geologisk forening, 2. ed., 2013.
- [29] H. Brekke and S. Olaussen, “Høyt hav og lave horisonter,” in *Landet blir til: Norges geologi*, ch. 13, pp. 421–447, Trondheim: Norsk geologisk forening, 2. ed., 2013.
- [30] J. M. Martinsen, A. Nøttvedt, and R. B. Pedersen, “Av hav stiger landet,” in *Landet blir til: Norges geologi*, ch. 14, pp. 448–493, Trondheim: Norsk geologisk forening, 2. ed., 2013.
- [31] T. O. Vorren and J. Mangerud, “Istider kommer og går,” in *Landet blir til: Norges geologi*, ch. 15, pp. 494–547, Trondheim: Norsk geologisk forening, 2. ed., 2013.

- [32] T. O. Vorren, J. Mangerud, L. H. Blikra, A. Nesje, and H. Sveian, "Norge av i dag trer frem," in *Landet blir til: Norges geologi*, ch. 16, pp. 548–575, Trondheim: Norsk geologisk forening, 2. ed., 2013.
- [33] V. Wiik Jacobsen and P. van Veen, "The Triassic offshore Norway north of 62°N," *Springer, Dordrecht*, pp. 317–327, 01 1984.
- [34] K. W. Glennie, *Lower Permian—Rotliegend*, ch. 5, pp. 137–173. John Wiley & Sons, Ltd, 2009.
- [35] K. Bjørlykke, "Clay mineral diagenesis in sedimentary basins — A key to the prediction of rock properties. Examples from the North Sea basin," *Clay Minerals*, vol. 33, pp. 15–34, 03 1998.
- [36] B. Lanson, D. Beaufort, G. Berger, A. Bauer, A. Cassagnabère, and A. Meunier, "Authigenic kaolin and illitic minerals during burial diagenesis of sandstones: A review," *Clay Minerals - Clay Miner*, vol. 37, pp. 1–22, 03 2002.
- [37] L. Stoch, "Transformations of micas in the process of kaolinitization of granites and gneisses," *Clays and Clay Minerals - Clays Clay Miner*, vol. 24, pp. 156–162, 08 1976.
- [38] F. S. Spear, "Heat flow and metamorphism," in *Metamorphic Phase Equilibria and Pressure-Temperature-Time Paths*, ch. Chapter 3: Heat flow and metamorphism, pp. 25–44, Department of Earth and Environmental Sciences Rensselaer Polytechnic Institute Troy, New York 12180 U.S.A.: Mineralogical Society of America, Washington, D.C., 1993.
- [39] P. Li, J. C. Deng, W. L. Zhao, and Y. C. Feng, "An experimental study on creep characteristics of salt rock and gypsum-salt rock in Puguang gas field," *Petroleum Science and Technology*, vol. 30, no. 16, pp. 1715–1724, 2012.
- [40] W. P. Choquette and C. L. Pray, "Geological nomenclature and classification of porosity in sedimentary carbonates," *The American Association of Petroleum Geologists*, vol. 54, pp. 207–250, 02 1970.
- [41] H. Fjellvåg, "Elektronmikroskop." <https://snl.no/elektronmikroskop>, December 2017. [Accessed 15.04.2019].
- [42] N. Mani, *Engineering Physics I: For WBUT*. Pearson Education India, 2010.

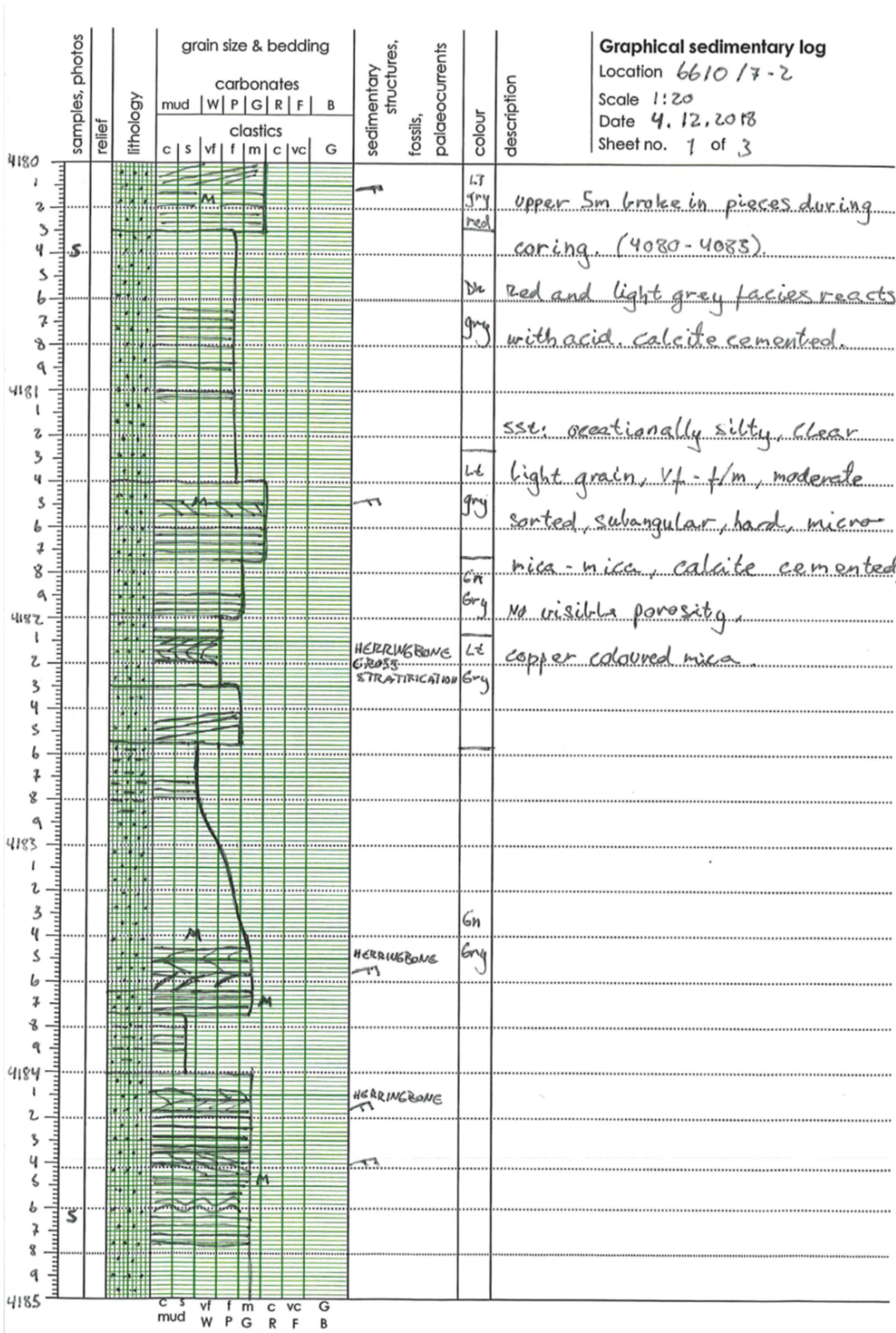
- [43] H. Brekke and F. Riis, "Tectonics and basin evolution of the Norwegian shelf between 62°N and 72°N," *Norsk Geologisk Tidsskrift*, vol. 67, pp. 295–322, 01 1987.
- [44] T. Bugge, J. E. Ringås, D. A. Leith, G. Mangerud, H. M. Weiss, and T. L. Leith, "Upper Permian as a new play model on the Mid-Norwegian continental shelf - Investigated by shallow stratigraphic drilling," *AAPG Bulletin*, vol. 86, pp. 107–127, 01 2002.
- [45] K. Jongepier, J. Rui, and K. Grue, "Triassic to Early Cretaceous stratigraphic and structural development of the northeastern Møre Basin margin, off Mid-Norway," *Norsk Geologisk Tidsskrift*, vol. 76, pp. 199–214, 01 1996.
- [46] B. Terje Oftedal, A. Andresen, and R. Müller, "Early Triassic syn-rift sedimentation at hold with hope, northeast Greenland," *Norwegian Petroleum Society Special Publications*, vol. 12, pp. 191–206, 12 2005.
- [47] M. B. E. Mørk and O. S. Johnsen, "Jurassic sandstone provenance and basement erosion in the Møre margin - Froan Basin area," *Norges Geol. Unders. Bull.*, vol. 443, 01 2005.
- [48] I. E. CPS, "Introduction to differential sedimentation."  
<http://www.cpsinstruments.eu/pdf/Introduction%20Differential%20Sedimentation.pdf>. [Accessed 15.03.2019].
- [49] A. Adams, W. Mackenzie, and C. Guilford, "Atlas of sedimentary rocks under the microscope," *Atlas of Sedimentary Rocks under the Microscope.*, pp. VI + 104, 01 1984.
- [50] C. Weaver, "Clays, muds, and shales," *Amsterdam: Elsevier*, vol. Developments in Sedimentology 44, p. 819, 1989.



# Appendix A

## Core logs

The following figures are sedimentary logs from the six wells; 6610/7-2, 6507/12-1, 6507/6-1, 6608/8-1, 6608/11-1 and 6507/12-2.



Graphical sedimentary log

Location 6610 17-2

Scale 1:20

Date 4.12.2018

Sheet no. 1 of 3

HERRINGBONE  
GROSS  
STRATIFICATION

HERRINGBONE

HERRINGBONE

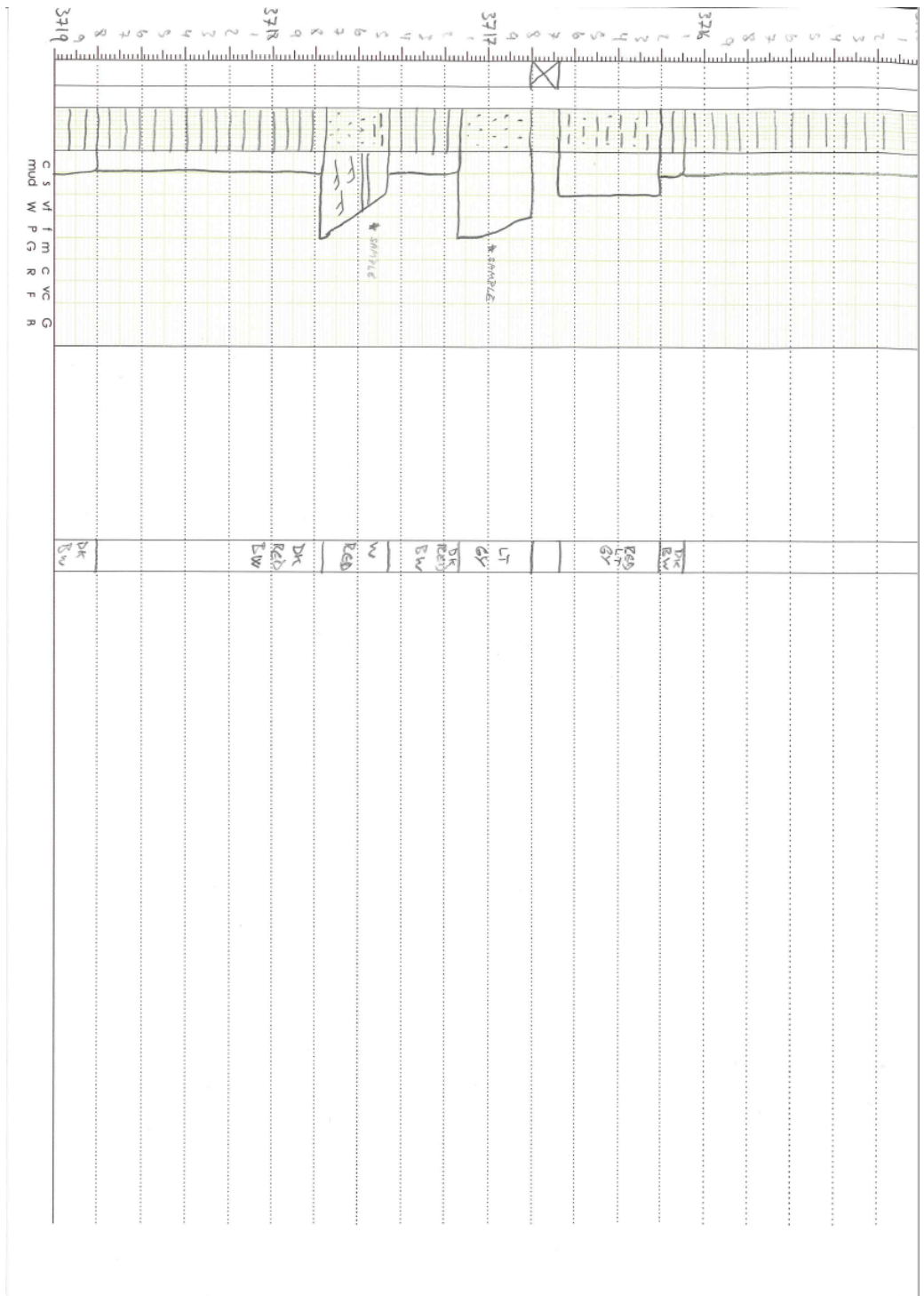
c s vf f m c vc G  
mud W P G R F B











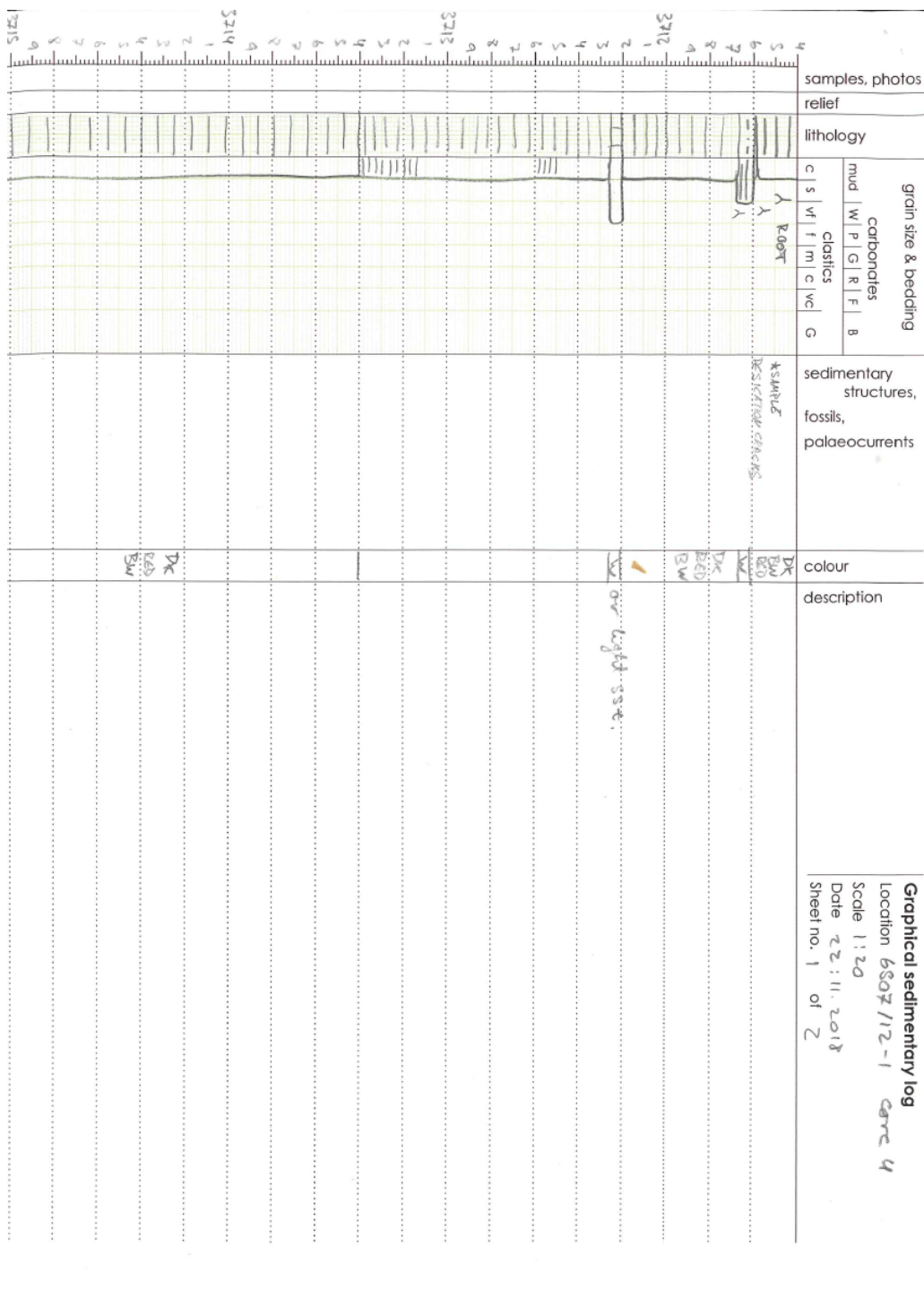
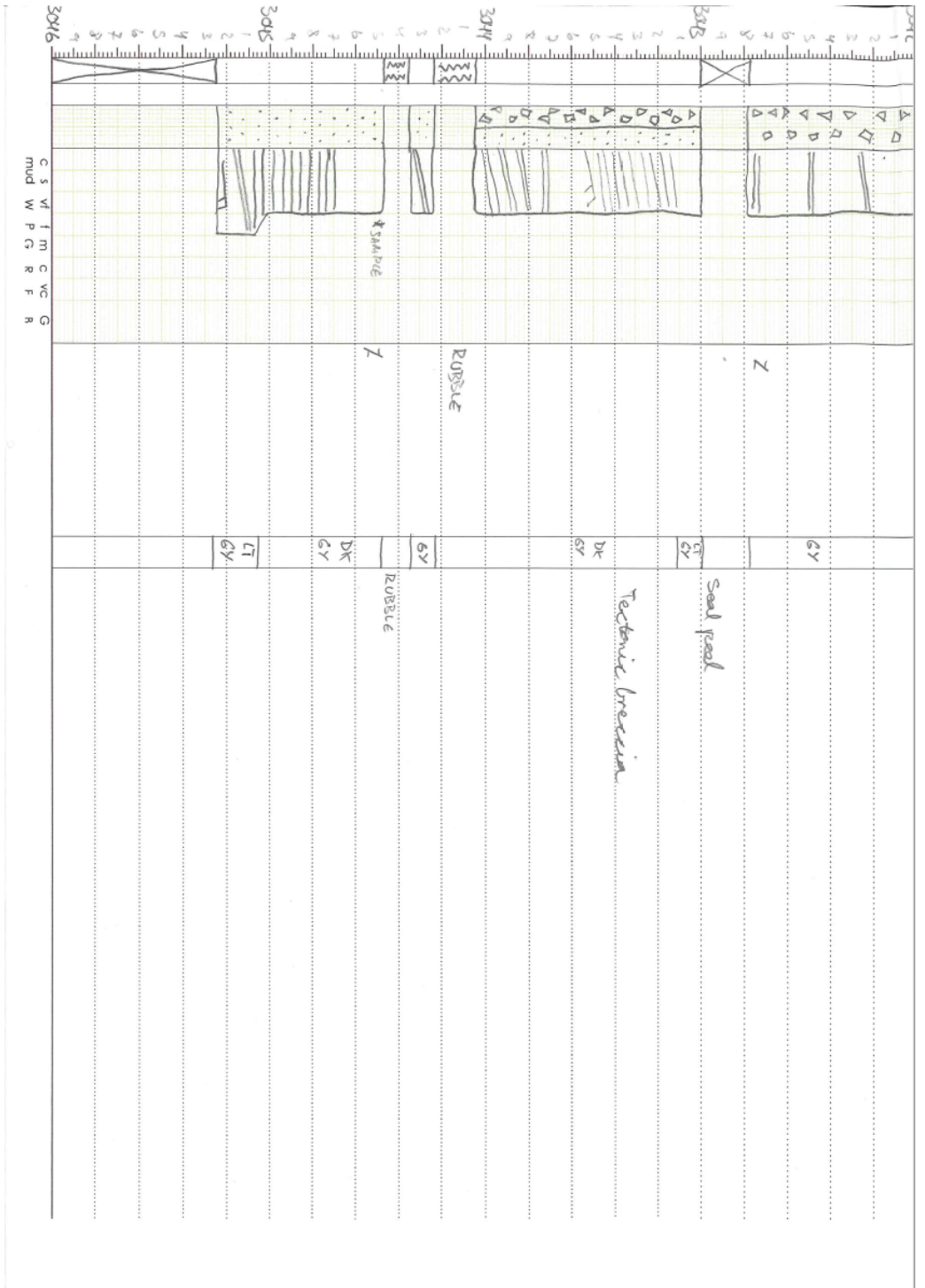
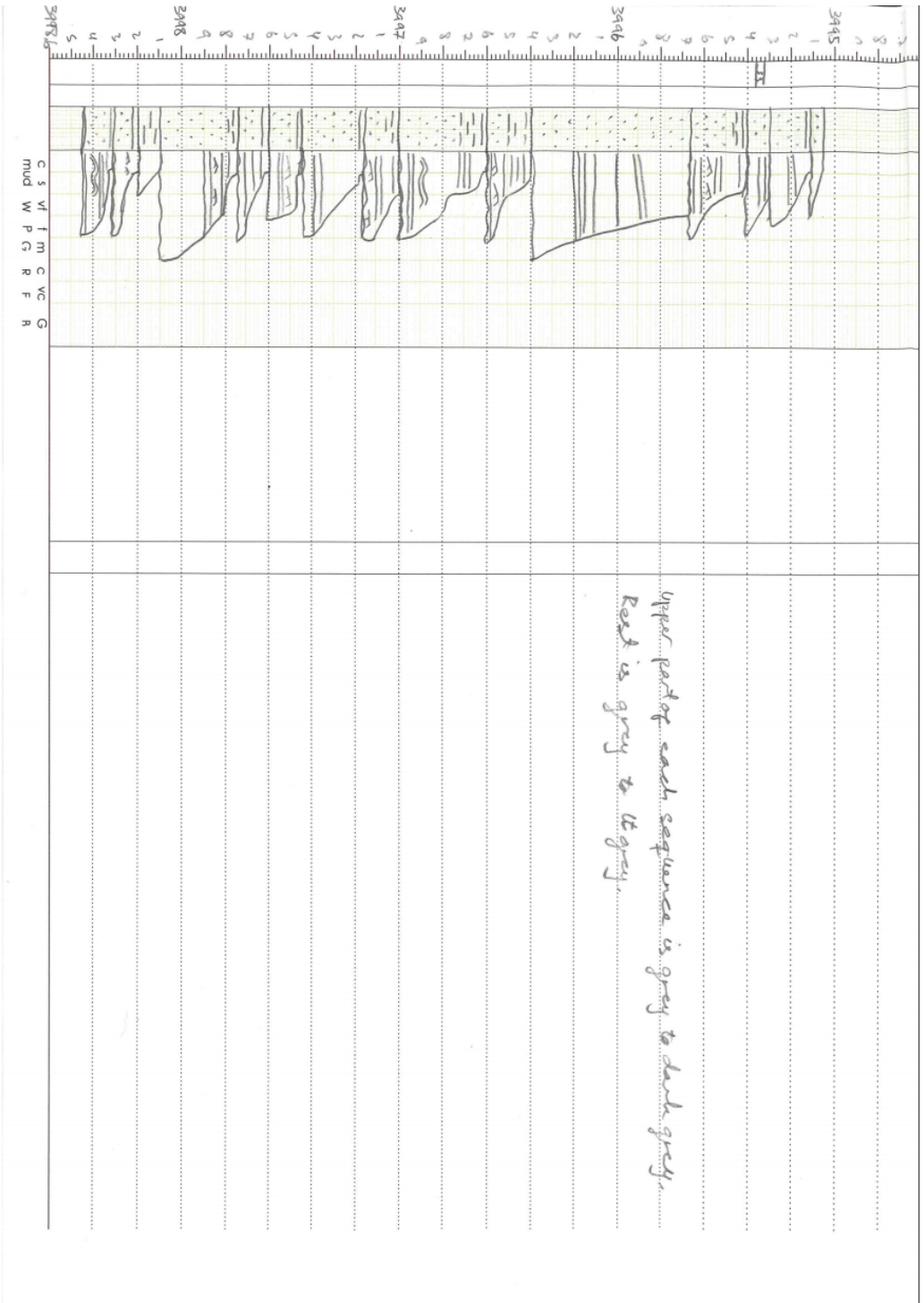


Figure A.2: Sedimentary log of well 6507/12-1



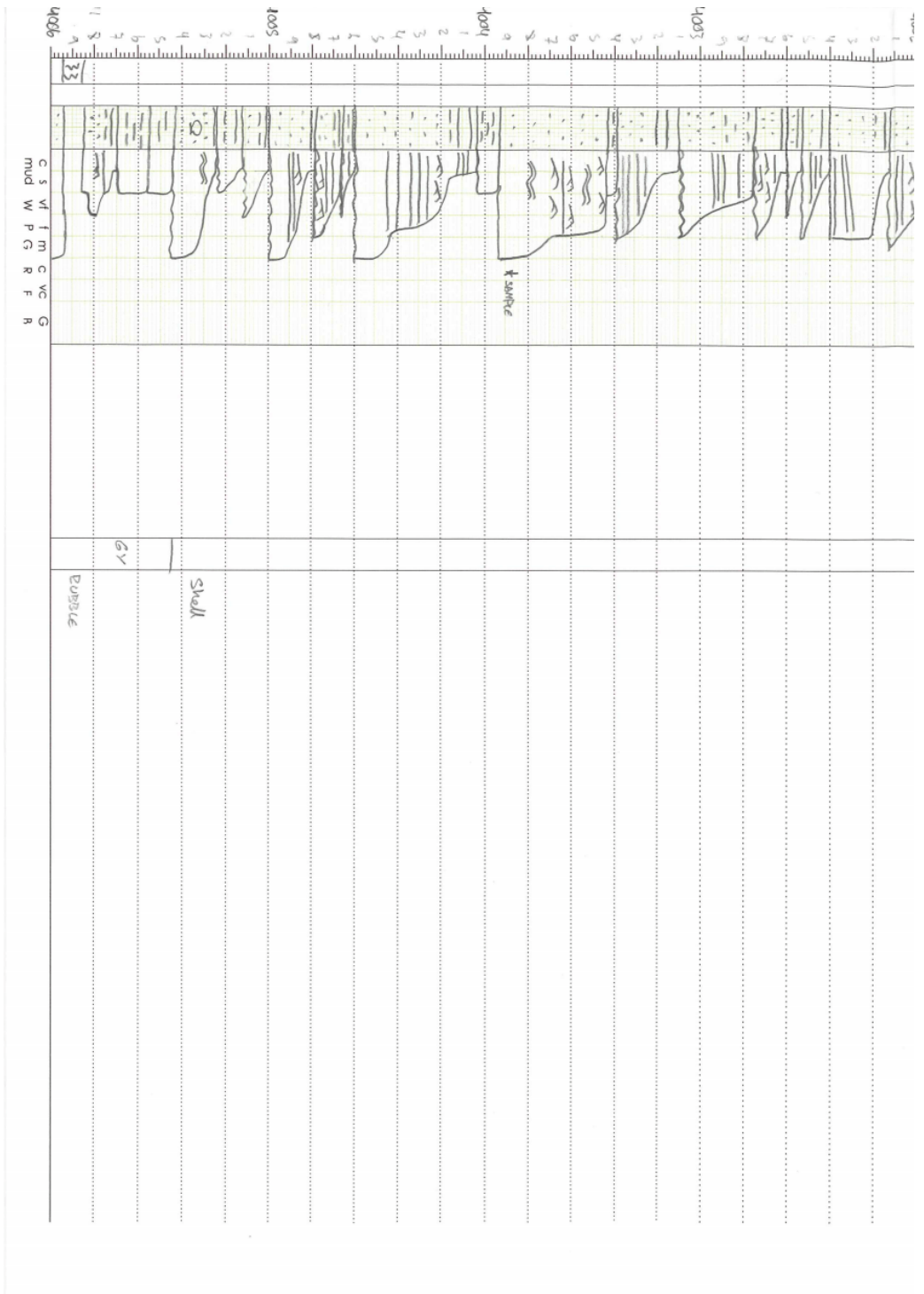


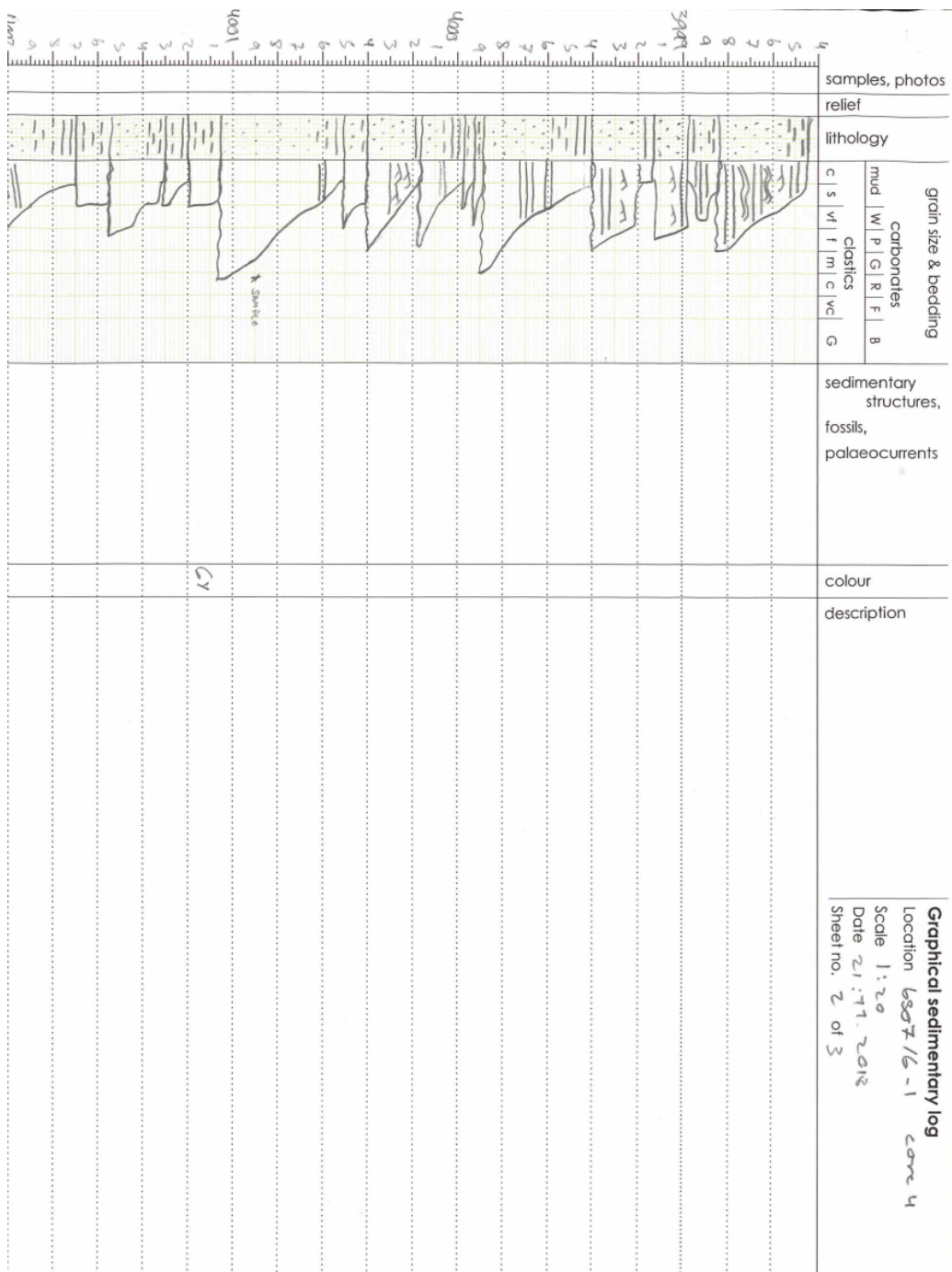




3444 1 2 3 4 5 6	samples, photos																											
	relief																											
	lithology																											
	<table border="1"> <tr> <td rowspan="2">grain size &amp; bedding</td> <td>mud</td> <td>W</td> <td>P</td> <td>G</td> <td>R</td> <td>L</td> <td>F</td> <td>B</td> </tr> <tr> <td>clastics</td> <td>C</td> <td>S</td> <td>Vf</td> <td>f</td> <td>m</td> <td>C</td> <td>vc</td> <td>G</td> </tr> <tr> <td>carbonates</td> <td></td> <td></td> <td></td> <td></td> <td></td> <td></td> <td></td> <td></td> </tr> </table>	grain size & bedding	mud	W	P	G	R	L	F	B	clastics	C	S	Vf	f	m	C	vc	G	carbonates								
grain size & bedding	mud		W	P	G	R	L	F	B																			
	clastics	C	S	Vf	f	m	C	vc	G																			
carbonates																												
	sedimentary structures, fossils, palaeocurrents																											
	colour																											
	description																											

**Graphical sedimentary log**  
 Location 6507/6-1 core 4  
 Scale 1:20  
 Date 21.11.2013  
 Sheet no. 3 of 3





**Graphical sedimentary log**  
 Location 6807/6-1 core 4  
 Scale 1:20  
 Date 21.11.2018  
 Sheet no. 2 of 3

CV

11m

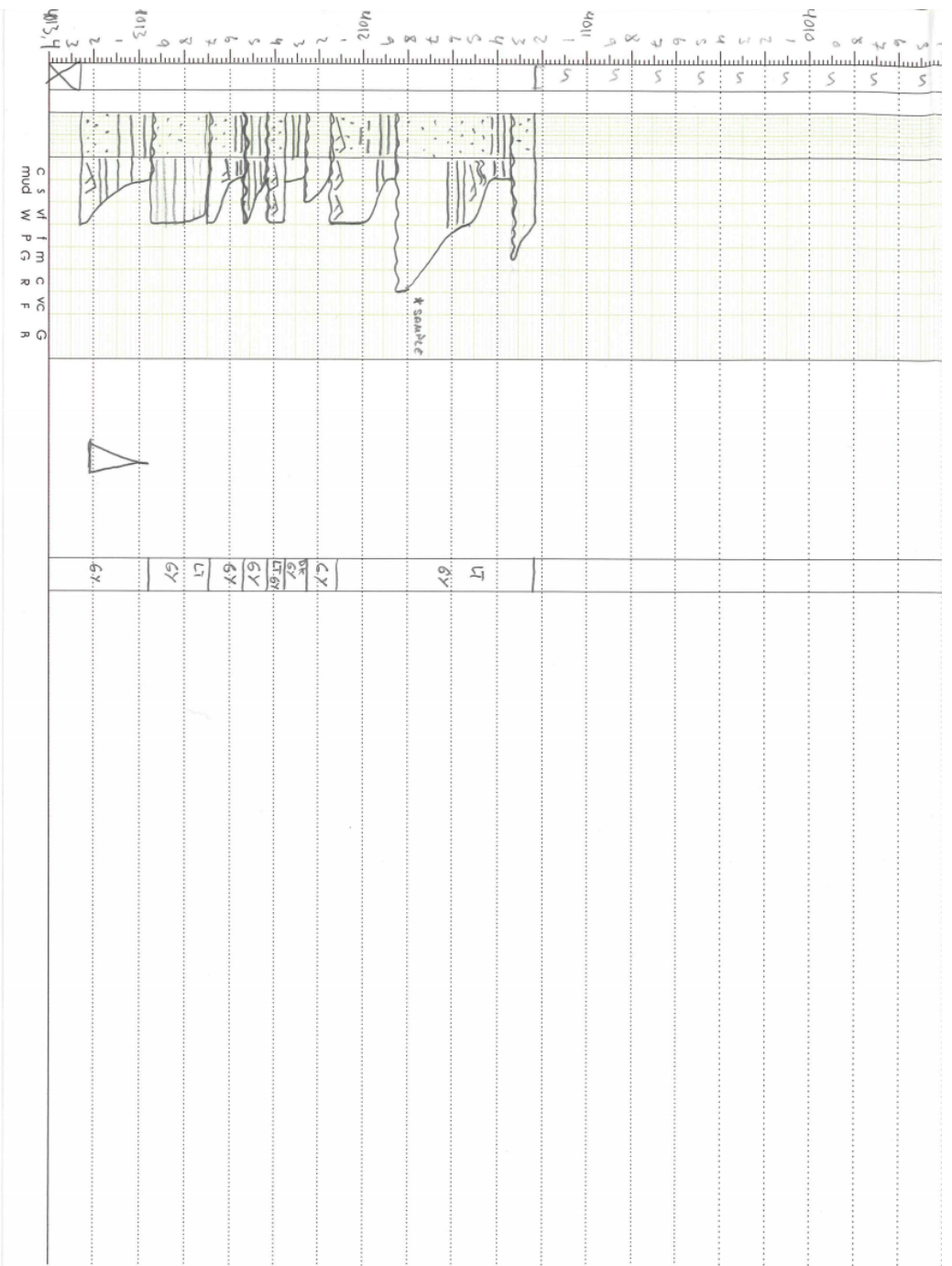
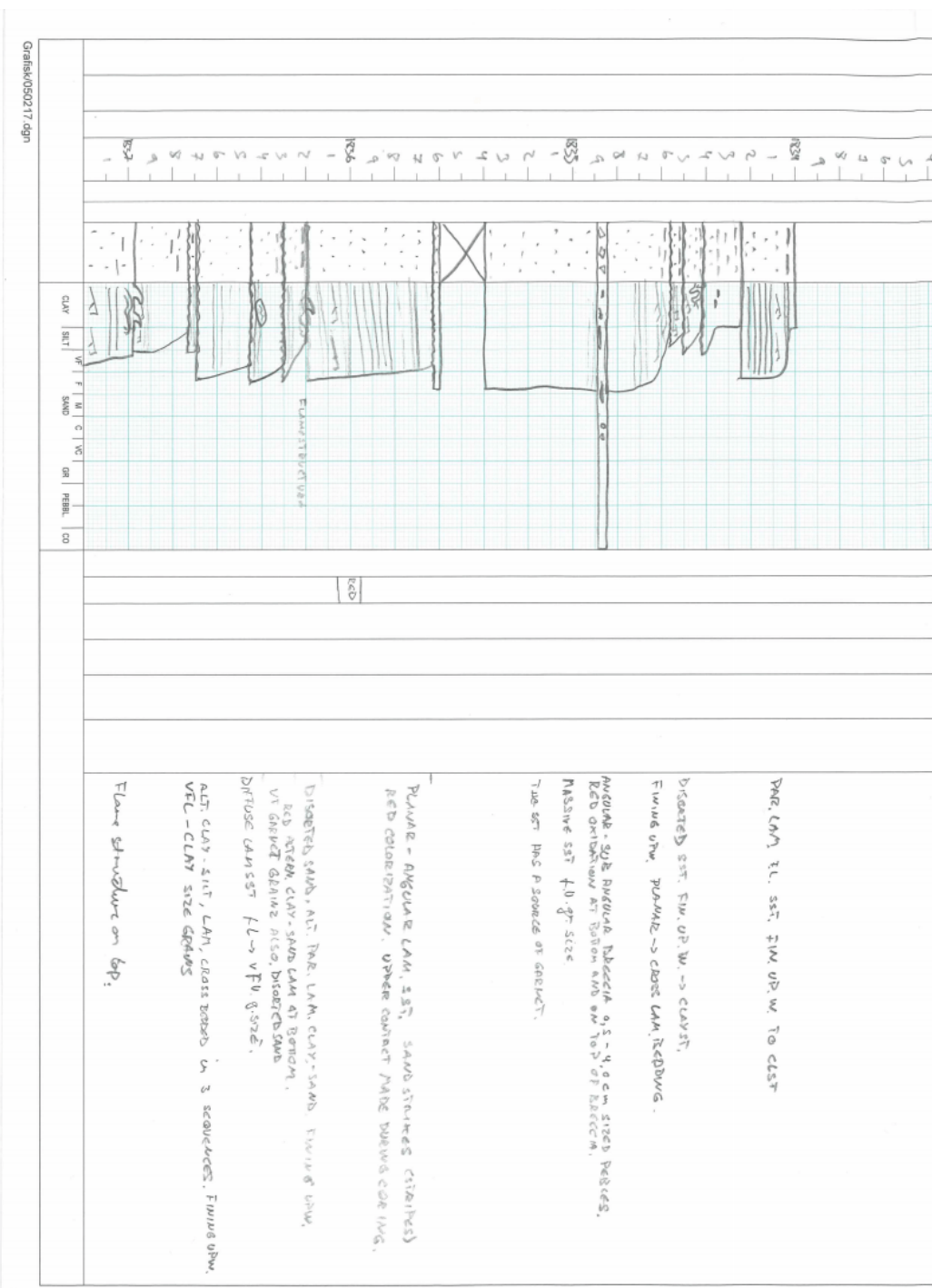

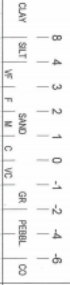


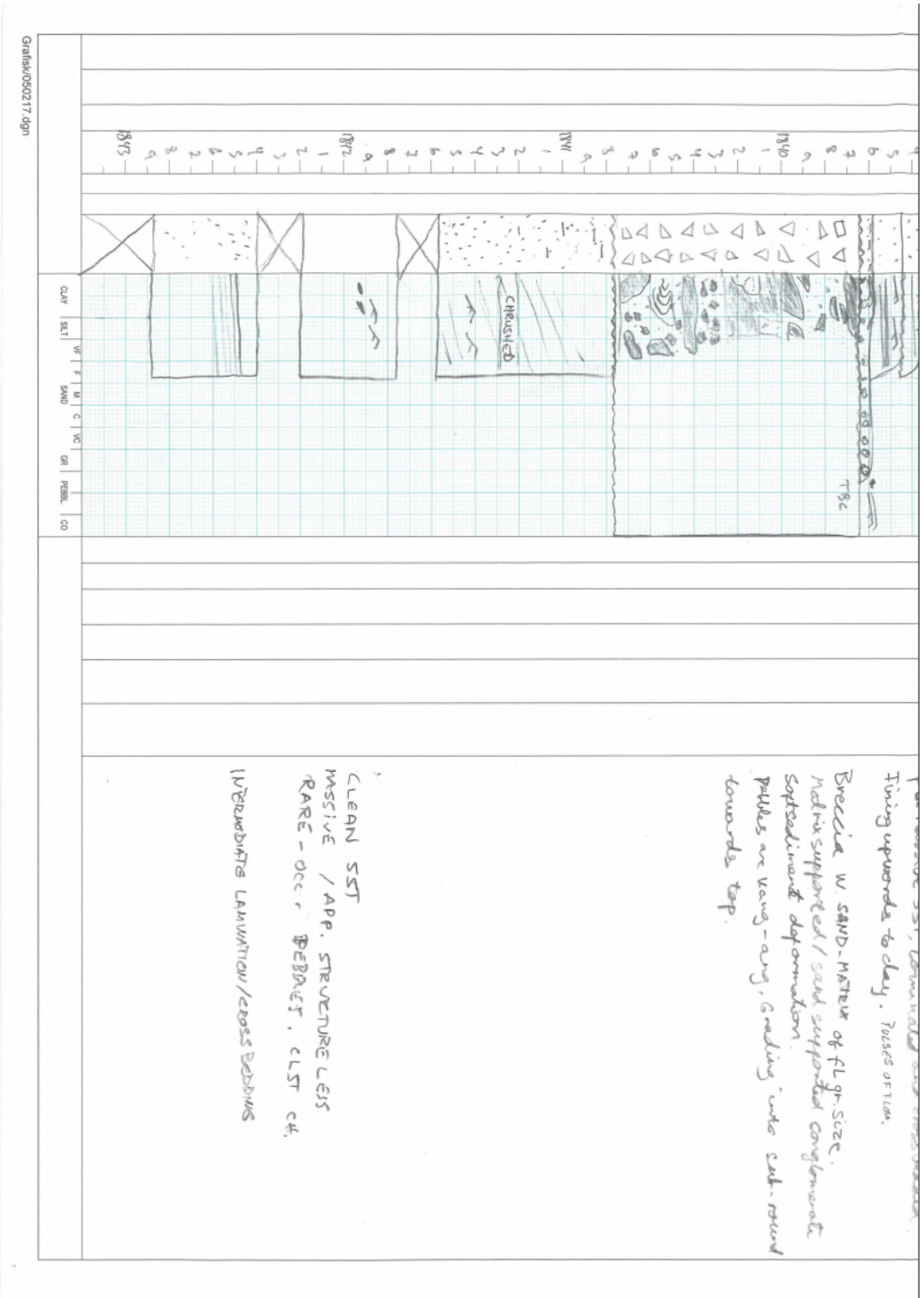


Figure A.3: Sedimentary log of well 6507/6-1



GrainW050217.dgn

SHEET 2 OF 2		<b>CORE DESCRIPTION</b>	
FIELD/AREA:		WELL NO: 6608/X-1	
UNIT:		CORE NO.: 2	
AGE:		INTERVAL:	
		SCALE:	
		DATE:	
		GEOLOGIST:	
			
AGE	LITHOSTRATIGR. UNIT	<div style="text-align: center;"> <b>GRAIN SIZE AND SEDIMENTARY STRUCTURES</b>  <math>\phi</math> </div> 	
RESERVOIR SUBDIV.	CORE DEPTH (m)		
CORE NO.	LITHOLOGY		
BIOTURBATION			
COLOUR			
FACIES/SUBFACIES			
DEPOSITIONAL ENVIRONMENT			
DESCRIPTION AND INTERPRETATION			
1 2 3 4 5 6 7 8 9 10 11 12 13 14 15 16 17 18 19 20 21 22 23 24 25 26 27 28 29 30 31 32 33 34 35 36 37 38 39 40 41 42 43 44 45 46 47 48 49 50 51 52 53 54 55 56 57 58 59 60 61 62 63 64 65 66 67 68 69 70 71 72 73 74 75 76 77 78 79 80 81 82 83 84 85 86 87 88 89 90 91 92 93 94 95 96 97 98 99 100			





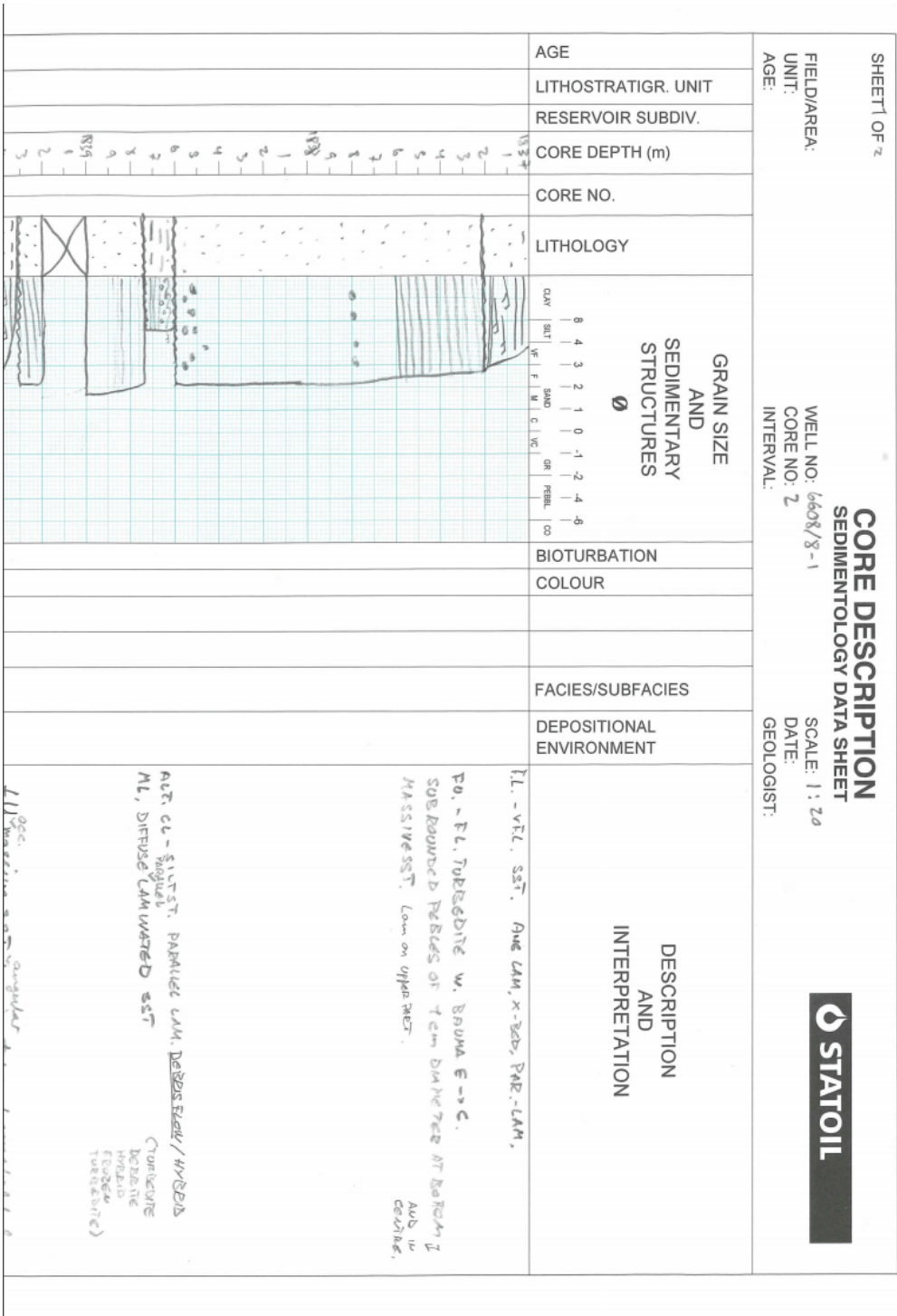
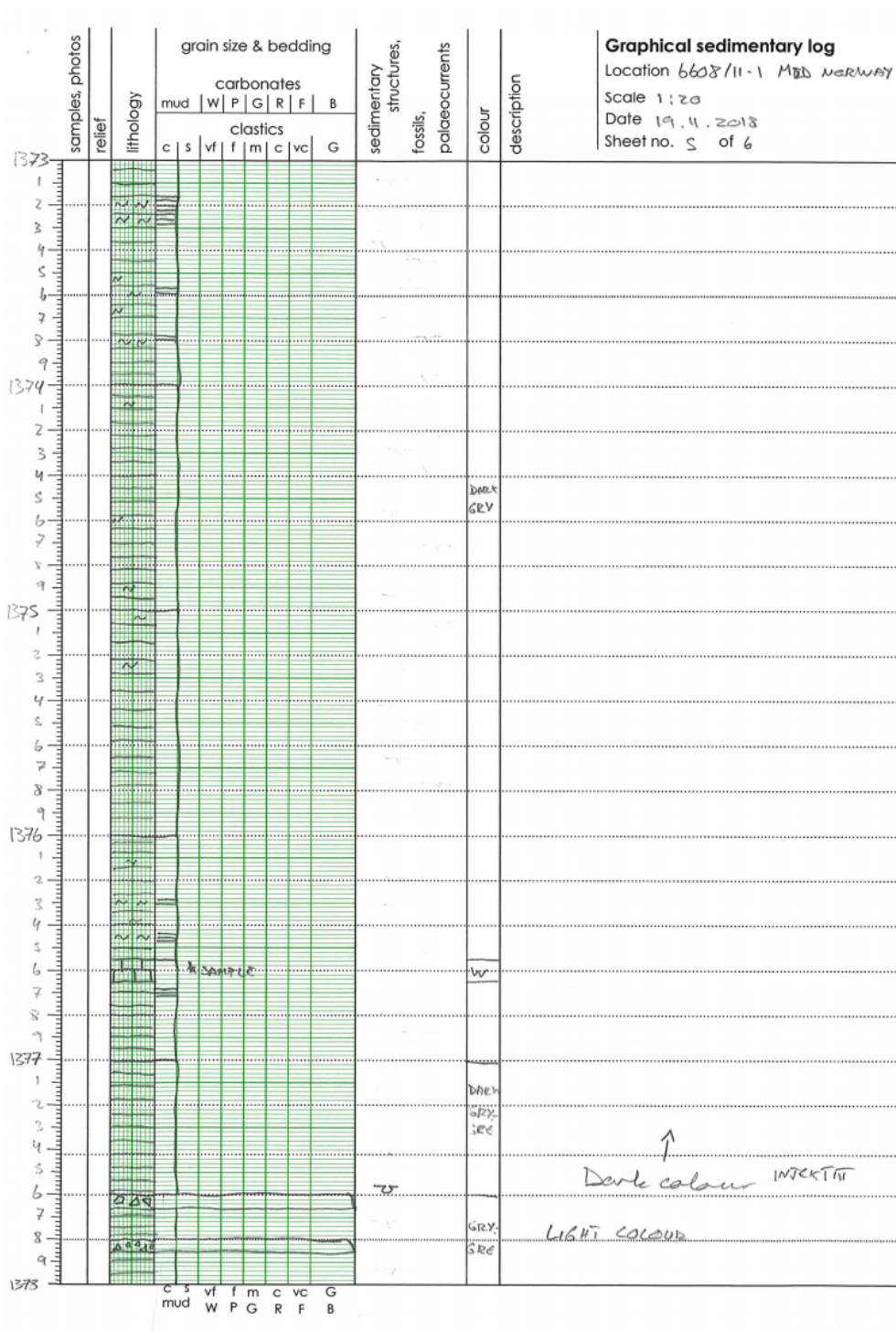


Figure A.4: Sedimentary log of well 6608/8-1











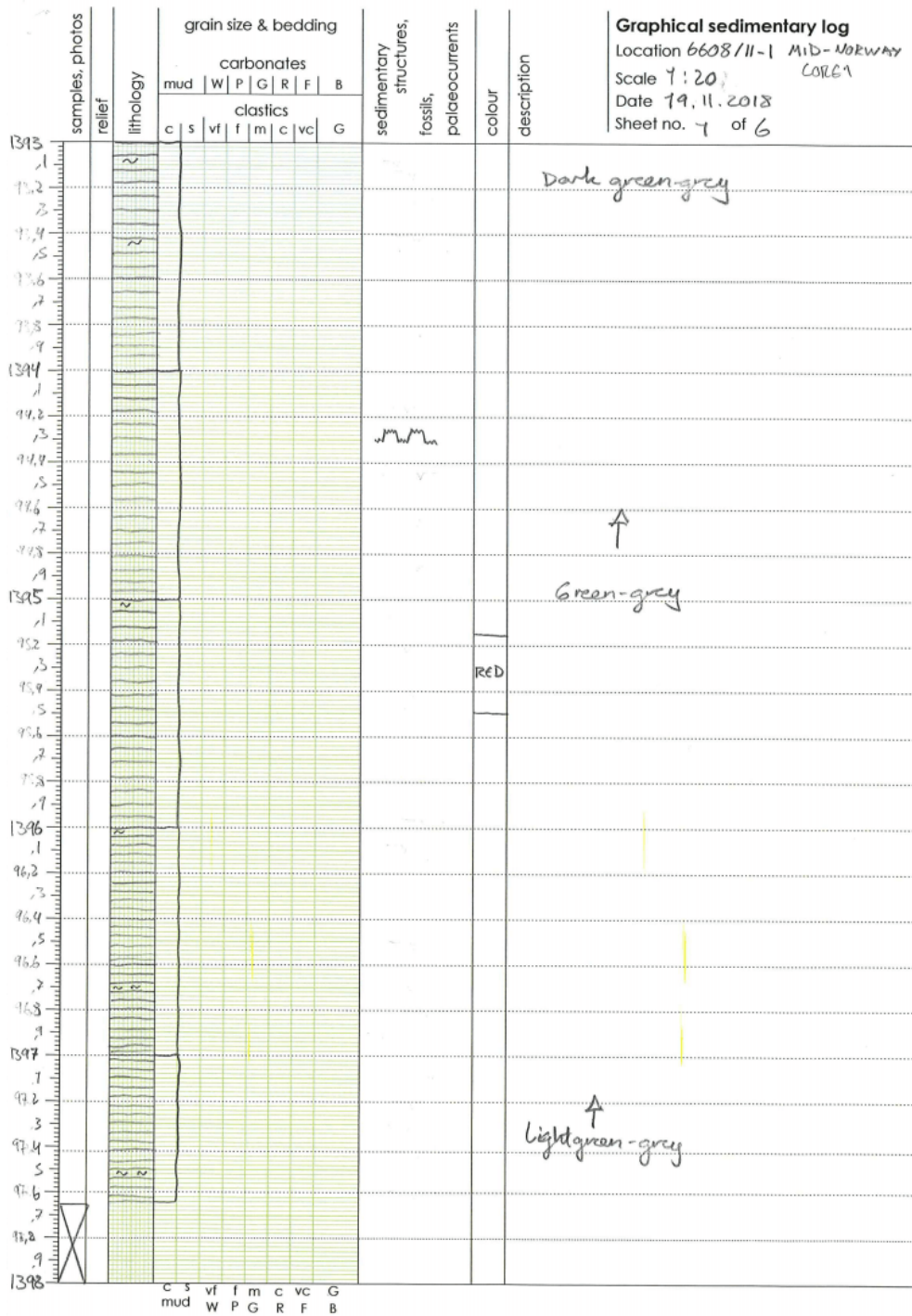
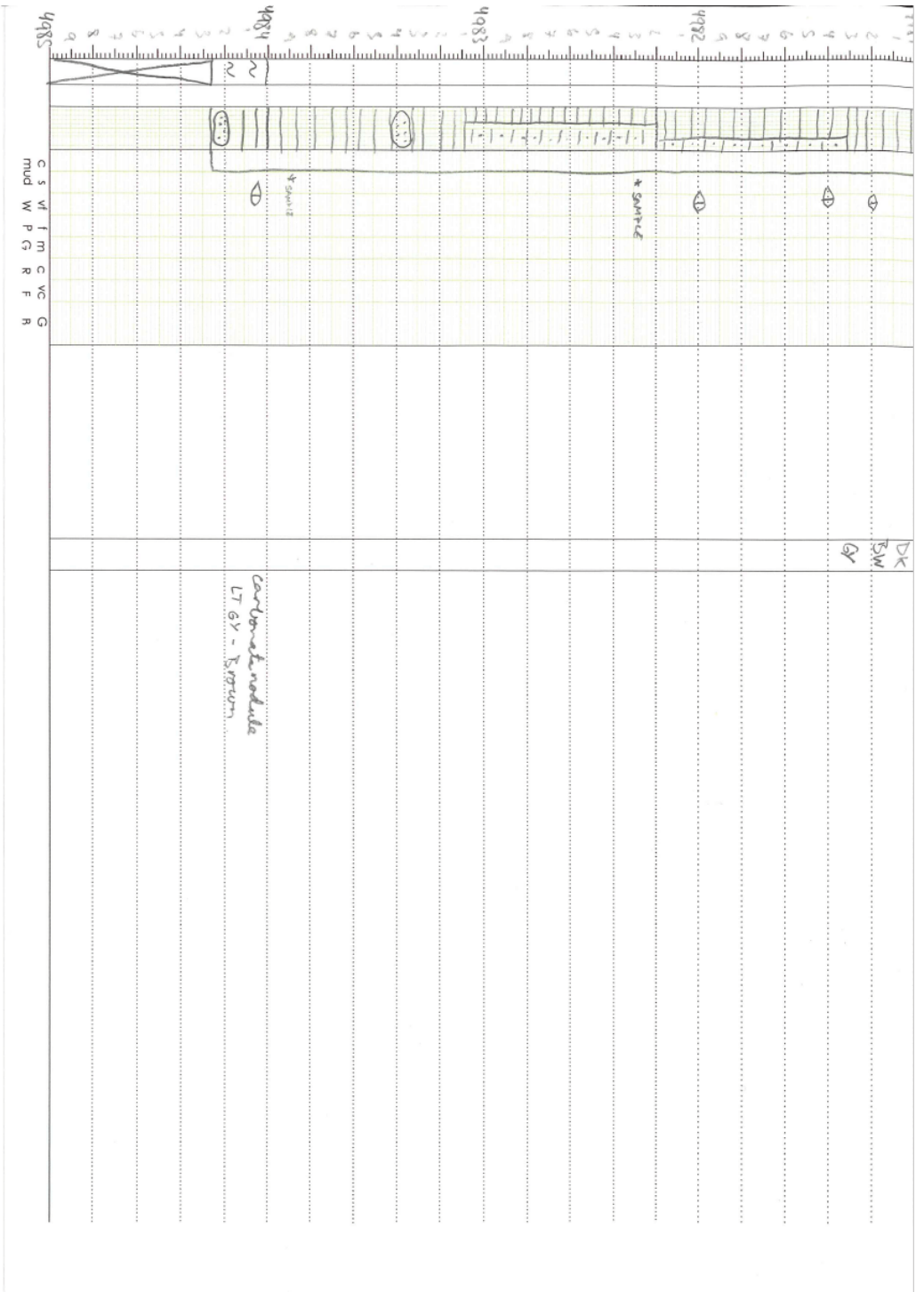


Figure A.5: Sedimentary log of well 6608/11-1







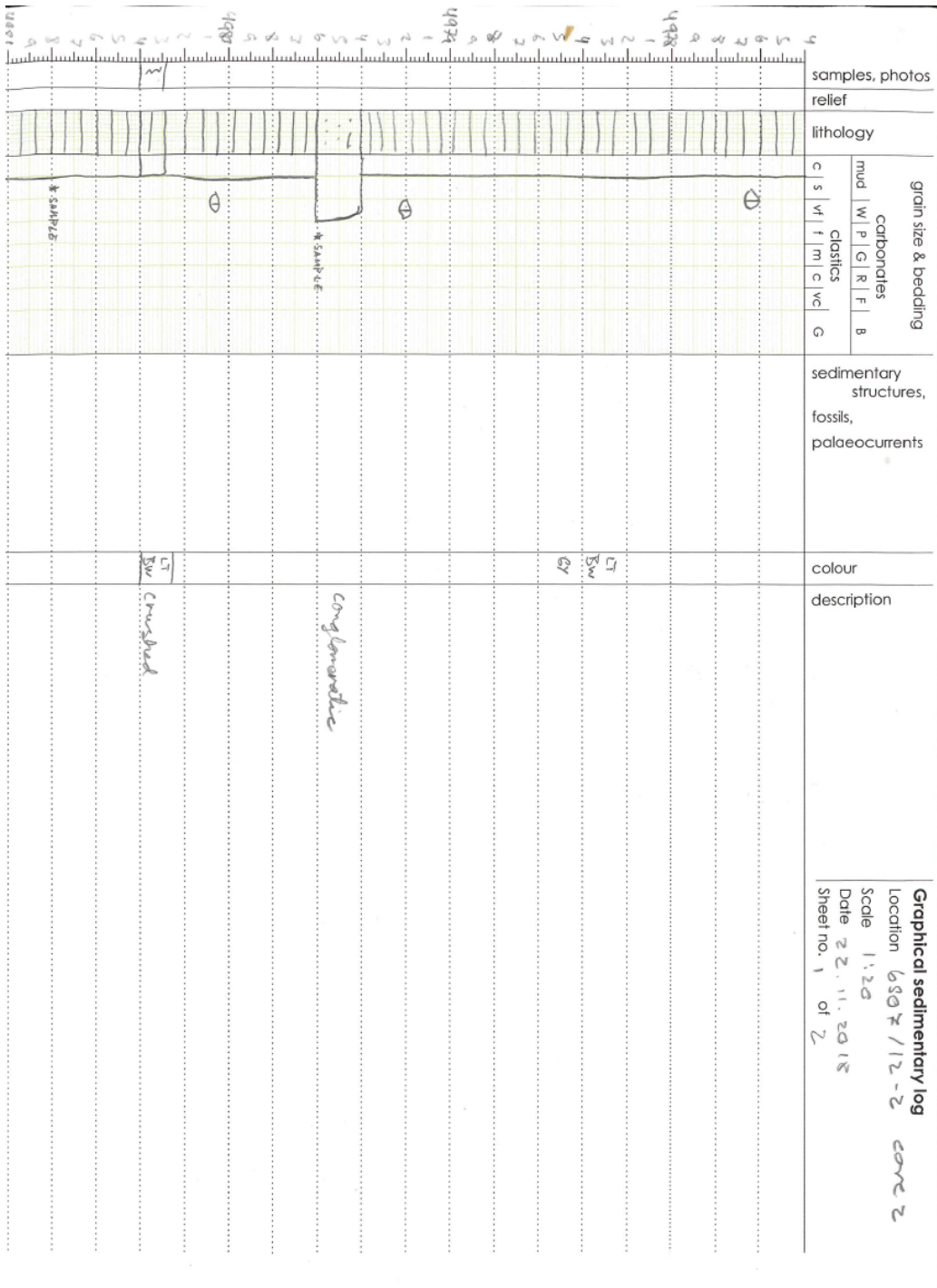


Figure A.6: Sedimentary log of well 6507/12-2

# Appendix B

## Geothermal gradient parameters

Table B.1 gives the parameters used to calculate the geothermal gradients,  $T(z)$ , by curve fitting methods. The four wellbores have slightly different parameter values according to fit the observed bottom hole temperature for the respective wells.

**Table B.1:** An overview of the parameters used to calculate the geothermal gradients,  $T(z)$ , by curve fitting methods.

Wellbore	$A$ [ $\frac{W}{m^3}$ ]	$k$ [ $\frac{W}{mK}$ ]	$Q$ [ $\frac{W}{m^2}$ ]	$D$ [ $km$ ]	$z$ [ $m$ ]
6507/12-2	0.70	2.40	70	10	0-4722
6507/12-1	0.75	2.25	75	10	0-3462
6507/6-1	0.70	2.45	70	10	0-3594
6610/7-2	0.70	2.60	65	10	0-3956



# Appendix C

## Thin section results

Table C.1, C.2 and C.3 give the thin section results from sample 1 to sample 14. Moreover, Table C.4 show the remarks of the investigated samples.

**Table C.1:** Thin section results from sample 1-5.

<b>Sample</b>	<b>1</b>	<b>2</b>	<b>3</b>	<b>4</b>	<b>5</b>
<b>Depth [m]</b>	3044.5	4011.8	3711.5	3717.0	4982.3
<b>FA</b>	FA4	FA2	FA3	FA3	FA1
<b>Lithology</b>	Litharenite	Arkose	Siltstone	Subarkose	Siltstone
<b>Framework</b>	Matrix	Grain	Matrix	Matrix	Matrix
<b>configuration</b>	supported	supported	supported	supported	supported
<b>Grain size</b>	vfL	mU	Silt	vfU	Silt
<b>Grain shape</b>	Subangular	Subrounded	Subangular	Subangular	Subangular
<b>Sorting</b>	Moderately sorted	Poorly sorted	Well sorted	Poorly sorted	Moderately sorted
<b>Color on hand sample</b>	Pale brown -pale red	Light green -bluish gray	Pale brown- grayish brown	Greenish gray	Pale brown- grayish brown

**Table C.2:** Thin section results from sample 6-10.

<b>Sample</b>	<b>6</b>	<b>7</b>	<b>8</b>	<b>9</b>	<b>10</b>
<b>Depth [m]</b>	1839.1	1839.5	1376.6	1376.0	4180.4
<b>FA</b>	FA4	FA4	FA3	FA3	FA1
<b>Lithology</b>	Subarkose	Claystone	Sublitharenite	Claystone	Arkose
<b>Framework configuration</b>	Grain	Matrix	Matrix	Matrix	Grain
<b>Grain size</b>	Supported	Supported	Supported	Supported	Supported
<b>Grain shape</b>	vfU	Clay	vfU	Clay	vfU
<b>Sorting</b>	Subrounded	Subangular	Subangular	Subrounded	Subangular
<b>Color on hand sample</b>	Moderately sorted	Well sorted	Moderately sorted	Well sorted	Moderately sorted
	Light green -ish gray	Light green -ish gray	Very light gray	Light green -ish gray	Pinkish gray

**Table C.3:** Thin section results from sample 11-14.

<b>Sample</b>	<b>11</b>	<b>12</b>	<b>13</b>	<b>14</b>
<b>Depth [m]</b>	4184.7	4194.1	4983.9	4187.2
<b>FA</b>	FA4	FA4	FA1	FA4
<b>Lithology</b>	Arkose	Arkose	Siltstone	Arkose
<b>Framework configuration</b>	Grain	Grain	Matrix	Grain
<b>Grain size</b>	Supported	Supported	Supported	Supported
<b>Grain shape</b>	vfU	cL	Silt	mU
<b>Sorting</b>	Subangular	Subrounded	Subangular	Subangular
<b>Color on hand sample</b>	Well sorted	Moderately sorted	Well sorted	Moderately sorted
	Light greenish gray	Very light gray	Pale brown	Very light gray

Table C.4: Remarks to the thin section results from sample 1-14.

Sample	Remarks
1	Black organic material, sideritized biotite, sericitized feldspar, mechanical ductile mica, pore filling kaolinite, pyrite, calcite cement.
2	Planar lamination, finer grain size on top of mU sized grains.
3	Synaeresis cracks filled with sparite, anhydrite with perpendicular cleavage, matrix possibly made of micrite. Planar laminated.
4	Fossil fragments, quartz overgrowth, dust rim, deformed quartz grains, anhydrite.
5	Rock fragments, micrite, pyrite, sparite, 0.1-0.5 mm light nodules.
6	Oxidized iron, high porosity values.
7	No structures observed.
8	Carbonate cemented, rounded fossil fragments, may be classified as rounded biosparite using Folk's carbonate classification.
9	Swelling clay type, sparite in microfractures, occasionally fossil fragments.
10	Calcite cement in pore structure, pyrite, chlorite, feldspar with twinning, sericitized feldspar, in situ euhedral quartz overgrowth.
11	Fracture goes along a muscovite surface on the hand specimen.
12	Hand specimen surface along a stylolite.
13	Planar lamination.
14	Calcite substituting mica, quartz with dust rim and quartz overgrowth, polysynthetic twins, 1.5 cm detrital foliated mica rich clay clast.





# Appendix D

## Point counting results

Table D.1, illustrate the QFL results used as a basis for constructing a QFL classification diagram. Table D.2 is an overview of the point counting results. 300 counts per thin section were preformed. Finally, Table D.3 demonstrates the content of the samples IGV.

**Table D.1:** This table is used as a basis for constructing a QFL classification diagram. Quartz is the sum of monocrystalline and polycrystalline quartz, feldspar is the sum of feldspar, K-feldspar and plagioclase, rock fragment is the sum of muscovites, reworked biotites, anhydrite grains, chlorite grains, heavy minerals, rock fragments, sparite rock fragments, micrite rock fragments and opaque minerals.

Sample	1	4	10	11	12	14
Quartz	33%	81%	52%	35%	51%	43%
Feldspar	6%	16%	43%	52%	40%	46%
Rock/lithic fragment	61%	3%	5%	13%	9%	11%
Sum QFL	100%	100%	100%	100%	100%	100%

Table D.2: Overview of point counting results.

Sample	1	4	10	11	12	14
Monocrystalline quartz	19%	25%	38%	25%	37%	29%
Polycrystalline quartz	0%	0%	1%	0%	2%	4%
Feldspar	2%	2%	18%	27%	12%	14%
K-feldspar	0%	1%	7%	5%	6%	5%
Plagioclase	1%	2%	7%	6%	13%	16%
Muscovite	13%	0%	2%	3%	3%	3%
Reworked biotite	18%	0%	0%	0%	0%	0%
Anhydrite grains	0%	0%	0%	0%	0%	0%
Chlorite grains	0%	0%	1%	3%	1%	2%
Heavy minerals	0%	0%	0%	0%	0%	0%
Opaque minerals	4%	0%	0%	3%	1%	1%
Rock fragments	0%	0%	0%	0%	1%	2%
Sparite rock fragment	0%	0%	0%	0%	1%	0%
Micrite rock fragment	1%	1%	1%	0%	0%	0%
Anhydrite Diagenetic	0%	20%	0%	0%	0%	0%
Chlorite diagenetic	1%	0%	0%	19%	0%	0%
Kaolinite diagenetic	8%	0%	0%	0%	0%	0%
Sparite matrix	0%	10%	0%	0%	0%	2%
Micrite Matrix	0%	35%	0%	0%	0%	0%
Calcite cement	21%	3%	24%	8%	12%	19%
Quartz cement	1%	0%	0%	0%	0%	0%
Stylolite	0%	0%	0%	0%	0%	2%
Organic material	0%	0%	0%	1%	0%	0%
Porosity	12%	0%	0%	1%	11%	1%

Table D.3: Matrix is the sum of sparite matrix and micrite matrix, cement is the sum of calcite cement and quartz cement, and diagenetic products is the sum of diagenetic anhydrite, chlorite and kaolinite.

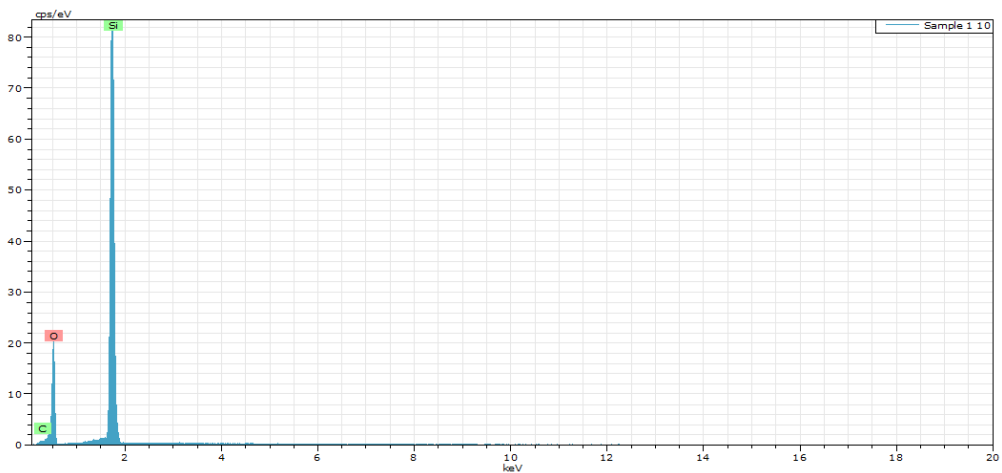
Sample	1	4	10	11	12	14
Matrix	0%	45%	0%	0%	0%	2%
Cement	22%	3%	24%	8%	12%	19%
Diagenetic products	9%	20%	0%	19%	0%	0%
Porosity	12%	0%	0%	1%	11%	1%
IGV	43%	68%	24%	28%	23%	22%

# Appendix E

## SEM results

### E.1 EDS spectra

The following section provides EDS spectra for the mineral assemblage discovered during SEM analysis. The respective spectra consist of a set of atoms, and the bulk volume of the different atoms can be found by measuring the frequency.



**Figure E.1:** The resulting EDS spectra for quartz -  $\text{SiO}_2$ .

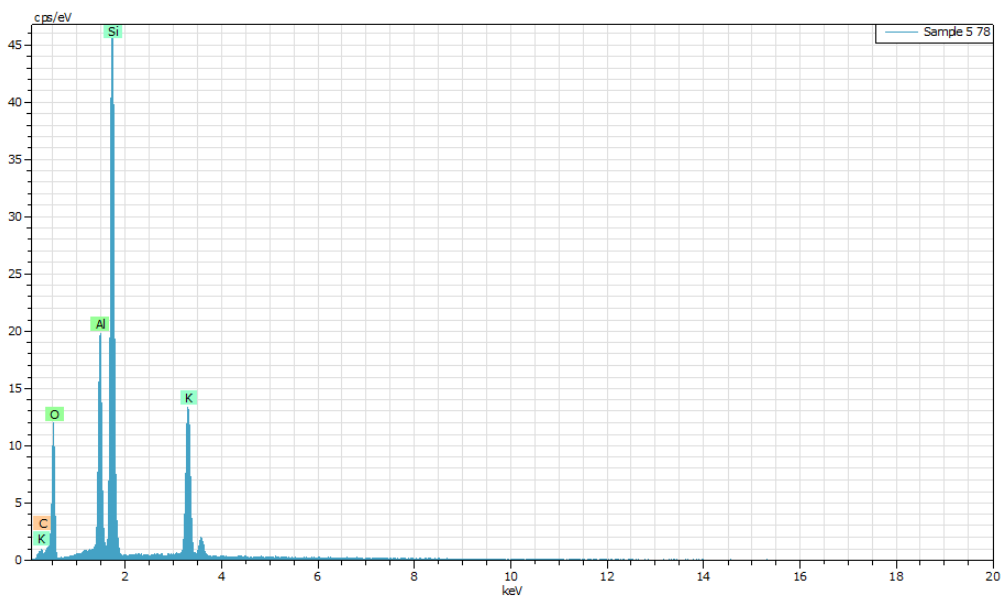


Figure E.2: EDS spectra for K-feldspar (orthoclase or microcline) -  $\text{KAlSi}_3\text{O}_8$ .

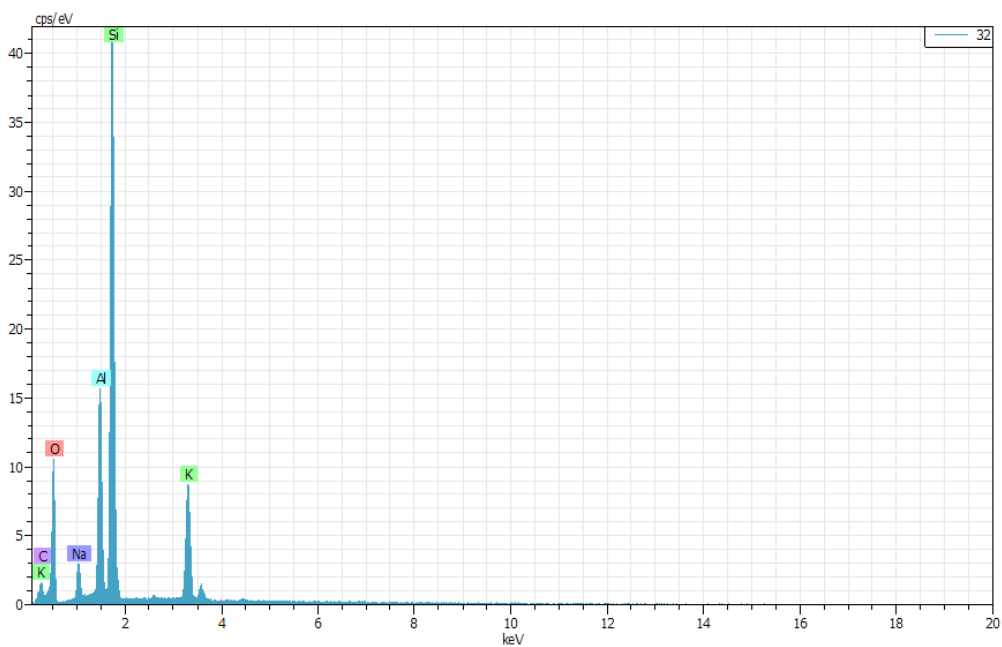


Figure E.3: EDS spectra for alkali feldspar (sanidine) -  $\text{Na}_{0,3}\text{K}_{0,7}\text{AlSi}_3\text{O}_8$ .

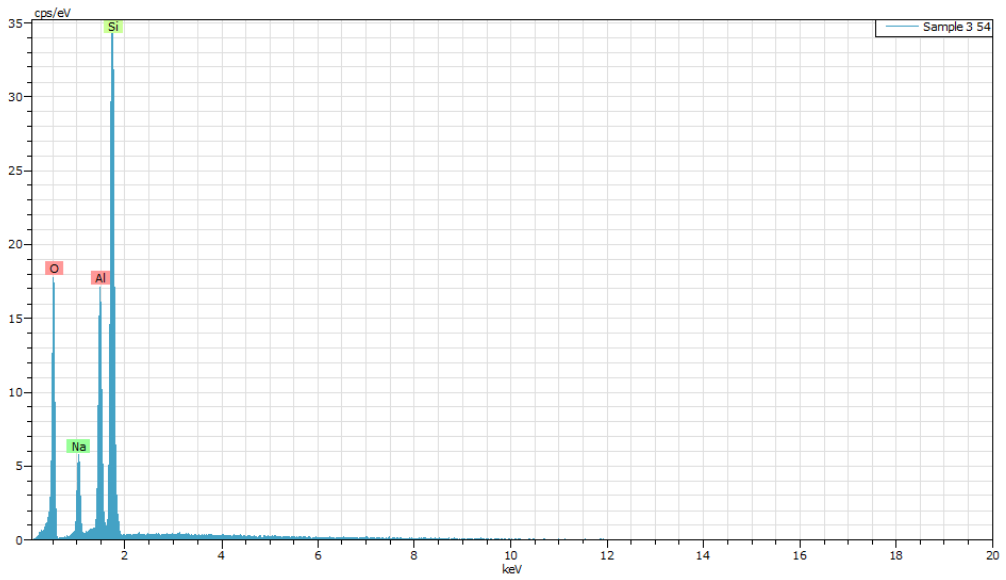


Figure E.4: The resulting EDS spectra of albite -  $\text{NaAlSi}_3\text{O}_8$ .

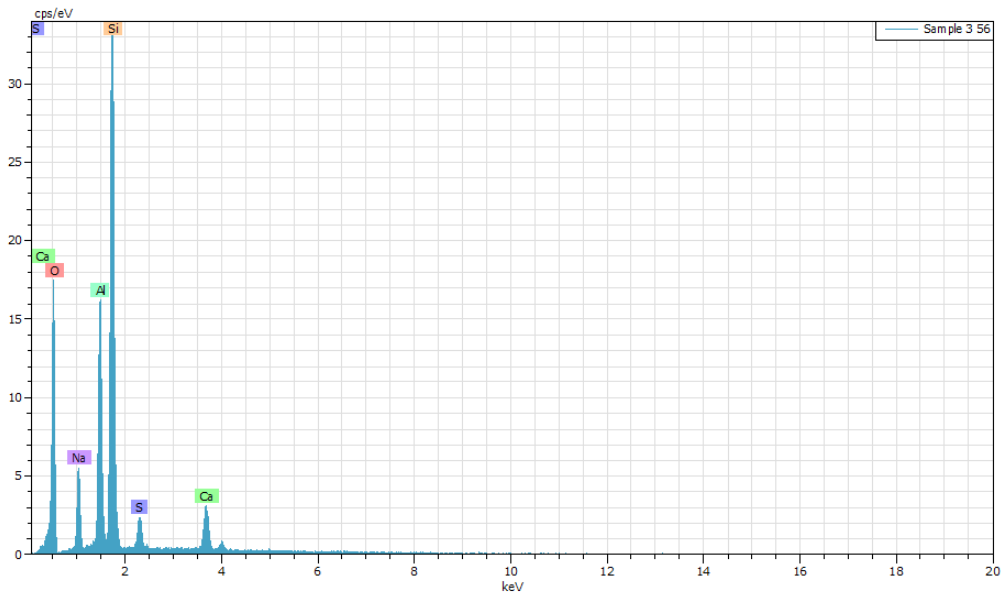


Figure E.5: The resulting EDS spectra for plagioclase (andesine): 33% albite -  $\text{NaAlSi}_3\text{O}_8$ , 67% anorthite -  $\text{CaAl}_2\text{Si}_2\text{O}_8$ .

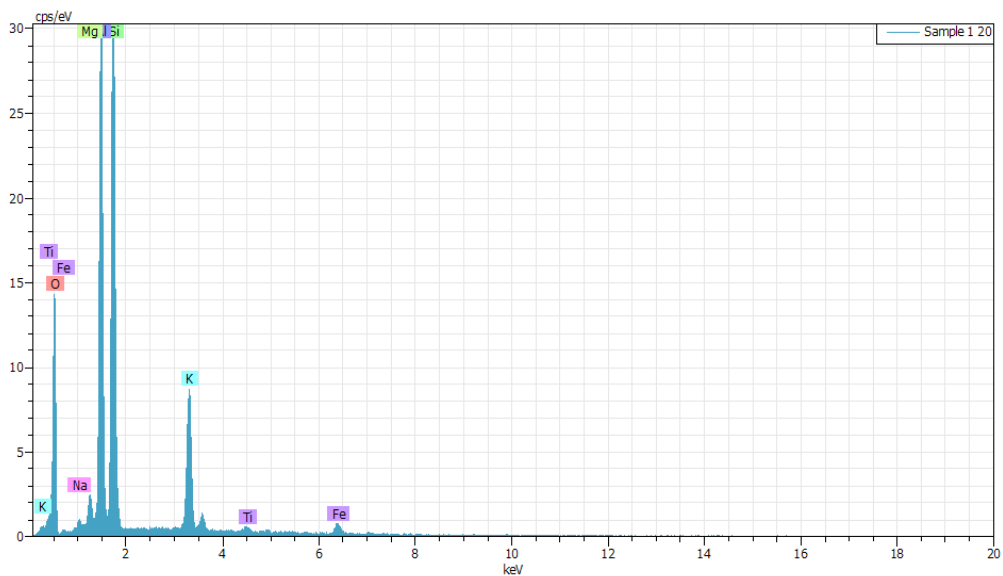


Figure E.6: The resulting EDS spectra for muscovite -  $KAl_2(AlSi_3O_{10})(F,OH)_2$ .

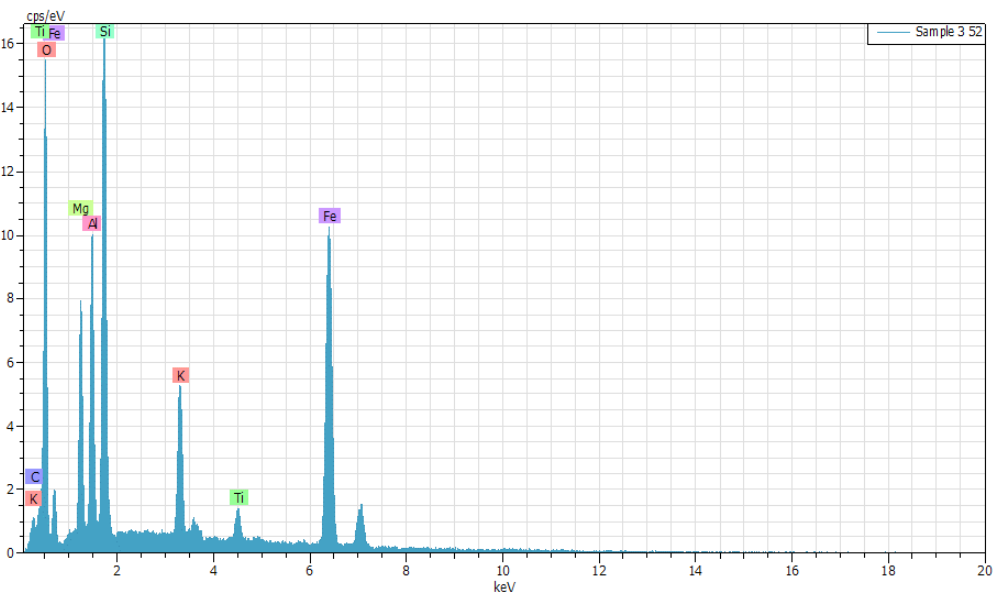


Figure E.7: The resulting EDS spectra for biotite -  $K(Mg,Fe)_3AlSi_3O_{10}(F,OH)_2$ .

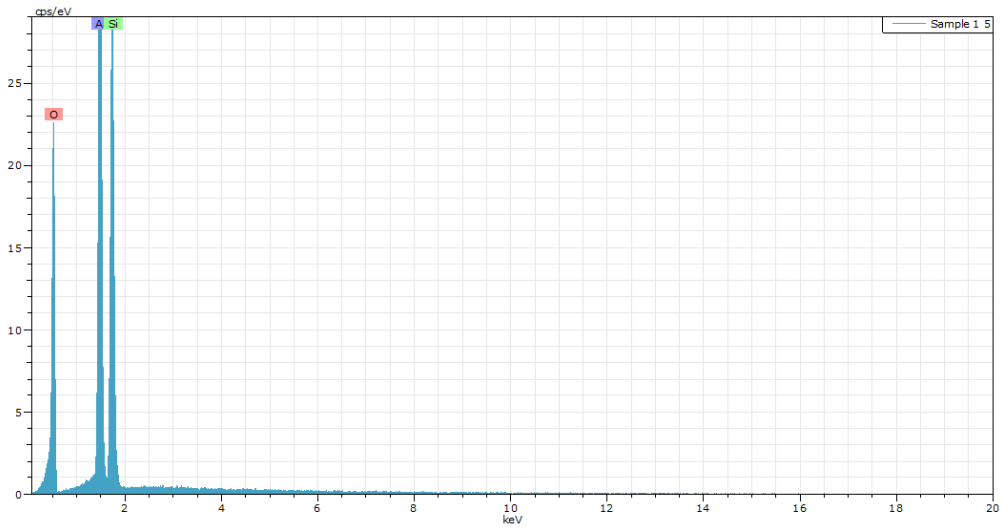


Figure E.8: The resulting EDS spectra for kaolinite -  $\text{Al}_4[\text{Si}_4\text{O}_{10}](\text{OH})_8$ .

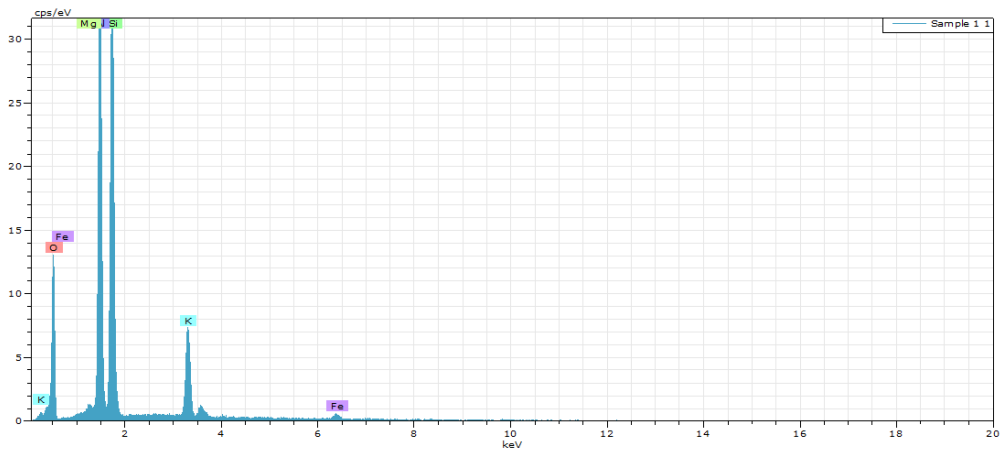


Figure E.9: EDS spectra for illite -  $\text{K}_{1.5}(\text{Si}_8\text{Al}_{1.5}(\text{Al}_4\text{Fe}_4\text{Mg}_4)\text{O}_{20}(\text{OH})_4$ .

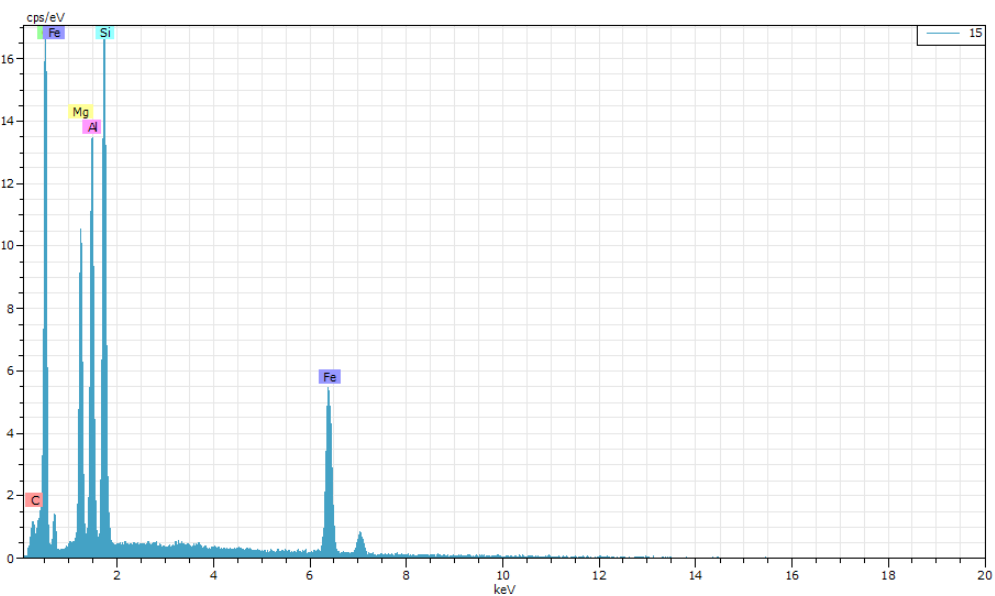


Figure E.10: Chlorite -  $(\text{Mg}, \text{Fe}^{2+}, \text{Fe}^{3+}, \text{Mn}, \text{Al})_{12}[(\text{Si}, \text{Al})_8 \text{O}_{20}](\text{OH})_{16}$ .

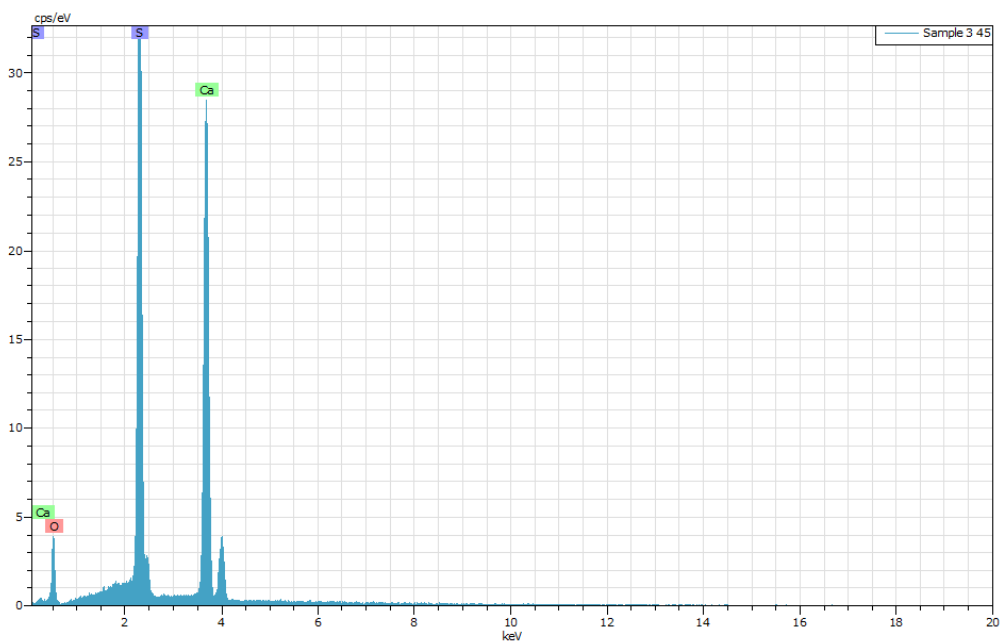


Figure E.11: The resulting EDS spectra for anhydrite -  $\text{CaSO}_4$ .



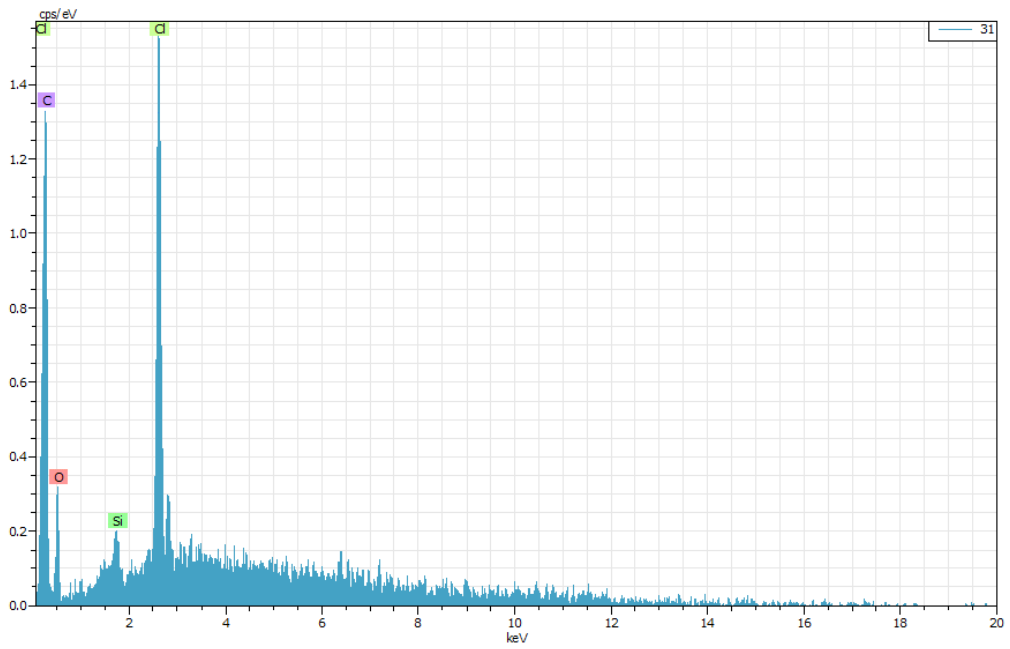


Figure E.12: The resulting EDS spectra for perchlorate salt -  $\text{ClO}_4^-$ .

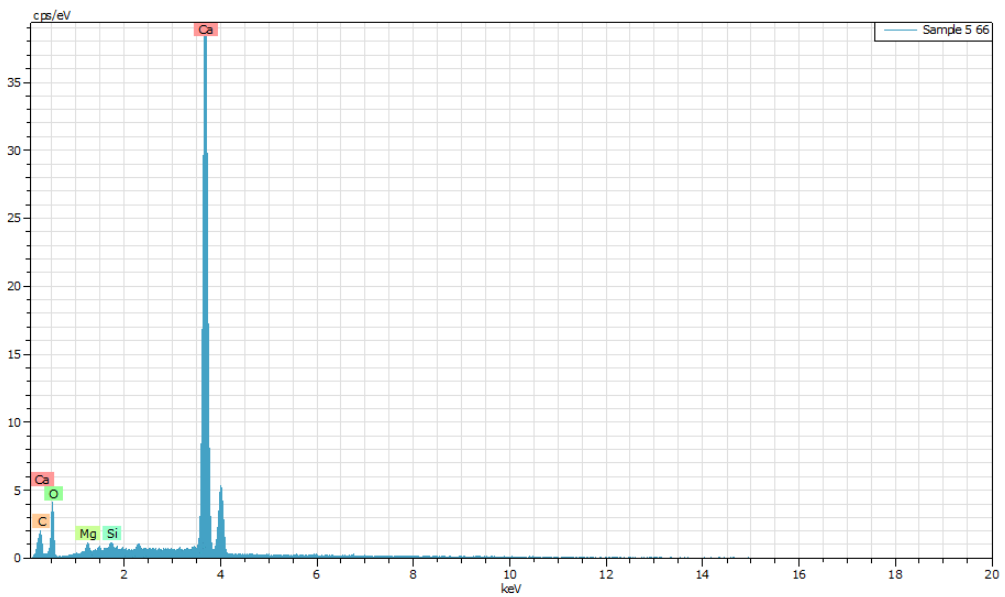


Figure E.13: The resulting EDS spectra for calcite -  $\text{CaCO}_3$ .

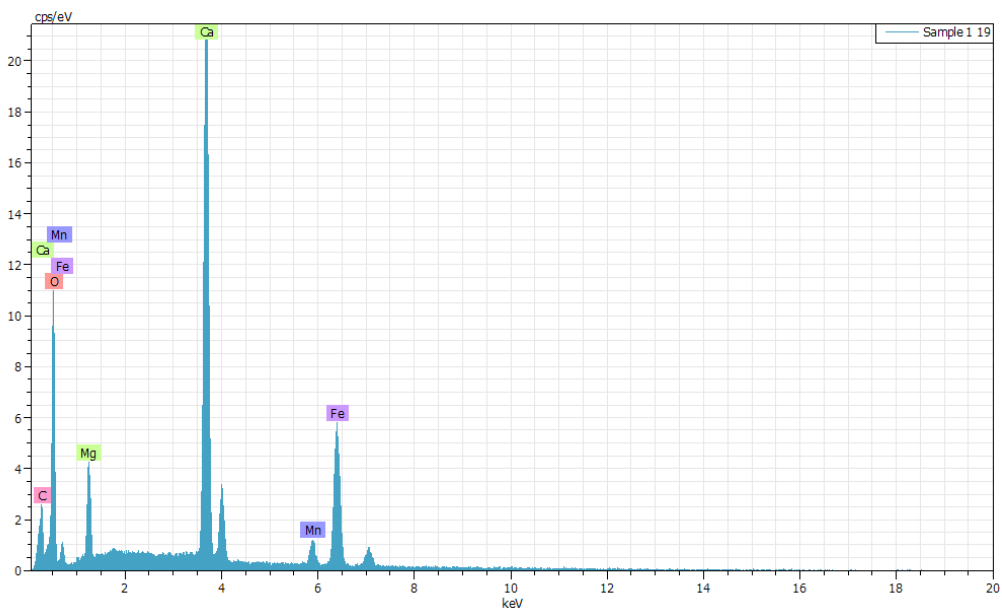


Figure E.14: The resulting EDS spectra for ankerite -  $\text{Ca}(\text{Fe},\text{Mg},\text{Mn})(\text{CO}_3)_2$ .

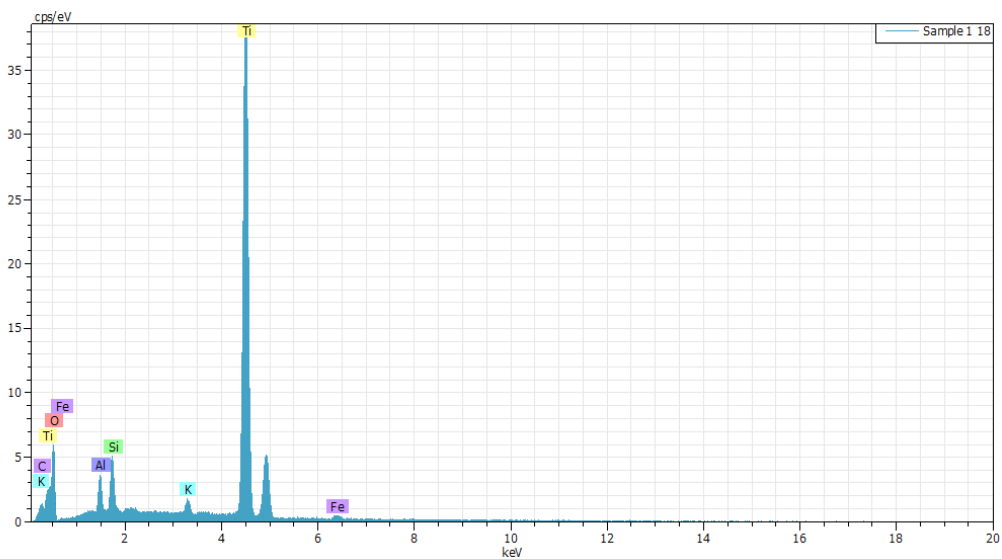
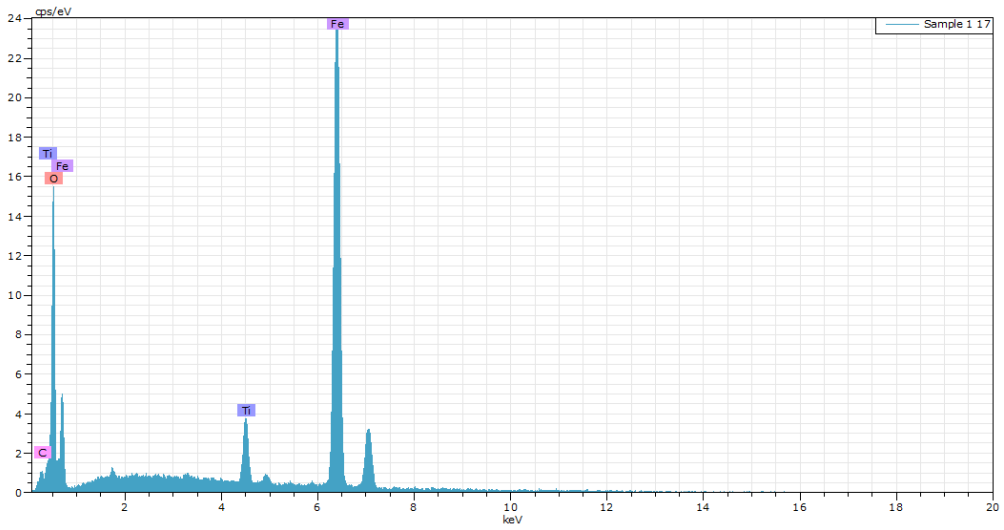
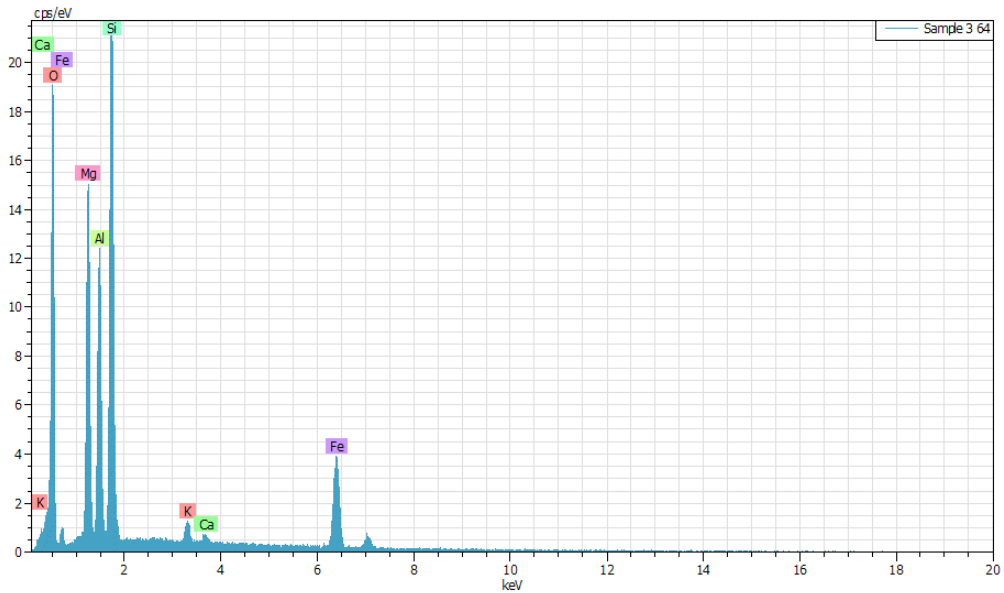


Figure E.15: The resulting EDS spectra for rutile -  $\text{TiO}_2$ .



**Figure E.16:** The resulting EDS spectra for ilmenite -  $\text{FeTiO}_3$  and Iron oxides -  $\text{Fe}_x\text{O}_{x+1}$ .



**Figure E.17:** The resulting EDS spectra for pyrope-almandine garnet -  $\text{Mg}_3\text{Al}_2\text{Si}_3\text{O}_{12}\text{-Fe}_3\text{Al}_2\text{Si}_3\text{O}_{12}$ .

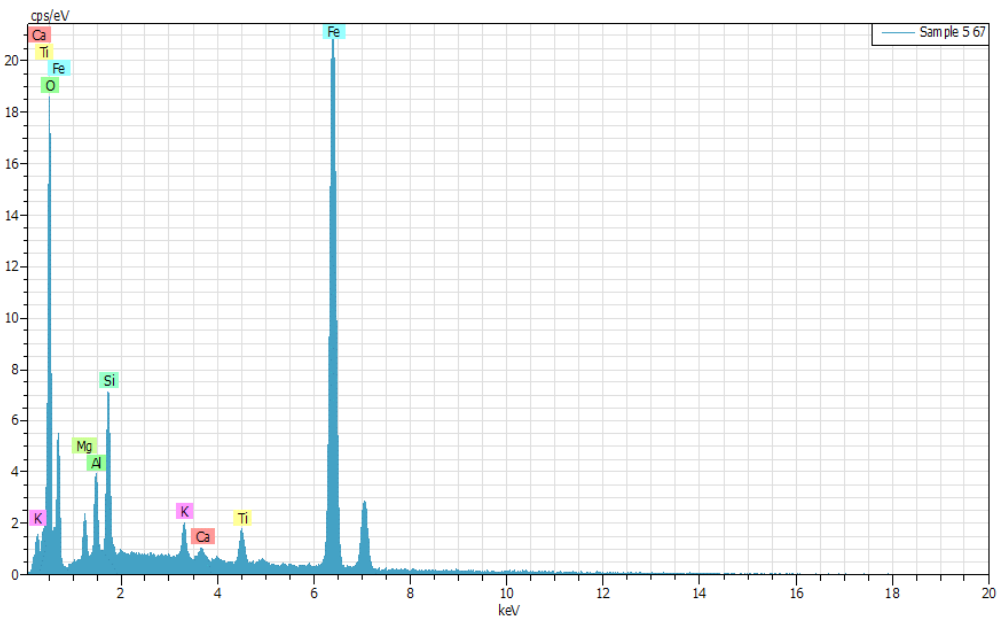


Figure E.18: The resulting EDS spectra for iron oxides -  $Fe_xO_x$ .

# Appendix F

## XRD results

Table F.1, illustrates an overview of the XRD results. Muscovite, illite, biotite and sericite fall within the mica group. The feldspars are grouped into the K-feldspar group and the plagioclase group.

**Table F.1:** Overview of the XRD results.

<b>Sample</b>	<b>1</b>	<b>3</b>	<b>5</b>	<b>11</b>	<b>12</b>	<b>13</b>
<b>Quartz</b>	35%	11%	22%	29%	38%	24%
<b>K-feldspar</b>	3%	2%	7%	9%	11%	6%
<b>Plagioclase</b>	<1%	6%	22%	35%	32%	30%
<b>Analcime</b>	-	8%	-	-	-	-
<b>Mica</b>	21%	10%	32%	6%	5%	21%
<b>Calcite</b>	-	10%	8%	9%	12%	10%
<b>Dolomite</b>	13%	46%	-	-	-	-
<b>Anhydrite</b>	-	1%	-	-	-	-
<b>Halite</b>	4%	-	-	-	-	-
<b>Siderite</b>	8%	<1%	-	-	-	-
<b>Ankerite</b>	15%	-	-	<1%	<1%	-
<b>Pyrite</b>	<1%	<1%	<1%	<1%	<1%	<1%
<b>Chalcopyrite</b>	<1%	-	-	-	-	-
<b>Pyrrhotite</b>	-	-	<1%	-	-	<1%
<b>Kaolinite</b>	2%	-	-	-	-	-
<b>Smectite</b>	-	Present	-	-	-	-
<b>Chlorite</b>	-	5%	9%	12%	1%	9%

